University of Massachusetts Amherst
ScholarWorks@UMass Amherst

Doctoral Dissertations 1896 - February 2014

1-1-1995

Nitrogen chemistry in the interstellar medium.

Douglas McGonagle
University of Massachusetts Amherst

Follow this and additional works at: https://scholarworks.umass.edu/dissertations_1

Recommended Citation

McGonagle, Douglas, "Nitrogen chemistry in the interstellar medium." (1995). *Doctoral Dissertations 1896 - February 2014*. 1954.
https://doi.org/10.7275/f47y-ee68 https://scholarworks.umass.edu/dissertations_1/1954

This Open Access Dissertation is brought to you for free and open access by ScholarWorks@UMass Amherst. It has been accepted for inclusion in Doctoral Dissertations 1896 - February 2014 by an authorized administrator of ScholarWorks@UMass Amherst. For more information, please contact scholarworks@library.umass.edu.

NITROGEN CHEMISTRY IN THE INTERSTELLAR MEDIUM

A Dissertation Presented

by

Douglas McGonagle

Submitted to the Graduate School of the
University of Massachusetts Amherst in partial fulfillment
of the requirements for the degree of

Doctor of Philosophy

September 1995

Department of Physics and Astronomy

© Copyright Douglas McGonagle 1995

All Rights Reserved

NITROGEN CHEMISTRY IN THE INTERSTELLAR MEDIUM

A Dissertation Presented

by

DOUGLAS MCGONAGLE

Approved as to style and content by:

William M. Irvine, Chair

C. Read Predmore, Member

F. Peter Schloerb, Member

Mark Heyer, Member

Charles Dickinson, Outside Member

John F. Dubach, Department Head
Department of Physics and Astronomy

Acknowledgments

On my first day as a graduate student at UMass, Prof. William Irvine stopped me in the hallway and asked if I would be interested in a research assistantship with FCRAO; that is how I became a radio astronomer. Later that first year, I attended a department colloquium given by Dr. Lucy Ziurys. I don't remember what the talk was about but before she began, Lucy announced that she was beginning a search for interstellar NO and that this might make a good second year project for a grad student; that is how I got involved with interstellar nitrogen chemistry. Several years later, when I ran afoul of the Committee for the Review of Academic Progress, Prof. Read Predmore championed my cause before the faculty; that is how I was granted the privilege to write this dissertation. To Bill, Lucy, and Read I wish to extend my most heart felt thanks and appreciation. Your patiences, support and encouragement have made this day possible. Again, thank you.

Not only did Bill Irvine provide me with a stipend, but he also agreed to be my thesis advisor. Though I am sure I have given Bill many an occasion to rue that decision, he has always suffered his duties as my advisor with patiences and good humor, and for that I am most grateful.

In this bureaucratic age, any noble endeavor must, in the fullness of time, spawn an oversight committee, and my thesis is no different. To the members of my thesis committee, Prof. Mark Heyer, Prof. Read Predmore, and Prof. Pete Schloerb of FCRAO, and Prof. Charles Dickinson of Polymer Science and Engineering, I wish to express my thanks and appreciation for your encouragement and support.

I wish to thank my collaborators, Dr. Masatoshi Ohishi of the Nobeyama Radio Observatory, and Dr. Shuji Saito of the Institute for Molecular Science (Japan) for

their help and encouragement. Thanks also to Dr. Sheldon Green of NASA/Goddard and Prof. David Flower of The University at Durham (UK) for their helpful correspondence. I would also like to thank the staff of NRAO Green Bank and NRAO Kitt Peak for their assistance during my observing runs at those observatories. I especially wish to thank Dr. Philip Jewell and Mr. Paul Hart of Kitt Peak.

Since I have also done my undergraduate work at UMass, I would like to take this opportunity to thank two of my undergraduate professors, Prof. Thomas Arny of the astronomy faculty at UMass and Prof. Roger B. Nelsen who was then on sabbatical from the math department at Lewis and Clark University. I wish to thank Tom for his kind and encouraging counsel when times got tough and I might have otherwise lost heart. Likewise, Prof. Nelsen was a source of encouragement during my first semester at UMass. When, after much coaching, I passed Prof. Nelsens' calculus course, I promised myself that I would thank him if ever I managed to earn a Ph.D. Prof. Nelson: thank you for taking the time and having confidence in me.

Behind every new Ph.D. there is a hoard of graduate students who helped him with his homework, assisted him with his observations, and provided support when support was needed. The astronomy department graduate students at UMass are, without a doubt, one of the finest group of people I have ever had the honor of being associated with (for the other group, see FCRAO staff below). First, let me thank my classmate Lori Allen for her kindness, support and friendship over these past years. I wish to thank my good friend David Hiriart for supplying me with encouragement when I needed it. I wish to thank Prof. German Cortes for his friendship and for helping me with my math homework. Special thanks go to Ted Bergin who has graciously allowed me to present unpublished results from his own thesis and who has always made time to talk astronomy. I wish to thank Michael Wenz, Michael Rudenko (honorary grad student), Dr. Gerald Moriarty-Stephens, and Dr. Young Chol Minh for teaching me how to conduct astronomical observations.

Finally, I wish to single out for special consideration Gene Lauria and Jimmy Dickens for their encouragement, support, and friendship. May all of you achieve your goals.

The staff at FCRAO are the most consciences group of professionals I have had the privilege to work with. I especially wish to thank Engineers Ronna Erickson and Ron Grosslein for their friendship and help over the years. I wish to thank Maryanne Laukaitis, Ta-Chun Li, Paul Luippold, John Karakla, Barry Stone and Mike Brewer for helping me with my observatory duties. I would also like to thank Tom Scott, Kelley Smith, and Bill Olanyk. I wish to express my special thanks to the office staff, Jackie Golonka, Pam Barlow, Sally Rule, Barbara Keyworth, Denise Parent, and Jan Whitaker for warning me when Bill was not in the best of moods, taking care of my travel advances, keeping the paychecks coming, and, most importantly, for being my friends.

For myself, the Ph.D. support group extends well beyond the astronomy department and the following individuals have all played an important role in my success. First, special thanks to my oldest and closest friend, Gordon Tinkham for being a constant source of encouragement, and to Frank Mehigan. To my brothers, Steven and Gary, thank you for supporting me. To Case Van Derstelt and his family, especially Arlene and Case Jr of loving memory, thank you for welcoming me into your home and into your family. Thanks go to John Gawienowski for his help with the black art of chemistry and to his family who have been so kind to me over the years. I wish to thank the members of the Newman Community, and in particular, Fr. Lee Gilbertson, Fr. Richard Bondi and Fr. Francis Lavelle for all their kindness and support. These individuals have all helped me to achieve my dream by placing into action Cardinal Newmans' motto, "*cor ad cor loquitur*", and for that I will be eternally grateful. To all those mentioned and to the many more which limited space does not allow me to name, *pax tecum.*

Finally, I wish to thank my first and most important teachers. Whatever I have or will achieve in this life will be as a direct result of the love and the Faith they have given to me. As a small token of my love for them, and of my gratitude for all they have sacrificed for me, I dedicate this dissertation to my parents,
Arthur F. and Barbara E. McGonagle.

It is done — *Agimus tibi gratias omnipotens Deus, pro universis beneficis tuis: Qui vivis et regnas in saecula saeculorum!*

Abstract

NITROGEN CHEMISTRY IN THE INTERSTELLAR MEDIUM

September 1995

Douglas McGonagle, B.S., University of Massachusetts Amherst

Ph.D., University of Massachusetts Amherst

Directed by: Professor William M. Irvine

We have carried out radio observations for the interstellar molecules NO, NS, and HCCN in order to investigate the role of nitrogen in the chemistry of the interstellar medium (ISM). Abundances of these species and implications for chemistry models are discussed.

The first detection of interstellar nitric oxide (NO) in a cold dark cloud (L134N) is reported, as well as confirming a subsequent detection towards TMC–1. The inferred NO fractional abundance relative to molecular hydrogen for L134N is $f_{NO} \sim 5 \times 10^{-8}$, and for TMC–1 is $f_{NO} \sim 2 \times 10^{-8}$. These fractional abundances are in good agreement with predictions of quiescent cloud ion-molecule chemistry.

The first detection of interstellar nitrogen sulfide (NS) in cold dark clouds is reported. The inferred fractional abundance for TMC–1 is $f_{NS} \sim 8 \times 10^{-10}$, and in L134N is $f_{NS} \sim 6 \times 10^{-10}$. The NS fractional abundances are significantly higher than those predicted by some recent gas-phase ion-molecule models. Our astronomical observations of NS have led to new laboratory spectroscopy which has resulted in more accurate NS transition frequencies.

We have carried out the first comprehensive survey of NS towards regions of massive star formation. The inferred fractional abundance of NS for sources with extended, optically thin emission ranges from $0.5 - 2 \times 10^{-11}$, which is in good agreement with some recent gas-phase ion–molecule chemistry models developed for cold dark cloud conditions. We have mapped the distribution of NS towards

OMC–1, where the NS integrated line intensity was found to be strongly peaked towards the (KL) position, but to extend all along the Orion ridge.

We have conducted a deep search for HCCN towards TMC–1 and several giant molecular clouds (GMC's); HCCN was not detected in any of the sources. The inferred fractional abundance upper limit for TMC–1 is $f_{HCCN} \leq 2\times10^{-10}$. The HCCN total column density upper limit towards GMC's is $N_{HCCN} \leq 4 - 10 \times 10^{13} \mathrm{cm\,s^{-1}}$.

Finally, a spectral survey of Orion–KL has been carried out in the 2 mm band covering the frequency range 159.6 – 170.4 GHz, using the FCRAO 14 m radio telescope. Over 235 spectral lines were detected, including $\sim$35 unidentified features. We report on the tentative detection of a new interstellar molecular-ion, H_2COH^+.

Table of Contents

List of Tables

List of Figures

Chapter 1

Introduction

The space between the stars, once thought to be void and of little interest, is now known to be a rich and dynamic medium from which the stars themselves are formed. This void-filling medium is not uniformly dispersed throughout the Galaxy, but shows a great propensity for gathering into massive, dense clouds of gas and dust. These clouds can be loosely classified into two types, those without a significant internal heating source such as a protostar, and those which do have pockets of active star formation. Lacking an internal heat source, modest sized quiescent dark clouds are cold; their gas kinetic temperature is typically $T_K \sim 10$ K. Regions of active star formation occur most prominently in the more massive clouds. In the vicinity of these embedded young stellar objects the gas temperature is comparatively hot, $T_K > 30$ K, and outflows from these young stars induce turbulence in the cloud material. Away from the regions of star formation, though, the massive clouds appear to be similar to the quiescent cold dark clouds (*see* Bergin 1995). What occurs within a quiet cloud that causes a portion of it to be transformed into a turbulent, hot region of star formation is an active topic of astronomical research in which astrochemistry plays an important role.

The intersellar medium (ISM) is composed primarily of hydrogen and helium, with trace amounts of other chemically reactive elements such as carbon, nitrogen, and oxygen. These and other elements come together in the dense clouds to form molecules, the most abundant of which is molecular hydrogen (H_2). Though some one-hundred molecular species and their isotopomers have been detected in the ISM, they are but impurities in what are otherwise giant molecular clouds

(GMC's) of H_2. However, these trace molecules are crucial to the structure of both large and small molecular clouds by virtue of the fact that they form the major pathways for heating and cooling in these clouds, which, in turn, govern cloud evolution. Thus, to understand physical changes in molecular clouds, such as fragmentation and collapse leading to star formation, it is not sufficient to merely study the physical properties of a cloud; it is also necessary to understand the cloud's chemistry. The importance of astrochemistry becomes even more evident when we note that, "... molecular clouds are the most massive objects in the universe whose composition is subject to the chemical bond ..." (Irvine, Goldsmith and Hjalmarson 1987).

To try to understand the interplay between physical and chemical processes, chemists and astrophysicists have constructed computer models in an attempt to simulate the conditions inside molecular clouds. Recent models include over 385 different atomic and molecular species participating in more than 3,000 reactions. (e. g., Hasegawa and Herbst 1993; Hasegawa, Herbst and Leung 1992; Millar, Herbst and Charnley 1991; Millar 1990; Millar and Herbst 1990; Herbst and Leung 1989). Though these simulations are collectively referred to as gas-phase ion–molecule chemistry models, they also include neutral-neutral reactions and, in some cases, interactions between the gas-phase and grain surfaces. Grains may modify the molecular composition of the gas-phase by "freezing" molecules from the gas-phase onto grain surfaces, or by acting as a catalyst for reactions which can not occur, or proceed only slowly, in the gas-phase.

The ion–molecule chemistry models work well for simple oxygen and carbon bearing molecules, but the situation is somewhat less clear for nitrogen-bearing species. Integrating nitrogen into ion–molecule chemistry models has been difficult in part because the important initiating reactions $N^+ + H_2$ and $N + H_3^+$ are slightly endothermic (Herbst and Leung 1989). The astrochemistry of nitrogen is notable

in that some of its important production and destruction pathways are through neutral-neutral reactions as opposed to ion-neutral reactions, which is the case for carbon and oxygen chemistry. Finally, and perhaps most important, there has been a lack of observational information concerning the interstellar abundances of simple nitrogen-bearing molecules with which to constrain the models.

This thesis began as an effort to provide basic observational data on the abundance and distribution of simple diatomic nitrogen-bearing molecules in molecular clouds for the purpose of aiding in the successful incorporation of nitrogen chemistry into ion–molecule chemistry models. Towards this goal, we proposed to survey the abundances of nitric oxide (NO) and nitrogen sulfide (NS) in several molecular clouds, and, where feasible, to investigate their spatial distribution. The NO molecule is important since it is thought to be an intermediary between atomic and molecular nitrogen (N_2), and also to form a link between atomic nitrogen and the hydrides branch of the nitrogen chemistry network, eventually leading to the production of NH_3. Gas phase ion-neutral chemistry models predict that the major nitrogen reservoirs in the ISM are atomic nitrogen and N_2, followed by NO.

In addition, certain nitrogen-bearing molecules can be used as probes for tracing chemical processes which are important to the chemical evolution of the ISM. Thus, the relative abundance of molecules which belong to series such as the cyanopolyynes, $HC_{2n}CN$ ($n = 1 - 5$), have been used to learn about the mechanisms by which carbon atoms are linked together to form chains (e. g., Herbst 1989; Suzuki 1983). The detection of the circumstellar molecule HCCN (Guélin and Cernicharo 1991) and the related interstellar molecule CCO (Ohishi *et al.* 1991) have suggested the possible existence of a new interstellar carbon chain series ($HC_{2n}N$). In these cases the presence of the nitrile group (CN) provides a large electric dipole moment and, thus, easily observed lines. We have undertaken

a search for HCCN towards molecular clouds for the purpose of studying carbon chain formation mechanisms.

Sulfur falls immediately below oxygen in the periodic table, and, given the observed abundance of NO (McGonagle *et al.*, 1990 [Chapter 2]; Ziurys *et al.*, 1991), it is reasonable to investigate NS in molecular clouds. Being a diatomic molecule, NS may have a relatively simple chemistry. Thus, measurements of its abundance will be helpful in understanding its role in the chemistry of the ISM and in studies of interlinked nitrogen-sulfur chemistry. The chemistry of sulfur-bearing molecules in the ISM, like nitrogen chemistry, is not well understood. Gas-phase reactions may need to be augmented with grain surface, and/or high temperature (shock) reactions in order to explain the observed abundances of sulfur-bearing molecules (*see* Minh *et al.*, 1990; Watson and Walmsley 1982; Duley, Millar, and Williams 1980).

Although nitric oxide and nitrogen sulfide were first observed in the millimeter band during the late seventies (NO: Liszt and Turner 1978; NS: Gottlieb *et al.* 1975; Kuiper *et al.* 1975), these detections were restricted to high column density sources such as Sgr B2. Since these initial detections of NO and NS, many advances in instrumentation technology have come about including the development of a millimeter wave focal plane array receiver (Erickson *et al.* 1992), and an increased availability of sensitive 2 mm band receivers. The 2 mm atmospheric window is important to the study of nitrogen chemistry because this spectral range is rich in lines arising from nitrogen-bearing molecules such as NS, isocyanic acid (HNCO), cyanoacetylene (HCCCN), methyl cyanide (CH_3CN), vinyl cyanide (CH_2CHCN), and ethyl cyanide (CH_3CH_2CN) (Ziurys and McGonagle 1995). Also, it contains the fundamental transition of NO.

In this thesis we present the observational results for interstellar NO, NS, and HCCN and discuss the implications for interstellar chemistry. We also present the

first systematic spectral line survey of the 2 mm band made possible by the development of a low noise receiver for this band at FCRAO (Ziurys, Erickson and Grosslein 1988). Each chapter is formatted as an individual paper either published or to be published separately. The published papers have been slightly modified where appropriate to include more resent results. The topics of the chapters which comprise this thesis are as follows: Chapter 2 presents the first detection of NO towards quiescent dark clouds [McGonagle, D., Ziurys, L.M., Irvine, W.M., and Minh, Y.C. (1990), *ApJ*, **359**, 121]; Chapter 3 reports the first detection of NS towards quiescent dark clouds [McGonagle, D., Irvine, W.M., and Ohishi, M. (1994), *ApJ*, **422**, 621]; Chapter 4 surveys the abundance of NS towards regions of active star formation [McGonagle, D., and Irvine, W.M. (1995), *in preparation*]; Chapter 5 presents the results of a search for HCCN in molecular clouds [McGonagle, D., Irvine, W.M., and Horvath, M. (1995), *in preparation*]; Chapter 6 present a 2 mm band spectral line survey towards Orion(KL) [McGonagle D., Ziurys L.M., and Irvine W.M. (1995), *in preparation*]. Finally in Chapter 7, we summarize our findings. Rotational spectra of NO and NS are described in the Appendix. Other published papers directly related to this thesis are the first portion of the 2 mm survey of Orion(KL) (Ziurys and McGonagle 1993) and a survey of NO towards GMC's (Ziurys *et al.* 1991).

1.1 Observed Molecules

1.1.1 Nitric Oxide

Interstellar nitric oxide (NO) has been suggested as an intermediary in the formation of molecular nitrogen (N_2) from atomic nitrogen. Gas phase ion–molecule chemistry models predict NO to be the dominant reservoir for nitrogen after atomic and molecular nitrogen. NO was first observed by Liszt and Turner (1978) in its $J = 3/2 \rightarrow 1/2$ transition at 150 GHz towards the giant molecular cloud Sgr B2. Until recently, NO had only been tentatively identified

towards one other source, Orion(KL) (Wootten, Loren, and Bally 1984; Blake *et al.* 1986). The paucity of NO observations was due, in part, to a lack of low noise 2 mm band receivers. Using the newly developed FCRAO 2 mm receiver, Ziurys *et al.* (1991) surveyed NO towards several regions of active star-formation. They found NO to be a common constituent of warm, dense molecular clouds. We have extended the search for NO to the quiescent dark clouds, and report our results in Chapter 2. The rotational spectrum of NO is discussed in the Appendix.

1.1.2 Nitrogen Sulfide

NS is chemically similar to NO, and the study of these two molecules should complement one another. In addition, the study of NS is a useful step in investigations into nitrogen-sulfur chemistry. NS was first detected by Gottlieb *et al.* (1975) towards the star-forming region Sgr B2 via its $J=5/2\rightarrow 3/2$ transition at 115 GHz. We have carried out a survey of NS towards several Galactic sources in its $J=3/2\rightarrow 1/2$ (69 GHz), $J=5/2\rightarrow 3/2$ (115 GHz) and $J=7/2\rightarrow 5/2$ (162 GHz) transitions. The quiescent dark cloud results are presented in Chapter 3 and the star-forming region results in Chapter 4. The rotational spectrum of NS is discussed in the Appendix.

1.1.3 HCCN

The detection of HCCN towards the evolved star IRC+10216 (Guélin and Cernicharo 1991) has raised the possibility of a new interstellar carbon chain series ($HC_{2n}N$). Through studies of carbon chain series it may be possible to identify the processes by which interstellar carbon chain molecules are formed. We conducted a search for HCCN towards several Galactic molecular clouds at 21 GHz, and report on our findings in Chapter 5.

1.2 Sources

Observations have been carried out towards a variety of dense molecular clouds including quiescent dark clouds, regions of active star formation in the Galactic disk and towards Galactic center clouds. The sources we have most extensively observed include the cold dark clouds L134N and TMC–1 (Chapters 2, 3, and 5), the Galactic disk cloud Orion(KL) (Chapters 4 and 6), and the Galactic center cloud Sgr B2 (Chapters 4 and 6). We have also observed the molecular clouds DR21(OH), G34.3+0.2, NGC7538, S140, W3, and W51 (Chapter 4). In addition to molecular clouds, we have also observed the evolved carbon star IRC+10216 (Chapters 4 and 5).

The morphology and chemistry of L134N, TMC–1, Orion(KL) and Sgr B2 are reviewed by Irvine, Goldsmith, and Hjalmarson (1987) and by the references in the following sections. The morphology and physical conditions of the other molecular clouds observed in this thesis are discussed in Chapter 4.

1.2.1 L134N and TMC–1

The cold, dark, low mass clouds L134N and TMC–1 share similar physical characteristics. Both clouds are located at a distance of $\sim$150 pc, they share similar kinetic temperature ($\sim$10 K) and density ($\sim 10^4$ cm^{-3}). However, these two physically similar clouds have notable differences in their chemical composition. Relatively oxygen-rich molecules, such as SO, SO_2, and HCOOH, are prominent in L134N (Irvine *et al.* 1987; Irvine, Good, and Schloerb 1983), while TMC–1 is richer in carbon-bearing species (e. g., HC_7N, C_4H, Olano, Walmsley and Wilson 1988; CS, HCS^+, Irvine *et al.* 1987). Among the possible explanations for the chemical variations between these two clouds are differing initial elemental abundances and differing cloud ages.

Mapping the distribution of molecular species in these clouds is an ongoing research topic. Swade (1987) extensively mapped the molecular emission of $C^{18}O$, CS, $H^{13}CO^+$, SO, NH_3, and C_3H_2 towards L134N. A model for this source envisions a high-density core ($n \sim 3 \times 10^4$ cm^{-3}), characterized by NH_3, C_3H_2, and $H^{13}CO^+$ surrounded by a lower density envelope ($n \sim 10^{3.5}$) traced by $C^{18}O$, CS ($J = 2 \rightarrow 1$), and SO (Swade and Schloerb 1992). Hirahara *et al.* (1992) mapped carbon-chain and sulfur-containing carbon-chain molecules along the TMC–1 ridge. They found the ridge to be comprised of at least six cores. The spatial distribution of sulfur-containing carbon-chains is correlated with other carbon-chain molecules, and is anticorrelated with NH_3. They conclude that the differences along the ridge can be explained by a difference in the chemical evolutionary state. Currently, some thirty molecular transitions are being systematically mapped towards both TMC–1 and L134N as part of the FCRAO dark cloud chemistry survey (*initial results* Pratap *et al.* 1994).

1.2.2 Orion(KL) and Orion(1.5S)

At a distance from the sun of $\sim$450 pc (Genzel and Stutzki 1989), the giant molecular cloud in Orion is the nearest region of massive star formation. Covering some 30 square degrees, this complex of clouds is perhaps one of the most intensively studied regions in the sky. Of particular interest is a dense core of material which lies behind the familiar HII region M42. Called OMC–1, this core contains the KL infrared nebula (Kleinmann and Low 1967) from which the name Orion(KL) is derived. In addition, OMC–1 contains the infrared source IRc2. Until recently, IRc2 had been thought to be a high luminosity star, which played a significant role in determining the structure, energetics and chemical composition of the Orion(KL) region. However, the role of IRc2 in the structure of the KL region has now been called into question. Menten and Reid (1995) have conducted

VLA observations which have found the centroid of SiO maser distribution in Orion(KL) to coincide precisely with the radio continuum source I (Garay, Moran, and Reid 1987; Churchwell *et al.* 1987) and that both are significantly offset from IRc2. Through analysis of the velocity structure of the SiO emission, Menten and Reid identify source I as the exciting source for the SiO masers. Since the identification of IRc2 as a high luminosity star rested on its association with the SiO maser emission, Menten and Reid suggest that IRc2, like IRc3-7, is not a self-luminous body.

Menten and Reid (1995) have also identified a double radio source centered on the compact IR source n. Source n was first identified by Lonsdale *et al.* 1982 and classified as a reddened star (Wynn-Williams *et al.* 1984). The bipolar radio structure is roughly aligned with the Orion(KL) H_2O maser outflow and is located within the 1σ error box of the center of expansion of the H_2O outflow (Genzel *et al.* 1981). Menten and Reid find source n to be at the center of the dense molecular "hot core", and suggest it may be a significant source of power for the KL nebula.

These new results call into question the paradigm that IRc2 is the dominant energy source of the KL region. The following discussion concerning the velocity structure of the spectral lines observed towards Orion(KL) is based on the "IRc2-centric" model. The reader should be aware that the roles filled by IRc2 in the old model are roughly distributed between sources I and n in the proposed new model.

Orion(KL) displays a complex morphology and chemistry (e. g., Plambeck *et al.* 1982; Vogel *et al.* 1984; Johansson *et al.* 1984; Blake *et al.* 1987; Ziurys and McGonagle 1993). From the velocity structure of the spectral lines observed towards this source, the following four components can be distinguished: the extended ridge, the hot core, the plateau, and the compact ridge. The extended ridge is comprised of quiescent material extending NE to SW through Orion(KL)

and has a gas kinetic temperature of $T_K \sim 50 - 60$ K (Askne *et al.* 1984) close to Orion(KL), lower otherwise (cf., Bergin 1995). The extent of the extended ridge is easily visible in CS and H_2CO emission. Molecular processes are probably dominated by ion-molecule chemistry. A massive clump, possibly residual from the formation of IRc2, is the source of the hot core emission. Radiative heating from IRc2 is thought to induce kinetic temperatures in the hot core of ~ 300 K. The molecular hydrogen density is estimated to be $\sim 10^7$ cm^{-3} (Mauersberger *et al.* 1986). The presence of hydrogenated species such as H_2S, HCN, HDO, NH_3, CH_2CHCN and CH_3CH_2CN, suggests that gas-grain interactions and grain mantle evaporation may be important to the chemistry of the hot core (*see* Minh 1990). The plateau emission provides evidence of an energetic outflow driven by IRc2. Spectral lines arising from sulfur and silicon containing species are prominent, and shock chemistry appears to dominate molecular processes in the plateau ($T_K \sim 100 - 200$ K). Interactions between the IRc2 outflow and quiescent ambient material is thought to give rise to the compact ridge emission, which is also referred to as the southern condensation. This component is the position of peak line emission intensity for many oxygen-rich molecules (Johansson *et al.* 1984; Blake *et al.* 1987). The compact ridge is so-called because the emission region appears to be spatially compact, while the line widths are relatively narrow. Blake *et al.* (1987) estimated the source size to be $\sim 30''$ from observations of oxygen-rich molecules. Observations of methyl cyanide (CH_3CN) led Andersson (1985) to deduce a source size of $\sim 10''$.

The chemical richness of Orion(KL) is evident in the many spectral line surveys conducted towards this source. Surveys have been conducted in the 3mm band (Johansson *et al.* 1984; Turner 1991), the 2mm band (Ziurys and McGonagle 1993), the 1.2mm band (Sutton *et al.* 1985; Blake *et al.* 1986), and in the 0.8mm band (Jewell *et al.* 1989).

Orion(1.5S) lies 1.5 arcmin south of Orion(KL) and appears to include an outflow from a heavily embedded young stellar object (YSO) (Ziurys and Friberg 1987). Observations of the distribution of SiO and CH_3CN in this region suggests a source size of $\sim 25''$, $n(H_2) \sim 10^5$ cm^{-3}, and $T_K \sim 75$ K (Ziurys, Wilson and Mauersberger 1990).

1.2.3 Sgr B2(M)

The star forming region Sgr B2 is one of the largest HII/molecular cloud complexes in the Galaxy, and represents an extreme case of high luminosity star formation. Sgr B2 is one of the best studied of the Galactic center clouds (e. g., Goldsmith *et al.* 1987; Vogel, Genzel and Palmer 1987; Carlstrom and Vogel 1989; Lis and Goldsmith 1989, 1990; Martin-Pintado *et al.* 1990; Gaume and Claussen 1990; Goldsmith *et al.* 1990, 1992; Lis *et al.* 1993; Gordon *et al.* 1993). Located $\sim 120 - 300$ pc from the Galactic center, Sgr B2 is the most massive of a group of dense cloud cores in the central (400–600 pc) region of the Galaxy (Lis, Carlstrom and Keene 1991; Lis and Carlstrom 1993). The Sgr B2 core ($5 - 10$ pc) is rich in molecular species (e. g., Cummins, Linke and Thaddeus 1986; Turner 1989, 1991). Sgr B2 contains OH and H_2O masers, which are grouped into three condensations: north (N), middle (M), and south (S). Different molecular species appear to have different distributions among these condensations; for example SO strongly peaks towards Sgr B2(M), while OCS peaks towards Sgr B2(N) (Goldsmith *et al.* 1987). The first confirmed detections of nitric oxide (NO) and nitrogen sulfide (NS) were both made towards Sgr B2 (NO, Liszt and Turner 1978; NS, Gottlieb *et al.* 1975).

Chapter 2

Detection of Nitric Oxide in Quiescent Dark Clouds

2.1 Summary

We report the first detection of interstellar nitric oxide (NO) in a cold dark cloud, L134N, and confirm the subsequent detection of NO emission towards TMC–1 by Gerin, Viala and Casoli (1993). Nitric oxide was observed by means of its two $^2\Pi_{1/2}$, $J=3/2\rightarrow 1/2$, $F=5/2\rightarrow 3/2$, rotational transition hyperfine components at 150.2 and 150.5 GHz, which occur because of Λ-doubling. The inferred total column density for L134N is $N_{NO} \sim 4\times10^{14}$ cm^{-2} towards the position of peak SO emission in that cloud. The inferred total column density for TMC–1 is $N_{NO} \sim 2\times10^{14}$ cm^{-2} towards the position of peak ammonia emission. These values corresponds to a fractional abundance relative to molecular hydrogen of $f_{NO} \sim 5\times10^{-8}$ and $f_{NO} \sim 2\times10^{-8}$ towards L134N and TMC–1, respectively, and are in good agreement with predictions of quiescent cloud ion-molecule chemistry. NO was not detected towards the position of peak cyanopolyyne emission in TMC–1 to an upper limit of $f_{NO} \leq 1\times10^{-8}$.

2.2 Introduction

Of the abundant elements (H, C, N, O), the least certain chemistry in the dense interstellar medium is that of nitrogen (e.g. Millar 1990). It is consequently important to establish the principal reservoirs for nitrogen in molecular clouds via observations. This is particularly true for cold dark clouds where low kinetic temperature and the absence of external radiation fields make the chemistry

simple. We report here the first detection of nitric oxide (NO) in a dark cloud, L134N, and comment on its chemical significance. We shall also compare our findings towards L134N with more recent detections of NO towards the dark cloud TMC–1.

Models predict that NO will be quite abundant in dense quiescent molecular clouds. For example, Herbst and Leung (1986) predict in their dark cloud model that NO will be the most abundant nitrogen-containing species after N_2 and atomic nitrogen if the elemental abundance ratio in the gas phase C/O < 1. On the other hand, if C/O > 1, as has been suggested as an explanation for the large atomic carbon abundance observed in some dense clouds (Langer *et al.* 1984), Herbst and Leung find that the NO abundance is decreased by two orders of magnitude. One might, therefore, expect significant differences in NO abundance between such dark clouds as TMC–1, which appears to be carbon-rich, and L134N, which contains relatively high abundances of oxygen-containing species such as SO_2 and HCO_2H (Irvine *et al.* 1987). Observational verification of such abundance differences would be very helpful in understanding interstellar chemistry.

NO was first observed astronomically in Sgr(B2) by Liszt and Turner (1978), who measured the $J = 3/2 \rightarrow 1/2$ transition at 150 GHz and obtained a column density of $N_{NO} \sim 2 \times 10^{16}$ cm^{-2} toward this source. Since the initial detection in Sgr(B2), there have been two tentative detections of NO in Orion. While studying high-velocity H_2CO emission toward Orion, Wootten, Loren, and Bally (1984) detected a line near 150.5 GHz at a level of $\sim$ 0.2 K which they tentatively identified as one of the $J = 3/2 \rightarrow 1/2$ Λ-doubling components. Blake *et al.* (1986) tentatively detected NO by its $J = 5/2 \rightarrow 3/2$ transition while conducting an emission-line survey of Orion between 247 and 263 GHz. They estimated the NO column density to be $N_{NO} \leq 1.5 \times 10^{16}$ cm^{-2}. Pwa and Pottasch (1986) have assigned absorption features in high-resolution IUE spectra to NO in diffuse clouds

(cf. Tarafdar and Dalgarno 1990). Subsequent to the observations described here, Gerin *et al.* (1992) observed NO at 2 and 1 mm wavelengths towards the dark cloud L134N and four giant molecular clouds: OMC–1, W51, Sgr B2, Sgr A. NO was first detected towards TMC–1 by Gerin, Viala, and Casoli (1993). To increase the understanding of NO chemistry, we have sought this species in cold dense molecular clouds, using the FCRAO 2 mm receiver (Ziurys, Erickson, and Grosslein 1988). In this chapter, we report our measurements toward the cold dark clouds L134N and TMC–1.

2.3 Observations

Nitric oxide has a $^2\Pi_r$ ground state and thus possesses fine structure, Λ–doubling, and because of the quadrupole moment of the nitrogen nucleus, hyperfine structure (Gallagher and Johnson 1956). The fundamental $J=3/2\rightarrow 1/2$ rotational transition thus consists of 10 hyperfine components, which are grouped into parity–e and parity–f bands due to the Λ–doublets. (The $^2\Pi_{3/2}$ rotation ladder lies $\sim$ 180 K above the ground state and is unlikely to be populated in cold clouds.) The main hyperfine component for both the parity–e and parity–f bands is the $F=5/2\rightarrow 3/2$ transition. Frequencies and relative line strengths of the observed hyperfine components are listed in Table 2.1.

2.3.1 Source: L134N

Measurements of the NO $J=3/2\rightarrow 1/2$, $F=5/2\rightarrow 3/2$, parity–e and parity–f Λ-doublet transitions were carried out during 1989 February and March, using the FCRAO 14 m telescope. At the observing frequency of 150 GHz the FWHM beamwidth was 41 arcsec and the antenna main beam efficiency was $\eta_B \sim 0.42$. The receiver used was a cooled Schottky diode mixer, which was tuned single-sideband; the image sideband was terminated at 20 K. The temperature

Table 2.1. NO Hyperfine Component Parameters

J_u	J_l	F_u	F_l	Parity	Freq.[a] (GHz)	S_F [b]
3/5	1/2	5/2	3/2	e	150.17630	0.250
		5/2	3/2	f	150.54625	0.250

(a) Frequencies from Gallagher and Johnson (1956).

(b) Hyperfine component relative line strengths are normalized to unity over both Λ-doublets.

scale was determined by the chopper-wheel method and is given in terms of T_A^*. The radiation temperature (T_R) is then approximated by $T_R \approx T_A^*/\eta_B$. All temperatures reported in this chapter are T_R. The spectrometer used was a 256 channel filter bank with 100 kHz filter resolution, which corresponds to a velocity resolution of 0.2 km s^{-1} at the observation frequency. The data was taken in frequency-switching mode. Total system temperatures were typically 700 K (SSB) on the sky. Observations were conducted toward the position of peak 3mm SO emission (Swade 1987), which we call L134N(SO). The source position and VLSR value are listed in Table 2.2.

2.3.2 Source: TMC–1

Our initial search for NO towards TMC–1, conducted during 1989 February and March, was unsuccessful (see above section for observation details). Observations of the NO $J = 3/2 \rightarrow 1/2$, $F = 5/2 \rightarrow 3/2$, transition were again carried out at the FCRAO 14 m telescope during March 1992 after improvements had been made to the FCRAO 2 mm receiver. Observational parameters were the

Table 2.2. NO Observations Source List

Source	α(1950)			δ(1950)			VLSR
	hh	mm	ss.s	dd	mm	ss	(km s^{-1})
L134N(SO)	15	51	26.0	-2	43	31	2.6
TMC–1(NH_3)	4	38	16.0	25	42	46	5.9
TMC–1(CP)	4	38	38.6	25	35	45	5.9

same as in the L134N search. All data were taken in a frequency-switching mode, with $\Delta\nu = 2.0$ MHz. Total system temperatures were typically 600 K (SSB) on the sky. Observations were carried out towards the ammonia peak, TMC–1(NH_3), and the cyanopolyyne peak, TMC–1(CP). Source positions and VLSR values are listed in Table 2.2.

2.4 Results

The main hyperfine component, $F = 5/2 \rightarrow 3/2$, of both Λ-doublet members of NO was detected toward L134N(SO), and the spectra are shown in Figure 2.1. The LSR velocity and line width are in the range observed for many other molecular transitions at this position (Swade 1987) within the uncertainties of the laboratory frequency measurements ($\pm$250 kHz) and the resolution of our observational measurements (100 kHz). In fact, the present data suggest that the laboratory frequencies in Table 2.1, particularly for the (f) component, may be slightly low ($\sim$100–200 kHz), although data in other narrow-line sources are needed to confirm this result. The parity-e $J = 3/2 \rightarrow 1/2$, $F = 5/2 \rightarrow 3/2$ hyperfine component was detected towards the TMC–1(NH_3) position, and the spectra is shown in Figure 2.2. We did not detect NO towards the TMC–1(CP) position.

Table 2.3. NO Observed Line Parameters

Source	Parity	RMS (mK)	V_{LSR} (km s^{-1})	T_R (K)	FWHM (km s^{-1})	$\int T_R\,dv$ (K km s^{-1})
L134N(SO)	e	31	2.3	0.45	0.66	0.30
	f	43	2.0	0.33	0.81	0.27
TMC–1(NH_3)	e	40	5.5	0.24	0.71	0.17
TMC–1(CP)	f	36	—	≤ 0.11	0.7[a]	≤ 0.08

(a) FWHM taken from TMC–1(NH_3).

Line parameters for NO detections towards L134N(SO) and TMC–1(NH_3) are given in Table 2.3 along with upper limits for the TMC–1(CP) observations.

Since NO has a very small dipole moment (0.1587 D; Ames and Huebner 1977), the A_u coefficient for the $J=3/2\rightarrow 1/2$ transition is relatively small: $A_u = 3.5\times10^{-7}$ s^{-1}. Therefore, the $J=3/2\rightarrow 1/2$ transitions only require $n(H_2) \sim 10^3 - 10^4$ cm^3 for thermalization. Such densities are likely to be present both in TMC–1 and L134N (Irvine, Schloerb, and Hjalmarson 1985). Consequently, to estimate a column density for NO, we have adopted an excitation temperature range for $J=3/2\rightarrow 1/2$ transitions of $T_{EX} = 5-10$ K, the nominal gas kinetic temperature range for the dark clouds (Irvine, Schloerb, Hjalmarson 1985).

To calculate a column density the following expression was used (see Irvine, Goldsmith and Hjalmarson 1987), which assumes optically thin emission and a Boltzmann population distribution at T_{EX}:

$$N_u = 10^5 \left(\frac{8\pi k\nu^2}{hc^3 A_u S_F f_u}\right)\left[1-\frac{\exp(h\nu/kT_{EX})-1}{\exp(h\nu/kT_{BG})-1}\right]^{-1}\int T_R\,dv\ . \qquad (2.1)$$

In this expression $\int T_R\,dv$ is the total integrated line intensity (K km s^{-1}) of the

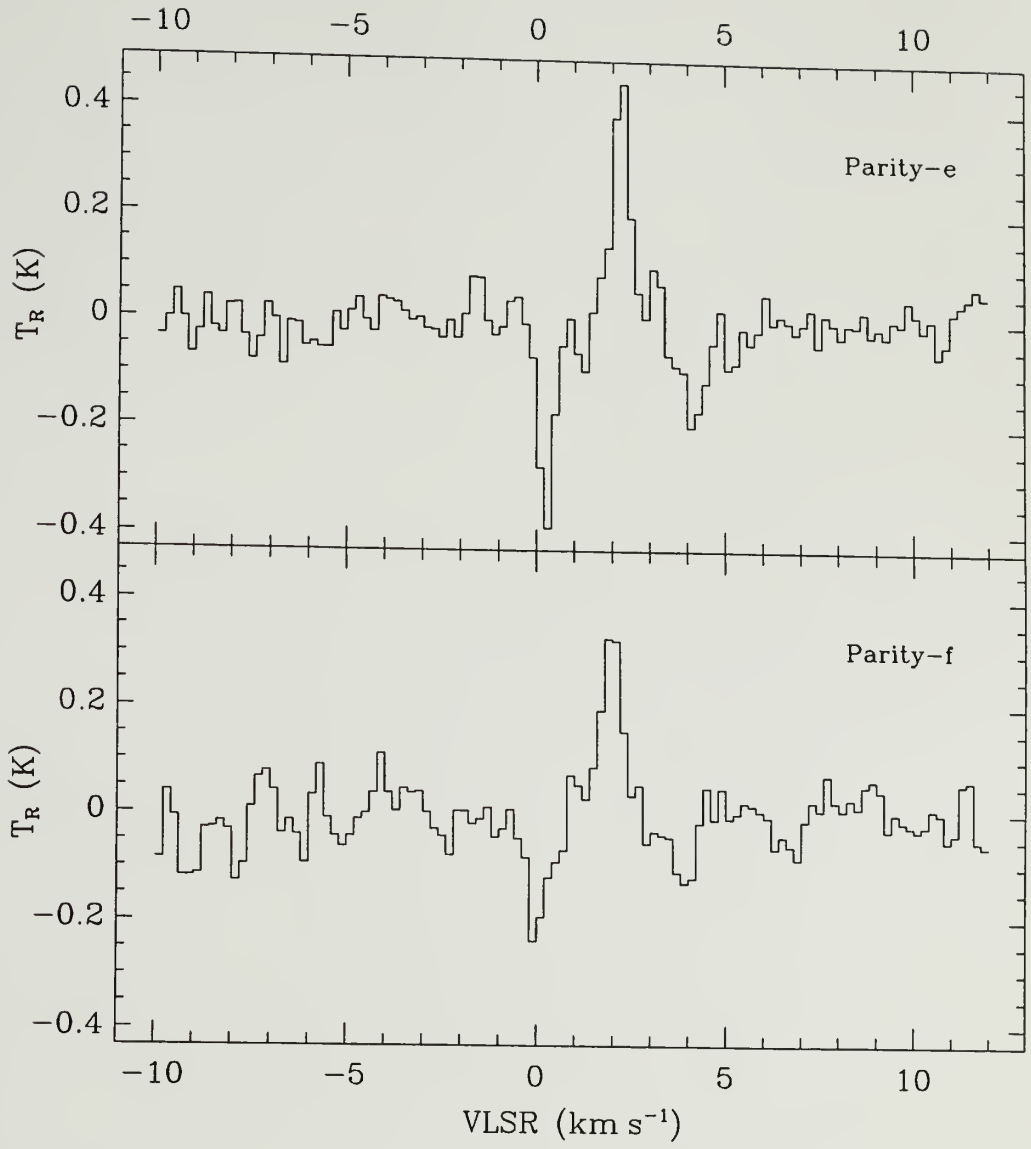

Figure 2.1. Spectrum of the J=3/2→1/2, F=5/2→3/2 Λ-doublet transitions of NO towards L134N(SO). The spectral resolution is 100 kHz (position given in Table 2.2). Frequencies from Gallagher and Johnson (1956). Negative-going spikes are artifacts of frequency switching.

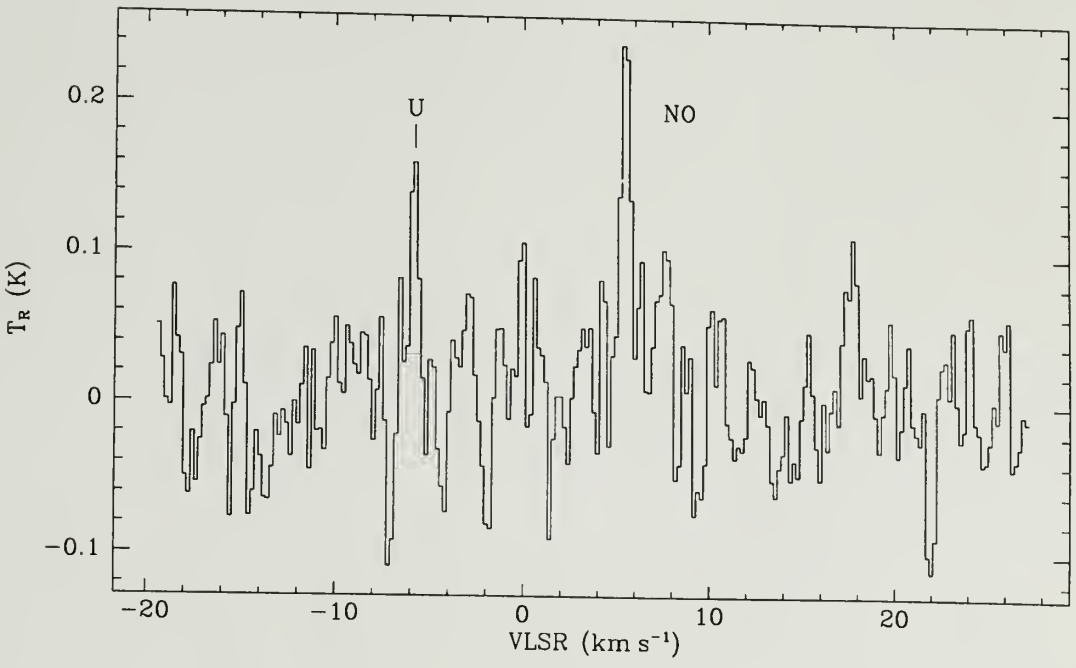

Figure 2.2. Spectrum of the J = 3/2 → 1/2, F = 5/2 → 3/2 parity-e transition of NO towards TMC-1(NH_3). The spectral resolution is 100 kHz (position given in Table 2.2). Frequencies from Gallagher and Johnson (1956). An unidentified spectral feature is also present (see text).

observed hyperfine components and ν is the transition frequency. A_u is the Einstein coefficient of the NO rotational transition, given by

$$A_u = \frac{64\pi^4\nu^3}{3hc^3}\left(\frac{\mu^2}{2J_u+1}S_{J_u}\right) , \qquad (2.2)$$

where J_u is the upper level total angular momentum quantum number (excluding nuclear spin). For pure Hund's case (a) coupling (e.g. Bennett 1970), the rotational line strength for a $J_u \rightarrow J_u - 1$ transition between two single rotational levels of a $^2\Pi_{1/2}$ state is given by:

$$S_{J_u} = \frac{4J_u^2 - 1}{4J_u} . \qquad (2.3)$$

More complicated expressions for intermediate Hund's case coupling do not change the results for NO to better than 1% (Gerin *et al.* 1992). The hyperfine component relative line strength, S_F, is normalized to unity over both Λ-doublet bands (Tatum, 1986; *see* Table 2.1). T_{EX} is the excitation temperature and T_{BG} is the microwave background radiation temperature, $T_{BG} = 2.7$K. f_u is the fractional population in the upper level. The partition function was calculated by an explicit summation, using the expressions outlined by Ames and Huebner (1977).

Using equations (2.1–3) and assuming $T_{EX} = 10$ K, column densities and fractional abundances relative to molecular hydrogen have been calculated for each source and are listed in Table 2.4. A total NO column density of $N_{NO} = 4\times10^{14}$ cm^{-2} was obtained toward L134N. This value corresponds to a fractional abundance, relative to molecular hydrogen, of $f_{NO} \sim 5\times10^{-8}$, using a total column density $N_{H_2} \sim 8.2\times10^{21}$ cm^{-2} [Swade 1987: by using $N(C^{18}O)/N_{H_2} = 1.7\times10^{-7}$]. Taking account of plausible ranges in the rotation temperature (5–10 K) and observational uncertainties, this value should be accurate to within a factor of 2.

Following the same procedure outlined above, we find towards TMC–1(NH_3) a total NO column density of $N_{NO} = 2\times10^{14}$ cm^{-2} assuming $T_{EX} = 10$ K, following

Table 2.4. NO Column Densities and Fractional Abundances

Source	Parity	N_u (cm^{-2})	N_{NO} (cm^{-2})	N_{H_2} (cm^{-2})	f_{NO}
L134N(SO)	e	1.7×10^{14}	4.5×10^{14}	8.2×10^{21}	5×10^{-8}
	f	1.5×10^{14}	4.0×10^{14}	8.2×10^{21}	5×10^{-8}
TMC–1(NH_3)	e	9.8×10^{13}	2.5×10^{14}	1×10^{22}	2×10^{-8}
TMC–1(CP)	f	$\leq 4.6\times10^{13}$	$\leq 1.2\times10^{14}$	1×10^{22}	$\leq 1\times10^{-8}$

Gerin *et al.* (1992). This corresponds to a fractional abundance of $f_{NO} \sim 2\times10^{-8}$ (using $N_{H_2} = 10^{22}$; Irvine, Goldsmith, and Hjalmarson 1987). The NH_3 position used towards this source is also the 3 mm HCO^+ emission peak (Guélin, Langer, and Wilson 1982). This position was viewed as more favorable to oxygen-containing molecules than is the frequently observed cyanopolyyne position. In addition to NH_3 and HCO^+, the molecules H_2S and SO peak at this position in TMC–1, making this location more similar to L134N than the TMC–1 cyanopolyyne peak (Olano, Walmsley, and Wilson 1988; Minh, Irvine, and Ziurys 1989; and SO data from P. Friberg, private communication).

We did not detect NO towards the TMC–1(CP) position. Using a limit of three times the spectrum baseline rms and $T_{EX} = 10$ K, we place an upper limit towards TMC–1(CP) of $N_{NO} \leq 1\times10^{14}$ cm^{-2}, which implies a fractional abundance of $f_{NO} \leq 1\times10^{-8}$. Our upper limit is nearly one third the level of the NO detection reported by Gerin, Viala, and Casoli (1993) towards TMC–1(CP) using the IRAM 30 m telescope. They report a total NO column density of $N_{NO} = 2.7 \pm 0.5\times10^{14}$ cm^{-2}, which corresponds to a column density relative to molecular hydrogen of, $f_{NO} = 2.7\times10^{-8}$. This apparent discrepancy may be understood if we assume that the NO emission originates from a small region in

this source so that the differing estimates of the total column density may be the result of beam dilution. The Gerin *et al.* data were taken using 5 point maps which were than averaged together giving an effective FWHM beam width of $\sim$23 arcsec. Comparing this with the FWHM beam width of 41 arcsec for the FCRAO 14 m telescope, the ratio of FCRAO to IRAM solid angles on the sky is $\sim$3.2 which is consistent with the observations.

2.5 Discussion

Nitric oxide, being a diatomic molecule, is likely to have a simple chemistry. Thus, measurement of its abundance may serve as a good test case for chemical models for quiescent, dark clouds. As outlined by Graedel, Langer, and Frerking (1982), the principle reaction path leading to the formation of NO is

$$N + OH \rightarrow NO + H, \tag{2.4}$$

with a reaction rate $k \sim 10^{-12}$ $cm^3 s^{-1}$. It is interesting to note that this is a neutral-neutral reaction, as opposed to an ion-molecule reaction. Some of the principal destruction routes are also neutral-neutral reactions, including reactions with neutral atomic C, O, and N, although there is inconsistency in the literature as to whether any of these routes may have activation barriers which could make them unimportant in cold clouds (see Langer and Graedel 1989; Smith 1988; Crutchers and Watson 1985). Nitric oxide is also destroyed by ion-molecule reactions, particularly reactions with ions such as C^+, He^+, H_3^+, H^+, and S^+ (C. Leung, private communication).

The ion-molecule chemical models of Langer and Graedel (1989), Herbst and Leung (1989), and Millar, Leung and Herbst (1987), which utilize typically more than 2000 reactions, agree in predicting an NO abundance $\sim 10^{-7}$ for dark cloud conditions. This value is in good agreement with our observed value in L134N. We

note that Herbst and Leung (1989) find somewhat lower values ($\sim 3\times10^{-8}$) at the "early times"($t\sim3\times10^5$ yrs) which produce the best match for many molecular species with abundances observed in TMC–1. Indeed, our value for the total column density of NO towards TMC–1 is in excellent agreement with the "early time" models and suggests that TMC–1 is in a somewhat earlier evolutionary state than L134N.

Hasegawa, Herbst, and Leung (1992, hereafter HHL92) expanded the large gas-phase reaction network of Herbst and Leung (1989) to include grain-surface chemistry. In this model, the gas temperature was held at 10 K and the density at $n(H) = 2\times10^4$ cm^{-3}, specifically to reproduce conditions in quiescent, dark clouds. Though NO was included as both a reactant and product in the grain-surface chemistry, this had no direct effect on the gas-phase NO abundance since the only desorption process allowed was thermal evaporation. With a dust temperature of 10 K, only H, H_2, and He had meaningful evaporation times. Using initial abundances found in pseudo-time-dependent gas-phase models, where hydrogen is molecular and easily ionized heavy atoms are found in their ionized state, the HHL92 model results are similar to those of gas-phase models through "early time" and agree well with observed abundances in TMC–1. The predicted NO abundance most closely matches our TMC–1(NH_3) abundance at $t=3.2\times10^5$ yrs, when $f(NO)=2.7\times10^{-8}$, and is in agreement with the NO abundance found at "early time" by Herbst and Leung (1989). This result is consistent with the suggestion that TMC–1 may be at an earlier state of evolution as compared to L134N. Hasegawa and Herbst (1993) further expanded this model to include the effects of H_2 tunnelling and cosmic ray induced desorption. The addition of these details did not significantly change the results for NO.

An alternative possibility to explain the clear differences in chemistry between these two physically similar clouds concerns the gas phase carbon-to-oxygen ratio

(C/O). As stated in the Introduction, Herbst and Leung (1986) find that NO is very sensitive to this ratio, with its abundance declining by two orders of magnitude between the model with a "standard" ratio and a model with C/O = 1.28. The latter value, reflecting a putative differential depletion of oxygen onto grains (perhaps as H_2O ice), was suggested by Langer *et al.* (1984) as a possible explanation for the large abundance of many carbon-rich compounds in clouds such as TMC–1. Our observations toward L134N are in approximate agreement with model predictions where a cosmic C/O ratio is assumed. Since L134N is not thought to be particularly carbon-rich (Irvine, Goldsmith, and Hjalmarson 1987), agreement with the model where C/O < 1 is encouraging. Our observation towards TMC–1(NH_3) falls midway between the "standard" and the C/O = 1.28 model predictions, which suggests that NO may be less prevalent in carbon-rich regions. We note, however, that Langer and Graedel (1989) find much less dependence of the NO abundance on the C/O ratio in their most recent calculations.

It is interesting to investigate the nitrogen chemistry further in L134N. Using values for the column density of N_2H^+ and $H^{13}CO^+$ from Swade (1987) and a $^{12}C/^{13}C$ ratio of 75, we may estimate the abundance of molecular nitrogen relative to carbon monoxide (following Link, Guélin, and Langer 1983) to be,

$$\frac{f(N_2)}{f(CO)} \approx \frac{f(N_2H^+)}{f(HCO^+)} \approx 0.08 \ . \tag{2.5}$$

Since comparing our present NO column density with that for CO found by Swade (1987) yields

$$\frac{f(NO)}{f(CO)} \sim 6\times10^{-4} \ , \tag{2.6}$$

we then deduce that

$$\frac{f(N_2)}{f(NO)} \sim 137 \ . \tag{2.7}$$

Table 2.5. Tentative TMC–1(NH_3) U-Line

V_{LSR} ($km\,s^{-1}$)	T_R (K)	FWHM ($km\,s^{-1}$)	$\int T_R\,dv$ ($K\,km\,s^{-1}$)	Freq. (MHz)
-5.84	0.17	0.50	0.08	150182.18 ± .05

This would suggest that the bulk of the gas phase nitrogen is probably in the form of N_2, as the models suggest. Note that we have assumed that the production and destruction rates for N_2H^+ and $H^{13}CO^+$ are similar.

Since this work, at least two more molecules with nitroso bonds have been observed in the ISM. The presence of interstellar HNO was confirmed by Hollis *et al.*, (1991) and interstellar N_2O has recently been observed by Ziurys *et al.*, (1994).

2.5.1 A Possible U-Line in TMC–1

While observing NO towards TMC–1(NH_3), a spectral feature was detected in the pass band to the low velocity side of NO. This feature did not appear in the TMC–1(CP) spectrum, nor does Gerin, Viala, and Casoli (1993) mention observing a U-line in their spectrum of TMC–1(CP). We have not had the opportunity to perform any tests to confirm this extremely tentative U-line detection. Table 2.5 reports the results of a Gaussian fit to this feature. We have assumed $V_{LSR} = 5.9\,km\,s^{-1}$ for the purpose of determining a rest frequency.

Chapter 3

Detection of Nitrogen Sulfide in Quiescent Dark Clouds

3.1 Summary

We report the first detection of interstellar nitrogen sulfide (NS) in cold dark clouds. Several components of the $^2\Pi_{1/2}$, $J=3/2\rightarrow 1/2$ and $J=5/2\rightarrow 3/2$ transitions were observed in TMC–1 and L134N. The inferred column density for TMC–1 is $N_{NS} \sim 8\times10^{12}$ cm^{-2} towards the NH_3 peak in that cloud, and in L134N is $N_{NS} \sim 3\times10^{12}$ cm^{-2} towards the position of peak NH_3 emission. These values correspond to fractional abundances relative to molecular hydrogen of $f_{NS} \sim 8\times10^{-10}$ for TMC–1, and $f_{NS} \sim 6\times10^{-10}$ for L134N. The NS emission is extended along the TMC–1 ridge and is also extended in L134N. The measured abundances are significantly higher than those predicted by some recent gas phase ion-molecule models. Our astronomical observations of NS have led to new laboratory spectroscopy which has resulted in more accurate NS transition frequencies, and a corresponding determination of the NS molecular constants to a much higher precision. We also report the detection of SO^+ by its $^2\Pi_{1/2}$ $J=3/2\rightarrow 1/2$ parity-e transition towards L134N. SO^+ was not detected towards TMC–1.

3.2 Introduction

Gas phase models of ion molecule chemistry have been rather successful in matching the observed abundance of small interstellar molecules containing carbon, hydrogen and oxygen. However, the situation is somewhat less clear for

nitrogen-containing species, partly because the important initiating reactions $N^+ + H_2$ and $N + H_3^+$ are slightly endothermic (Herbst and Leung 1989). Likewise, although there are a number of interstellar molecules containing sulfur, the chemistry of sulfur remains a problem, including the basic question of whether it is necessary to invoke surface reactions on grains to match the observed abundances (Herbst, DeFrees, and Koch 1989). We have been pursuing these problems from an observational perspective, and have measured abundances for H_2S (e.g., Minh *et al.* 1990) and NO in both dark clouds and GMCs (McGonagle *et al.* 1990, Ziurys *et al.* 1991). It appears that the abundance of NO is matched quite well by the most recent gas phase models, while that of H_2S may well require contributions from the grains.

Sulfur falls immediately below oxygen in the Periodic Table, and, given the observed abundance of NO, it is reasonable to investigate nitrogen sulfide (NS) in molecular clouds. As a relatively simple species, the abundance of NS provides a good test for coupled chemistry models of nitrogen and sulfur. Until recently, only two molecules containing both these elements were known in the interstellar medium, NS (Gottlieb *et al.* 1975) and HNCS (Frerking and Linke 1979), and both had been observed towards Sgr(B2). We report here the first detection of NS in dark clouds and comment on its chemical significance. NS is also commonly found in regions of massive star–formation (McGonagle, Irvine, and Minh 1992); these results will be discussed in detail elsewhere (McGonagle and Irvine 1995).

3.3 Observations

Nitrogen sulfide has a $^2\Pi_r$ ground state and thus possess fine structure, Λ–doubling, and, because of the quadrupole moment of the nitrogen nucleus, hyperfine structure (Anacona *et al.* 1986). Thus, both the $J = 3/2 \rightarrow 1/2$ and $J = 5/2 \rightarrow 3/2$ rotational transitions consist of several hyperfine lines, which are

Table 3.1. NS Transition Frequencies and Line Intensities

J_u	J_l	F_u	F_l	parity	Frequency [a] (MHz)	Line Intensity [b]
3/2	1/2	5/2	3/2	e	69002.890(3)	0.2500
		5/2	3/2	f	69411.943(2)	0.2500
5/2	3/2	7/2	5/2	e	115153.935(6)	0.2222
		5/2	3/2	e	115156.812(4)	0.1400
		3/2	1/2	e	115162.982(2)	0.0833

(a) Frequencies are quoted from Lee, Ozeki, and Saito (1995).

(b) Line intensities were calculated following Tatum (1986).

(c) Intensities have been normalized to unity over both Λ–doublets.

grouped into parity–e and parity–f bands due to the Λ–doubling. All observed transitions belong to the $^2\Pi_{1/2}$ ladder, since the $^2\Pi_{3/2}$ ladder begins $\sim$ 322 K above the absolute ground state and is unlikely to be populated in cold clouds. The transition frequencies used during our observations were from laboratory spectroscopy conducted by Anacona *et al.* (1986). Recently, Lee, Ozeki, and Saito (1995) remeasured the NS transition frequencies to higher accuracy, and we have used their laboratory spectroscopy results in our data analysis (*see* Table 3.1.).

Observed positions toward L134N and TMC–1 are both referenced to standard origins. In this chapter, positions are identified by their offsets form these origins in minutes of arc. The origin positions and V_{LSR} values used during our observations are listed in Table 3.2.

Observations of NS J=3/2$\rightarrow$1/2 were conducted at the NRAO 12m telescope at Kitt Peak in 1991 November and 1993 April. At the observation frequencies near 69 GHz the FWHM beamwidth was 1.41 arcminutes, and the quantity

Table 3.2. NS Observations Source List

Source	α(1950) hh	mm	ss.s	δ(1950) dd	mm	ss	V_{LSR} (km s^{-1})
L134N(0,0)	15	51	30.0	-2	43	31	2.3
TMC–1(0,0)	4	38	38.6	25	35	45	5.9

defined by NRAO as the corrected beam efficiency (Users Manual for the NRAO 12 m Telescope, 1990) was $\eta_m^* \simeq 0.93$. An SIS mixer, dual polarization, SSB receiver was used to make the observations, which were carried out in position switching mode. Both receiver channels were utilized to maximize sensitivity. The temperature scale was determined using the chopper–wheel method and is given in terms of T_R^*. The radiation temperature (T_R) was then approximated by $T_R \approx T_R^*/(\eta_m^* F)$, where F is a beam dilution correction. Since the TMC-1 ridge is $\sim$ 1 arcminute in width and is thus smaller than the measured beam FWHM in one dimension, we have applied a beam dilution correction of the form F = (Source Width)/(Beam FWHM) = 1/1.41 to the TMC–1 J=3/2$\rightarrow$1/2 T_R values.

The spectrometers used were a 128 channel filter bank with 100kHz filters which corresponds to a velocity resolution of 0.43 km s^{-1}, and (in the second set of observations) an autocorrelating spectrometer set to 24 and 49 kHz resolution which corresponds to 0.11 and 0.21 km s^{-1}, respectively, at the observed frequencies. The system temperatures were typically 300 – 500 K (SSB) on the sky in the T_R^* scale. The main hyperfine components of both the parity–e and parity–f bands were searched for towards TMC–1 and L134N.

Observations of the NS J=5/2$\rightarrow$3/2 parity–e transitions were made towards TMC–1 and L134N at the FCRAO 14m telescope during 1992 February. At the observing frequency of 115.2 GHz the FWHM beamwidth was 45 arcsec, and the

antenna main beam efficiency was $\eta_B \simeq 0.55$. The receiver used was a cooled Schottky diode mixer, which was tuned single-sideband; the image sideband was terminated at 20 K. Observations were carried out in frequency switching mode where $\Delta\nu = 1.5$ MHz. The temperature scale was determined using the chopper–wheel method and is given in terms of the T_A^* scale. The radiation temperature was then approximated by $T_R \approx T_A^*/\eta_B$. Since the sources are extended relative to the beamwidth, no correction for beam dilution was applied. The spectrometer used was a 256 channel filter bank with 100 kHz filter resolution which corresponds to a velocity resolution of 0.26 $km\,s^{-1}$. Total system temperatures were typically $\sim$700 K (SSB) on the sky in the T_A^* scale. The three strongest hyperfine components of the parity–e band were searched for towards both TMC–1 and L134N.

For the remainder of this chapter, all temperature values quoted have been converted to the T_R scale as outlined above.

3.4 Results

NS emission was detected towards five positions along the TMC–1 ridge and at three positions in L134N. The strongest $J=3/2\rightarrow 1/2$ hyperfine components, $F=5/2\rightarrow 3/2$ parity–e and parity–f, were both detected towards TMC–1 and L134N. These spectra towards the TMC–1 ammonia peak are shown in Figures 3.1, toward the TMC–1 cyanopolyyne-peak in Figure 3.2, and toward the L134N SO peak in Figure 3.3. Parity–f transitions were searched for in four additional positions along the TMC–1 ridge and the spectra are shown in Figure 3.4. In addition to observations towards the SO peak in L134N, parity–f transitions were sought at two other positions and the spectra are shown in Figure 3.5. No other hyperfine components associated with the $J=3/2\rightarrow 1/2$ rotational transition were present in the spectrometer passbands. A gaussian fit,

where the amplitude, line width, and line center were all free variables, was applied to each of the line profiles. The results are quoted in Table 3.3 and sample fits are shown in Figures 3.1, 3.2, and 3.3. The line widths are consistent with observations of other molecular transitions towards L134N and TMC–1.

The two strongest $J=5/2 \rightarrow 3/2$ parity-e hyperfine components, $F=7/2 \rightarrow 5/2$ and $F=5/2 \rightarrow 3/2$, were detected towards TMC-1 but not L134N. The TMC–1 spectrum is shown in Figure 3.6. The line intensity ratio is in good agreement with theoretical calculations for the optically thin case (*see* Table 3.1 for calculated LTE line intensities). The third strongest component, $F=3/2 \rightarrow 1/2$, was detected only at the 3σ level, which is consistent with the expected intensity of the transition and the baseline noise level of 22 mK RMS if the lines are optically thin. This $J=5/2 \rightarrow 3/2$ triplet was fit using three gaussians with the inter-gaussian spacing held fixed relative to the $F=7/2 \rightarrow 5/2$ line center, which was a free variable. All three gaussians shared the same FWHM value which was also a free variable, as were the amplitudes of each of the gaussians. The results of this fit are reported in Table 3.3.

Our original reference for NS transition rest frequencies was Anacona *et al.* (1986). Using those rest frequencies, we found that the LSR velocities of the $J=3/2 \rightarrow 1/2$ parity–f transitions appeared slightly low relative to values observed for many molecular lines at these positions (L134N: Swade 1987; TMC–1: Rydbeck *et al.* 1980), while the corresponding LSR velocities of the $J=3/2 \rightarrow 1/2$ parity–e transition were systematically high towards both L134N and TMC–1. These discrepancies corresponded to about 100 kHz and 200 kHz, respectively, whereas the quoted precision of the laboratory values is ± 50 kHz. We also noticed that the frequency difference between the $J=5/2 \rightarrow 3/2$, $F=7/2 \rightarrow 5/2$ and $F=5/2 \rightarrow 3/2$ hyperfine components was ~ 100 kHz smaller than the value deduced from Anacona *et al.* (1986).

We reported these findings to Dr. Shuji Saito of the Institute for Molecular Science in Japan. Dr. Saito, and Dr. Sang K. Lee, then visiting from Pusan National University Korea, remeasured the NS radical spectrum. The result of their effort is a new listing of NS rest frequencies in the frequency region 69 to 350 GHz. The measurement errors for most of the observed transitions are less than 20 kHz and are, thus, a great improvement over earlier measurements. Molecular constants such as the Λ-doubling constants, rotational constant, centrifugal distortion constants, and the hyperfine coupling constants have been determined with improvements to their precision of 2 to 10 times over earlier results.

When we reevaluated the LSR velocities using the new rest frequencies, we found that the discrepancy between the $J=3/2 \rightarrow 1/2$ parity–e and parity–f transitions had been reduced by a factor of two. The parity–e derived LSR velocities are still greater than the parity–f derived velocities by ~ 0.6 km s^{-1}, which corresponds to ~ 140 kHz. This discrepancy is seen towards both L134N and TMC–1. Neither uncertainties in our observations nor in the laboratory spectroscopy seem sufficient to explain this discrepancy. In addition, the $J=5/2 \rightarrow 3/2$ parity–e transition has the same derived LSR velocity as the $J=3/2 \rightarrow 1/2$ parity–e transitions (*see* Table 3.3). Further high spectral resolution astronomical observations of NS are needed to further investigate the apparent uncertainty in the $J=3/2 \rightarrow 1/2$, $F=5/2 \rightarrow 3/2$ parity–f transition frequency. The Lee, Ozeki and Saito (1995) laboratory measured NS frequencies provide a much improved fit to the astronomically observed $J=5/2 \rightarrow 3/2$ parity–e hyperfine component separations, which leads us to believe that the earlier discrepancy in the hyperfine pattern for this transition has been resolved.

Upper level NS column densities may be calculated using the standard equation (*see* Irvine, Goldsmith, and Hjalmarson 1987), which assumes optically thin emission:

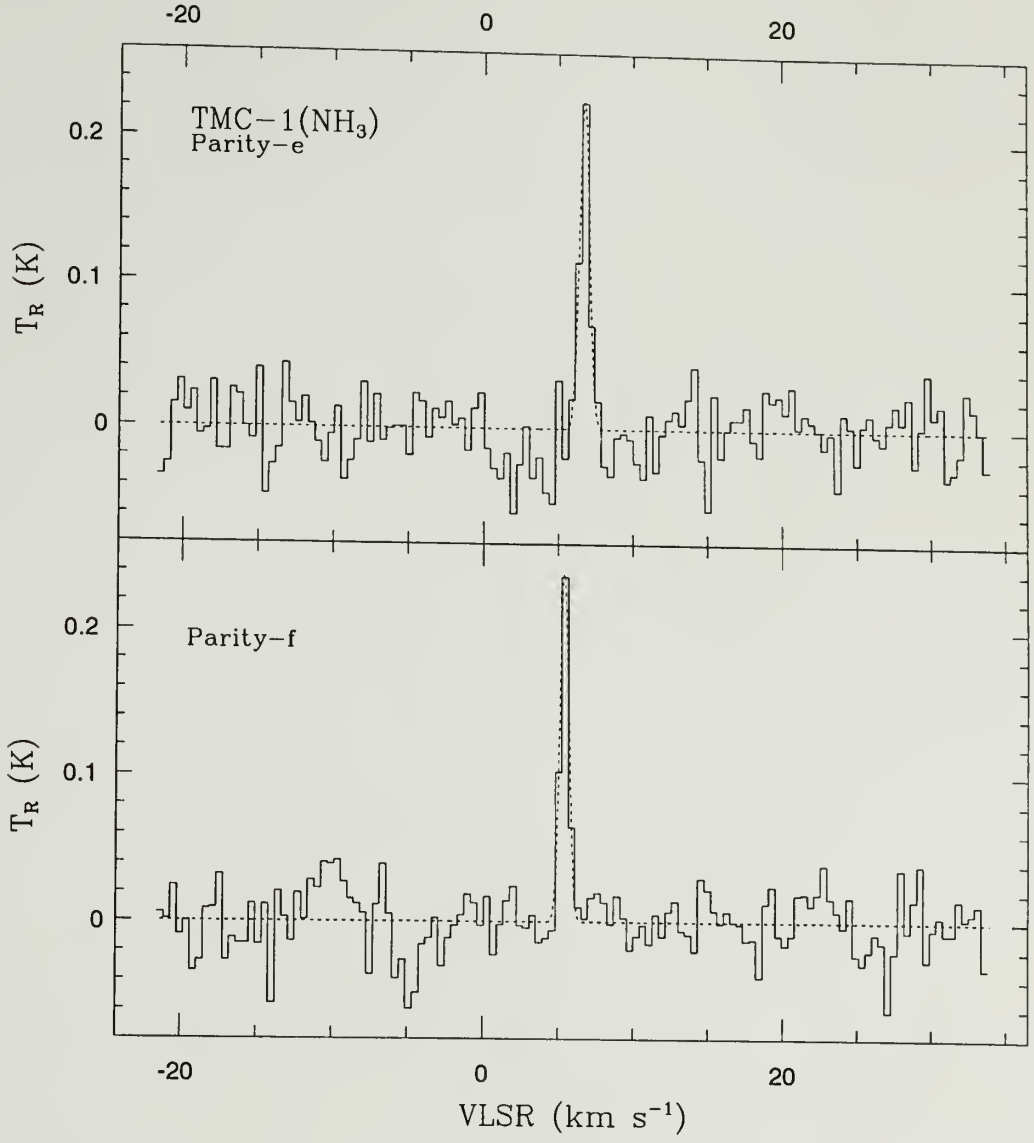

Figure 3.1. Spectra (solid histogram) of the $J = 3/2 \rightarrow 1/2$, $F = 5/2 \rightarrow 3/2$, Λ-doublet transitions of NS taken toward TMC-1 (-5.1,7.0). The spectral resolution is 100 kHz, and the position of the source origin (0,0) is given in Table 3.2. Frequencies from Lee, Ozeki, and Saito (1995). Dashed curve show the results of a Gaussian fit to the spectrum. Fit parameters are given in Table 3.3.

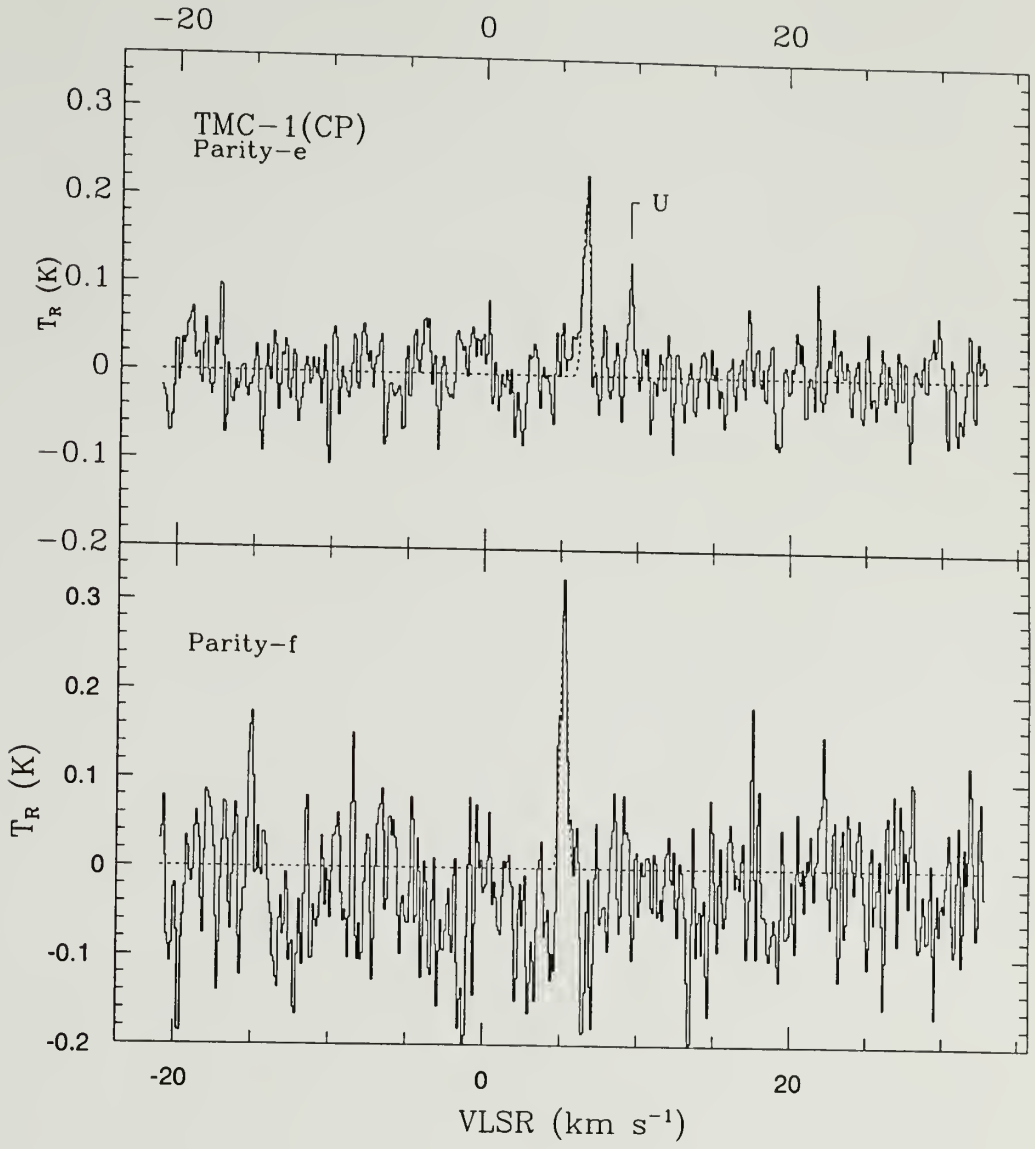

Figure 3.2. Spectra (solid histogram) of the J = 3/2 → 1/2, F = 5/2 → 3/2, Λ-doublet transitions of NS taken toward TMC-1 (0,0). The spectral resolution is 24 kHz, and the position of the source origin (0,0) is given in Table 3.2. Frequencies from Lee, Ozeki, and Saito (1995). Dashed curve show the results of a Gaussian fit to the spectrum. Fit parameters are given in Table 3.3.

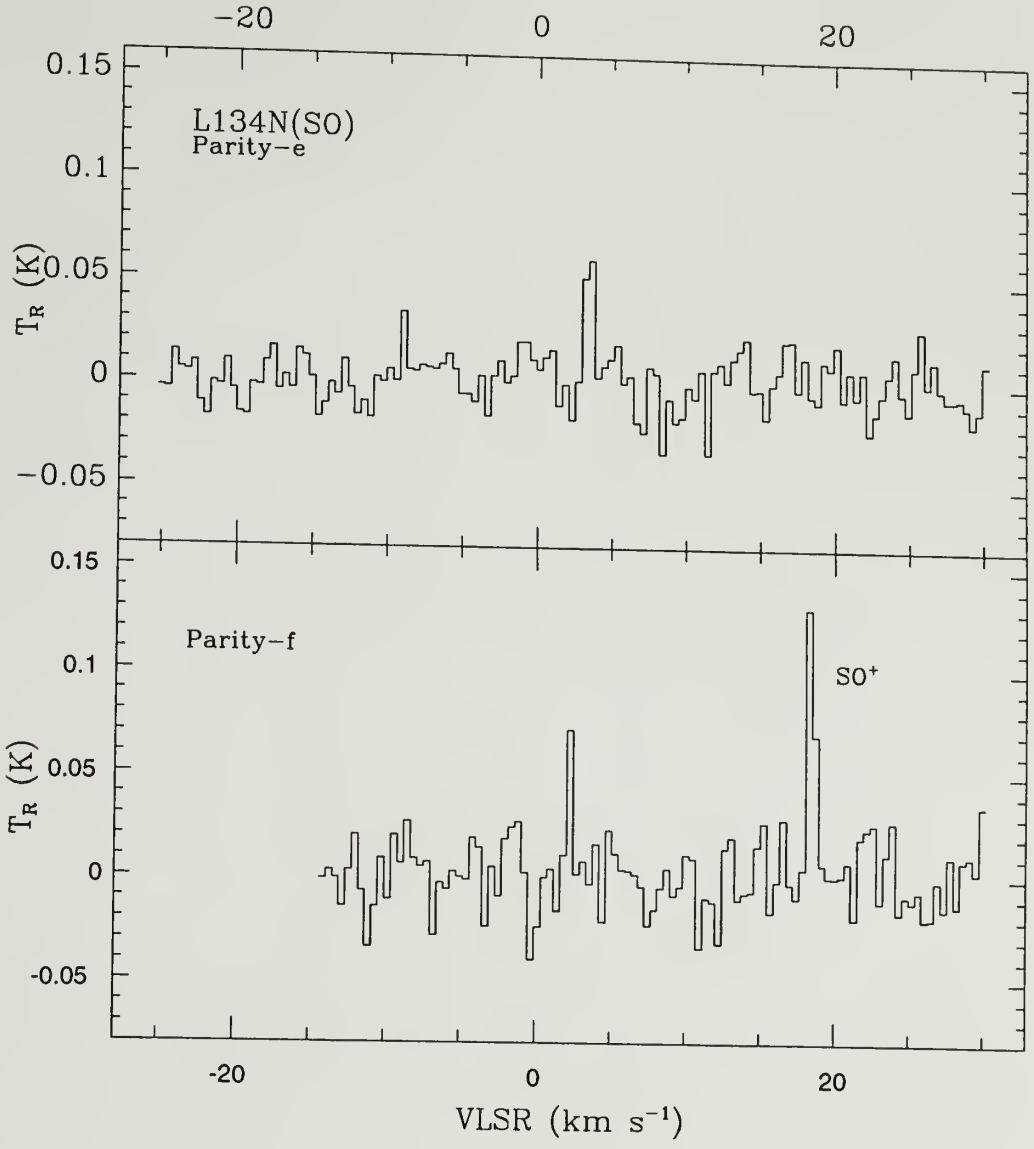

Figure 3.3. Spectra (solid histogram) of the J = 3/2 → 1/2, F = 5/2 → 3/2, Λ–doublet transitions of NS taken toward L134N(-1.0,0.0). The spectral resolution is 100 kHz, and the position of the source origin (0,0) is given in Table 3.2. Frequencies from Lee, Ozeki, and Saito (1995). Dashed curve show the results of a Gaussian fit to the spectrum. Fit parameters are given in Table 3.3.

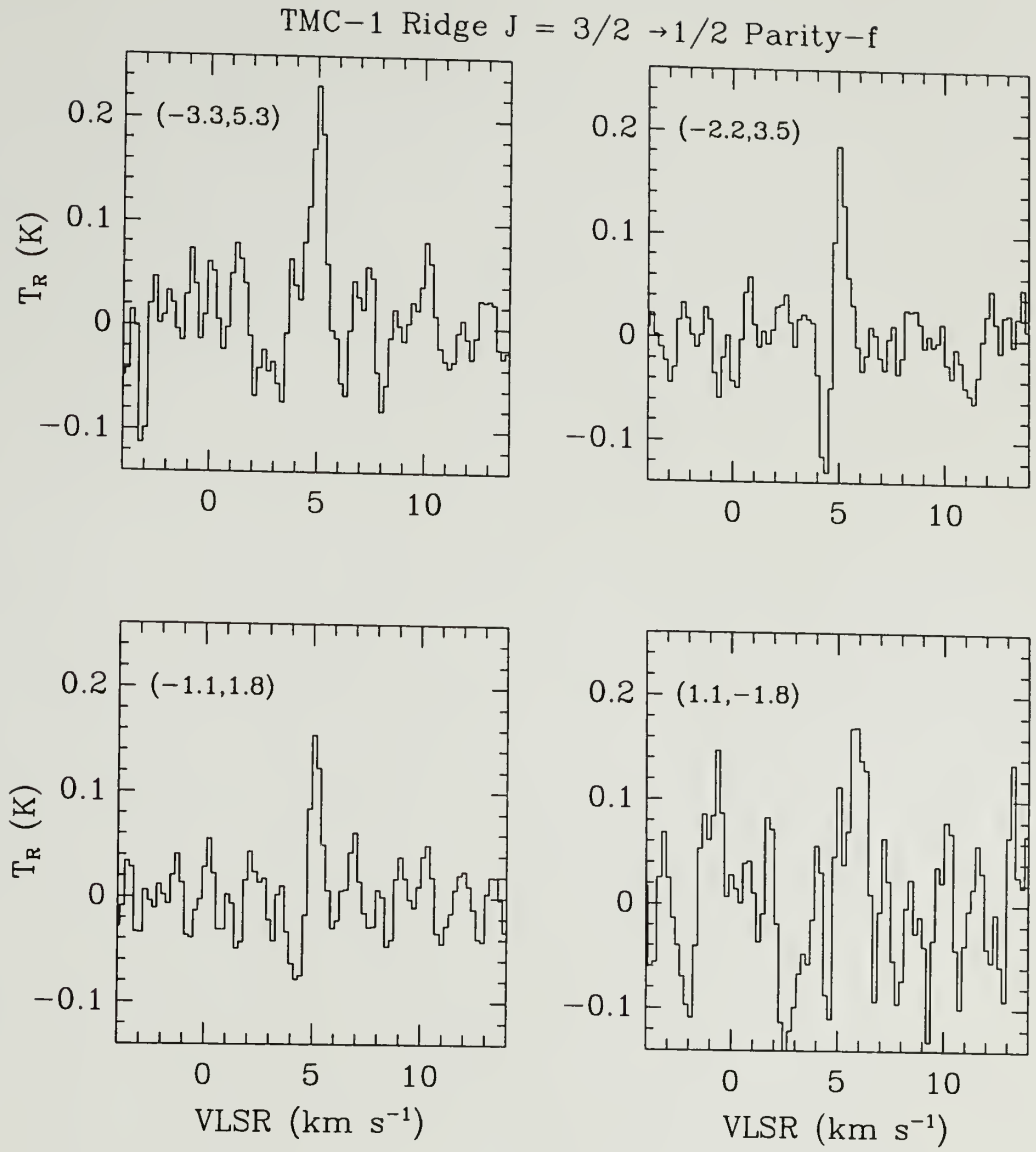

Figure 3.4. Spectra (solid histogram) of the J=3/2→1/2, F=5/2→3/2, parity-f transition of NS taken toward several positions along the TMC-1 ridge. The spectral resolution is 49 kHz. The positions (RA, DEC) are given in minutes of arc from the origin in Table 3.2. Frequencies from Lee, Ozeki, and Saito (1995).

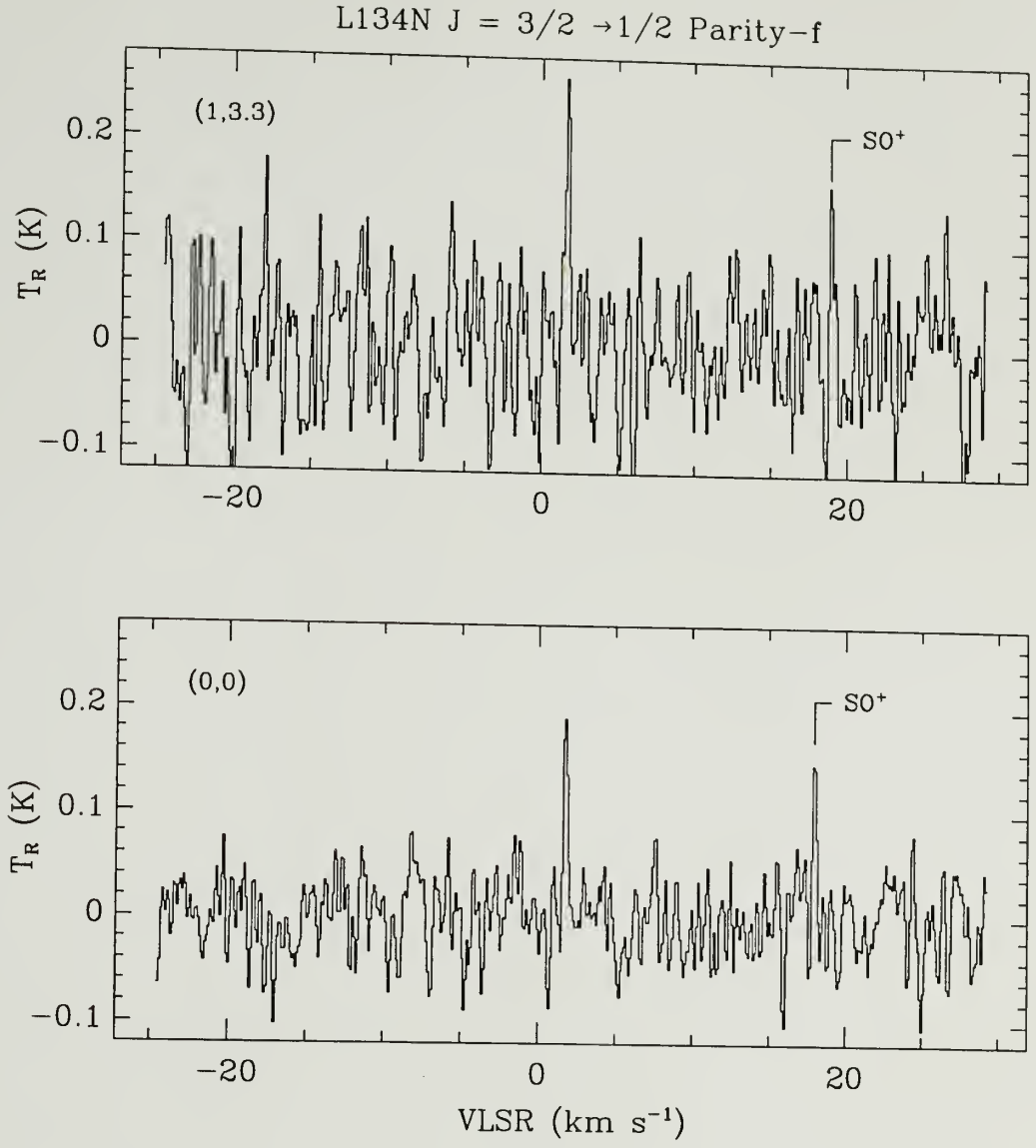

Figure 3.5. Spectra (solid histogram) of the J=3/2→1/2, F=5/2→3/2, parity-f transition of NS taken toward two positions in L134N. The spectral resolution is 24 kHz. The positions are given in minutes of arc from the origin in Table 3.2. Frequencies from Lee, Ozeki, and Saito (1995).

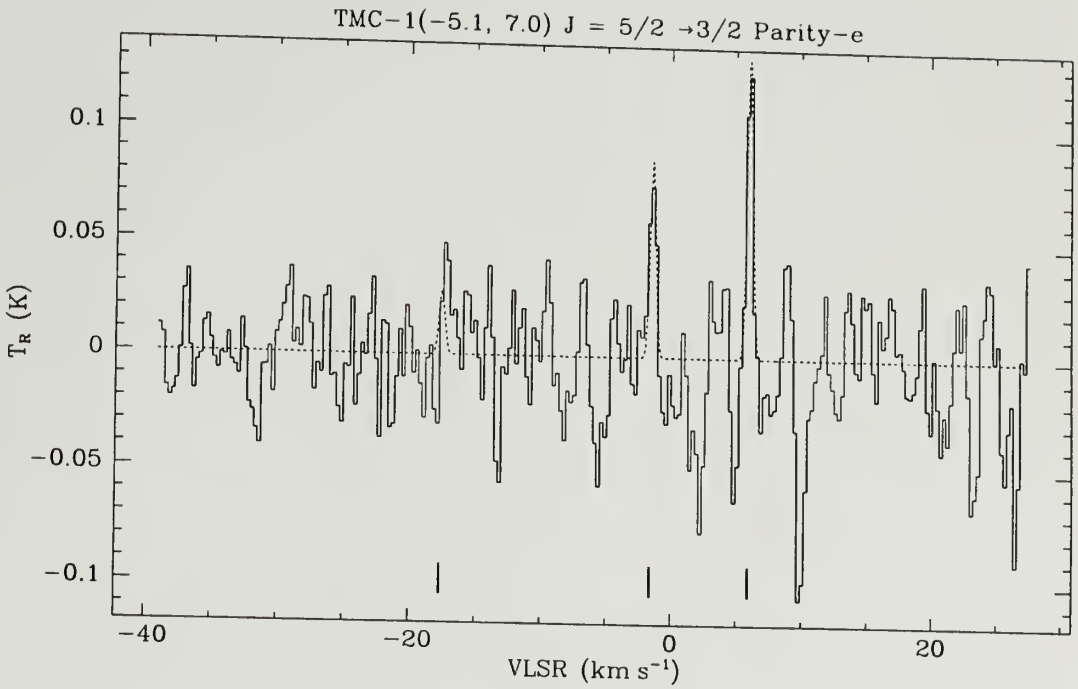

Figure 3.6. Spectra (solid histogram) of the J=5/2→3/2, parity–f, hyperfine transitions of NS taken toward TMC–1 (-5.1,7.0). The spectral resolution is 100 kHz, and the position of the source origin (0,0) is given in Table 3.2. Frequencies from Lee, Ozeki, and Saito (1995). Dashed curve show the results of a Gaussian fit to the spectrum. Fit parameters are given in Table 3.3. Tick marks indicate the position of NS hyperfine components. Negative-going spikes are artifacts of frequency switching.

Table 3.3. Summary of Gaussian Fits to NS Observations

Source [a]	J_u	F_u	F_l	P [b]	Res. (kHz)	V_{LSR} ($km\,s^{-1}$)	T_R [c,d] (K)	$\Delta V_{1/2}$ ($km\,s^{-1}$)	$\int T_R\,dV$ ($K\,km\,s^{-1}$)
TMC–1:									
(-5.1,7.0)	3/2	5/2	3/2	e	100	6.28±.22	0.32	0.78	0.25
		5/2	3/2	f	100	5.65±.22	0.33	0.69	0.24
		5/2	3/2	f	24	5.40±.05	0.46	0.42	0.19
	5/2	7/2	5/2	e	100	6.03±.13	0.14	0.52	0.07
		5/2	3/2	e	100	"	0.09	"	0.05
		3/2	1/2	e	100	—	≤0.07	—	—
(-3.3,5.3)	3/2	5/2	3/2	f	49	5.35±.11	0.28	0.71	0.20
(-2.2,3.5)	3/2	5/2	3/2	f	49	5.36±.11	0.30	0.53	0.16
(-1.1,1.8)	3/2	5/2	3/2	f	49	5.23±.11	0.22	0.48	0.11
(0,0)	3/2	5/2	3/2	e	24	6.05±.05	0.30	0.55	0.19
		5/2	3/2	f	24	5.45±.05	0.47	0.56	0.26
(1.0,-1.8)	3/2	5/2	3/2	f	49	—	≤0.33	0.57[e]	≤0.19
L134N:									
(-1.0,0.0)	3/2	5/2	3/2	e	100	2.97±.22	0.08	0.57	0.05
		5/2	3/2	f	100	2.45±.22	0.08	0.42	0.03
	5/2	7/2	5/2	e	100	—	≤0.07	—	—
(0,0)	3/2	5/2	3/2	f	100	2.11±.22	0.16	0.37	0.06
	3/2	5/2	3/2	f	24	2.00±.05	0.21	0.29	0.06
(1.0,3.3)	3/2	5/2	3/2	f	24	1.67±.05	0.25	0.35	0.09

(a) Positions are given as offsets in minutes of arc from the origin: see Table 3.2

(b) Parity for the Λ–doublet members in the notation of Anacona *et al.* (1986). NS frequencies from Lee, Ozeki, and Saito (1995).

(c) Upper limits are 3σ.

(d) TMC–1 $J=3/2\rightarrow 1/2$ T_R values include a beam dilution correction factor (see text).

(e) Average of all measured TMC–1, $J=3/2\rightarrow 1/2$ line widths.

$$N_u = 10^5 \left(\frac{8\pi k\nu^2}{hc^3 A_u S_F}\right) \left[1 - \frac{\exp(h\nu/kT_{EX}) - 1}{\exp(h\nu/kT_{BG}) - 1}\right]^{-1} \int T_R \, dv \; . \qquad (3.1)$$

In this expression $\int T_R \, dv$ is the total integrated line intensity (K km s^{-1}) of the observed hyperfine component, ν is the transition frequency, A_u is the Einstein coefficient of the NS rotational transition, while S_F is the hyperfine component line strength normalized to unity over both Λ-doublet members (Tatum, 1986). T_{EX} is the excitation temperature and T_{BG} is the microwave background radiation temperature, $T_{BG} = 2.7$K.

Since in dark clouds we do *not* have $T_{EX} \gg T_{BG}$, we must estimate T_{EX} to calculate N_u and then estimate a rotational temperature in order to calculate the partition function and hence fractional population f_u in a given level. Fortunately, for one position in TMC–1 we have data on two consecutive rotational transitions from which to estimate these temperatures. Where detections are available for more than one Λ-doublet member, or more than one hyperfine component, the total column density (N_{NS}) quoted in Table 3.4 is derived from the sum of the observed components of a given rotational transition (corrected for the unobserved components through the known values of S_F) in order to increase the signal-to-noise of the calculated column density.

Since NS has a substantial dipole moment (1.81 D), the A_u coefficients are relatively large: $A(J=3/2 \rightarrow 1/2) = 4.7 \times 10^{-6}$ s^{-1}, $A(J=5/2 \rightarrow 3/2) = 2.4 \times 10^{-5}$ s^{-1}. Therefore, the $J=3/2 \rightarrow 1/2$ transitions require $n(H_2) \sim 10^4 - 10^5$ cm^{-3} to approach thermalization, while the $J=5/2 \rightarrow 3/2$ transitions require $n(H_2) \sim 10^5 - 10^6$ cm^{-3}. Since the density thought to exist in TMC–1 is $n(H_2) \sim 10^4 - 10^5$, we expect that T_{EX} may be less than the gas kinetic temperature, $T_K \simeq 10$ K (Irvine, Schloerb, and Hjalmarson 1985). This would especially be true for the $J=5/2 \rightarrow 3/2$ transitions.

Initial attempts to describe both rotational transitions observed in TMC–1 with a single value T_{EX}, which in turn equaled the rotation temperature defined by

Table 3.4. NS Column Densities and Fractional Abundances

Source [a]	J_u	F_u	F_l	P [b]	N_u (cm^{-2})	N_{NS} (cm^{-2})	N_{H_2} (cm^{-2})	f_{NS} [c]
TMC–1:								
(-5.1,7.0)	3/2	5/2	3/2	e,f	3.6×10^{12}			
	5/2	7/2	5/2	e				
		5/2	3/2	e	8.5×10^{11}			
		3/2	1/2	e				
					$\overline{N_{NS}}$ =	8.3×10^{12}	1×10^{22}	8×10^{-10}
(-3.3,5.3)	3/2	5/2	3/2	f	2.9×10^{12}	6.4×10^{12}	1×10^{22}	6×10^{-10}
(-2.2,3.5)	3/2	5/2	3/2	f	2.2×10^{12}	5.0×10^{12}	1×10^{22}	5×10^{-10}
(-1.1,1.8)	3/2	5/2	3/2	f	1.6×10^{12}	3.6×10^{12}	1×10^{22}	4×10^{-10}
(0,0)	3/2	5/2	3/2	e,f	3.1×10^{12}	6.8×10^{12}	1×10^{22}	7×10^{-10}
(1.0,-1.8)	3/2	5/2	3/2	f	$\leq2.6\times10^{12}$	$\leq5.9\times10^{12}$	1×10^{22}	$\leq6\times10^{-10}$
L134N:								
(-1.0,0.0)	3/2	5/2	3/2	e,f	5.8×10^{11}	1.3×10^{12}	8.2×10^{21}	2×10^{-10}
(0,0)	3/2	5/2	3/2	f	8.6×10^{11}	1.9×10^{12}	7.6×10^{21}	2×10^{-10}
(1.0,3.3)	3/2	5/2	3/2	f	1.3×10^{12}	2.9×10^{12}	4.0×10^{21}	7×10^{-10}

(a) For positions, see Table 3.2 notes.

(b) Parity for the Λ–doublet members in the notation of Anacona *et al.* (1986).

(c) For N_{H_2} column density references, see text.

the Boltzmann equation,

$$\frac{N_m}{N_n} = \frac{g_m}{g_n} \exp\left[-\frac{h\nu_{mn}}{kT_{Rot}}\right], \tag{3.2}$$

where m = 5/2, n = 3/2 and the statistical weight is defined as $g_J = 2J + 1$, failed to match the observed intensity ratio ([3/2 → 1/2]/[5/2 → 3/2]). However, by using an excitation temperature which decreases with increasing energy above the ground state,

$$T_{EX}(3/2 \rightarrow 1/2) > T_{EX}(5/2 \rightarrow 3/2) = T_{Rot}\ , \tag{3.3}$$

consistent results were obtained. The higher excitation temperature across the J=3/2→1/2 transition is consistent with its smaller value for the Einstein A coefficient.

Our most extensive observations are towards the position TMC–1(-5.1,7.0), where HCO^+, NH_3, H_2S and SO have their peak intensity (Olano, Walmsley, and Wilson 1988; Minh, Irvine, and Ziurys 1989; and SO data from P. Friberg, private communication). From our analysis the NS total column density is in the range $N_{NS} = 12 - 7\times10^{12}$ cm^2 towards TMC–1(-5.1,7.0), where $T_{EX}(J=3/2\rightarrow1/2) \sim 4 - 7$K; $T_{EX}(J=5/2\rightarrow3/2) \sim 3.2 - 3.6\text{K} = T_{Rot}$ (assumed to link all higher levels). Note that the fractional population in levels with $J \geq 7/2$ under these conditions is 0.014, so that the partition function is rather well defined. Although T_{Rot} for the higher levels has a low value, it is in fact consistent with results for some other high dipole moment molecules with optically thin lines (e.g., CH_3CN, Minh *et al.* 1993; H_2C_3 and H_2C_4, Kawaguchi *et al.* 1991; CH_3C_3N, Broten *et al.* 1984). The quoted value of N_{NS} corresponds to a fractional abundance, relative to molecular hydrogen, of $f_{NS} \sim 7 - 12\times10^{-10}$ (using $N_{H_2} \sim 10^{22}$; Irvine, Goldsmith, and Hjalmarson 1987). Table 3.4 lists the column density for the intermediate values, $T_{EX}(J = 3/2 \rightarrow 1/2) = 5$K and $T_{EX}(J = 5/2 \rightarrow 3/2) = 3.4$K.

NS emission is extended along the TMC–1 ridge (*see* Table 3.3). Using the same values of T_{EX} and T_{Rot} as at the position (-5.1,7.0) described in the previous paragraph, we find a second peak in the NS column density at the cyanopolyyne-peak TMC–1(0,0) (Based on the $C^{18}O$ map of Hjalmarson and Friberg [1988] we assume that $N[H_2]$ is roughly constant along the ridge). Between these two positions the NS abundance steadily decreases from its highest value at the ammonia-peak to a minimum $\sim$2 arcminutes NW of the cyanopolyyne-peak. The NS abundance declines again SE of the cyanopolyyne-peak.

Other nitrogen bearing species which have been studied in TMC–1 include NH_3 and the cyanopolyynes. A curious feature of TMC–1 is that the spatial distribution of the cyanopolyynes is anticorrelated with that of NH_3 (Little *et al.* 1979; Tölle *et al.* 1981; Olano, Whalmsley, and Wilson 1988). Recent work by Hirahara *et al.* (1992) shows that the sulfur containing species $C^{34}S$, CCS, and C_3S are also well correlated with other carbon-chain molecules and are anticorrelated with NH_3. The NS total column density distribution, however, does not strictly correlate with either the cyanopolyynes nor NH_3, as may be seen in Figure 3.7. NS does appear to follow the general distribution of $C^{18}O$ (Hjalmarson and Friberg, 1988) and CH_3OH (Friberg *et al.* 1988). Very recently, Pratap *et al.* (1994) mapped SO emission towards TMC–1 using the FCRAO 15 pixel focal plane array receiver (QUARRY: Erickson *et al.* 1992) coupled with the new focal plane array autocorrelation spectrometer (FAAS: Predmore 1995) as part of the FCRAO dark cloud chemistry survey program. Preliminary results indicate that the SO distribution may be correlated with NH_3 and does not appear to strongly peak towards the cyanopolyyne position TMC–1(0,0). Figure 3.8 compares the integrated intensity of NS along the TMC–1 ridge to the integrated intensity of $C^{18}O$ and SO. More extensive mapping of NS in TMC–1 would be helpful in understanding its relation to these and other molecular species.

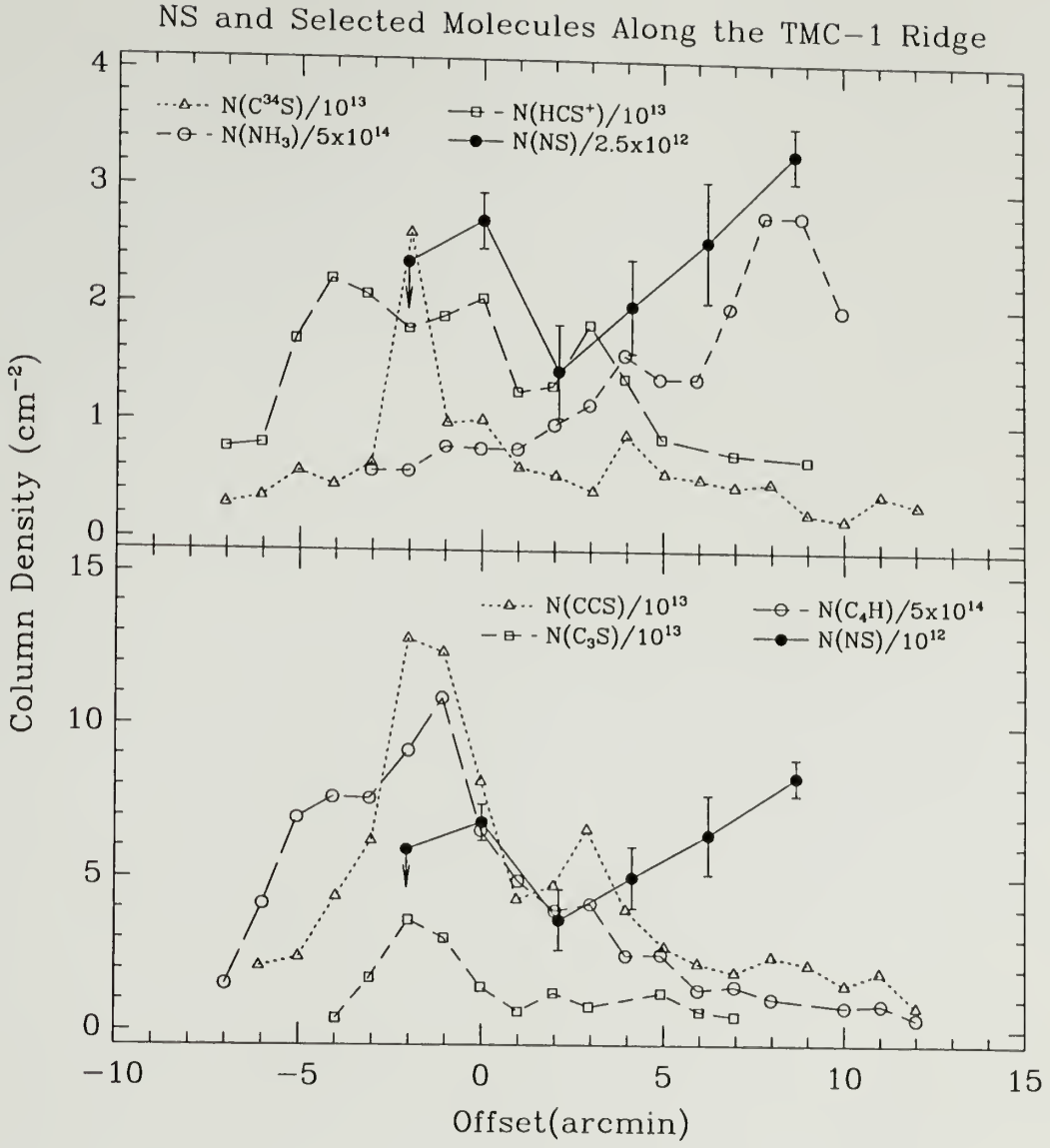

Figure 3.7. The distribution of NS and other selected molecules along the TMC–1 ridge. The data for all molecules except NS comes from Hirahara *et al.*, 1992. The error bars attached to the NS data points are $\pm 1\sigma$ and the arrow indicates an upper limit set to 3 times the spectrum rms. The offsets are the distance along the TMC–1 ridge (defined as a line connecting the cyanopolyyne and NH_3 peaks) referenced to TMC–1(0,0)

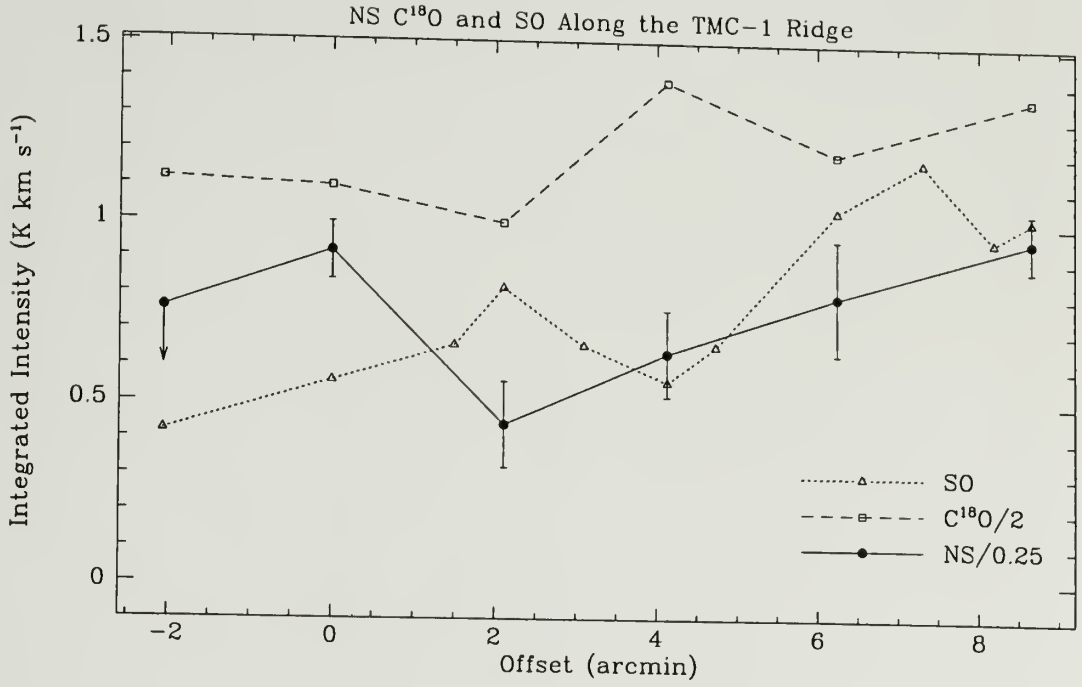

Figure 3.8. A comparison of the NS, C^{18}, and SO integrated intensity along the TMC–1 ridge. The SO data comes from Pratap *et al.* (1994), for the $J_K = 3_2 \rightarrow 2_1$ transition. The $C^{18}O$ $J = 1 \rightarrow 0$ data is from Hjalmarson and Friberg, (1988). The NS integrated intensity is for the $J = 3/2 \rightarrow 1/2$ $F = 5/2 \rightarrow 3/2$ transition. The error bars attached to the NS data points are $\pm 1\sigma$ and the arrow indicates an upper limit set to 3 times the spectrum rms. The offsets are the distance along the TMC–1 ridge (defined as a line connecting the cyanopolyyne and NH_3 peaks) referenced to TMC–1(0,0).

As is the case in TMC–1, the NS emission towards L134N is extended. Using the same excitation temperatures as for TMC–1, column densities in the range $N_{NS} = 1 - 3 \times 10^{12}$ cm^2 were obtained towards three positions in L134N. These values correspond to fractional abundances, relative to molecular hydrogen, of $f_{NS} \sim 2 - 6 \times 10^{-10}$, using total column densities $N_{H_2} \sim 8.2 - 4.9 \times 10^{21}$ cm^{-2} [Swade 1987: by using $N(C^{18}O)/N_{H_2} = 1.7 \times 10^{-7}$]. The highest observed column density was at the (1.0,3.3) position, which coincides with the peak emission of NH_3, C_3H_2, HC_3N, and $H^{13}CO^+$, and is well away from the $C^{18}O$ and SO peaks (Swade 1987). An intermediate column density occurs at a secondary NH_3 peak at position (0,0), while the lowest column density was seen towards the SO peak, (-1.0,0). Here, as with TMC–1, more extensive mapping of NS is required to understand its relation to other molecular species.

It is of interest to note that the relative abundance of NS in TMC–1 and L134N seems to be the opposite of what is found for the related molecule, nitric oxide (NO). Whereas NS is more abundant towards the NH_3 peak in TMC–1 than the SO peak in L134N, the situation is the reverse for NO (McGonagle *et al.* 1990; Gerin, Viala, and Casoli 1993). This is not surprising given the differing chemistries of oxygen and sulfur in the ISM; unlike O^+, S^+ does not react with H_2 (Millar and Herbst 1990; Smith and Adams 1985; Watson and Walmsley 1982)

3.5 Discussion

It appears that these abundances are significantly higher than those predicted by some recent gas phase ion-molecule models, although there are large variations among the model results. For instance, the model of Millar and Herbst (1990) predicts for dark cloud conditions f(NS) $\sim 3 \times 10^{-12}$ at "early–times" (when the best match is obtained for many carbon-containing species in TMC–1) and $\sim 9 \times 10^{-12}$ at steady state (which produces a better match with abundances in

L134N). Millar *et al.* (1991) find very low values in both situations ($\sim 10^{-14}$). More recent calculation by C. Leung (private communication 1992) using 3517 reactions among 385 species, give f(NS) $\sim 10^{-11} - 10^{-10}$. It thus seems that theoretical predictions remain quite uncertain, although none of the models predict abundances as large as those observed here.

In at least one model the most important formation mechanisms for NS under dark cloud conditions involve as yet unobserved species (Leung 1993, private communication):

$$HS + N \rightarrow NS + H \,, \tag{3.4}$$

$$HNS^{+} + e \rightarrow NS + H \,, \tag{3.5}$$

where HS can form from reaction of S^{+} with organic species such as H_2CO, while HNS^{+} can be formed (e.g.) from $NH_2^{+} + S$. Since the initial hydrogenation of both sulfur and nitrogen in the ISM is thought to be indirect (e.g., $N + OH \rightarrow NO, +N \rightarrow N_2, +H_3^{+} \rightarrow N_2H^{+} \ldots$; $S^{+}+$ *organics* $\rightarrow HS + \ldots$), the abundance of NS depends, in gas phase models, on a relatively long series of reactions. Let us hope that the present observational values will help to constrain the model parameters and hence to improve our understanding of both sulfur and nitrogen chemistry in the interstellar medium.

3.5.1 Detection of a New SO^{+} Transition in L134N

While conducting the initial NS survey in dark clouds, with the KPNO 12 meter telescope in November 1991, an unidentified spectral feature was discovered towards L134N. This strong spectral feature was at $\nu_{\rm rest} \sim 69408$ MHz assuming $V_{\rm LSR} = 2.3\,{\rm km\,s^{-1}}$ (*see* Figure 3.3). Observations were made with the $V_{\rm LSR}$ changed from 2.3 to 10.3 km s^{-1} to test if the feature was leakage from the other sideband or a "birdy" in the IF. Both the NS and the U69408 feature

Table 3.5. L134N SO^+ Observation Coordinates and V_{LSR}

Source	α(1950) hh	mm	ss.s	δ(1950) dd	mm	ss.s	V_{LSR} ($km\,s^{-1}$)
L134N(0,0)	15	51	30.0	-02	43	31	2.3
L134N(NH_3)	15	51	34.0	-02	40	16	2.3
L134N(SO)	15	51	26.0	-02	43	31	2.3

remained at the same absolute V_{LSR} values, indicating that the feature is at the RF value given above.

During similar observations towards TMC–1, U69408 was not detected to an RMS level of <20 mK. However, the U69408 has been detected toward the GMC, W51(MS) (*see* Chapter 4).

A more recent series of observations were carried out in April of 1993 at the 12 meter telescope, which confirmed the existence of a spectral feature at 69408.260 ± 0.012 MHz towards several positions in L134N. These results were reported in McGonagle *et al.* (1994).

Subsequently, Dr. Karl Menten of the Harvard-Smithsonian Center for Astrophysics suggested to us that our reported U–line might be the $^2\Pi_{1/2}$, $J=3/2\rightarrow 1/2$, parity–e transition of SO^+ at 69408.371 MHz (Amano, Amano and Warner 1991), which matches our rest frequency for the feature to within errors. The presence of SO^+ in L134N has also been confirmed by Turner (1994) by observations of the $^2\Pi_{1/2}$ $J=5/2\rightarrow 3/2$e,f and $J=9/2\rightarrow 7/2$e transitions. Thus, we now identify U69408 as belonging to SO^+. Table 3.5 lists the positions were the $^2\Pi_{1/2}$, $J=3/2\rightarrow 2/2$, parity–e transition has been observed. Table 3.6 reports the results of Gaussian fits to the spectra.

Table 3.6. L134N SO^+ $^2\Pi_{1/2}$, J=3/2→1/2e Gaussian Fit Results

Source	Res. kHz	RMS (K)	T_R ($km\,s^{-1}$)	V_{LSR} ($km\,s^{-1}$)	$\Delta V_{1/2}$ ($K\,km\,s^{-1}$)	$\int T_R\,dV$
L134N(0,0)	100	0.021	0.11	2.6	0.54	0.08
	24	0.032	0.16	2.8	0.25	0.04
L134N(NH_3)	100	0.033	0.07	2.6	0.50	0.03
L134N(S0)	100	0.020	0.15	3.0	0.52	0.08

3.5.2 U-Line in TMC–1

A narrow spectral feature seen in the TMC–1(CP) parity–e spectrum has been tentatively identified as a U-line. This feature was observed with a spectral resolution of 24 kHz and a Gaussian fit to the feature gives $T_R \sim 0.1$ (no beam dilution correction) and FWHM ~ 0.4 $km\,s^{-1}$. Assuming a $V_{LSR} \sim 5.9$ $km\,s^{-1}$, we find a rest frequency of 69003 MHz. U69003 did not appear in either the TMC–1(NH_3) or L134N(SO) parity–e spectra; however, both of these spectra only had a spectral resolution of 100 kHZ.

Chapter 4

Nitrogen Sulfide in Giant Molecular Clouds

4.1 Summary

We report on the results of the first comprehensive survey of nitrogen sulfide (NS) towards regions of massive star formation. NS was observed by means of its $^2\Pi_{1/2}$, $J=3/2\rightarrow 1/2$, $J=5/2\rightarrow 3/2$, and $J=7/2\rightarrow 5/2$ transitions at 69 GHz, 115 GHz, and 161 GHz, and was detected towards 12 of 14 giant molecular clouds (GMCs) observed. It was not detected towards the carbon-rich star IRC+10216. For those sources where 2 or more NS hyperfine transitions have been observed, analysis of the hyperfine component relative line strengths suggests that NS emission is optically thin, with the possible exception of Sgr B2(M). The estimated fractional abundance of NS relative to molecular hydrogen for the optically thin extended sources ranges from $0.5-2\times10^{-11}$, which is in good agreement with some recent gas phase ion-molecule chemistry models developed for cold dark clouds. The largest NS fractional abundance, 14×10^{-11}, was observed towards the Galactic center cloud Sgr B2(M). We have mapped the NS emission towards Orion(KL) using the FCRAO 3mm focal plane array. The NS integrated intensity is strongly peaked toward KL, but also extends all along the Orion ridge; the distribution of NS in Orion resembles that of SO and CH_3OH. We have identified a spectral feature seen towards DR21(OH), Orion(KL), Orion(1.5S) and W51(MS) as being the ortho $N_{KK}=4_{04}\rightarrow 3_{13}$, $J=3\rightarrow 2$, fine structure component of methylene (CH_2). The existence of interstellar methylene had been tentatively reported previously and only recently confirmed (Hollis, Jewell, and Lovas 1995). We also report the detection of the SO^+ $^2\Pi_{1/2}$, $J=3/2\rightarrow 1/2$, parity-e transition towards W51(MS).

4.2 Introduction

Observations of H_2S (Minh, Irvine, and Ziurys, 1989) and the discovery of the organo-sulfur species C_2S and C_3S (Saito *et al.*, 1987; Yamamoto *et al.*, 1987) in the quiescent dark cloud TMC–1 have increased interest in interstellar sulfur chemistry. Though SO and SO_2 provide familiar spectral features to millimeter wavelength astronomers, the chemistry of sulfur is not well understood, including the fundamental question of whether grain surface reactions must be invoked in order to adequately model the observations (Herbst, DeFrees, and Koch, 1989). Indeed, investigations into sulfur chemistry carried out by Minh *et al.* (1991) through the study of H_2S indicated that the then-existing ion-molecular chemistry models needed to be augmented with grain reaction schemes in order to explain the abundances of at least some sulfur-bearing molecules.

NS has only recently begun to find its way into the ion-molecule chemical reaction networks. In the gas-phase, the reaction paths proposed for the formation of NS,

$$HS + N \rightarrow NS + H\ , \tag{4.1}$$

$$HNS^+ + e \rightarrow NS + H\ , \tag{4.2}$$

involve as yet unobserved species, HS and HNS^+ (Leung 1993, private communication). HS can form from reaction of S^+ with organic species such as H_2CO, while HNS^+ can be formed (e.g.) from $NH_2^+ + S$. Since the initial hydrogenation of both sulfur and nitrogen in the ISM is thought to be indirect (e.g., $N + OH \rightarrow NO, +N \rightarrow N_2, +H_3^+ \rightarrow N_2H^+ \ldots$; $S^+ +$ *organics* $\rightarrow HS + \ldots$), the abundance of NS depends on a relatively long series of reactions. We hope that the observational values presented here will help to constrain the model parameters and thus improve our understanding of both sulfur and nitrogen chemistry in the interstellar medium.

4.3 Observations

Nitrogen sulfide has a $^2\Pi_r$ ground state and thus possesses fine structure, Λ–doubling, and, because of the quadrupole moment of the nitrogen nucleus, hyperfine structure (Anacona *et al.* 1986). Thus, the rotational transitions consist of several hyperfine lines, which are grouped into parity–e and parity–f bands due to the Λ–doubling. Most observed transitions belong to the $^2\Pi_{1/2}$ ladder, since the $^2\Pi_{3/2}$ ladder begins ~322 K above the absolute ground state and is unlikely to be populated in quiescent molecular clouds.

Observations of NS $J = 3/2 \rightarrow 1/2$ parity–e and parity–f transitions were conducted at the NRAO 12m telescope at Kitt Peak in 1991 November. At the observation frequencies near 69 GHz (*see* Table 4.1) the FWHM beamwidth was 1.41 arcminutes, and the quantity defined by NRAO as the corrected beam efficiency (Users Manual for the 12 m Telescope, 1990) was $\eta_m^* = 0.93$. A dual polarization, SSB, SIS mixer receiver was used to make the observations. The observations were carried out in position switching mode, and both receiver channels were utilized to maximize sensitivity. The temperature scale was determined using the chopper–wheel method and is given in terms of T_R^*. The radiation temperature (T_R) was then approximated by $T_R \approx T_R^*/\eta_m^*$. The spectrometers used were a 128 channel filterbank with 1000 kHz filters which corresponds to a velocity resolution of 4.3 km s^{-1}, and 250 kHz filters which corresponds to a velocity resolution of 1.1 km s^{-1}. The system temperatures were typically 300–500 K (SSB) on the sky in the T_R^* scale. The main hyperfine components of the parity–e band were searched for in all sources, while the parity–f band was searched for towards W51(MS).

Observations of the NS $J = 5/2 \rightarrow 3/2$ parity–e transitions were made at the FCRAO 14m telescope during 1992 November and December. At the observing frequency of 115.2 GHz (*see* Table 4.1) the FWHM beamwidth was 45 arcsec, and

the antenna main beam efficiency was $\eta_B = 0.55$ for all sources except Sgr B2(M). The Sgr B2(M) observations were made at elevations $< 20°$, where the antenna main beam efficiency is $\eta_B \sim 0.40$ for frequencies near 115 GHz (Kenny and Taylor, 1988). The receiver used was a cooled Schottky diode mixer, which was tuned single-sideband; the image sideband was terminated at 20 K. Observations were carried out in position switching mode. The temperature scale was determined using the chopper–wheel method and is given in terms of the T_A^* scale. The radiation temperature was then approximated by $T_R \approx T_A^*/\eta_B$. The spectrometers used were a 512 channel filterbank with 1000 kHz filter resolution which corresponds to a velocity resolution of 2.6 $\mathrm{km\,s^{-1}}$, and a 512 channel 250 kHz resolution filterbank which corresponds to a velocity resolution of 0.65 $\mathrm{km\,s^{-1}}$. Total system temperatures were typically $\sim$700 K (SSB) on the sky in the T_A^* scale. The strongest hyperfine components of the parity–e band were searched for towards all sources.

Observations of the NS $J = 7/2 \rightarrow 5/2$ parity–e and parity–f band transitions towards Orion(KL) were made at the FCRAO 14m telescope during 1992 October and 1993 March as part of the Orion(KL) 2mm band spectral survey (Ziurys and McGonagle 1993; McGonagle, Ziurys and Irvine 1995). At the observing frequency of 161.5 GHz (*see* Table 4.1) the FWHM beamwidth was estimated to be $\sim$35 arcsec, and the antenna main beam efficiency was $\eta_B \sim 0.40$. The receiver used was a cooled Schottky diode mixer, which was tuned single-sideband; the image sideband was terminated at 20 K. Observations were carried out in position switching mode, and the temperature scale was determined using the chopper–wheel method and is given in terms of the T_A^* scale. The radiation temperature was then approximated by $T_R \approx T_A^*/\eta_B$. The spectrometers used were a 512 channel filterbank with 1000 kHz filter resolution which corresponds to

a velocity resolution of 1.9 km s^{-1}. Total system temperatures were typically $\sim$1000 K (SSB) on the sky in the T_A^* scale.

The first systematic mapping of NS emission towards a GMC was made using the FCRAO focal plain array camera (Erickson *et al.*, 1992), more commonly known by the acronym QUARRY (QUabbin ARRaY). The QUARRY receiver is comprised of fifteen, 3mm band Schottky/HEMT mixers in a 3 by 5 array. Unlike most multi-channel receivers now found on radio telescopes, typically two independent receivers pointed at the same spot on the sky monitoring orthogonal polarizations, the QUARRY system fully integrates its 15 mixers into a single receiver which allows the 15 beams to form a closely spaced rectangular matrix on the sky. The close spacing, typically one beamwidth along the 5–mixer axis and two beamwidths along the 3–mixer axis, allows for fast and efficient mapping of astronomical sources. The NS $J=5/2\rightarrow3/2$ parity–e $F=7/2\rightarrow5/2$ and $F=5/2\rightarrow3/2$ transitions were beam-sample mapped towards Orion(KL) during 1993 November to 1994 April using QUARRY. At the observing frequency of 115.2 GHz the FWHM beamwidth was $\sim$45 arcsec, and the antenna main beam efficiency was $\eta_B = 0.50$. The QUARRY receiver employs an optical sideband filter; the image sideband was terminated at 20 K. Observations were carried out in position switching mode. The temperature scale was determined using the chopper–wheel method and is given in terms of the T_A^* scale. The radiation temperature was then approximated by $T_R \approx T_A^*/\eta_B$. The spectrometers used were a 32 channel per pixel filterbank with 1000 kHz filter resolution which corresponds to a velocity resolution of 2.6 km s^{-1}, and a 32 channel per pixel 250 kHz resolution filterbank which corresponds to a velocity resolution of 0.65 km s^{-1}. Total system temperatures were typically $\sim$900 K (SSB) on the sky in the T_A^* scale.

The transition frequencies used are from laboratory spectroscopy conducted by Lee, Ozeki and Saito (1995) and are listed in Table 4.1. Source positions and V_{LSR}

values used during the observations are listed in Table 4.2. For the remainder of this chapter, all temperature values quoted have been converted to the T_R scale as outlined above unless otherwise noted.

4.4 Spectral Line Measurements

The NS emission was modeled as a superposition of one or more velocity "emission systems", with each system having a particular V_{LSR} and being composed of the hyperfine components present in the spectrometer passband. The hyperfine components were modeled with gaussian line profiles with fixed inter-component spacing corresponding to the laboratory spectroscopy (Lee, Ozeki and Saito, 1995). The V_{LSR} fit parameter was measured for the emission system's reference hyperfine component, chosen to be the hyperfine component with the largest intrinsic line strength. The hyperfine components comprising an emission system all shared a common FWHM fit parameter, while the amplitude of each component was an independent fit parameter. The Levenberg-Marquardt method was used to fit the emission systems to the data (*see* Press *et al.* 1988, §14.4). The function used in modeling the NS emission is given in the following expression,

$$f_{NS}(x) = \sum_{i=1}^{m} \sum_{j=0}^{n} A_{ij} \exp\left[-C\left(\frac{x - V_i - H_{ij}}{F_i}\right)^2\right], \qquad (4.3)$$

were A_{ij} is the hyperfine component amplitude for the j-th hyperfine component of the i-th emission system, V_i is the velocity of the i-th emission system with respect to the LSR as measured for the emission system's hyperfine component with the largest intrinsic line strength, H_{ij} is the velocity offset for the j-th hyperfine component from the reference component (i.e. for the reference component, $H_{i0} = 0$), F_i is the emission systems full line width at half maximum, and $C = 4\ln(2)$.

The emission system fitting routine also generated a covariance matrix which was used to determine the errors associated with the line parameter

Table 4.1. NS Transition Frequencies and Line Intensities

J_u	J_l	F_u	F_l	parity	Frequency [a] (MHz)	Line Intensity [b]
				$^2\Pi_{1/2}$ state		
3/2	1/2	5/2	3/2	e	69002.989(3)	0.2500
		3/2	1/2	e	69017.895(3)	0.0926
		3/2	3/2	e	69037.336(10)	0.0074
		5/2	3/2	f	69411.943(2)	0.2500
5/2	3/2	7/2	5/2	e	115153.935(6)	0.2222
		5/2	3/2	e	115156.812(4)	0.1400
		3/2	1/2	e	115162.982(6)	0.0833
		3/2	3/2	e	115185.411(2)	0.0267
		5/2	5/2	e	115191.288(4)	0.0267
7/2	5/2	9/2	7/2	e	161297.246(6)	0.2083
		7/2	5/2	e	161298.411(5)	0.1531
		5/2	3/2	e	161301.747(5)	0.1111
		9/2	7/2	f	161697.256(5)	0.2083
		7/2	5/2	f	161703.404(7)	0.1531
		5/2	3/2	f	161703.987(5)	0.1111
		7/2	7/2	f	161636.517(6)	0.0136
		5/2	5/2	f	161657.816(5)	0.0136
				$^2\Pi_{3/2}$ state		
7/2	5/2	9/2	7/2	e,f	162658.520(6)	0.2083

(a) Frequencies are quoted from Lee, Ozeki, and Saito (1995). Values in parentheses denote one standard deviation of the frequency measurement and apply to the last digits.

(b) Line intensities were calculated following Tatum (1986). Intensities have been normalized to unity over both Λ-doublets.

Table 4.2. NS Source List

Source	α(1950) hh	mm	ss.s	δ(1950) dd	mm	ss	V_{LSR} ($km\,s^{-1}$)
DR21(OH)	20	37	15.0	42	12	8	-2.9
G34.3+0.2	18	50	46.0	1	11	10	57.8
IRC+10216	9	45	14.8	13	30	39	-24.0
NGC7538(E)	23	11	53.0	61	10	58	-58.4
NGC7538(N)	23	11	36.6	61	11	48	-66.7
NGC7538(S)	23	11	36.6	61	10	48	-55.8
Orion(1.5S)	5	32	44.8	-5	25	60	6.4
Orion(KL)	5	32	47.0	-5	24	23	7.6
S140	22	17	41.2	63	3	41	-8.0
Sgr B2(M)	17	44	10.6	-28	22	5	60.6
W3(IRS5)	2	21	53.2	61	52	21	-40.0
W3(OH)	2	23	17.3	61	38	58	-46.7
W49(N)	19	7	49.6	9	1	15	8.0
W51(MS)	19	21	26.4	14	24	42	55.6
W51(N)	19	21	22.0	14	25	20	59.8

Table 4.3. CH_2 $N_{KK} = 4_{04} \rightarrow 3_{13}$, $J = 3 \rightarrow 2$ Gaussian Fit Results [a]

Source	V_{LSR} (km s^{-1})	T_R (K)	FWHM (km s^{-1})
DR21(OH)	-1.9 ± 0.4	0.042 ± 0.013	2.45 ± 0.93
Orion(1.5S)	8.3 ± 0.5	0.046 ± 0.009	4.23 ± 1.32
Orion(KL)	8.8 ± 0.3	0.054 ± 0.007	4.55 ± 0.82
W51(MS)	57.3 ± 0.4	0.045 ± 0.017	2.50 ± 0.37

(a) Feature is a blend of the $F = 4 \rightarrow 3, 3 \rightarrow 2, 2 \rightarrow 1$ hyperfine components. All errors are $\pm 1\sigma$. V_{LSR} determined for a rest frequency of 70678.633(42) MHz (Hollis, Jewell and Lovas 1995).

measurements. The covariance terms were generally much smaller than the variance terms in the matrix, so we have simply used the square root of the variance term as the 1σ error of each measured line parameter. Covariance terms were included when determining the errors associated with line strength ratios and integrated intensities. For the remainder of this chapter, all errors are 1σ unless otherwise specified.

An unidentified spectral feature was found to be blended with the parity–e $J = 3/2 \rightarrow 1/2$, $F = 3/2 \rightarrow 1/2$, hyperfine component in the spectra of DR21(OH), Orion(KL), Orion(1.5S), and W51(MS). This feature has since been identified as the ortho $N_{KK} = 4_{04} \rightarrow 3_{13}$, $J = 3 \rightarrow 2$ fine structure transition of methylene, CH_2, (Hollis, Jewell, and Lovas 1995), and is a blend of the $F = 4 \rightarrow 3$, $3 \rightarrow 2$, and $2 \rightarrow 1$ hyperfine components. To accommodate the CH_2 spectral feature, we modified our gaussian fit routine to include an independent gaussian, which fit the CH_2 line, thus preventing it from effecting the NS emission fit. The results of the fits to the CH_2, $J = 3 \rightarrow 2$, transition are listed in Table 4.3.

Observations of the NS parity-e $J=3/2 \rightarrow 1/2$ transition towards Orion(KL) show a broad feature blended with the $F=5/2 \rightarrow 3/2$ hyperfine component. We have ruled out a second emission system, perhaps arising from the Orion plateau, since no corresponding emission feature was seen in the $J=5/2 \rightarrow 3/2$ spectrum. Recent observations by Hollis, Jewell, and Lovas (1995) of this same frequency range do not show a broad feature blended with the NS emission. Thus, we suspect that this feature is an instrumental artifact. Millimeter-wave mixer receivers are sensitive to sidebands centered at

$$\nu = (N\nu(\mathrm{LO})) \pm \nu(\mathrm{IF}) \ , \tag{4.4}$$

where $N = 1, 2, 3 \ldots$, $\nu(\mathrm{LO})$ is the local oscillator frequency, and $\nu(\mathrm{IF})$ is the intermediate frequency (Kollberg and Zirath, 1983; Vanden Bout *et al.*, 1985). For $N = 2$, our Orion(KL) observations would have been sensitive to emission centered near $\sim$ 139517 MHz and $\sim$ 142517 MHz. However, no strong emission feature is reported near either of these frequencies in the Observed Interstellar Molecule Microwave Transition Catalogue (Lovas, 1992). Given the possible problems with our NS spectrum towards Orion(KL), we have adopted the NS $J=3/2 \rightarrow 1/2$ parity-e $F=5/2 \rightarrow 3/2$ and $F=3/2 \rightarrow 1/2$ line parameters reported by Hollis, Jewell, and Lovas (1995).

Observations of the NS parity-f band were carried out for the $J=3/2 \rightarrow 1/2$ $F=5/2 \rightarrow 3/2$ hyperfine component towards W51(MS). This feature was fitted with a single Gaussian and the results are reported in Table 4.5. In addition to the NS feature, there is a blended emission feature belonging to the SO^+, $^2\Pi_{1/2}$, $J=3/2 \rightarrow 1/2$, parity-e transition, which has a rest frequency of 69408.371 MHz (Amano, Amano and Warner 1991). SO^+ was previously detected towards W51(MS) by its $J=5/2 \rightarrow 3/2$ef, $J=9/2 \rightarrow 7/2$e, and $J=11/2 \rightarrow 9/2$f transitions (Turner 1994). A Gaussian was also fitted to this feature and the results are listed in Table 4.4. Our line parameters match those of Turner (1994) to within errors.

Table 4.4. Gaussian Fit to SO^+, $^2\Pi_{1/2}$, $J=3/2\rightarrow 1/2e$ Transition

Source	T_R (K)	V_{LSR} (km s^{-1})	FWHM (km s^{-1})
W51(MS)	0.052±0.005	54±1	13.8±2.5

Figures 4.1–4.11 display the $J=3/2\rightarrow 1/2$ and $J=5/2\rightarrow 3/2$ spectra, along with the Gaussian fits, for sources where both transitions were observed. The source W51(N) was only observed by its $J=5/2\rightarrow 3/2$ transition and the spectrum is shown in Figure 4.13. The results of these Gaussian fits are listed in Table 4.5 and in Table 4.7 for the $J=3/2\rightarrow 1/2$ and $J=5/2\rightarrow 1/2$ spectra, respectively. The 1σ errors associated with the $J=3/2\rightarrow 1/2$ and $J=5/2\rightarrow 3/2$ fit parameters are reported in Table 4.6 and Table 4.8, respectively.

In the course of conducting the 2mm spectral line survey of Orion(KL), NS was observed by means of its $J=7/2\rightarrow 5/2$ parity–e and parity–f transitions. The results of gaussian fits to these features are listed in Table 4.9, the fit errors are reported in Table 4.10, and the spectra shown in Figure 4.14. It is clear that the NS parity–e transitions are severely blended with ethyl cyanide, and the parity–f transitions are blended with vinyl cyanide. Attempts were made to subtract out the non-NS spectral features in order to measure the NS line parameters. Unfortunately, no good method was found to do this, so the values quoted in Table 4.9 are highly suspect. The uncertainty is most pronounced in the measured line widths, which led us to fix the line widths to the value measured for the Orion(KL) NS $J=5/2\rightarrow 3/2$ transition, which was chosen because it is the only uncontaminated spectrum.

The Orion(KL) 2mm spectral line survey has also detected an emission feature tentatively identified as a blend of the parity-e,f $J=7/2\rightarrow5/2$, $F=9/2\rightarrow7/2$ transitions from the $^2\Pi_{3/2}$ ladder of NS (Lee, Ozeki, and Saito 1995; the Λ-doubling is very small in this ladder). The line amplitude is $T_R = 0.13 \pm 0.04$ K, width $\Delta v = 5.3 \pm 1.7$ km s^{-1}, and velocity $V_{LSR} = 5.3 \pm 0.7$ km s-1. The line width is consistent with the observed $^2\Pi_{1/2}$ ladder line width; however, the velocity is somewhat lower. The significance of this will be discussed in section 4.5.3.5.

Figure 4.15 shows a QUARRY beam-sampled contour map of the NS parity-e $J=5/2\rightarrow3/2$ transition, integrated over the $F=7/2\rightarrow5/2$ and $F=5/2\rightarrow3/2$ hyperfine components. A contour map of the peak intensity of the NS parity-e $J=5/2\rightarrow3/2$ $F=7/2\rightarrow3/2$ line is shown in Figure 4.16. Figures 4.17—4.19 show the spectra which make up the contour maps grouped into three 6 by 5 arrays, referred to as QUARRY "foot prints", where the spectra, or pixels, are separated in right ascension and declination by 50 arcsec. Table 4.11 lists the results of gaussian fits to selected pixels from the $J=5/2\rightarrow3/2$ QUARRY map of the Orion GMC complex, while Table 4.12 lists the fit uncertainties.

The integrated intensity contour map, Figure 4.15, shows NS to to be extended north and south of Orion(KL), although the integrated intensity is strongly peaked towards Orion(KL). A secondary integrated intensity peak is seen beginning ~3 arc minutes south of Orion(KL) and extending south for another ~2.5 arc minutes. NS extends north of Orion(KL) for ~4 arcminutes, but appears weaker in comparison to the southern emission. With the exception of two pixels just south of the (KL) position, there appears to be a lack of NS emission between the Orion(KL) peak and the start of the southern emission. One of these two pixels coincides with the location of a bipolar outflow 1.5 arc minutes south of Orion(KL) (Ziurys, Wilson, and Mauersberger 1990). The NS emission features are generally

narrow, FWHM $\sim 1.0-2.5$ km s^{-1}, throughout the mapped region except towards Orion(KL), where the line width is ~ 6 km s^{-1}.

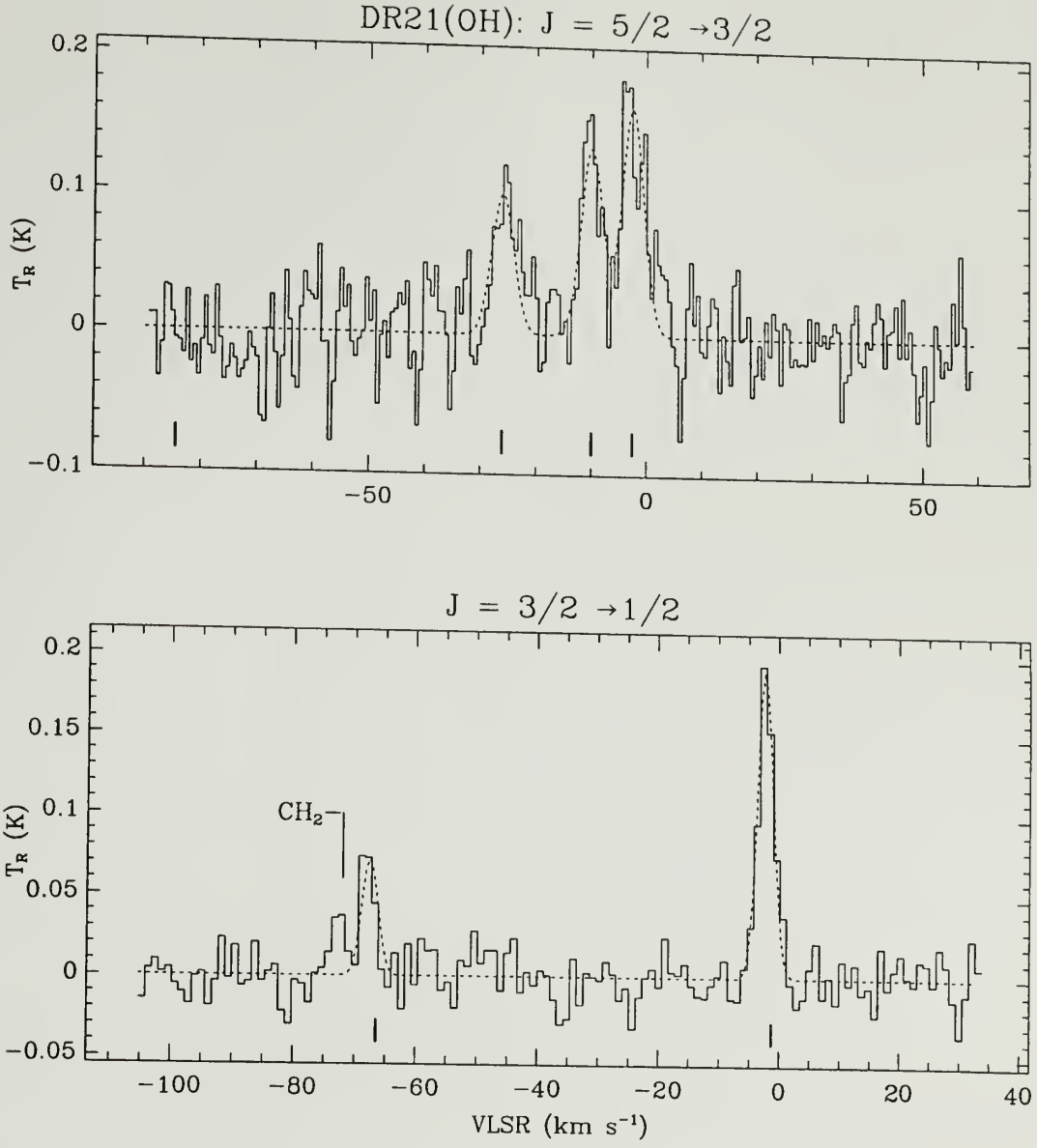

Figure 4.1. Spectra (solid histograms) of the J=5/2→3/2 and J=3/2→1/2 parity-e transitions towards DR21(OH). The resolution is 250 kHz for both spectra, and the source position is given in Table 4.2. The dashed curve is the result of a Gaussian fit to the data (*see text*). Fit parameters are given in Table 4.5 and Table 4.7. Tick marks indicate hyperfine component positions. Frequencies from Lee, Ozeki and Siato (1995).

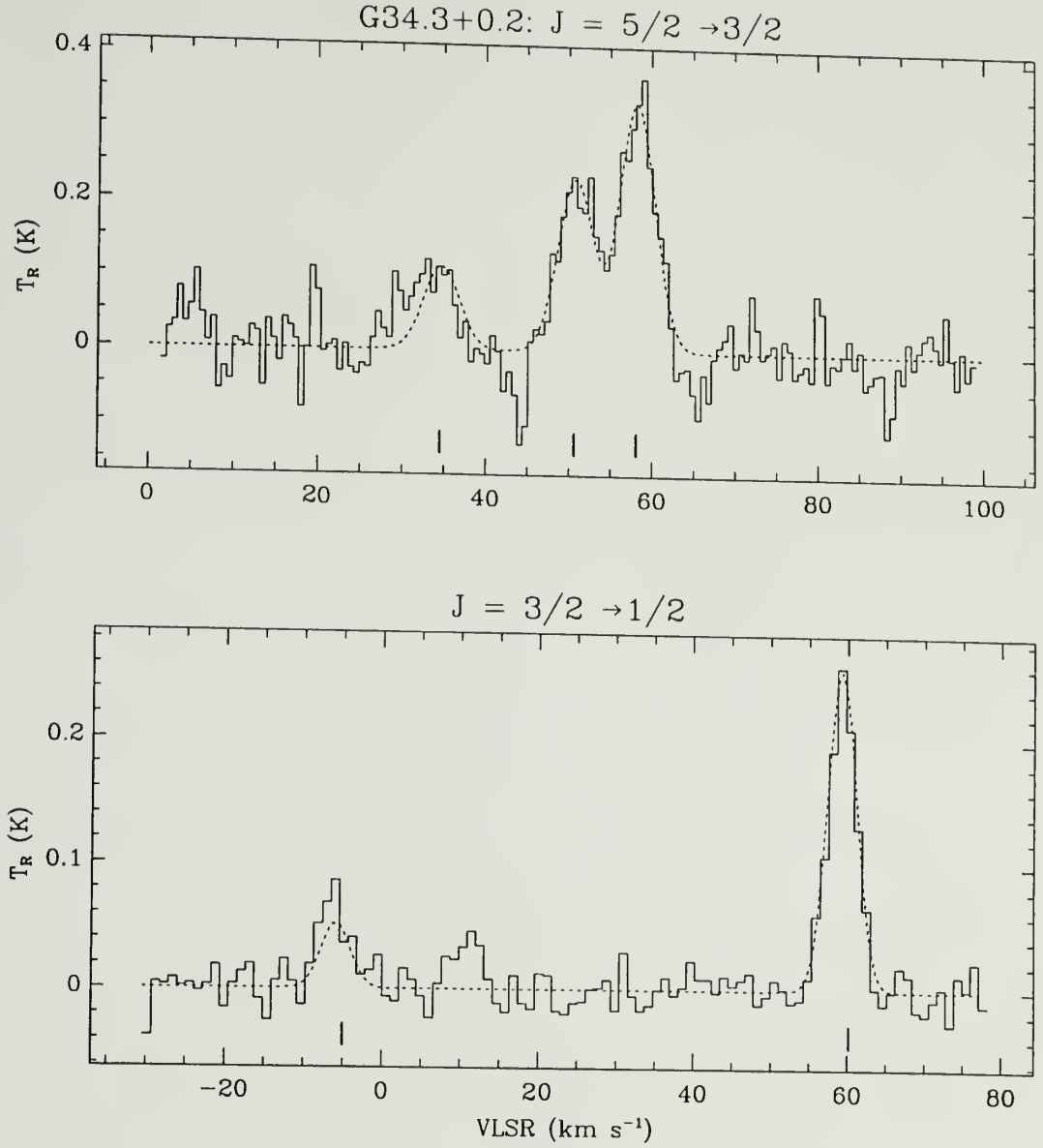

Figure 4.2. Spectra (solid histograms) of the J=5/2→3/2 and J=3/2→1/2 parity–e transitions towards G34.3+0.2. For details see caption to Figure 4.1.

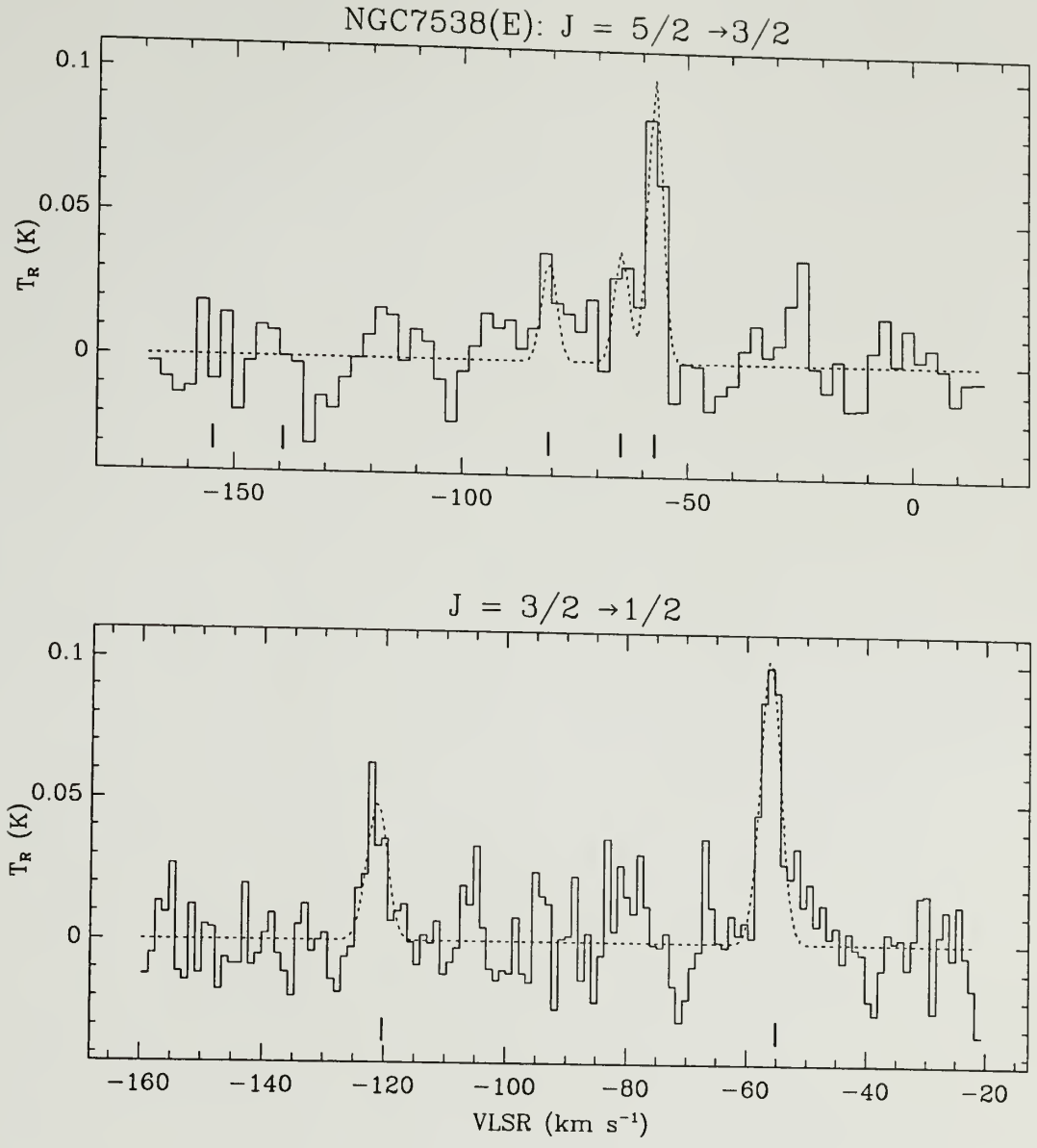

Figure 4.3. Spectra (solid histograms) of the J=5/2→3/2 and J=3/2→1/2 parity–e transitions towards NGC7538(E). The J=5/2→3/2 spectral resolution is 1000 kHz and the J=3/2→1/2 spectral resolution is 250 kHz. For details see caption to Figure 4.1.

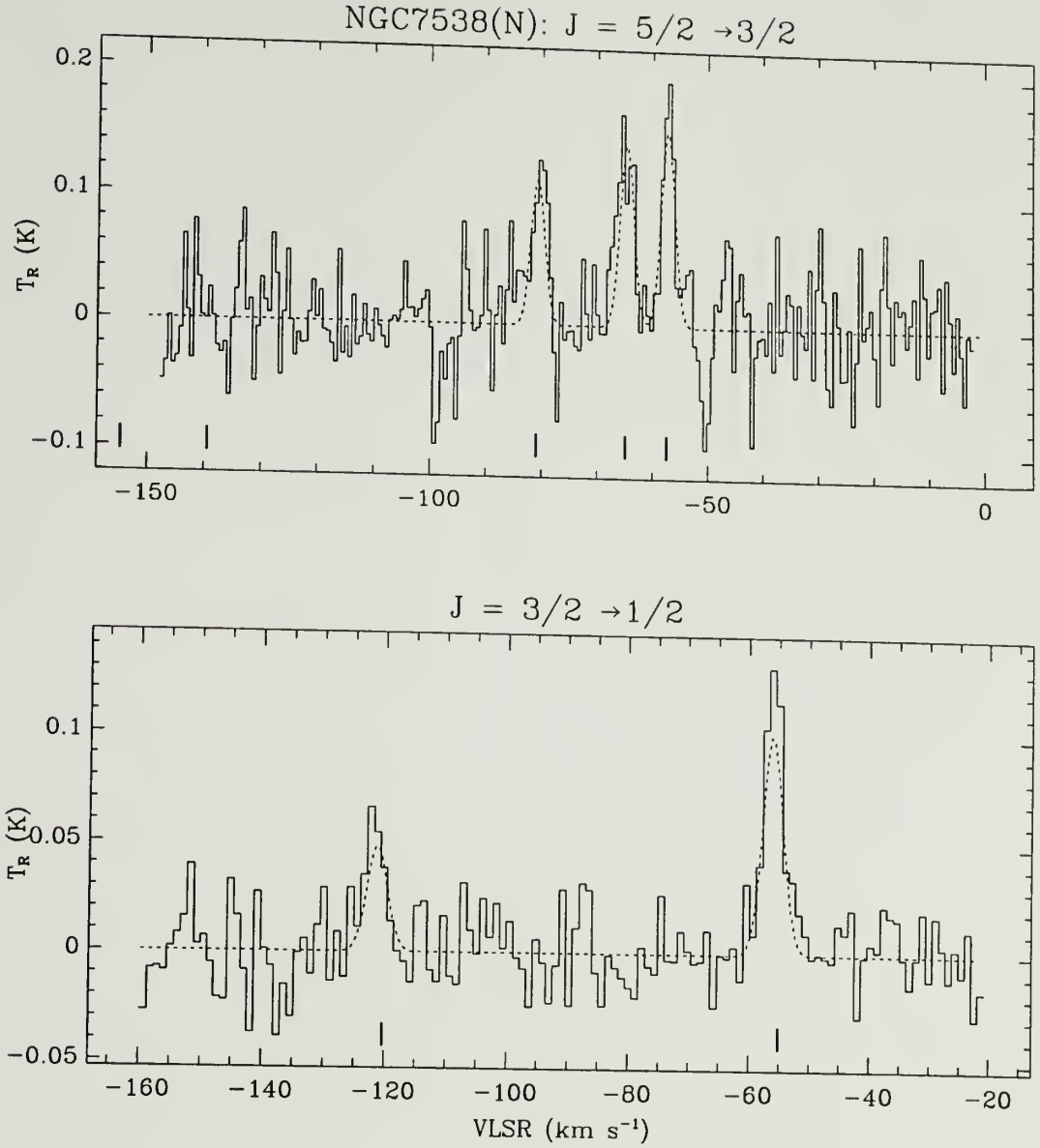

Figure 4.4. Spectra (solid histograms) of the J=5/2→3/2 and J=3/2→1/2 parity–e transitions towards NGC7538(N). For details see caption to Figure 4.1.

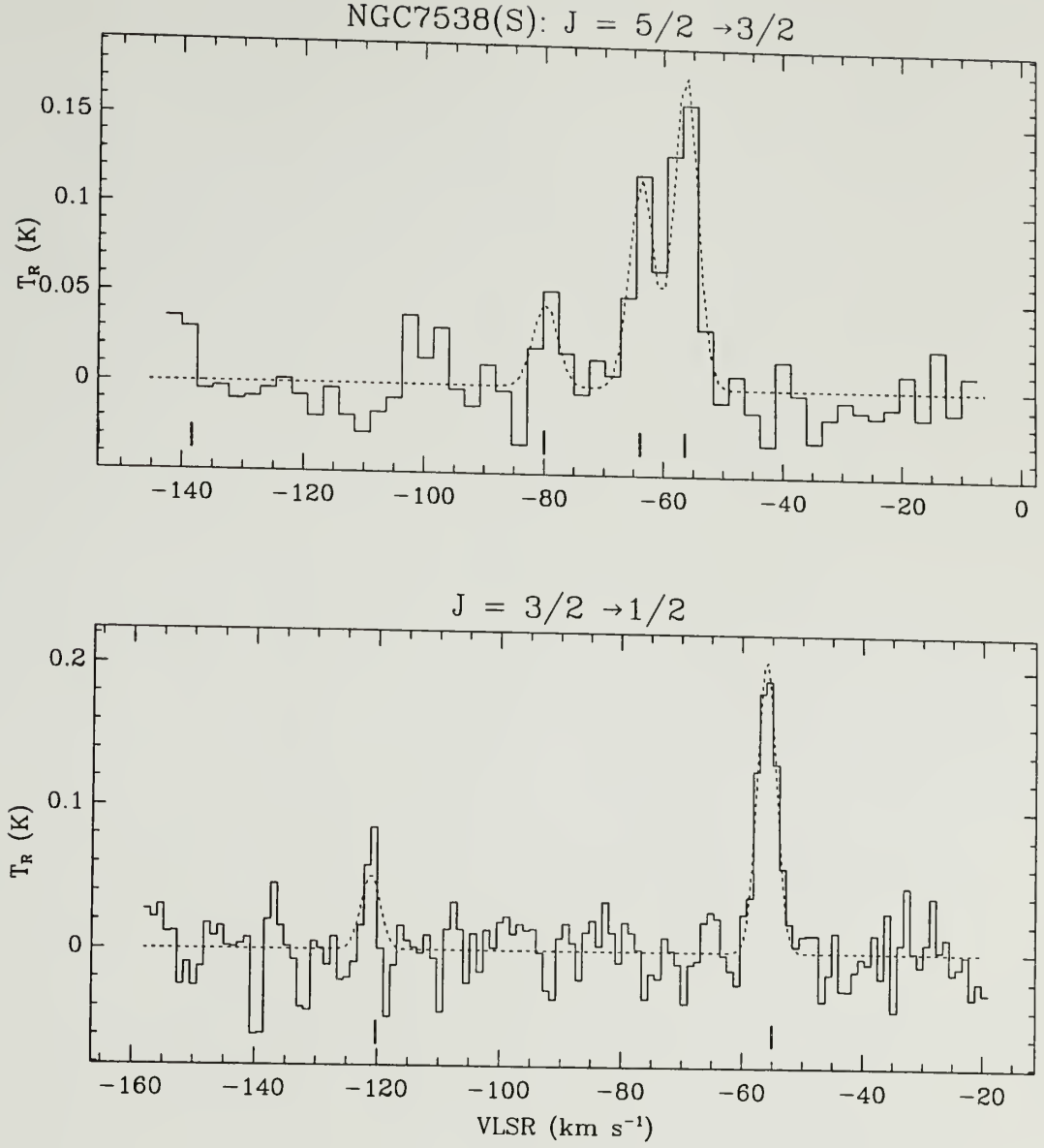

Figure 4.5. Spectra (solid histograms) of the J=5/2→3/2 and J=3/2→1/2 parity-e transitions towards NGC7538(S). The J=5/2→3/2 spectral resolution is 1000 kHz and the J=3/2→1/2 spectral resolution is 250 kHz. For details see caption to Figure 4.1.

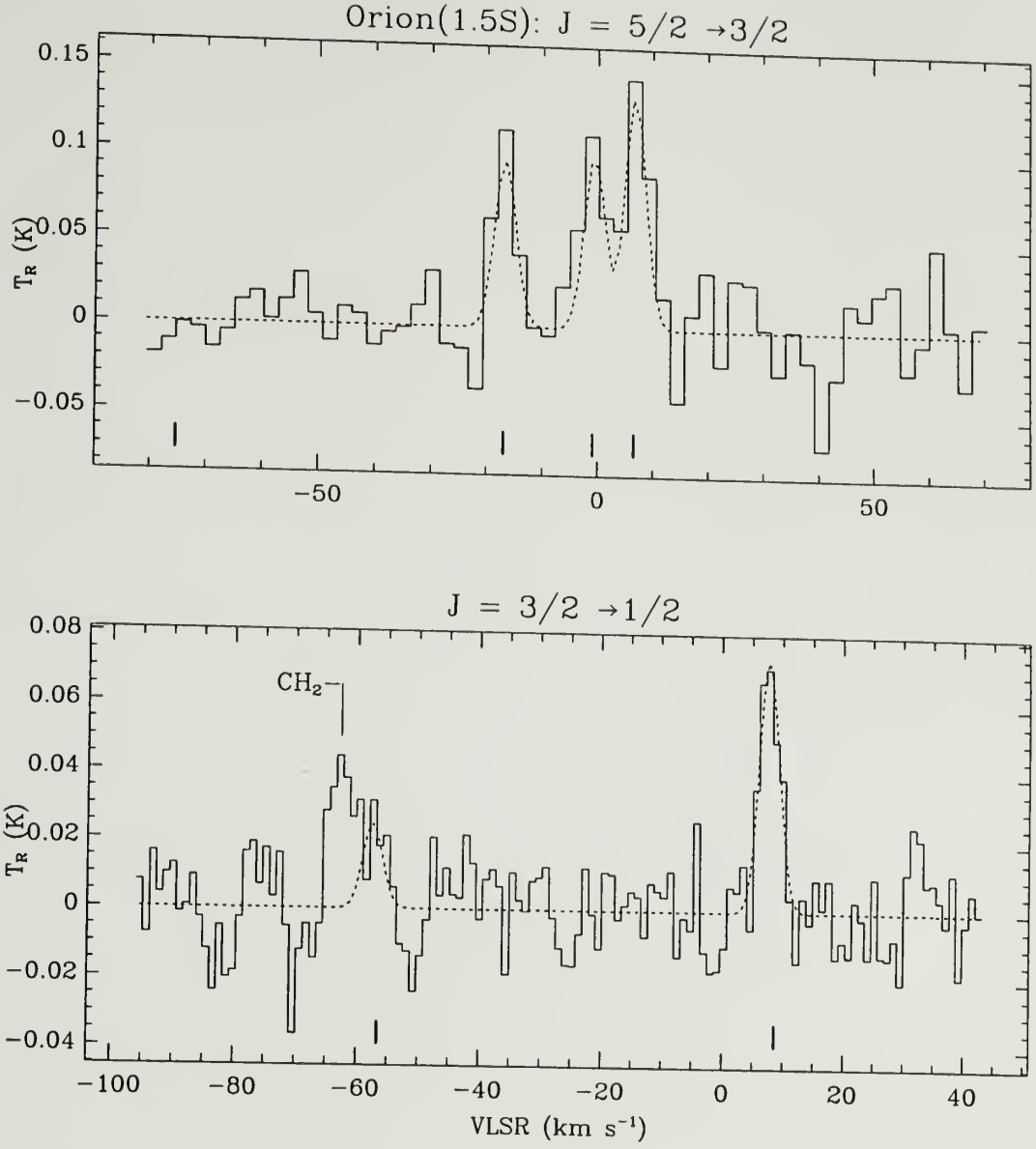

Figure 4.6. Spectra (solid histograms) of the J=5/2→3/2 and J=3/2→1/2 parity–e transitions towards Orion(1.5S). The J=5/2→3/2 spectral resolution is 1000 kHz and the J=3/2→1/2 spectral resolution is 250 kHz. For details see caption to Figure 4.1.

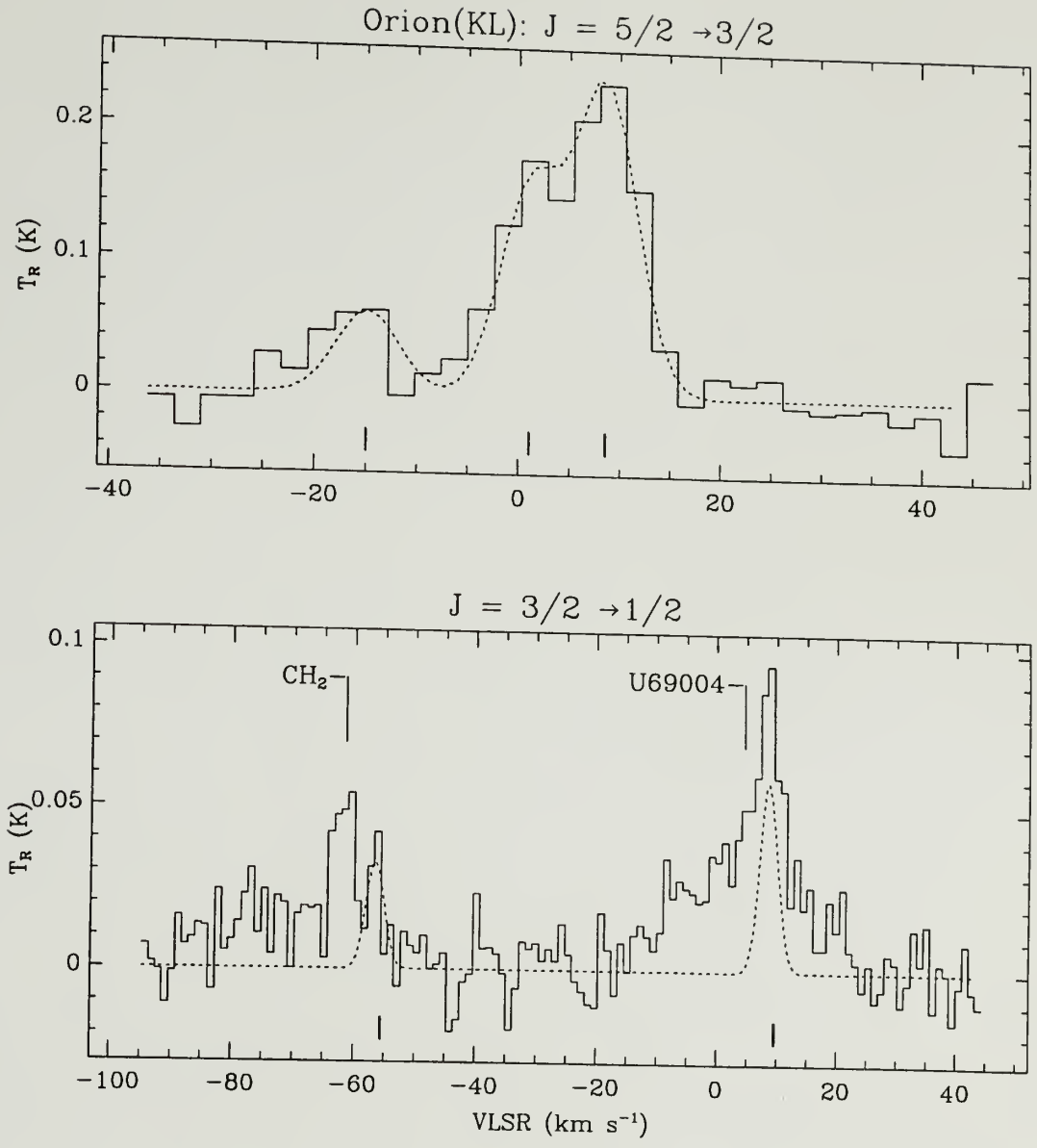

Figure 4.7. Spectra (solid histograms) of the J=5/2→3/2 and J=3/2→1/2 parity–e transitions towards Orion(KL). The J=5/2→3/2 spectral resolution is 1000 kHz and the J=3/2→1/2 spectral resolution is 250 kHz. Broad emission around $V_{LSR}=5$ km s^{-1} in the lower spectrum appears to be an instrumental artifact (*see text*). For other details, see caption to Figure 4.1.

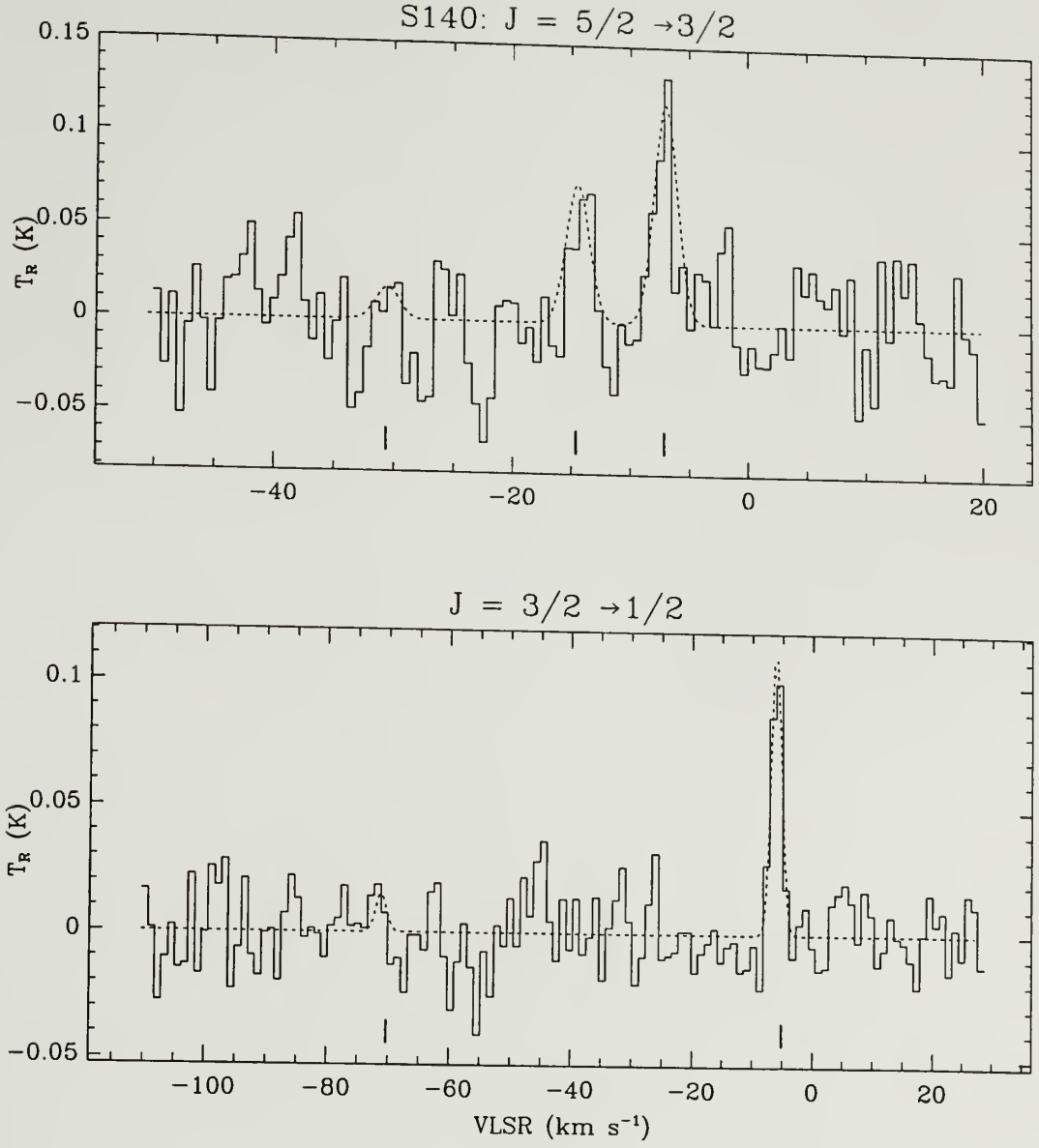

Figure 4.8. Spectra (solid histograms) of the J=5/2→3/2 and J=3/2→1/2 parity–e transitions towards S140. For details see caption to Figure 4.1.

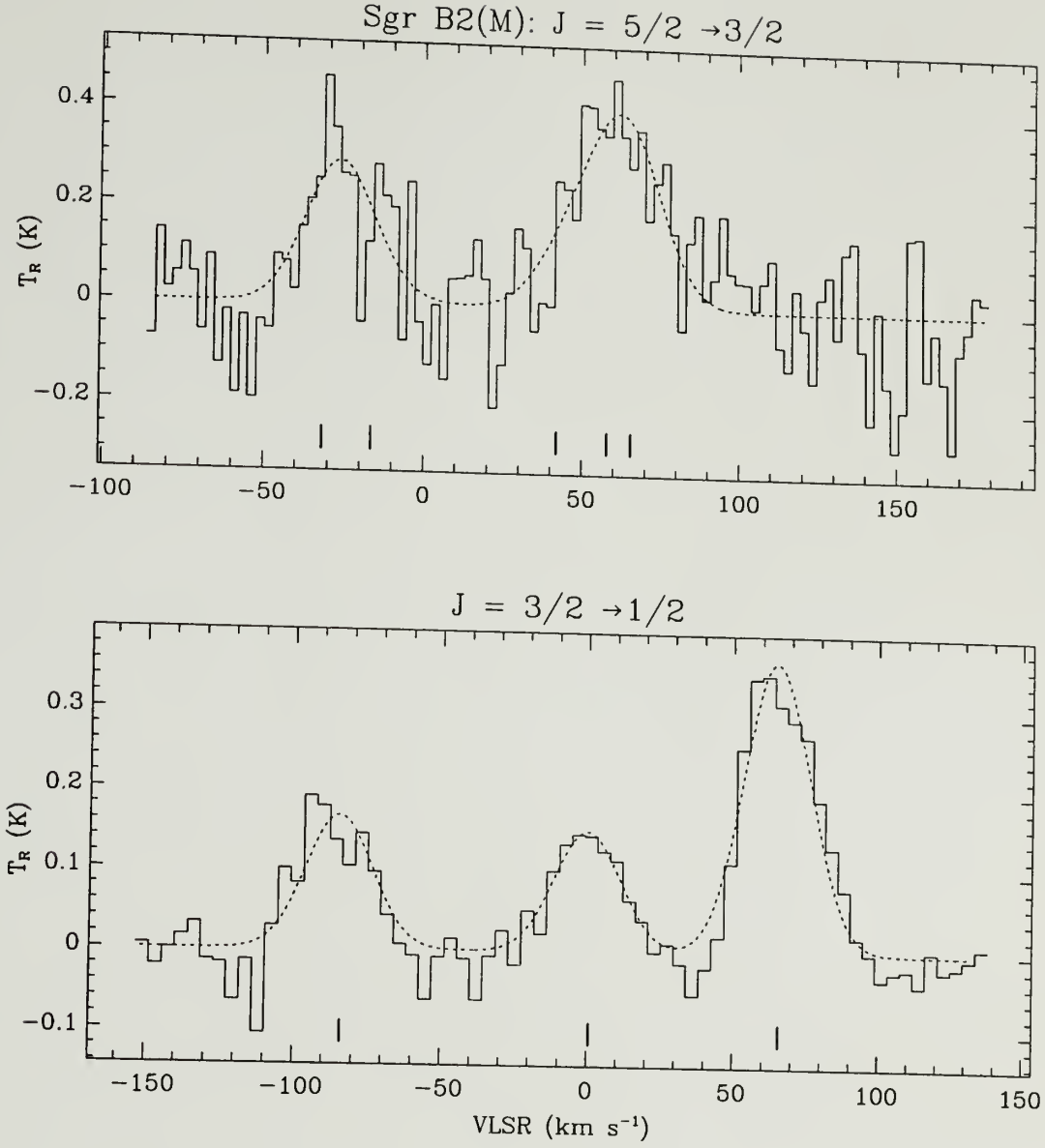

Figure 4.9. Spectra (solid histograms) of the J=5/2→3/2 and J=3/2→1/2 parity–e transitions towards Sgr B2(M). The resolution is 1000 kHz for both spectra. For details see caption to Figure 4.1.

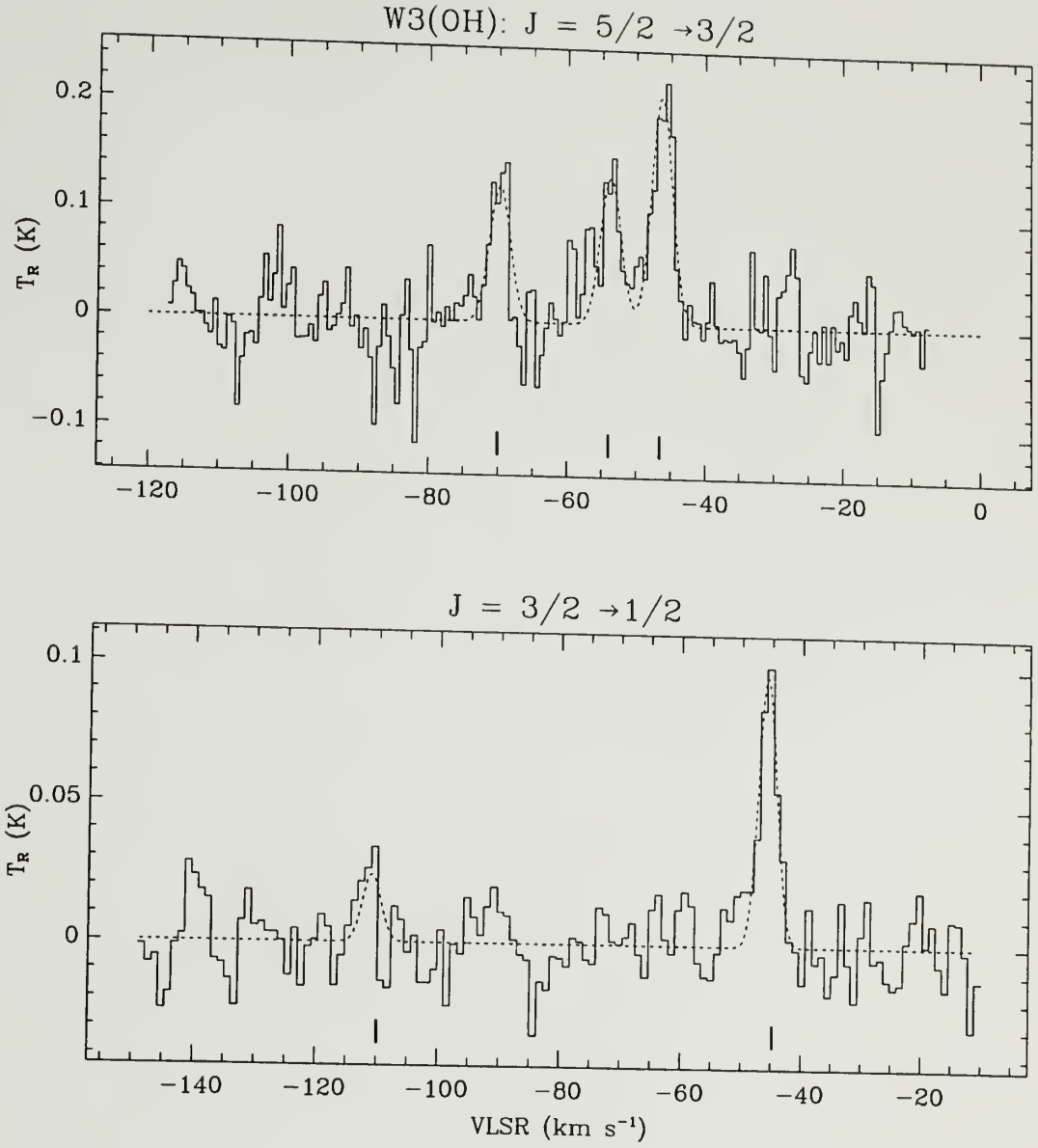

Figure 4.10. Spectra (solid histograms) of the J=5/2→3/2 and J=3/2→1/2 parity–e transitions towards W3(OH). For details see caption to Figure 4.1.

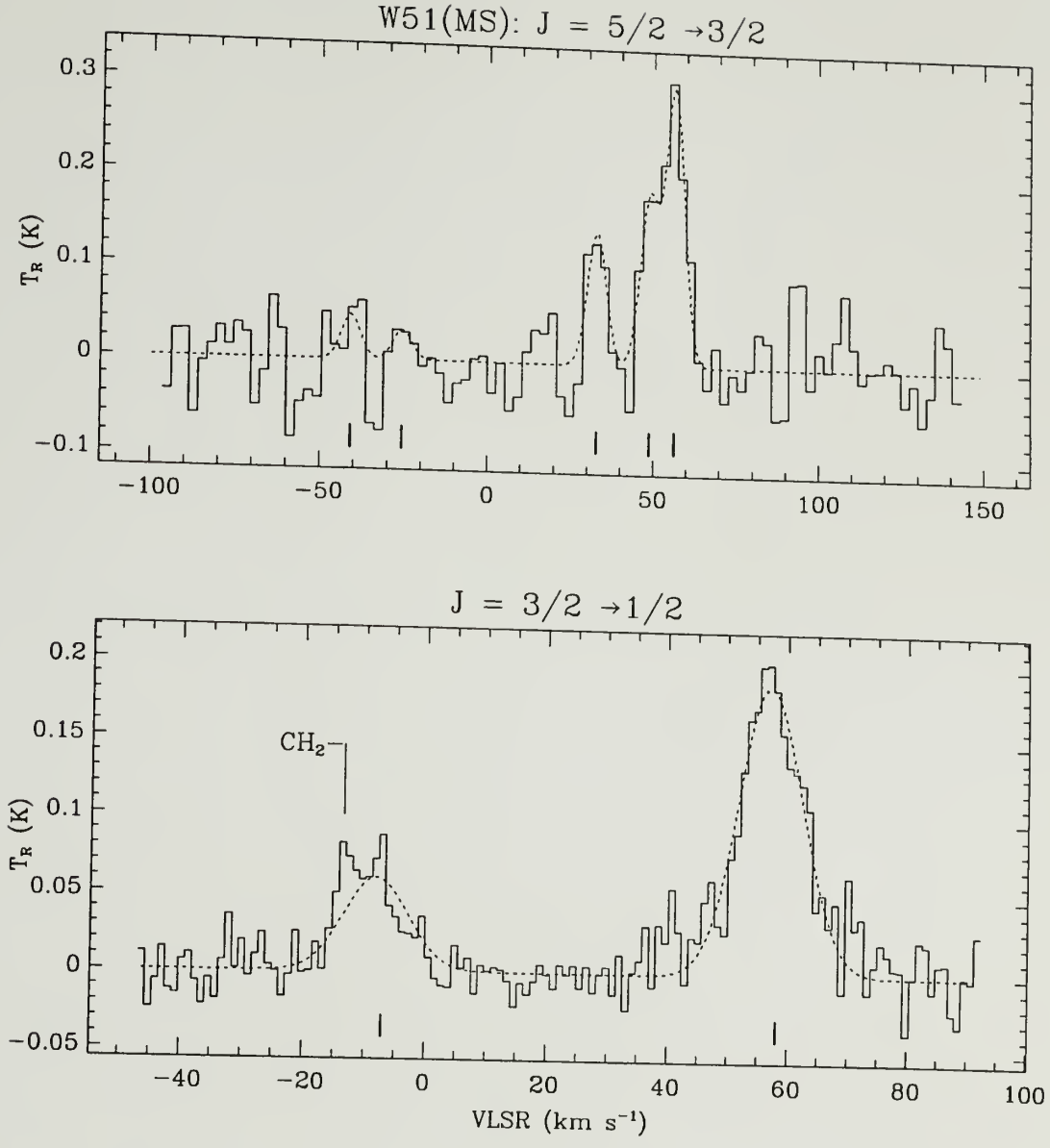

Figure 4.11. Spectra (solid histograms) of the J=5/2→3/2 and J=3/2→1/2 parity-e transitions towards W51(MS). The J=5/2→3/2 spectral resolution is 1000 kHz and the J=3/2→1/2 spectral resolution is 250 kHz. For details see caption to Figure 4.1.

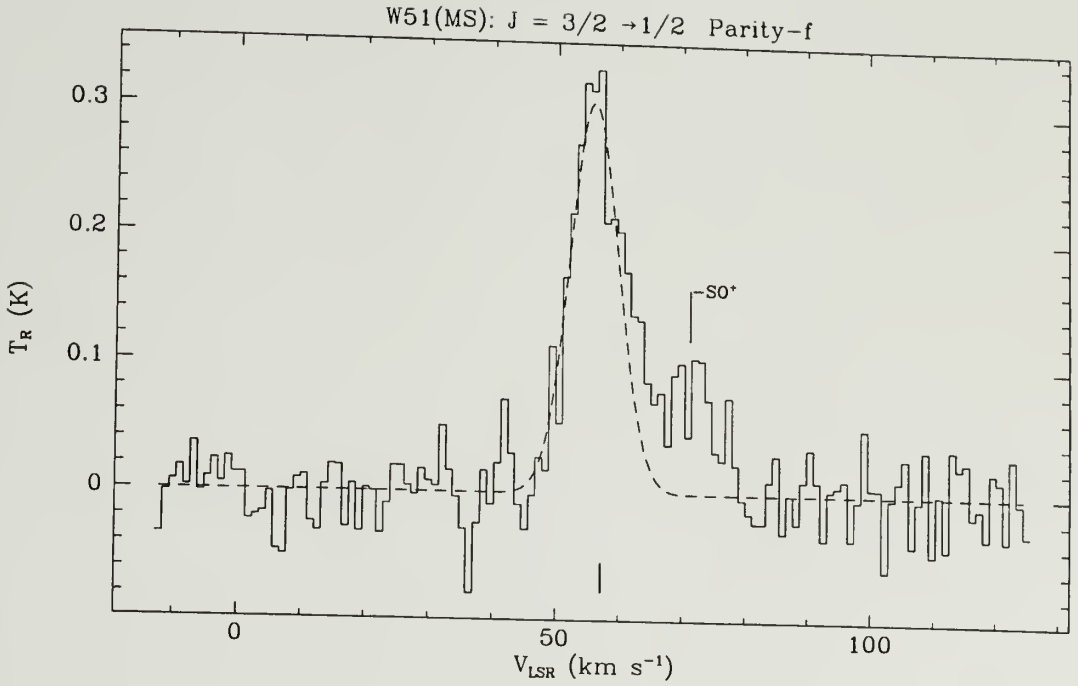

Figure 4.12. Spectrum (solid histogram) of the J=3/2→1/2, parity-f, hyperfine transitions of NS taken toward W51(MS). The spectral resolution is 1000 kHz, and the postion is given in Table 4.2. Dashed curve show the results of a Gaussian fit to the spectrum (*see text*). Fit parameters are given in Table 4.5. Tick mark indicates hyperfine component position. Frequencies from Lee, Ozeki and Siato (1995). This spectrum also contains the first detection of the SO^+ $^2\Pi_{1/2}$ J=3/2→1/2e transition towards a GMC (*see also*, Chapter 3).

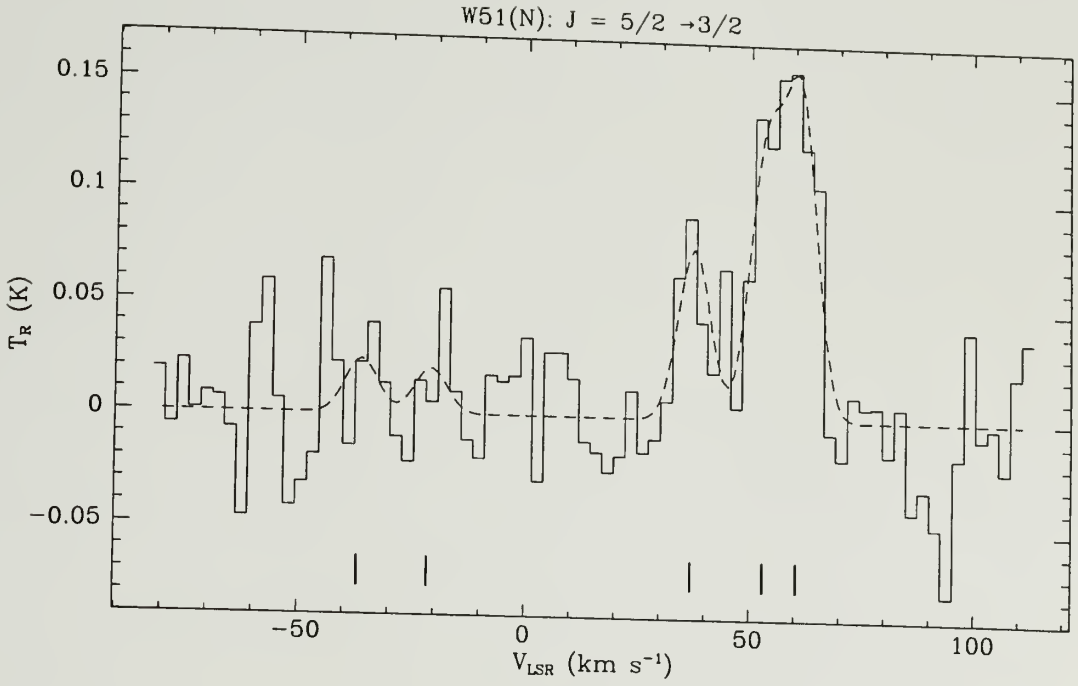

Figure 4.13. Spectrum (solid histogram) of the J=5/2→3/2, parity-f, hyperfine transitions of NS taken toward W51(N). The spectral resolution is 1000 kHz, and the postion is given in Table 4.2. Dashed curve show the results of a Gaussian fit to the spectrum (*see text*). Fit parameters are given in Table 4.7. Tick marks indicate hyperfine component positions. Frequencies from Lee, Ozeki and Siato (1995).

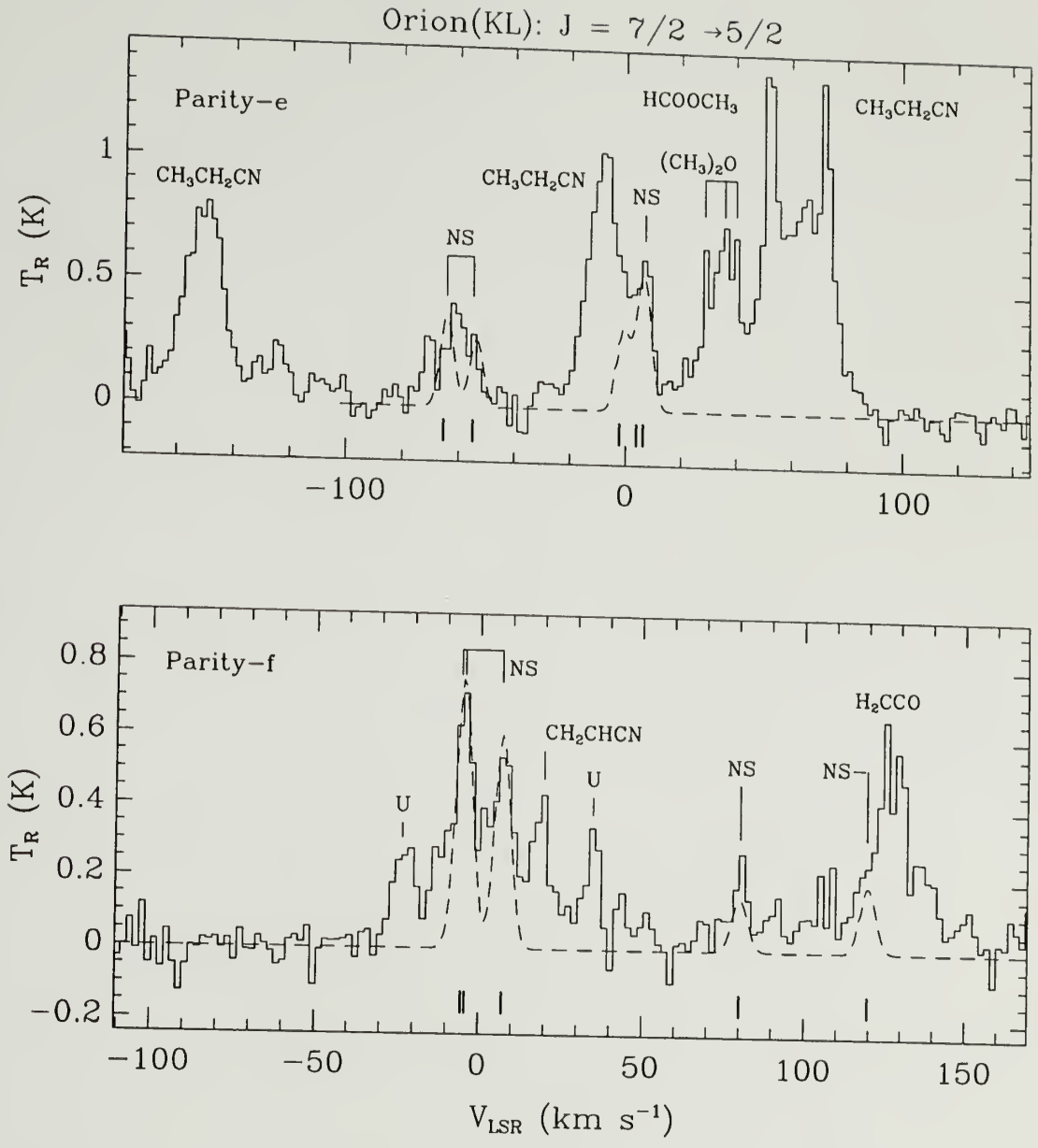

Figure 4.14. Spectrum of the NS J = 7/2 → 5/2 Λ-doublet transitions in Orion(KL). The spectral resolution is 1000 kHz. The dashed curves are the results of a Gaussian fit to the data (*see text*). Fit parameters are given in Table 4.9. Tick marks indicate hyperfine component positions. NS frequencies from Lee, Ozike and Siato (1995). Other spectral features are discussed in Chpater 6.

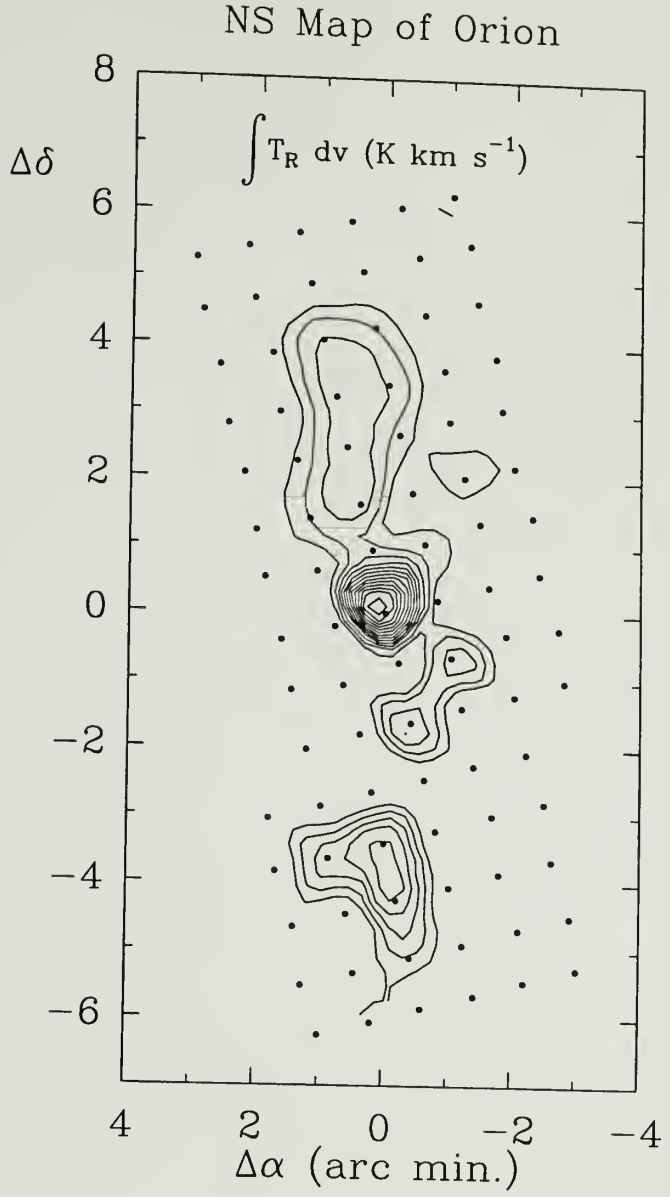

Figure 4.15. Contour map of the NS J=5/2→3/2 parity-e transition integrated over the F=7/2→5/2 and F=5/2→3/2 hyperfine components towards the Orion GMC. The spectral resolution is 250 kHz. Contours are: 0.3–2.1 (K km s^{-1}) at 0.2 (K km s^{-1}) intervals. The map is beamwidth sampled on 50 arcsec centers. Positions are given in arc minute offsets from the origin: α 5^h 32′ 47.0″; δ −5° 24′ 23″ (1950; Orion(KL) position).

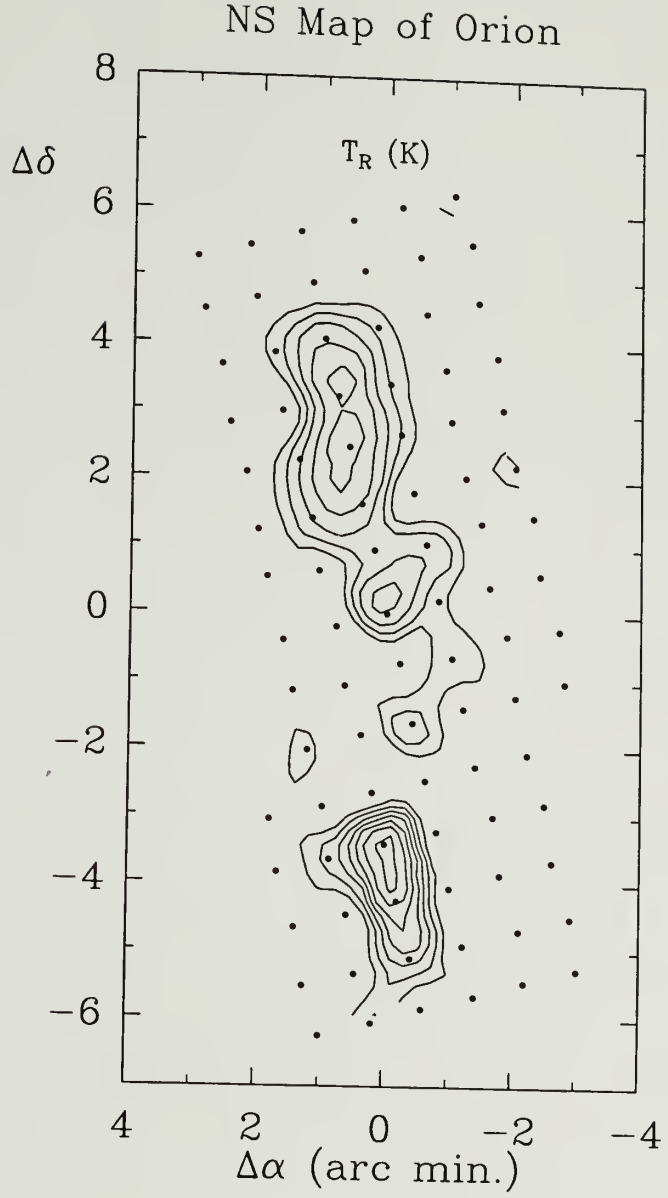

Figure 4.16. Contour map of the peak intensity of the NS $J=5/2\rightarrow3/2$ parity-e, $F=7/2\rightarrow3/2$ hyperfine component towards the Orion GMC. The spectral resolution is 250 kHz. Contours are: 0.15–0.35 K at 0.05 K intervals. See caption to Figure 4.15 for details.

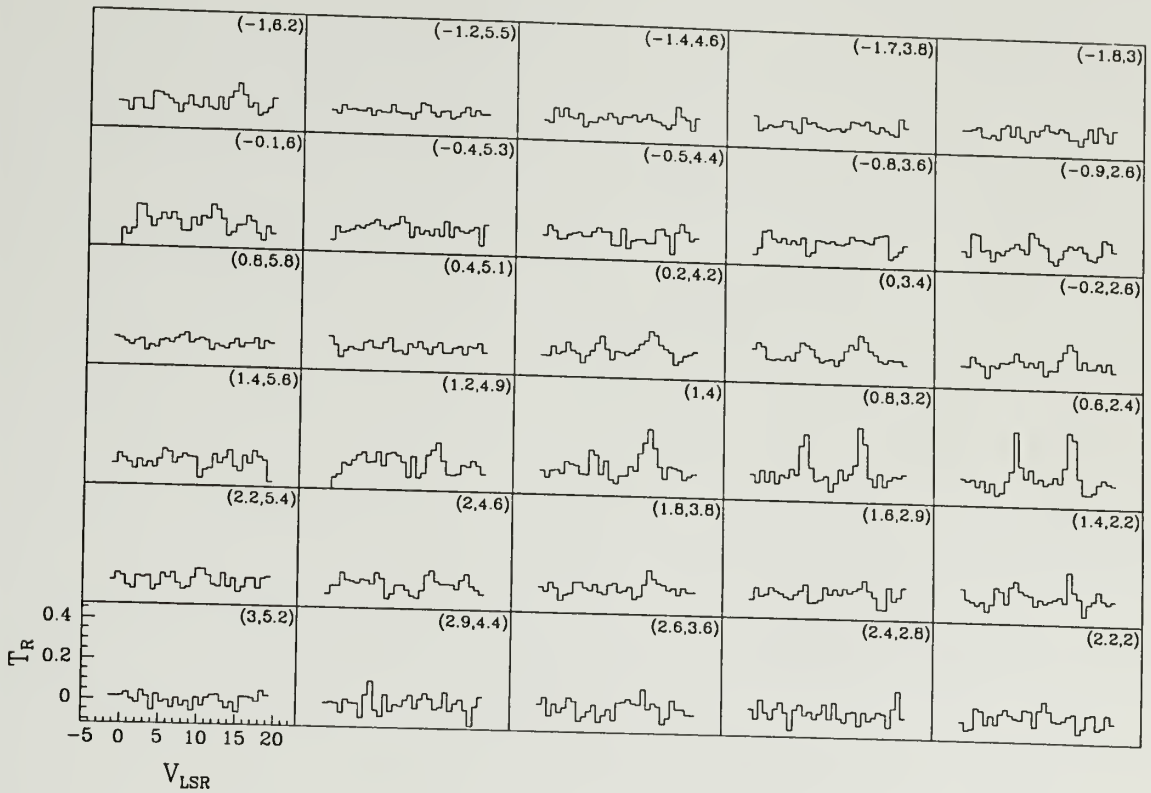

Figure 4.17. Spectra of NS J = 5/2 → 3/2 parity-e F = 7/2 → 5/2 and F = 5/2 → 3/2 hyperfine components towards positions north of Orion(KL). Spectral resolution is 250 kHz. Numbers in brackets are right ascension and declination offsets, in minutes of arc, from the origin: α $5^h\,32'\,47.0''$; δ $-5°\,24'\,23''$ (1950; Orion(KL) position).

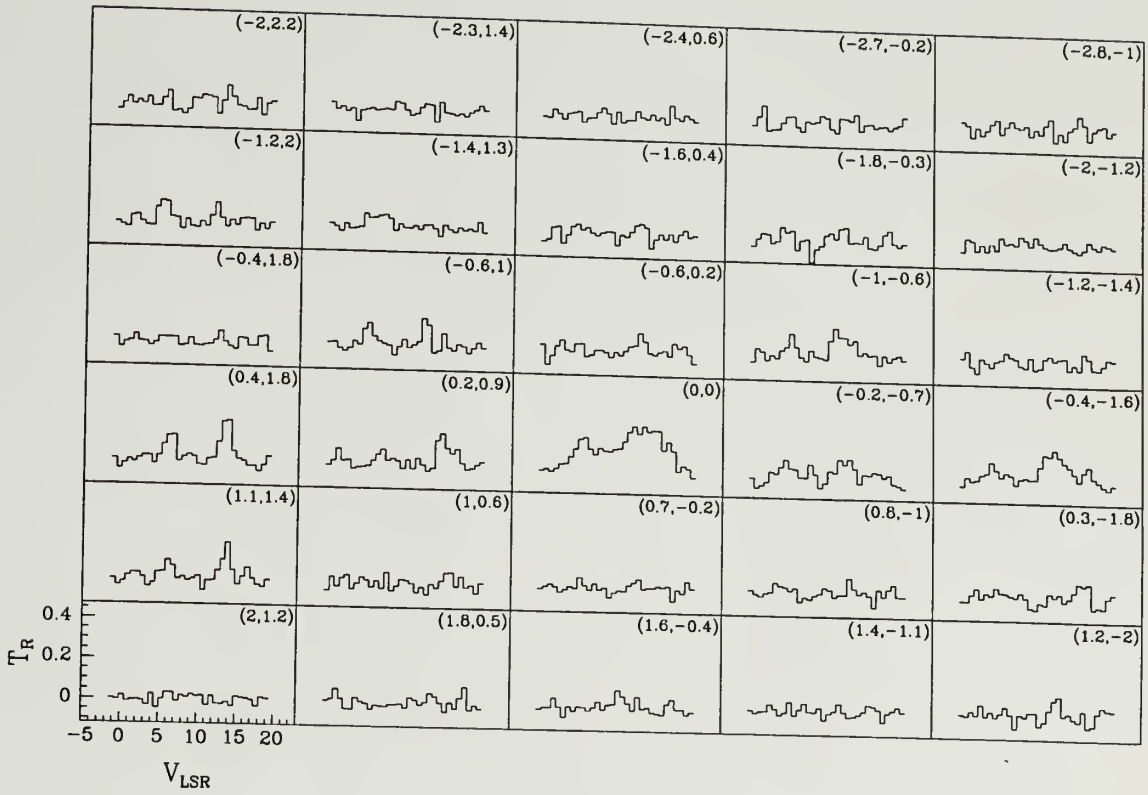

Figure 4.18. Spectra of NS J = 5/2 → 3/2 parity–e F = 7/2 → 5/2 and F = 5/2 → 3/2 hyperfine components towards postions centered on Orion(KL). See caption to Figure 4.17 for details.

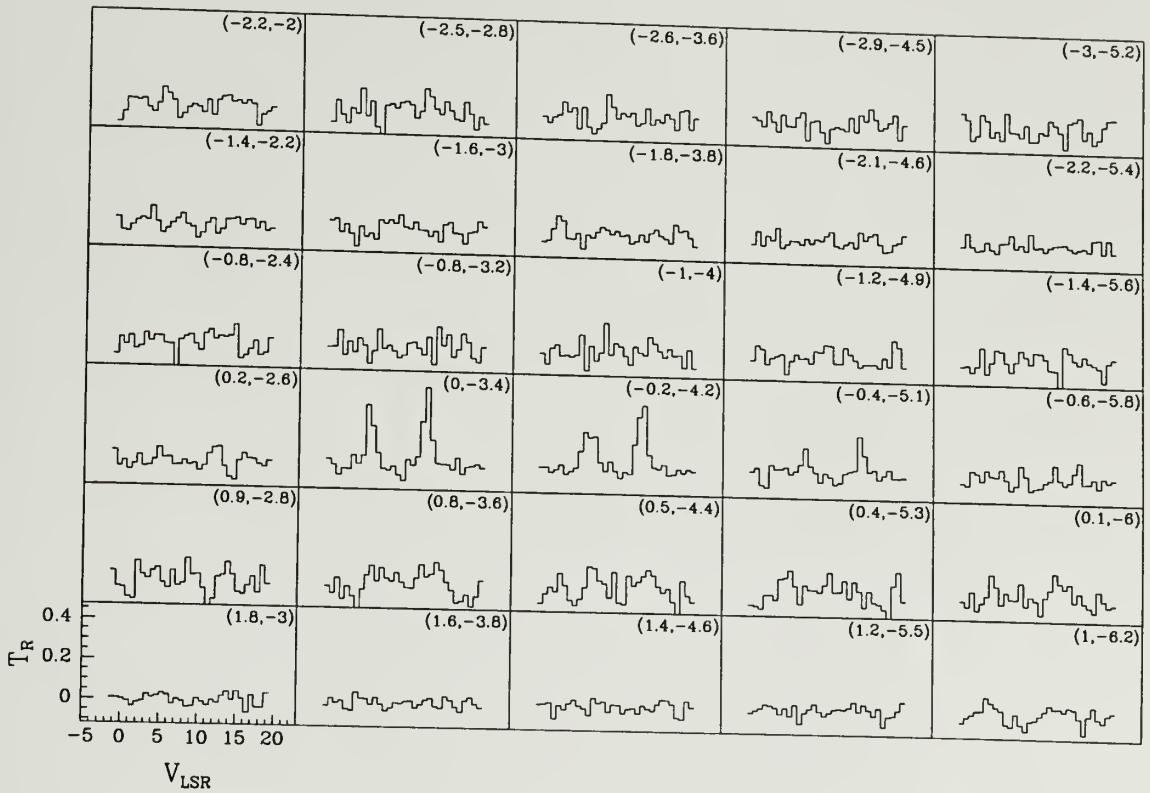

Figure 4.19. Spectra of NS J=5/2→3/2 parity-e F=7/2→5/2 and F=5/2→3/2 hyperfine components towards positions south of Orion(KL). See caption to Figure 4.17 for details.

Table 4.5. NS J=3/2→1/2 Gaussian Fit Results [a]

Source	Res. (kHz)	RMS (mK)	V_{LSR} (km s^{-1})	T_R [b] (K)	T_R [c] (K)	T_R [d] (K)	FWHM (km s^{-1})
DR21(OH)	250	14	-1.9	0.19	0.07		3.07
G34.3+0.2	250	15	59.7	0.26	0.05		4.39
NGC7538(E)	250	13	-55.7	0.10	0.05		3.97
NGC7538(N)	250	16	-55.7	0.13	0.06		3.79
NGC7538(S)	250	22	-55.5	0.21	0.05		3.68
Orion(1.5S)	250	12	8.2	0.074	0.025		3.83
Orion(KL) [e]	98	10	~9.0	0.060	0.029		5.41
S140	250	14	-5.6	0.11	0.02		2.06
Sgr B2(M)	1000	39	65.3	0.37	0.15	0.17	26.64
W3(OH)	250	12	-45.3	0.10	0.02		3.53
W51(MS)	250	14	57.5	0.19	0.06		12.44
W51(MS)[a]	250	11	55.9	0.18			9.06

(a) All transitions belong to the parity–e band except W51(MS), which was also observed in the parity–f band. For errors in measured quantities see Table 4.6.

(b) F=5/2→3/2

(c) F=3/2→1/2

(d) F=3/2→3/2

(e) Line parameters from Hollis, Jewell and Lovas (1995).

Table 4.6. NS J = 3/2 → 1/2 Gaussian Fit Errors [a]

Source	Res. (kHz)	RMS (mK)	V_{LSR} (km s^{-1})	T_R [b] (K)	T_R [c] (K)	T_R [d] (K)	FWHM (km s^{-1})
DR21(OH)	250	14	0.09	0.011	0.010		0.20
G34.3+0.2	250	15	0.10	0.012	0.010		0.23
NGC7538(E)	250	13	0.17	0.010	0.008		0.40
NGC7538(N)	250	16	0.16	0.012	0.010		0.37
NGC7538(S)	250	22	0.14	0.016	0.014		0.33
Orion(1.5S)	250	12	0.23	0.009	0.008		0.53
Orion(KL)[e]	98	10	0.43	0.010	0.010		0.32
S140	250	14	0.12	0.015	0.012		0.33
SGR(B2M)	1000	39	0.68	0.021	0.019	0.019	1.59
W3(OH)	250	12	0.16	0.009	0.008		0.38
W51(MS)	250	14	0.18	0.006	0.005		0.43
W51(MS)[a]	250	11	0.23	0.010	—		0.47

(a) All transitions belong to the parity–e band except W51(MS), which was also observed in the parity–f band.

(b) F = 5/2 → 3/2

(c) F = 3/2 → 1/2

(d) F = 3/2 → 3/2

(e) Line parameters from Hollis, Jewell and Lovas (1995).

Table 4.7. NS J=5/2→3/2 Parity-e Gaussian Fit Results [a]

Source	Res. (kHz)	RMS (mK)	V_{LSR} (km s^{-1})	T_R [b] (K)	T_R [c] (K)	T_R [d] (K)	T_R [e] (K)	T_R [f] (K)	FWHM (km s^{-1})
DR21(OH)	1000	18	-2.3	0.14	0.12	0.08			5.26
	250	29	-2.6	0.16	0.14	0.10			4.68
G34.3+0.2	1000	26	58.2	0.31	0.22	0.12			5.52
	250	40	58.2	0.34	0.23	0.11			5.02
IRC+10216	1000	31		$\leq$ 0.09					
NGC7538(E)	1000	16	-57.2	0.10	0.04	0.04			3.78
NGC7538(N)	1000	24	-57.4	0.09	0.11	0.08			4.20
	250	36	-57.3	0.16	0.14	0.11			2.93
NGC7538(S)	1000	16	-56.3	0.18	0.12	0.05	0.03	0.03	4.70
Orion(1.5S)	1000	36	6.8	0.14	0.10	0.10			4.46
	250	33	7.1	0.15	0.10	0.11			5.07
Orion(KL)[g]	1000	30	8.2	0.26	0.19	0.15			5.71
	250	>19	8.7	0.22	0.12				5.71
S140	250	25	-7.0	0.12	0.08	0.02			2.31
Sgr B2(M)	1000	104	65.3[h]	0.19	0.26	0.06	0.12	0.22	23.49
W3(IRS5)	1000	31		$\leq$ 0.09					
W3(OH)	1000	20	-46.6	0.18	0.12	0.10	0.04	0.07	4.52
	250	33	-46.3	0.21	0.14	0.13			3.54
W49(N)	1000	40		$\leq$ 0.12					
W51(MS)	1000	45	56.4	0.30	0.18	0.15			6.52
	250	47	56.2	0.33	0.22	0.18			6.91
W51(N)	1000	44	61.1	0.14	0.12	0.08			8.45

(a) For errors in measured quantities see Table 4.8.

(b) F=7/2→5/2

(c) F=5/2→3/2

(d) F=3/2→1/2

(e) F=3/2→3/2

(f) F=5/2→5/2

(g) 250 kHz measurements are from QUARRY data (*see text*).

(h) V_{LSR} fixed to the value observed for the J=3/2→1/2 transition.

Table 4.8. NS J=5/2→3/2 Parity-e Gaussian Fit Errors

Source	Res. (kHz)	V_{LSR} ($km\,s^{-1}$)	T_R [a] (K)	T_R [b] (K)	T_R [c] (K)	T_R [d] (K)	T_R [e] (K)	FWHM ($km\,s^{-1}$)
DR21(OH)	1000	0.22	0.014	0.013	0.012			0.39
	250	0.16	0.014	0.014	0.013			0.31
G34.3+0.2	1000	0.18	0.021	0.021	0.018			0.31
	250	0.13	0.019	0.018	0.017			0.24
IRC+10216	1000							
NGC7538(E)	1000	0.31	0.022	0.017	0.016			0.97
NGC7538(N)	1000	0.25	0.020	0.020	0.019			0.70
	250	0.15	0.022	0.022	0.021			0.34
NGC7538(S)	1000	0.17	0.015	0.014	0.013	0.013	0.013	0.34
Orion(1.5S)	1000	0.31	0.022	0.022	0.021			0.54
	250	0.23	0.016	0.016	0.015			0.44
Orion(KL)[f]	1000	0.26	0.03	0.03	0.02			0.48
	250	0.17	0.012	0.0012				0.31
S140	250	0.16	0.019	0.017	0.016			0.37
SGR(B2M)	1000	—	0.116	0.111	0.077	0.054	0.022	4.50
W3(IRS5)	1000							
W3(OH)	1000	0.18	0.017	0.016	0.016	0.016	0.016	0.33
	250	0.12	0.018	0.017	0.017			0.28
W49N	1000							
W51(MS)	1000	0.37	0.035	0.035	0.029			0.69
	250	0.27	0.027	0.028	0.021			0.50
W51(N)	1000	0.78	0.028	0.031	0.020			1.35

(a) F=7/2→5/2

(b) F=5/2→3/2

(c) F=3/2→1/2

(d) F=3/2→3/2

(e) F=5/2→5/2

(f) 250 kHz resolution measurements are from QUARRY data (*see text*).

Table 4.9. NS in Orion(KL); J = 7/2 → 5/2 Gaussian Fit Results

Par	Res. (kHz)	RMS (mK)	V_{LSR} ($km\,s^{-1}$)	T_R [a] (K)	T_R [b] (K)	T_R [c] (K)	T_R [d] (K)	T_R [e] (K)	FWHM[f] ($km\,s^{-1}$)
e	1000	45	7.3	0.39	0.26	0.34	—	—	5.71
f	1000	52	7.0	0.60	0.48	0.30	0.19	0.15	5.71

(a) F = 9/2 → 7/2.

(b) F = 7/2 → 5/2.

(c) F = 5/2 → 3/2.

(d) F = 7/2 → 7/2.

(e) F = 5/2 → 5/2.

(f) The FWHM parameter was held fixed to the measured J = 5/2 → 3/2 Orion(KL) transition value.

Table 4.10. NS in Orion(KL); J = 7/2 → 5/2 Gaussian Fit Errors

Par	Res. (kHz)	RMS (mK)	V_{LSR} [a] ($km\,s^{-1}$)	T_R [b] (K)	T_R [c] (K)	T_R [d] (K)	T_R [e] (K)	T_R [f] (K)	FWHM ($km\,s^{-1}$)
e	1000	45	0.9	0.09	0.08	0.03	—	—	0.9
f	1000	52	0.9	0.03	0.17	0.17	0.03	0.03	0.9

(a) V_{LSR} and FWHM errors are defined to be half the spectral resolution. All other errors are 1σ from fit.

(b) F = 9/2 → 7/2.

(c) F = 7/2 → 5/2.

(d) F = 5/2 → 3/2.

(e) F = 7/2 → 7/2.

(f) F = 5/2 → 5/2.

Table 4.11. NS Orion Map; J = 5/2 → 3/2 Parity-e Gaussian Fit Results

Offset [a] (arcmin)	Res. (kHz)	RMS (mK)	V_{LSR} ($km\,s^{-1}$)	T_R [b] (K)	T_R [c] (K)	T_R [d] (K)	FWHM ($km\,s^{-1}$)	$\int T_R\,dv$ [e] ($K\,km\,s^{-1}$)
(0.20, 4.26)	250	25	9.96	0.11	0.04		2.29	0.34 ± .08
(1.02, 4.07)	250	29	9.56	0.22	0.08		1.70	0.51 ± .08
(-0.02, 3.41)	250	26	9.74	0.12	0.07		2.59	0.49 ± .10
(0.80, 3.22)	250	29	9.89	0.28	0.24		1.11	0.58 ± .08
(-0.20, 2.66)	250	24	9.69	0.12	0.05		1.68	0.29 ± .07
(0.62, 2.47)	250	36	10.02	0.30	0.23		1.13	0.60 ± .10
(1.40, 2.26)	250	31	9.85	0.17	0.13		∼0.75	0.23
(-1.22, 2.03)	250	22	8.91	0.05	0.12		1.68	0.29 ± .06
(0.41, 1.62)	250	23	9.99	0.22	0.13		1.63	0.57 ± .07
(1.19, 1.40)	250	25	10.16	0.18	0.10		1.28	0.36 ± .06
(-0.61, 1.04)	250	23	7.95	0.16	0.13		1.01	0.29 ± .07
(0.21, 0.94)	250	20	10.35	0.15	0.06		1.89	0.40 ± .06
(-0.81, 0.20)	250	28	8.30	0.09	0.02		1.22	0.13 ± .06
(0.00, 0.00)	250	> 19	9.10	0.22	0.12		5.75	1.95 ± .10
	1000	18	8.66	0.24	0.16	0.06	7.12	3.28 ± .29
(-1.03,-0.65)	250	19	7.16	0.12	0.05		3.22	0.55 ± .08
(-0.41,-1.62)	250	26	7.42	0.15	0.04		3.22	0.61 ± .10
	1000	16	7.48	0.13	0.08	0.05	4.98	1.29 ± .19
(0.00,-3.42)	250	28	8.31	0.39	0.30		1.20	0.83 ± .08
(-0.20,-4.26)	250	18	8.79	0.34	0.20		1.46	0.79 ± .06
(-0.42,-5.11)	250	29	9.89	0.20	0.13		∼1.00	0.33

(a) Map Origin: RA $5^h\,32^m\,47.0^s$; DEC $-5°\,24^m\,23^s$.

(b) F = 7/2 → 5/2.

(c) F = 5/2 → 3/2.

(d) F = 3/2 → 1/2.

(e) Not corrected for unobserved components.

Table 4.12. NS Orion Map; J = 5/2 → 3/2 Parity-e Gaussian Fit Errors

Offset [a] (arcmin)	Res. (kHz)	RMS (mK)	V_{LSR} ($km\,s^{-1}$)	T_R [b] (K)	T_R [c] (K)	T_R [d] (K)	FWHM ($km\,s^{-1}$)	$\int T_R\,dv$ ($K\,km\,s^{-1}$)
(0.20, 4.26)	250	25	0.173	0.018	0.015		0.407	0.081
(1.02, 4.07)	250	29	0.090	0.025	0.021		0.212	0.084
(-0.02, 3.41)	250	26	0.173	0.018	0.016		0.407	0.099
(0.80, 3.22)	250	29	0.044	0.031	0.030		0.133	0.084
(-0.20, 2.66)	250	24	0.134	0.020	0.017		0.315	0.069
(0.62, 2.47)	250	36	0.056	0.038	0.035		0.149	0.098
(1.40, 2.26)	250	31	0.059	0.036	0.037		—	—
(-1.22, 2.03)	250	29	0.124	0.016	0.018		0.292	0.064
(0.41, 1.62)	250	21	0.066	0.020	0.018		0.157	0.074
(1.19, 1.40)	250	25	0.074	0.024	0.022		0.177	0.065
(-0.61, 1.04)	250	23	0.057	0.031	0.028		0.214	0.075
(0.21, 0.94)	250	20	0.095	0.016	0.014		0.223	0.062
(-0.81, 0.20)	250	28	0.186	0.028	0.024		0.391	0.062
(0.00, 0.00)	250	25	0.120	0.009	0.008		0.220	0.102
	1000	16	0.270	0.017	0.017	0.013	0.477	0.293
(-1.03,-0.65)	250	19	0.148	0.012	0.010		0.344	0.077
(-0.41,-1.62)	250	31	0.174	0.017	0.014		0.406	0.105
	1000	15	0.275	0.016	0.015	0.014	0.535	0.190
(0.00,-3.42)	250	28	0.041	0.031	0.030		0.086	0.079
(-0.20,-4.26)	250	18	0.034	0.015	0.015		0.092	0.059
(-0.42,-5.11)	250	29	0.063	0.028	0.028		—	—

(a) Map Origin: RA $5^h\,32^m\,47.0^s$; DEC $-5°\,24^m\,23^s$.

(b) F = 7/2 → 5/2.

(c) F = 5/2 → 3/2.

(d) F = 3/2 → 1/2.

4.5 NS Abundance in Star Forming Regions

In this section, we shall discuss our attempts to determine the NS abundance towards each of the observed GMCs. The first subsection describes our analysis of the NS hyperfine component line strength as a test for optically thin emission. The second subsection reports on the results derived from a simple source model which assumed optically thin emission with a Boltzmann population distribution and no beam dilution. The third subsection describes a more complicated statistical equilibrium modeling of the observed sources and the NS total column densities and fractional abundances derived by this method.

4.5.1 Hyperfine Component Test For Optically Thin Emission

We first estimated the abundance of NS towards our sources assuming optically thin emission, Boltzmann population distributions, and no beam dilution. We tested for optically thin emission by comparing the observed hyperfine line strength ratios with the intrinsic hyperfine line strengths (*see* Table 4.1). The observed ratios for the $J=3/2 \rightarrow 1/2$ rotational transition are listed in Table 4.13 and the $J=5/2 \rightarrow 3/2$ ratios in Table 4.14. In the following text, the ratio under discussion is identified by the hyperfine component in the numerator (i.e., all ratios would be < 1 barring anomalous excitation).

Comparing the observed hyperfine line strength ratios with the expected values for optically thin emission, we find the sources DR21(OH), G34.3+02, NGC7538, Orion(1.5S), Orion(KL), S140, W3(OH), W51(MS), and W51(N) to be consistent with optically thin emission to within the accuracy of our observations.

We also have spectra of the $J=7/2 \rightarrow 5/2$ parity-e and parity-f transitions towards Orion(KL), and the relative hyperfine line strength ratios are given in Table 4.15. Unfortunately, no firm conclusion may drawn from these results since the NS emission is severely blended with other spectral lines, which obliges us to

Table 4.13. NS J=3/2→1/2 Hyperfine Line Strength Ratios [a] [b]

Source	Res. (kHz)	$R_{F=3/2,1/2}$ [0.37]	$R_{F=3/2,3/2}$ [0.30]
DR21(OH)	250	0.38 ±.06	
G34.3+0.2	250	0.20 ±.04	
NGC7538(E)	250	0.48 ±.10	
NGC7538(N)	250	0.46 ±.09	
NGC7538(S)	250	0.25 ±.07	
Orion(1.5S)	250	0.33 ±.11	
Orion(KL)	250	0.48 ±.18	
S140	250	0.13 ±.10	
Sgr B2(M)	1000	0.41 ±.06	0.46 ±.06
W3(OH)	250	0.25 ±.08	
W51(MS)	250	0.32 ±.03	

(a) Ratios of the parity-e hyperfine components taken relative to F=5/2→3/2. The calculated value for optically thin emission is quoted in square brackets.

(b) Reported errors are 1σ.

treat the formal errors derived from the emission fitting as lower limits. In addition, the parity-e F=9/2→7/2 and F=7/2→5/2 as well as the parity-f F=7/2→5/2 and F=5/2→3/2 hyperfine components are separated by less than the 1 MHz spectral resolution, which makes the amplitude fit for each member of these pairs highly uncertain. We tried to resolve this problem by combining the amplitudes of the blended pair and then taking their ratio with respect to the remaining non-blended component. In this way we find for the parity-e hyperfine components,

$$\frac{T_R(F=5/2\rightarrow 3/2)}{T_R(F=9/2\rightarrow 7/2)+T_R(F=7/2\rightarrow 5/2)} = 0.52 \pm .08,\ [0.31]\ , \qquad (4.5)$$

and for the parity-f hyperfine components,

Table 4.14. NS J=5/2→3/2 Hyperfine Line Strength Ratios [a] [b]

Source	Res. (kHz)	$R_{F=5/2,3/2}$ [0.64]	$R_{F=3/2,1/2}$ [0.36]	$R_{F=3/2,3/2}$ [0.14]	$R_{F=5/2,5/2}$ [0.14]
DR21(OH)	1000	0.83 ±.11	0.54 ±.10	0.13 ±.09	0.13 ±.09
	250	0.82 ±.10	0.62 ±.09		
G34.3+0.2	1000	0.70 ±.08	0.38 ±.07	0.06 ±.06	0.23 ±.06
	250	0.69 ±.06	0.34 ±.05		
NGC7538(E)	1000	0.39 ±.17	0.36 ±.16		
NGC7538(N)	1000	1.23 ±.30	0.94 ±.26		
	250	0.93 ±.18	0.74 ±.16		
NGC7538(S)	1000	0.66 ±.08	0.26 ±.07	0.15 ±.07	.17 ±.07
Orion(1.5S)	1000	0.74 ±.19	0.71 ±.18		
	250	0.65 ±.12	0.78 ±.12		
Orion(KL)	1000	0.73 ±.12	0.57 ±.11		
	250	0.71 ±.08	0.58 ±.07		
S140	250	0.63 ±.14	0.15 ±.14		
Sgr B2(M)	1000	1.28 ±1.3	0.26 ±.30	0.62 ±.39	1.07 ±.62
W3(OH)	1000	0.69 ±.10	0.54 ±.10	0.24 ±.09	0.38 ±.09
	250	0.64 ±.09	0.59 ±.09		
W51(MS)	1000	0.61 ±.13	0.50 ±.10		
	250	0.67 ±.09	0.53 ±.07		
W51(N)	1000	0.83 ±.28	0.54 ±.16		

(a) Ratio taken relative to F=7/2→5/2 component. The calculated value for optically thin emission is quoted in square brackets.

(b) Reported errors are 1σ.

Table 4.15. Orion(KL) NS J=7/2→5/2 Hyperfine Line Strength Ratios [a] [b]

Parity	Res. (kHz)	$R_{F=5/2,3/2}$ [0.74]	$R_{F=3/2,1/2}$ [0.53]	$R_{F=7/2,7/2}$ [0.07]	$R_{F=5/2,5/2}$ [0.07]
e	1000	0.67 ±.28	0.87 ±.22		
f	1000	0.80 ±.29	0.50 ±.28	0.05 ±.28	0.25 ±.05

(a) Ratio taken relative to F=9/2→7/2 component. The ratios calculated value for optically thin emission is quoted in square brackets.

(b) Reported errors are 1σ.

$$\frac{T_R(F=7/2\rightarrow 5/2)+T_R(F=5/2\rightarrow 3/2)}{T_R(F=9/2\rightarrow 7/2)} = 1.3\pm.3,\ [1.3]\ , \qquad (4.6)$$

where the ratio's calculated value for optically thin emission is quoted in square brackets. Unfortunately, the results do not agree with one another. The parity-e ratio suggests partially optically thick emission, while the parity–f ratio says its optically thin. Hence, we can not draw any firm conclusions as to the opacity of NS J=7/2→5/2 emission. To summarize, these results suggest that the NS emission towards Orion(KL) is optically thin, but a moderate optical depth can not be ruled out because of the complexity of the spectra.

Towards Sgr B2(M), the J=3/2→1/2 1000 kHz resolution spectrum shows three hyperfine components present in the passband. The F=3/2→1/2 ratio is consistent with the optically thin case, while the F=3/2→3/2 ratio is larger than expected by $\sim 3\sigma$. Five blended hyperfine components are present in the J=5/2→3/2 1000 kHz resolution spectrum. The SNR of this spectra is relatively poor compared to the J=3/2→1/2 spectrum. The spectrum was fit with a single emission system where the V_{LSR} was held fixed to the value obtained from the J=3/2→1/2 fit (65.3 km s^{-1}). These results are consistent with optically thin

emission, though the errors are so large as to make any conclusions virtually meaningless.

NS was observed by only its $J=5/2\rightarrow 3/2$ transition towards the sources W51(N), W3(IRS5) and W49(N). NS was detected towards W51(N) and the relative hyperfine line strength ratios suggest that the emission is optically thin. NS was not detected towards W3(IRS5), W49(N) or the carbon-star IRC+10216.

We conclude from our hyperfine line strength analysis that, with the possible exception of Sgr B2(M), all of our fourteen sources are consistent with optically thin emission.

4.5.2 Optically Thin Emission Source Model

Upper level NS column densities were calculated for optically thin emission using the expression,

$$N_u = (1.94\times 10^3)\frac{\nu^2}{A_u S_F}\int T_R\, dv\ , \qquad (4.7)$$

(*see* Irvine, Goldsmith, and Hjalmarson 1987). In this equation, ν is the rotational transition frequency (GHz), $\int T_R\, dv$ is the total integrated line intensity of the observed hyperfine components ($K\,km\,s^{-1}$), A_u is the Einstein coefficient for the NS rotational transition (s^{-1}), and S_F is the hyperfine component line strength normalized to unity over both Λ-doublet members (Tatum 1986; *see* Table 4.1). The results of the N(J=3/2) column density calculations are listed in Table 4.16, the N(J=5/2) column densities are listed in Table 4.17, and the Orion(KL) N(J=7/2) column density is reported in Table 4.18.

We next needed to determine a rotation temperature (T_{Rot}) in order to calculate the partition function and, in turn, calculate the total NS column

Table 4.16. NS J=3/2→1/2 Upper Level Column Density

Source	$\int T_R\,dv$ (K km s^{-1})	$\sum S_F$	$(\sum S_F)^{-1}\int T_R\,dv$ (K km s^{-1})	N_u 1×10^{12} (cm^{-2})
DR21(OH)	0.81 ±.05	0.3426	2.36 ±.15	5.23 ±0.33
G34.3+0.2	1.36 ±.07	0.3426	3.97 ±.20	8.80 ±0.44
NGC7538(E)	0.59 ±.05	0.3426	1.72 ±.15	3.81 ±0.33
NGC7538(N)	0.73 ±.06	0.3426	2.13 ±.18	4.72 ±0.40
NGC7538(S)	0.95 ±.08	0.3426	2.77 ±.23	6.14 ±0.51
Orion(1.5S)	0.38 ±.05	0.3426	1.11 ±.15	2.46 ±0.33
Orion(KL)	0.48 ±.08	0.3426	1.41 ±.23	3.12 ±0.51
S140	0.27 ±.04	0.3426	0.79 ±.12	1.75 ±0.27
Sgr B2(M)	18.19 ±.96	0.4167	43.65 ±2.3	96.72 ±5.1
W3(OH)	0.43 ±.04	0.3426	1.25 ±.12	2.79 ±0.27
W51(MS)	4.71 ±.15	0.5926	7.95 ±.44	17.62 ±0.98

density. We calculated a rotational temperature from the observed J=3/2→1/2 and J=5/2→3/2 transitions by the Boltzmann equation,

$$\frac{N_m}{N_n} = \frac{g_m}{g_n} \exp\left[-\frac{h\,\nu_{mn}}{k\,T_{Rot}}\right], \tag{4.8}$$

where N_m and g_m are, respectively, the column density and the statistical weight of level m, and ν_{mn} is the frequency of the m→n transition. The statistical weight is defined as $g_m = 2m + 1$, h is the Planck constant, and k is the Boltzmann constant. The derived rotation temperatures for m=5/2, n=3/2 are reported in Table 4.17, and the Orion(KL) m=7/2, n=5/2 derived T_{Rot} is reported in Table 4.18. All errors are ±1σ. If the ratio

$$\frac{N_m}{N_n} > \frac{g_m}{g_n}, \tag{4.9}$$

then Equation 4.8 will derive a negative temperature for T_{Rot}. If both ratios in Equation 4.9 are nearly equal, the derived rotation temperatures go to infinity.

Table 4.17. NS $J=5/2\rightarrow3/2$ Upper Level Column Density and T_{Rot} [a]

Source	$\int T_R\,dv$ (K km s^{-1})	$\sum S_F$	$(\sum S_F)^{-1}\int T_R\,dv$ (K km s^{-1})	N_u 1×10^{12} (cm^{-2})	T_{Rot} [a] (K)
DR21(OH)	1.88 ±.11	0.4455	4.22 ±.25	4.67 ±0.28	11 ±2
G34.3+0.2	3.43 ±.15	0.4455	7.70 ±.34	8.52 ±0.38	13 ±2
IRC+10216	≤ 0.09	0.2222	≤ 0.41	≤ 0.5	
NGC7538(E)	0.66 ±.10	0.4455	1.48 ±.22	1.64 ±0.24	4 ±1
NGC7538(N)	1.21 ±.12	0.4455	2.72 ±.27	3.01 ±0.30	6 ±1
NGC7538(S)	1.89 ±.14	0.5000	3.78 ±.28	4.18 ±0.31	7 ±1
Orion(1.5S) (45″)	1.48 ±.17	0.4455	3.32 ±.38	3.67 ±0.42	1000±30000
Orion(1.5S) (86″)	0.48 ±.04	0.3622	1.34 ±.11	1.48 ±0.12	6 ±1
Orion(KL) (45″)	1.95 ±.10	0.3622	5.38 ±.28	5.95 ±.31	−23 ±16
Orion(KL) (86″)	1.03 ±.07	0.3622	2.84 ±.20	3.14 ±.22	14 ±6
S140	0.49 ±.07	0.4455	1.10 ±.16	1.22 ±0.18	7 ±2
Sgr B2(M)	19.7 ±0.7	0.5000	39.4 ±1.4	43.6 ±1.6	5 ±1
W3(IRS5)	≤ 0.09	0.2222	≤ 0.41	≤ 0.5	
W3(OH)	1.67 ±.11	0.4455	3.75 ±.25	4.15 ±0.28	650±9000
W49(N)	≤ 0.27	0.2222	≤ 1.22	≤ 1.4	
W51(MS)	5.06 ±.24	0.4455	11.4 ±.54	12.6 ±.60	7 ±1
W51(N)	3.24 ±0.31	0.5000	6.48 ±.62	7.17 ±.69	

(a) Both Orion(1.5S) and Orion(KL) include integrated intensities based on the 45″ beam width used during observations and a 86″ beam width simulated from the $J=5/2\rightarrow3/2$ NS map (equal to the beam width for the $J=3/2\rightarrow1/2$ observations; see text).

Table 4.18. Orion(KL) NS J=7/2→5/2 Upper Level Column Density and T_{Rot}

Parity	$\int T_R\,dv$ (K km s^{-1})	ΣS_F	$(\Sigma S_F)^{-1}\int T_R\,dv$ (K km s^{-1})	N_u [a] 1×10^{12} (cm^{-2})	T_{Rot} [b] (K)
e	5.65 ±1.06	0.4725	11.96 ±2.24	8.8 ±1.6	−75 ±200
f	9.82 ±1.92	0.5000	19.64 ±3.84	14.4 ±2.8	−13 ±6
			$\overline{N_u}$ =	11.6 ±1.6	−20 ±11

(a) N_u is the total column density for the J=7/2→5/2 transition and is calculated independently from both the parity–e and parity–f data.

(b) T_{Rot} calculated from ratio of J=7/2→5/2 to J=5/2→3/2 ($\theta_S = 45''$) transitions.

High N_m/N_n ratios were found for Orion(KL), Orion(1.5S) and W3(OH). We interpret these results as indicating that the NS emission from these sources is spatially confined. Since we observed the J=3/2→1/2 transitions with an 86″ beam width while the J=5/2→3/2 observations were made with a 45″ beam, an unresolved emission source at the lower frequency would cause a selective lowering of the J=3/2→1/2 transition antenna temperature with respect to the J=5/2→3/2 antenna temperature. Fortunately, we were able to use our map of the NS J=5/2→3/2 emission in Orion to generate spectra with 86″ resolution for both the (KL) and (1.5S) positions. The line parameters for our 86″ beam width spectra are listed in Table 4.19. As can be seen in Table 4.17, matching the beam sizes has made the T_{Rot} derived for Orion(1.5S) more consistent with the other sources; however, the T_{Rot} derived for Orion(KL) is still high as compared with most of the other sources. Unfortunately, we do not have a similar map of the NS distribution towards W3(OH).

Table 4.19. NS J=5/2→3/2 Parity-e Gaussian Fit Results (86″ Beam Width)

Source	Res. (kHz)	T_R [a] (K)	T_R [b] (K)	FWHM ($km\,s^{-1}$)
Orion(1.5S)	250	0.089 ±0.005	0.041 ±0.005	3.73 ±0.23
Orion(KL)	250	0.122 ±0.007	0.067 ±0.006	5.45 ±0.28

(a) F=7/2→5/2

(b) F=5/2→3/2

Since NS has a substantial dipole moment (1.81 D), the A_u coefficients are relatively large: $A(J = 3/2 \rightarrow 1/2) = 4.7 \times 10^{-6}\ s^{-1}$, $A(J = 5/2 \rightarrow 3/2) = 2.4 \times 10^{-5}\ s^{-1}$. Therefore, the J=3/2→1/2 transitions require $n(H_2) \sim 10^4 - 10^5\ cm^{-3}$ to approach thermalization, while the J=5/2→3/2 transitions require $n(H_2) \sim 10^5 - 10^6\ cm^{-3}$. These densities are thought to exist in the cloud cores which we observed. Thus, we naively expected that T_{Rot} might be equal to or slightly less than the gas kinetic temperature, $T_K \simeq 30 - 100$ K (*see* § 4.5.3). However, for most of our sources T_{Rot} fell in the much lower range of 5–15 K. Note that including beam dilution would lead to even lower values of T_{Rot}, since it would increase the calculated intensity of the J=3/2→1/2 transition relative to the J=5/2→3/2 transition. We conclude that the NS results assuming optically thin emission and no beam dilution should be tested with a more rigorous model, and this is done in section 4.5.3 below.

Total NS column densities derived from the J=5/2 level column densities, assuming a Boltzmann population distribution at the values of T_{Rot} given in Table 4.17, are presented in Table 4.23 for comparison with values derived from a statistical equilibrium analysis in the next section.

4.5.3 Statistical Equilibrium Calculations

Faced with these uncertainties, we tried modeling our sources using a statistical equilibrium large velocity gradient (SE) method (Sobolov 1960; Castor 1970; Goldreich and Kwan 1974; Scoville and Solomon 1974; deJong, Chu, Dalgarno 1975) using a computer program developed by Goldsmith, Langer, Brewer, and Bergin (*private communication*).

Since there are no published collision rates for the molecule NS, we have adopted the rates for CS–H_2 collisions (Green, and Chapman 1978; rates were calculated for CS collisions with para–H_2 J = 0) reasoning that both these molecules have similar rotation constants, similar number of electrons, and similar location of the center of mass in relationship to the nuclei (Green 1994; *private communication*). According to Green, the collisional excitation of molecules in the ISM by neutral species, such as H_2 and He, is dominated by short-range repulsive interactions, and the rate constants reflect mainly the 'size and shape' of the colliding molecules. Green also notes that long-range attractive interactions may also be important, though they are often ignored in situations where true collisional rates are unavailable.

Since CS is a closed shell $^1\Sigma$ molecule with no hyperfine structure, we had to reduce the observed Λ–doubling and hyperfine structure of NS down to an equivalent single rotational transition. The corresponding equivalent single line intensities were estimated from the observed hyperfine components by assuming optically thin hyperfine component line strengths and correcting for the weaker unobserved components (Tatum 1986). This may seem at odds with one of our motivations for trying an SE analysis, namely verifying that our NS emission is optically thin. However, as stated in §4.5.1, our analysis of the relative hyperfine component line strengths generally supported optically thin emission. In addition, the strongest hyperfine components were detected towards all sources, and the

correction factor for the weaker and most probably optically thin components is at most a factor of <4, which includes a factor of 2 correction for the unobserved parity band transitions due to Λ–doubling.

The model was supplied with the NS rotational transition energy above the ground state, degeneracy, and Einstein A coefficient, calculated for the $^2\Pi_{1/2}$ state $J_u = 3/2$ through $J_u = 23/2$ transitions. The $^2\Pi_{3/2}$ ladder was omitted since it lies ~ 322 K above the absolute ground state and is not thought to be significantly populated in typical molecular clouds. The CS–H_2 collision rates were applied without modification. The SE model was fit to peak line intensities, which were calculated for observed rotational transitions by first measuring the integrated intensity of each line and then correcting for any unobserved components. We next calculated a mean FWHM line width from all the spectra and used this value to convert the rotational transition integrated intensities to equivalent peak intensities. These values are listed in Table 4.20. We carried out the SE calculations assuming a velocity gradient $dV/dr = 1$ (km s^{-1} pc^{-1}) for the calculation of f(NS).

When modeling the sources where only two transitions were observed, we assumed a gas kinetic temperature (T_K) derived from observations of NH_3 and or CH_3C_2H, and then adjusted the H_2 volume density [$n(H_2)$] until the SE model line intensity ratio, $[J = 5/2 \rightarrow 3/2]/[J = 3/2 \rightarrow 1/2]$, matched the observed value. We next used the f(NS) parameter to set the absolute line intensities. Though $n(H_2)$ and f(NS) are inversely related, in most cases these two parameters acted sufficiently "orthogonal" as to make this method quite efficient.

Care was taken to try and find values for T_K in the literature which were derived from beam sizes similar to those used to observe NS (a detailed, source-by-source discussion of the T_K references follows below). The sources were

Table 4.20. NS Statistical Equilibrium Model Input Values [a]

Source	$T_R\frac{3}{2}$ (K)	$T_R\frac{5}{2}$ (K)	R [b]	$\overline{\text{FWHM}}$ ($km\,s^{-1}$)
DR21(OH)	0.61 ±.14	1.09 ±.08	1.79 ±.32	3.88 ±.18
G34.3+0.2	0.84 ±.10	1.64 ±.19	1.94 ±.32	4.71 ±.17
NGC7538(E)	0.44 ±.08	0.38 ±.09	0.86 ±.25	3.88 ±.52
NGC7538(N)	0.63 ±.10	0.81 ±.13	1.28 ±.28	3.36 ±.25
NGC7538(S)	0.66 ±.09	0.90 ±.12	1.36 ±.27	4.19 ±.24
Orion(1.5S)	0.29 ±.04	0.81 ±.03	2.79 ±.40	4.45 ±.54
Orion(1.5S)[c]	0.29 ±.01	0.36 ±.02	1.24 ±.09	3.78 ±.29
Orion(KL)	0.26 ±.04	0.94 ±.04	3.62 ±.58	5.58 ±.40
Orion(KL)[d]	0.26 ±.05	0.53 ±.03	2.02 ±.39	5.43 ±.21
S140	0.36 ±.08	0.50 ±.11	1.39 ±.42	2.19 ±.25
Sgr B2(M)	1.74 ±.26	1.57 ±.22	0.90 ±.19	25.1 ±2.4
W3(OH)	0.35 ±.05	1.06 ±.15	3.00 ±.62	3.54 ±.24
W51(MS)	0.82 ±.10	1.18 ±.14	1.43 ±.24	9.68 ±.33

(a) Fractions in the header denote J_u. Errors are 1σ.

(b) $R = T_R(5/2)/T_R(3/2)$.

(c) $T_R\frac{5}{3}$ values were generated from the Orion $J=5/2\rightarrow3/2$ NS map for a 86″ beam size.

(d) $T_R\frac{3}{2}$ data from Hollis, Jewell and Lovas (1995). $T_R\frac{5}{2}$ values were generated from the Orion $J=5/2\rightarrow2/2$ NS map for a 86″ beam size.

initially assumed to be resolved at all transitions (i.e. $\theta_S > 86''$ FWHM). The results of the SE modeling are presented in Table 4.21.

We found the model to be particularly sensitive to the ratio of the observed $J=5/2 \rightarrow 3/2$ and $J=3/2 \rightarrow 1/2$ line strengths. Uncertainties in this ratio result in uncertainties in the value derived for $n(H_2)$, which, in turn, effected the NS fractional abundance. Potentially significant sources of systematic error in this approach include uncertainties in the antenna main beam efficiencies (η_B, η_m^*) and the assumed source size. We used the same efficiency values for all sources except Sgr B2(M), where a larger efficiency correction to the $J=5/2 \rightarrow 3/2$ data was necessary due to the low elevations at which this source was observed (*see* §4.3). For those sources where identical efficiencies were used, and where the sources were taken to be extended, we find the model results for the NS abundance to be consistent with the results at early-times of recent ion-molecule gas phase chemistry models for dark cloud conditions which include certain grain-surface reactions, i.e. $f_{NS} \sim 7 \times 10^{-11}$ (Hasegawa and Herbst 1993).

Three sources, Orion(KL), Orion(1.5S) and W3(OH), have $[J=5/2 \rightarrow 3/2]/[J=3/2 \rightarrow 1/2]$ ratios which are significantly higher (3.6, 2.8 and 3.0 respectively) than the other sources (~ 1.5 on average) when we make no correction for the different beam sizes at the two observing frequencies. We initially interpreted these high values as indicating significant beam dilution, especially for the $J=3/2 \rightarrow 1/2$ transitions. For Orion(KL) and Orion(1.5S) we were able to average together pixels from our NS map in order to generate $J=5/2 \rightarrow 3/2$ spectra with spatial resolution similar to that of the $J=3/2 \rightarrow 1/2$ observations. The corresponding ratios for both Orion(KL) and Orion(1.5S) became consistent with the other sources (2.0 and 1.2 respectively). Furthermore, when we used these values in our SE model the derived NS fractional abundances and H_2 densities were consistent with our other sources (*see* Table 4.21).

Table 4.21. NS Statistical Equilibrium Model Results [a]

Source	T_K (K)	n_{H_2} ($10^4 cm^3$)	f_{NS} (10^{-11})	$\tau_{\frac{3}{2}}$	$\tau_{\frac{5}{2}}$
DR21(OH)	30	30^{+23}_{-12}	$0.5^{-0.2}_{+0.3}$	0.02	0.1
G34.3+0.2	55	23^{+14}_{-8}	$1.0^{-0.3}_{+0.5}$	0.01	0.1
NGC7538(E)	32	5 ± 4	$2.1^{-1.2}_{+23}$	0.1	0.2
NGC7538(N)	40	11^{+6}_{-5}	$1.3^{-0.5}_{+1.4}$	0.04	0.2
NGC7538(S)	27	16^{+9}_{-7}	$0.9^{-0.3}_{+0.7}$	0.04	0.2
Orion(1.5S) (45″) [b]	45	300	0.05 ± 0.01	0.01	0.02
Orion(1.5S) (86″)	32	11 ± 2	0.5 ± 0.1	0.02	0.1
Orion(KL) (45″) [b]	60	300	0.08 ± 0.01	0.01	0.02
Orion(KL) (86″)	45	28^{-12}_{+27}	$0.2^{+0.2}_{-0.1}$	0.003	0.04
S140	40	13^{+10}_{-7}	$0.6^{-0.3}_{+1.0}$	0.02	0.1
Sgr B2(M)	50	4 ± 3	14.1^{-8}_{+302}	$0.4^{-0.3}_{+2.9}$	$0.9^{-0.4}_{+3.4}$
W3(OH)[c]	50	> 47	> 0.3	< 0.01	< 0.04
W51(MS)	50	12^{+5}_{-4}	$1.6^{-0.5}_{+0.9}$	0.03	0.2

(a) T_K from NH_3 and CH_3C_2H data discussed for each source in §4.5.3.1–4.5.3.9. Fractions in the header denote J_u. Errors calculated for $\pm 1\sigma$ variations in the $T_R(5/2)$ to $T_R(3/2)$ ratio, see text. See Table 4.17 for more details.

(b) T_K and $n(H_2)$ taken from Bergin (1995).

(c) SE Model would not converge to the observed line intensities, the values given are for the -1σ limit of the line strength ratio.

Unfortunately, we do not have a similar map of the $J=5/2\rightarrow 3/2$ NS distribution towards W3(OH) with which to try a similar analysis.

Another explination for the large intensity ratios may be that the NS emission is coming from regions of higher $n(H_2)$ densities than are typical for the other sources. We tested this idea by adopting temperatures and densities for Orion(1.5S) and Orion(KL) derived by Bergin (1995), and then adjusting the NS fractional abundance to match our observed $J=5/2\rightarrow 3/2$ line intensities (*see* Table 4.21). In both cases the SE model found the NS emission to be approaching thermalization, so that the predicted line ratio was closer to the observed value. However, the predicted $J=3/2\rightarrow 1/2$ line intensities were 5% to 30% larger than what was observed for Orion(1.5S) and Orion(KL), respectively. These discrepancies may be due to calibration errors, or they may indicate modest beam dilution for the $J=3/2\rightarrow 1/2$ transitions. The Orion(1.5S) and Orion(KL) results are discussed more fully in sections 4.5.3.4 and 4.5.3.5, respectively.

Generally, the statistical equilibrium model could reproduce the observed NS line intensities for physical conditions, T_K and $n(H_2)$, known to exist in these regions. The 1σ uncertainties in the model results reported in Table 4.21 were obtained by running the model for $\pm 1\sigma$ deviations in the relative line strength ratio (*see,* Table 4.20), and including a 10% uncertainty in the temperature scale calibration. Our analysis suggests that the NS emission towards Orion(KL) and Orion(1.5S) is thermalized. In addition, moderate beam dilution can not be ruled out.

The excitation temperatures derived from the SE model are compared, in Table 4.22, with the rotation temperatures we obtained assuming optically thin conditions and a Boltzmann population distribution (LTE). In most cases, the SE $J=5/2\rightarrow 3/2$ T_{EX} was similar to the T_{Rot} values calculated for the LTE model. In none of our sources does NS appear to be thermalized. In fact, most of the sources

had values of T_{EX} significantly below the assumed gas kinetic temperature for at least one transition. The corresponding optical depths (*see* Table 4.21) are generally small, consistent with the findings of our hyperfine components relative line strengths analysis.

A total NS column density, N(NS), was derived from the SE model results using the expression,

$$N(NS) = \frac{f(NS)\, n(H_2)\, \overline{FWHM}}{dV/dr} \,. \qquad (4.10)$$

In this expression, f(NS) is the fractional abundance of NS relative to molecular hydrogen, $n(H_2)$ is the volume density of molecular hydrogen, $\overline{FWHM}$ is the mean NS emission line width at half maximum, and dV/dr is the velocity gradient in $(km\,s^{-1}\,pc^{-1})$ and has the assumed value dV/dr = 1. The results of these calculations are listed in Table 4.23.

We have also derived a total column density assuming optically thin LTE conditions. Since the rotational temperatures and the excitation temperatures for NS are small, we have included a correction term for the background radiation in Equation 4.7 (*see* Irvine, Goldsmith, and Hjalmarson 1987). Thus, we calculated a column density from the $J = 5/2 \rightarrow 3/2$ data using the expression,

$$N(NS) = 10^5 \left(\frac{8\pi k \nu^2}{hc^3 A_u f_u}\right) \left[1 - \frac{\exp(h\nu/kT_{EX}) - 1}{\exp(h\nu/kT_{BG}) - 1}\right]^{-1} \frac{1}{S_F} \int T_R\, dv \,. \qquad (4.11)$$

In this expression $\int T_R\, dv$ is the total integrated line intensity $(K\,km\,s^{-1})$ of the observed hyperfine component, ν is the transition frequency, A_u is the Einstein coefficient of the NS rotational transition, while S_F is the hyperfine component line strength normalized to unity over both Λ-doublet members (Tatum, 1986). T_{EX} is the excitation temperature, which we have assumed for the $J = 5/2 \rightarrow 3/2$ transition to equal T_{Rot}. The partition function, f_u, was calculated for T_{Rot}. T_{BG} is the microwave background radiation temperature, $T_{BG} = 2.7K$. The results of these calculations are listed in Table 4.23. The total column densities derived from

Table 4.22. Comparision of T_K, T_{EX} and T_{Rot} [a]

Source	T_K (K)	SE Model $T_{EX\frac{3}{2}}$ (K)	SE Model $T_{EX\frac{5}{2}}$ (K)	LTE T_{Rot} (K)
DR21(OH)	30	36^{+2}_{-13}	14^{+4}_{+5}	11 ± 2
G34.3+0.2	55	150^{+134}_{-96}	16^{+8}_{-4}	13 ± 2
NGC7538(E)	32	7^{+5}_{-3}	5^{+1}_{-2}	4 ± 1
NGC7538(N)	40	18^{+14}_{-9}	8^{+2}_{-2}	6 ± 1
NGC7538(S)	27	18^{+8}_{-7}	8^{+3}_{-2}	7 ± 1
Orion(1.5S) (45″)	45	46 ± 1	52 ± 1	1000 ± 30000
Orion(1.5S) (86″)	32	15^{-2}_{+3}	7^{-2}_{+1}	6 ± 1
Orion(KL) (45″)	60	65 ± 1	78^{-13}_{+1}	-23 ± 16
Orion(KL) (86″)	45	97^{-53}_{-6}	18^{-7}_{+12}	14 ± 6
S140	40	24^{+31}_{-4}	9^{+4}_{-3}	7 ± 2
Sgr B2(M)	50	8^{+4}_{-3}	6^{+1}_{-1}	5 ± 1
W3(OH) [b]	50	141	30	650 ± 9000
W51(MS)	50	28^{+26}_{-13}	9^{+3}_{-5}	7 ± 1

(a) T_{EX} from SE model and T_{Rot} from Equation 4.8, which assumes optically thin emission and LTE conditions. Errors calculated for plus and minus 1σ variations in the $T_R(5/2)$ to $T_R(3/2)$ ratio, which includes a calibration uncertainty of 10%. See Tables 4.17 and 4.21 for other details.

(b) SE Model could not reproduce the observed line strengths. The values given are for the -1σ limit of the line strength ratio.

Table 4.23. SE Derived NS Total Column Density [a]

Source	N(NS) (10^{13} cm^{-2}) SE [b]	LTE [c]
DR21(OH)	1.8 ± 1.4	2.1 ± 0.2
G34.3+0.2	3.3 ± 2.2	3.8 ± 0.4
NGC7538(E)	1.3^{-1}_{+14}	2.0 ± 0.4
NGC7538(N)	1.5 ± 1.4	1.8 ± 0.3
NGC7538(S)	1.9 ± 1.4	2.2 ± 0.3
Orion(1.5S) (45″)	2.1 ± 0.6	62 ± 10
Orion(1.5S) (86″)	0.7 ± 0.2	1.0 ± 0.1
Orion(KL) (45″)	4.1 ± 0.7	—
Orion(KL) (86″)	1.2 ± 1	1.6 ± 0.2
S140	0.5 ± 0.7	0.6 ± 0.1
Sgr B2(M)	44^{-4}_{+940}	33 ± 4
W3(OH) [d]	< 1.5	46 ± 6
W51(MS)	5.7 ± 3.4	6.6 ± 0.7

(a) See Table 4.17 for details.

(b) Errors calculated for plus and minus 1σ variations in the $T_R(5/2)$ to $T_R(3/2)$ ratio, which includes a calibration uncertainty of 10%.

(c) Errors calculated for plus and minus 1σ variations in the integrated intensity, which includes a calibration uncertainty of 10%. Dash indicates a T_{Rot} was a negitive value and were unable to determine an LTE total column density.

(d) SE Model could not reproduce the observed line strengths. The value given is for the -1σ limit of the line strength ratio.

the SE analysis agree with those derived for optically thin LTE conditions to within errors.

In the following subsections, we present a source-by-source discussion of how a value for the gas kinetic temperature was adopted and the results of the SE model:

4.5.3.1 DR21(OH)

Recent VLA observations of ammonia transitions have revealed, what had been suspected, that the DR21 region is made up of many compact sources with a wide variety of gas kinetic temperatures and H_2 densities (Mangum, Wootten, and Mundy 1992). The demonstrably non-homogeneous nature of this source requires that we choose a gas kinetic temperature derived from observations with beam sizes comparable to those of our NS observations. Askne *et al.* (1984) have carried out observations of methyl acetylene towards DR21(OH) using the Onsala Space Observatory 20 m telescope. These observations had a FWHM beamwidth of 110 arcsec, and set the gas kinetic temperature to be in the range, $15 < T_K < 30K$ via statistical equilibrium analysis and assuming $n(H_2) \geq 10^{3.5} cm^3$. Rotational diagram analysis gave a value of $T_K = 27 \pm 6K$. Wilson and Mauersberger (1990) have carried out ammonia observations of DR21(OH) using the MPIfR 100 m telescope with a FWHM beamwidth of 40 arcsec. From these observations they derive $T_K = 35K$, $n(H_2) \geq 10^5 cm^{-3}$, and an NH_3 source size of $\theta_S \sim 51$ arcsec. We should note that for this source size, the $J = 5/2 \rightarrow 3/2$ observations would be resolved, while the $J = 3/2 \rightarrow 1/2$ observations would have a beam filling factor of 0.64. For the purposes of our SE analysis we have chosen an intermediate value, $T_K = 30K$.

Our SE model was able to reproduce the observed $J = 3/2 \rightarrow 1/2$ and $J = 5/2 \rightarrow 3/2$ line strengths for values of $n(H_2)$ and T_K thought to exist in this source (*see* Table 4.21). The emission was assumed to be extended in both

transitions. The estimated NS fractional abundance relative to molecular hydrogen, $f(NS) \sim 0.5 \times 10^{-11}$, which is in fair agreement with results of gas phase ion-molecule chemical models (C. Leung (1992), *private communication. See* §4.6). The SE model finds the emission to be optically thin and estimates $T_{EX} \sim 36$ and 14 K the for $J = 3/2 \rightarrow 1/2$ and $J = 5/2 \rightarrow 3/2$ transitions respectively.

4.5.3.2 G34.3+0.2

Ammonia observations of the molecular cloud G34.3+0.2 show it to be comprised of a "halo" of size 5 arcmin, and a "core" of 1–2 arcmin (Heaton *et al.* 1985). VLA observations by Andersson and Garay (1986) revealed a molecular clump, hereafter "compact core", with size 12 × 2.5 arcsec. A multilevel study of ammonia emission towards this source by Henkel, Wilson, and Mauersberger (1987) has determined the gas kinetic temperature and H_2 density for these various components. For the halo, $T_K = 25$K and $n(H_2) = 7.9 \times 10^4 cm^{-3}$, for the core, $T_K = 55$K and $n(H_2) = 3.2 \times 10^5 cm^{-3}$, and for the compact core, $T_K = 225$K and $n(H_2) = 1.6 \times 10^7 cm^{-3}$. The compact core region is unresolved for both our $J = 5/2 \rightarrow 3/2$ and $J = 3/2 \rightarrow 1/2$ NS observations. We have made a simple estimate of the contribution from the compact core to the beam averaged gas kinetic temperature and found that it only raised the $J = 5/2 \rightarrow 3/2$ beam averaged T_K by 3 degrees, while raising the $J = 3/2 \rightarrow 2/2$ beam averaged T_K by > 1 K. In light of this, we have chosen the core kinetic temperature, $T_K = 55$K, for or SE model.

Our SE model was able to reproduce the observed $J = 3/2 \rightarrow 1/2$ and $J = 5/2 \rightarrow 3/2$ line strengths for values of $n(H_2)$ and T_K thought to exist in this source (*see* Table 4.21). The emission was assumed to be extended in both transitions. The estimated NS fractional abundance relative to molecular hydrogen, $f(NS) \sim 1 \times 10^{-11}$, which is in good agreement with results of gas phase

ion-molecule chemical models (C. Leung (1992), *private communication. See* §4.6). The SE model found the emission to be optically thin.

4.5.3.3 NGC7538

The source NGC7538 is a molecular cloud associated with several compact HII regions. Our (N) position is approximately 2 arcmin SE of the optically visible HII region. Within our beam there are three compact HII regions: IRS1, IRS2, and IRS3 (Martin 1973). Ho, Martin and Barrett (1981) observed several other positions towards NGC7538 for NH_3, CS, and CO with a FWHM beamwidth ranging from 80 to 40 arcsec. From these observations they determined the gas kinetic temperature to be: (N) $T_K = 40^{+27}_{-10}$K, (S) $T_K = 27^{+1}_{-1}$K, (E) $T_K = 32^{+7}_{-6}$K. They also derived a molecular hydrogen density for the (S) position of $n(H_2) \geq 3.7 \times 10^3$ cm^{-3}. We have adopted these T_K values in our SE modeling.

NS was observed towards three positions in this source and our SE model was able to reproduce the $J=3/2 \rightarrow 1/2$ and $J=5/2 \rightarrow 3/2$ line strengths in each case. The emission was assumed to be extended in all transitions. The estimated NS fractional abundance relative to molecular hydrogen found for these three positions fall in the range, $f(NS) \sim 1 - 2 \times 10^{-11}$, which is in good agreement with results of gas phase ion-molecule chemical models (C. Leung (1992), *private communication. See* §4.6). The SE model found the emission to be optically thin and estimates the $J=3/2 \rightarrow 1/2$ and $J=5/2 \rightarrow 3/2$ excitation temperatures to be respectively: $T_{EX} \sim 7$ and 5 K towards NGC7538(E); $T_{EX} \sim 18$ and 8 K towards NGC7538(N) and NGC7538(S).

4.5.3.4 Orion(1.5S)

The Orion(1.5S) source is part of OMC-1 and lies 1.5 arcmin south of Orion(KL). This source appears to be an outflow from a highly embedded YSO

(Ziurys, and Friberg 1987). Ziurys, Wilson and Mauersberger (1990) mapped this region in SiO and CH_3CN and found the size of the source to be $\sim$ 25 arcsec in both species, the gas kinetic temperature to be $T_K = 50-100K$, and the gas volume density to be $n(H_2) \sim 10^5 cm^3$.

Our SE model was unable to reproduce the observed $J=3/2 \rightarrow 1/2$ and $J=5/2 \rightarrow 3/2$ line strengths for $T_K = 75$ K and no beam dilution. The ratio of the observed NS $J=5/2 \rightarrow 3/2$ to $J=3/2 \rightarrow 1/2$ line strengths (~ 3) is one of the largest observed in our sources, which suggests that this source may be unresolved. This would be consistent with our NS map of Orion, which shows the emission from the Orion(1.5S) position to be limited to one pixel. We then average together pixels from our NS map in order to generate $J=5/2 \rightarrow 3/2$ spectra with spatial resolution similar to that of the $J=3/2 \rightarrow 1/2$ observations (86″). The intensity ratio for Orion(1.5S) was now consistent with the other sources; a value of 1.2 for (1.5S) as compared to an average of 1.4 for the other sources. We also adopted $T_K = 32$ K from Bergin (1995), which was derived from observations of CH_3CH_2 over a similar beam size. The estimated values for the $J=3/2 \rightarrow 1/2$ and $J=5/2 \rightarrow 3/2$ excitation temperatures are $T_{EX} \sim 15$ and 7 K, respectively, and are consistent with our LTE derived $T_{Rot} = 6$ K. The results of the SE model are reported in Table 4.21 and are consistent with the findings for our other sources. However, the NS emission clearly has a peak toward Orion(1.5S), so that the SE results for the NS fractional abundance should be understood as a lower limit.

In a single 45″ pixel toward Orion(1.5S) (as opposed to the 86″ beam results used in the previous paragraph) Bergin (1995) found $T_K = 45$ K and $n(H_2) = 300 \times 10^4$ cm^{-3}. Adopting these values, we then adjusted the NS fractional abundance untill the SE model reproduced the observed $J=5/2 \rightarrow 3/2$ line intensity. The SE model predicted $J=3/2 \rightarrow 1/2$ line intensity 5% larger than what we had observed. This discrepancy could be due to calibration errors, which are

typically ±10%, our it could indicate that the J=3/2→2/2 line is slightly beam diluted. A spatially confined NS emission source is consistent with our mapping results. The model also predicts that the emission is optically thin, which is consistent with our analysis of the hyperfine lines relative intensities.

4.5.3.5 Orion(KL)

The Orion-A giant molecular cloud (OMC–1) is nearby, at a distance of only ~ 450 pc, and is the site of ongoing massive star formation. This combination makes it an extremely complex source for study in both its morphology and chemistry. At the center of this complex is the source Orion(KL). There are four generally accepted components which comprise Orion(KL): the "extended ridge", "hot core", "plateau", and the "compact ridge". The extended ridge is made up of quiescent gas which extends NE to SW through Orion(KL) and is characterized by V_{LSR} in the range 7–10 km s^{-1} (Johansson *et al.* 1984; Blake *et al.* 1986; Irvine, Goldsmith Hjalmarson 1987), line widths of 2–4 km s^{-1}, and gas kinetic temperatures of 50–60 K (Minh 1990; Askne *et al.* 1984). Recent VLA observations by Menten and Reid (1995) has called into question the current view of what powers the Orion(KL) region, and these new results are discussed in Chapter 1. In the following discussion, we place our results in the context of the traditional Orion(KL) morphology.

The "hot core" component is thought to be a leftover molecular clump from the formation of the highly luminous infrared star, IRc 2. Most of the luminosity of the BN/KL region may arise from IRc 2, about $10^4 - 10^5$ $L_\odot$, with the rest coming from BN which is itself a BO star. It is currently thought that IRc 2 is surrounded by a torus or circumstellar disk. Radiative heating from IRc 2 is thought to induce gas kinetic temperatures ~300 K. The lines emanating from the hot core characteristically have V_{LSR} in the range 3–5 km s^{-1} and FWHM of 10–15

km s^{-1} (Blake *et al.*, 1987). The molecular hydrogen density is thought to be $\sim 10^7$cm^{-3} (Mauersberger *et al.* 1986).

The "plateau" component is most notable for the broad line widths, FWHM 20–30 km s^{-1}, and is dominated by sulfur and silicon containing species. Shock chemistry, driven by outflows from IRc 2, dominates the plateau chemistry ($T_K \sim 100 - 200$K). Like the extended ridge, the plateau lines have a V_{LSR} in the range 7–10 km s^{-1} (Blake *et al.* 1987).

The "compact ridge" component is the position where most of the large, oxygen-rich molecules found in Orion have their peak intensity (Johansson *et al.* 1984; Blake *et al.*, 1987). This emission is thought to arise from the interaction of the outflow from IRC 2 with the 8 km s^{-1} quiescent ridge material; it is characterized by $V_{LSR} \sim 7 - 8$ km s^{-1}, FWHM $\sim 3 - 5$ km s^{-1}. Studies of CH_3OH emission from the compact ridge by Johansson *et al.* (1984) and Blake *et al.* (1987) indicates that though the line parameters are fairly uniform, there does appear to be a line width dependence as a function of the transition's energy above the ground state. For instance, the CH_3OH $5_{-1} - 4_0$ E transition ($E_l = 36$ K) has a line width of ~ 3.4 km s^{-1}, while a transition at $E_l = 324$ K has a line width of 5.1 km s^{-1}. The observed NS line parameters are consistent with the V_{LSR} and FWHM values associated with the compact ridge. In addition, a line width gradient as a function of energy level, similar to that seen for CH_3OH (Bergin 1995), may also exist for NS. The $^2\Pi_{1/2}$ $J = 3/2 \rightarrow 1/2$ transition (the transition to the ground state) has a line width of 3.5km s^{-1}, while the tentatively identified $^2\Pi_{3/2}$ $J = 7/2 \rightarrow 5/2$ transition, which lies ~ 322 K above the absolute ground state, has a line width of ~ 5.3 km s^{-1}.

From analysis of mainly large oxygen-rich molecules Blake *et al.* (1987) estimates a rotation temperatures for the compact ridge $T_{Rot} = 80 - 140$ K, an H_2 density $n(H_2) > 10^6$ cm^3, and a source size $\theta_S < 30''$. From observations of methyl

cyanide (CH_3CN), Andersson (1985) estimated $T_K = 100 - 250$ K, $n(H_2) = 10^{4.5} - 10^6$, and a source size $\theta_S \sim 10''$. The weak line strength of the NS $J = 3/2 \rightarrow 1/2$ transition, relative to the $J = 5/2 \rightarrow 3/2$ and $J = 7/2 \rightarrow 5/2$ transitions, suggests that the NS emission may arise from a spatially confined source such as the compact ridge. The $[J = 5/2 \rightarrow 3/2]/[J = 3/2 \rightarrow 1/2]$ ratio of 3.6 is the largest of any of the sources observed. Hence, given the similarity in NS line parameters with those seen toward the compact ridge, and evidence suggesting that the NS emission source may be spatially compact, we conclude that a significant fraction of the NS emission towards Orion(KL) arises from the compact ridge source. However, our mapping of the NS emission in OMC–1 shows NS to be also part of the extended ridge emission. Given our large beam sizes relative to the compact ridge source, our spectra most probably contain extended ridge as well as compact ridge emission.

Because of possible beam dilution resulting from the apparent maximum in emission toward Orion(KL), we have averaged together pixels from our NS map in order to generate $J = 5/2 \rightarrow 3/2$ spectra with spatial resolution similar to that of the $J = 3/2 \rightarrow 1/2$ observations ($86''$), just as we did for the similar case of Orion(1.5S). In this way, the intensity ratio for Orion(KL) went from 3.6 to 2.0, making it more consistent with the other sources (1.4 on average). We also adopted $T_K = 45$ K from Bergin (1995), which was derived from observations of CH_3CH_2 over a similar beam size. The results of the SE model are reported in Table 4.21 and are consistent with the findings for our other sources. The SE results for the NS fractional abundances towards (KL) and (1.5S) should be understood as lower limits. Further, we have neglected the higher energy $^2\Pi_{3/2}$ states in our SE model, though we have tentatively observed the $J = 7/2 \rightarrow 5/2$ parity-e,f transition from this ladder towards Orion(KL). We estimate the upper level column density of this transition to be $N_u \sim 3 \times 10^{11}$ cm^{-2}, which is thirty times less than the $^2\Pi_{1/2}$

$J = 7/2 \rightarrow 5/2$ transition's upper level column density. Though the omission of the high energy ladder transitions will cause us to underestimate the total column density, we do not believe that this error is significant.

In order to better estimate the conditions toward this compact ridge itself, we adopted the physical conditions $T_K = 60$ K and $n(H_2) = 300 \times 10^4$ cm^{-3} found by Bergin (1995) for the 45″ pixel toward Orion(KL), and then adjusted the NS fractional abundance until the SE model reproduced the observed $J = 5/2 \rightarrow 3/2$ line intensity (*see* Table 4.21). The SE model predicted a $J = 3/2 \rightarrow 1/2$ line intensity 30% larger than what we had observed, which may indicate that the NS emission region is small compared to our beam size. Correcting the observed $J = 3/2 \rightarrow 1/2$ line intensity for a $\theta_S = 75''$ makes it match the SE model result. In addition, we compared the SE model prediction with the observed $J = 7/2 \rightarrow 5/2$ line intensity. In this case, the SE model underestimated the line intensity by $\sim 50\%$, which indicates that both the $J = 3/2 \rightarrow 1/2$ and $J = 5/2 \rightarrow 3/2$ observations may be beam diluted. This would also be consistent with our mapping results for NS towards Orion(KL). The model also predicts that the emission is optically thin, which is consistent with our analysis of the hyperfine lines relative intensities. Based on evidence suggesting a compact emission source size, as well as the observed NS line widths and V_{LSR}, we conclude that a significant portion of the NS emission seen towards Orion(KL) is originates from the compact ridge.

4.5.3.6 S140

NS observations were made towards the H_2O maser position in the HII region S140. Ho, Martin and Barrett (1981) observed this source in NH_3, CS, and CO. They found $T_K = 31^{+11}_{-6}$ K. The ammonia observations were carried out with the Haystack 36.6 m telescope with a FWHM beam size of 1.4 arcmin. They also derived a molecular hydrogen density of $n(H_2) > 2.9 \times 10^3 \mathrm{cm\,s^{-1}}$. Ungerechts,

Walmsley and Winnewisser (1986) measured the gas kinetic temperature by multilevel ammonia observations to be $T_K = 40K$ within ~ 20 arcsec of the H_2O maser position, and smoothly decreasing to 20 K within the surrounding neighborhood. Within ~ 40 arcsec, T_K only drops to ~ 35 K and so for the purpose of our SE analysis we have chosen $T_K = 40K$.

Our SE model was able to reproduce the observed $J=3/2 \rightarrow 1/2$ and $J=5/2 \rightarrow 3/2$ line strengths assuming the emission is extended in both transitions. However, the derived value of $n(H_2) \sim 13 \times 10^4$ is larger than the value quoted by Ho, Martin, and Barrett (1981). Assuming a higher kinetic temperature in the SE model would decrease the molecular hydrogen density. The estimated NS fractional abundance relative to molecular hydrogen, $f(NS) \sim 0.6 \times 10^{-11}$, is in fair agreement with the results of gas phase ion-molecule chemical models (C. Leung (1992), *private communication. See* §4.6). The SE model finds the emission to be optically thin and estimates the $J=3/2 \rightarrow 1/2$ and $J=5/2 \rightarrow 3/2$ excitation to be $T_{EX} \sim 24$ and 9 K, respectively.

4.5.3.7 Sgr B2(M)

The Sgr B2 molecular cloud is locate approximately 120–130 pc from the Galactic center and is the location of high luminosity star-formation as well as a rich source of molecular species. This large core, 5–10 pc in diameter, is also a site of H_2O and OH masers. These masers form three groups referred to as: north (N), middle (M), and south (S); each source separated by $\sim$ 45 arcsec in declination. These various condensations have differing distributions of molecular species, eg. SO strongly peaks in Sgr B2(M) while OCS peaks in Sgr B2(N) (Goldsmith *et al.* 1987). Molecular hydrogen column densities towards Sgr B2(M) are $N(H_2) = 10^{24}$ (Goldsmith, Snell, and Lis 1987; Goldsmith *et al.* 1987). Churchwell and Hollis (1983) found the gas kinetic temperature to be a nearly uniform $T_K \sim 50$ K

across Sgr B2 with CH_3CCH data. VLA observations of NH_3 towards Sgr B2(M) by Vogel, Genzel, and Palmer (1987) estimated the kinetic temperature to be $T_K > 40$ K with $T_K > 100$ K in embedded cores. Following Minh (1990), we have adopted $T_K = 50$ K for the purposes of SE analysis.

Our SE model was able to reproduce the observed $J=3/2 \rightarrow 1/2$ and $J=5/2 \rightarrow 3/2$ line strengths for values of $n(H_2)$ and T_K thought to exist in Sgr B2(M) (*see* Table 4.21). The emission was assumed to be extended in both transitions. The estimated NS fractional abundance relative to molecular hydrogen, $f(NS) \sim 14 \times 10^{-11}$, is larger than the results of quiescent dark cloud gas phase ion-molecule chemical models (C. Leung (1992), *private communication. See* §4.6). However, calculating a total column density from the SE results we find $N(NS) \sim 4 \times 10^{14}$ cm^{-2}, which agrees with the findings of Gottlieb *et al.* (1975) of $N(NS) \sim 2 \times 10^{14}$ cm^{-2}, under optically thin conditions. When combined with the values of $N(H_2)$ given above, we find a value of $f(NS) \sim 40 \times 10^{-11}$, which agrees approximately with the value obtained from the SE model.

The SE model finds the emission to be partially optically thick, which is consistent with our analysis of the relative hyperfine component line strengths. The excitation temperatures for the $J=3/2 \rightarrow 1/2$ and $J=5/2 \rightarrow 3/2$ transitions are estimated to be $T_{EX} \sim 7$ and 6 K respectively.

4.5.3.8 W3(OH)

Askne *et al.* (1984) estimated the gas kinetic temperature towards W3(OH) to be $T_K = 40 - 70$ K from observations of CH_3C_2H using the Onsala Space observatory 20 m telescope with a beamsize of 44 arcsec. Observations of CH_3CN made by Andersson (1985) found the V_{LSR} to be similar to that seen for CH_3C_2H though the line widths were twice as broad (~ 6 km s^1). Andersson suggested that these observations are consistent with differences in the NH_3 emission and

absorption line widths observed by Wilson, Bieging and Downes (1978). Wilson, Bieging and Downes proposed a source model where an extended cloud ($T_{Rot} \sim 30K$) surrounds a denser core ($T_{Rot} \sim 55K$). Mauersberger, Wilson, and Henkel (1988) studied ammonia emission lines observed towards the W3(OH) position using the MPIfR 100 m telescope which gave a FWHM beam of 40 arcsec. They derived a range of gas kinetic temperature from 27 K for the low energy transitions to more than 500 K for the higher energy transitions. They suggested that the emission line core may follow a density distribution proportional to r^{-3} and may, in fact, surround a young stellar object. The NH_3 emission V_{LSR} was centered about -47.5 km s^{-1}, which is consistent with our observed V_{LSR} for NS.

Recent VLA observations by Wilson, Gaume, and Johnston (1993) of ammonia emission regions found the rotational temperatures towards the H_2O and OH masers to be 40 and 95 K, respectively. These T_{Rot} values place lower limits on T_K. They deduced a molecular hydrogen density towards the H_2O and OH maser as 4×10^8 and $3 \times 10^7 cm^{-3}$, respectively. However, both these sources are of order $\sim$ 2.5 arcsec, which is much smaller than the 45 and 85 arcsec beam sizes we used to observe NS. Wilson, Gaume, and Johnston mapped the region surrounding the OH and H_2O masers and found the majority of the gas to have $T_K \sim 20$ K and $n(H_2) \sim 10^6$ cm^{-3}.

We initially tried to model the observed NS emission towards W3(OH) by assuming the extended gas temperature of $T_K = 30K$; however, we were unable to match the relatively large, $[J = 5/2 \rightarrow 3/2]/[J = 3/2 \rightarrow 1/2] \sim 3$, line strength ratio. We then assumed a gas kinetic temperature of $T_K = 55$ K, which is thought to characterize the warmer, denser core. Though we were still unable to exactly match the observed line strength ratio, we were able to find convergence of the model with the -1σ limit of the line strength ratio. Our SE derived molecular hydrogen density of 4.7×10^5 cm^3 is consistent with densities reported for the H_2O

and OH maser regions. The SE derived lower limit for the NS fractional abundance relative to molecular hydrogen, $f(NS) \sim 3 \times 10^{-12}$ is in good agreement with gas phase chemistry models.

The high value for the $J = 5/2 \rightarrow 3/2$ to $J = 3/2 \rightarrow 1/2$ line intensity ratio suggests that the observations may suffer from beam dilution. Correcting for beam dilution would decrease the line strength ratio, making it more likely that the SE model could then reproduce the observed line intensities. Unfortunately, unlike the cases for Orion(1.5S) and Orion(KL), there are no obvious source sizes to try. Given the complex nature of W3(OH), along with our lack of knowledge as to the NS distribution within the beam, we can only say that the observed NS line strengths can be modeled for gas kinetic temperatures and molecular hydrogen densities observed towards this source.

4.5.3.9 W51(MS)

This source, which in ammonia emission extends over a region of at least 8 arcminutes, is made up of a collection of clouds at various V_{LSR}'s. In one model, the complex is made up of three large clouds (at $52 km\,s^{-1}$, $58 km\,s^{-1}$, and $63 - 70 km\,s^{-1}$), that interact with HII regions sandwiched between them (Matsakis *et al.*, 1980). Matsakis *et al.* observed the NH_3 emission using the MPIfR 100 m telescope and the NRAO 140 ft telescope which provided 40 and 120 arcsec FWHM beams, respectively. They identified a clump with $T_K = 40K$ about 40 arcsec south of the MS position and estimated the surrounding gas temperature to be 20 K. This is consistent with the findings of Scoville and Solomon (1973), who estimated the CO temperature to be 26 K and Askne *et al.* (1984) who estimated a temperature range, $27 < T_K < 60K$ based on observations of methyl acetylene. However, these numbers are highly uncertain given the velocity confusion in the spectra. Submillimeter CO observation by Jaffe, Harris and Genzel (1987) found

$T_K = 76K$, while dust continuum observation at 230 GHz by Gordon (1987) places $T_K = 64K$ (32 arcsec FWHM beam size for both observations). We have chosen an intermediate value $T_K = 50K$.

Our SE model was able to reproduce the observed $J=3/2 \rightarrow 1/2$ and $J=5/2 \rightarrow 3/2$ line strengths with an assumed gas kinetic temperature, $T_K = 50K$, and a derived molecular hydrogen density $n(H_2) \sim 1 \times 10^5 cm^{-3}$. The emission was assumed to be extended in both transitions. The estimated NS fractional abundance relative to molecular hydrogen, $f(NS) \sim 1.6 \times 10^{-11}$, which is in good agreement than the values predicted by ion-molecule chemical models (C. Leung (1992), *private communication. See* §4.6). The SE model finds the emission to be optically thin and estimates the $J=3/2 \rightarrow 1/2$ and $J=5/2 \rightarrow 3/2$ excitation to be $T_{EX} \sim 28$ and 9 K respectively.

4.6 Discussion

In the following section, we outline the findings of recent ion–molecule chemistry models as they pertain to NS. We next compare the NS abundances derived from our observations with those predicted by ion–molecule chemistry models. Finally, we compare the observed distribution of NS in OMC–1 with the results of the FCRAO chemistry survey.

4.6.1 The Chemistry Models

Only recently has NS been included in gas-phase ion-molecule chemistry models, and primarily in models for quiescent dark clouds (i.e. $T_K \sim 10$ K; $n(H_2) \sim 10^4$ cm^{-3}). Millar and Herbst (1990) estimated the fractional abundance of NS relative to molecular hydrogen to be $f(NS) \sim 3 \times 10^{-12}$ at "early-times" (3.16×10^5 yrs) and $f(NS) \sim 9 \times 10^{-12}$ at steady-state. Millar *et al.* (1991) found very low NS abundance values for both situations ($\sim 10^{-14}$). Clearly these models do not match the observed abundances of $f(NS) \geq 10^{-11}$ for our several sources.

Hasegawa, Herbst and Leung (1992; HHL92) have developed reaction networks which include the effects of grains, though NS is allowed to interact with the grain surfaces only through accretion. These models are built upon the extensive pseudo-time-dependent gas phase chemical models of Herbst and Leung (1989, 1990), which unfortunately, do not report their findings for NS. HHL92 considered several cases, each assuming different initial conditions for the gas-phase. In one case, the initial gas-phase abundances were set equal to the steady-state abundances of Millar and Herbst (1990). At early-times, this model found NS gas-phase abundances of 2×10^{-11} which is similar to those we have observed ($1-10\times10^{-11}$). The surface-phase NS abundance was also 2×10^{-11}. By 10^6 yrs, the gas-phase NS abundance had decreased by an order of magnitude, while the surface-phase abundance remained fairly constant. In another case, the initial gas-phase hydrogen was assumed to be molecular, and carbon, sulfur, and metals to be atomic and singly ionized. These conditions are often used in gas-phase pseudo-time-dependent models to represent dense portions of diffuse clouds. As in the previous model, the early-time NS is found to be equally distributed between the gas-phase and the surface-phase ($\sim9\times10^{-11}$), while at 10^6 yrs the NS abundance on the grain surfaces remained relatively constant, while the gas-phase NS abundance had dropped to 2.5×10^{-12}. These models suggest that $\geq50\%$ of NS is to be found on the grains at any given time.

The NS abundance predicted by HHL92, which is an order of magnitude greater than the results of Millar and Herbst (1990) and three orders of magnitude when compared to Millar *et al.* (1991), can not be due to the addition of grains to the model, since HHL92 only allowed NS to interact with grains through accretion, which would only lead to the depletion of NS from the gas-phase. Millar, Leung, and Herbst (1987) investigated the differences between the Herbst *et al.* ion–molecule chemistry models and the Miller *et al.* models, and found that the

differences in predicted abundances for many molecular species may be a result of the differing philosophies used by the two groups in estimating reaction rate coefficients. Essentially, Herbst and Leung tend to estimate reaction rate coefficients and products of processes involving larger species based on analogous results when smaller species are involved even if the process reduces the abundance of complex molecules, whereas Miller *et al.* prefer to neglect these processes if they hinder chain growth (Millar, Leung, and Herbst 1987). Without observed abundances for NS, neither group could judge the impact of their rate coefficients choices on this simple diatomic molecule.

Hasegawa and Herbst (1993; HH93) have gone on to expanded the HHL92 reaction network to include more gas-phase reactions (mainly more organo-sulphur reactions). The surface-phase reactions were also extended to include exothermic surface-chemistry reactions of the type [$X + H_2 \rightarrow XH + H$] where X is a molecule, and where an activation energy of uncertain magnitude exists. These reactions may occur at appreciable rates due to tunnelling if the activation energies are sufficiently low. This model also allows for cosmic ray desorption of material from the grain surfaces into the gas-phase. They considered several cases assuming the initial gas-phase abundance to be either "normal" (similar to the Herbst and Leung (1989, 1990) steady-state), or atomic and neutral. Assuming normal initial gas-phase conditions and no cosmic ray desorption, the gas-phase abundance of NS at early-times was $\sim 7 \times 10^{-11}$, while the surface-phase was 6×10^{-13}. By 10^7 yrs, though, the gas-phase NS abundance had dropped precipitously to 10^{-34}, while the surface-phase abundance had remained relatively constant. Repeating the same model, this time including cosmic ray desorption, the NS abundance was found to be essential the same as before at early-times. The big change occurred at 10^7 yrs, at which time the gas-phase NS abundance was now 2×10^{-15}. The NS abundance in these models do not vary significantly whether the initial gas-phase conditions

are "normal" or "atomic". As was the case for HHL92, the HH93 early-time results best match our estimates for NS abundances in GMC's, based upon our observations.

4.6.2 Comparison With Observations

Statistical equilibrium (SE) analysis of our NS observations found a majority of the sources to have molecular hydrogen densities close to $n(H_2) \sim 10^5$ cm^3, and, consequently, only partially thermalized excitation temperatures. The low excitation temperatures derived from SE models are consistent with the T_{Rot} values which were calculated assuming optically thin emission and a Boltzmann population distribution. We were able to duplicate the observed NS line intensities in our SE models without assuming a beam filling factor, with the two notable exceptions of Orion(KL) and Orion(1.5S) (and possibly W3(OH)). The SE models found most of the sources to be optically thin, which is consistent with our analysis of the relative strengths of the observed hyperfine components. The only source where both the relative strengths of the hyperfine components and the SE model results are consistent with optically thick emission is Sgr B2(M). In Sgr B2(M), the NS emission appears to come from relatively low density regions, $n(H_2) \sim 4 \times 10^4$ cm^{-3}, which, within errors, is in fair agreement with other results for Sgr B2(M) (e. g., $\sim 1 \times 10^5$ Turner 1991).

The NS emission observed towards Orion(KL) and Orion(1.5S) may be arising from higher density regions than is deduced for the other clouds. Furthermore, we can not rule out that these may be spatially confined regions.

Our survey of NS in star forming regions has found the molecule to be a ubiquitous if not a strong source of emission. Weak NS emission was also noted in our survey of the cold, dark clouds L134N and TMC-1 (McGonagle, Irvine, and Ohishi 1994). We have found the NS emission to be, in most cases, optically thin

and extended. For the extended emission from GMC's, we find the range of NS fraction abundances, relative to molecular hydrogen, to be $f(NS) = 0.5 - 1.5 \times 10^{-11}$, which is higher than the peak abundances predicted by Miller (1990) and Miller *et al.* (1993), but is in fair agreement with the "early-time"results of HHL92 and HL93. For Sgr B2(M), where NS appears to be optically thick, the fractional abundance, $f(NS) \sim 14 \times 10^{-11}$, is slightly greater than any of the chemistry model's peak abundances.

4.6.3 The Distribution of NS in OMC–1

The only GMC for which we have extensive mapping of NS emission is the Orion molecular cloud (Figures 4.15 and 4.16). NS emission strongly peaks toward Orion(KL) and extends both north and south for $\sim 4'$ along the "extended ridge". We may compare the NS distribution in Orion with the results from the FCRAO Orion Chemistry Survey (Bergin 1995; Ungerechts *et al.*, 1994; Ungerechts *et al.*, 1992), which has systematically mapped OMC–1 for a variety of molecular species with 45″ beam size on 25″ centers. The total column densities for observed species were estimated by Bergin using an SE model where $n(H_2) = 3 \times 10^6$ was determined for each pixel in the map from observations of HC_3N and T_K was determined from observations of CH_3CH_2. The total column densities for sample positions were found by averaging over five pixels centered on the positions (for more details, see Bergin 1995). Using the same temperature and densities, we have estimated the total column densities towards the same positions using data from our NS $J = 5/2 \rightarrow 3/2$ map of OMC–1, which has 45″ beam size on 50″ centers. Since the NS data was not Nyquist-sampled, we have not averaged together adjacent pixels. We find an NS distribution with an enhanced abundance towards KL, similar to the distribution found by Bergin (1995) for SO and CH_3OH. This can be clearly seen in Figure 4.20. In this figure, total column densities relative to $C^{18}O$ are

plotted at 6 positions along the Orion ridge for the molecules mentioned above. These six positions (chosen by Ungerechts *et al.* [1994]) are, going North to South;

(a) The radical-ion region $\sim 3.5'$ north of KL.

(b) The quiescent ridge $\sim 1 - 2'$ north of KL.

(c) The BN/KL region.

(d) Orion(1.5S) near the second FIR peak and outflow.

(e) The molecular bar near the brightest part of the optical bar in M42.

(f) The junction of ridge and molecular bar $4'$ south of KL.

As discussed in §4.5.3.5, the Orion(KL) emission appears to arises from a spatially confined source, which we have identified as the "compact ridge". It is interesting to note that CH_3OH have been identified as compact ridge species (*see* Blake *et al.* 1987), while Blake *et al.* have suggested that SO may also be present in the compact ridge. The fact that we do not see evidence of a plateau component in the NS emission line profile, nor strong evidence for a hot core component, suggests that NS is not abundant in dense hot regions (i.e. $n(H_2) > 10^6$ cm^{-3}; $T_K > 100$K). This is perhaps not surprising considering that NS is a radical, and we would expect the NS destruction rate to increase at high density and temperature. The compact ridge, though, is only slightly cooler and less dense than the plateau or hot core regions, so its enhanced NS abundance may depend on something more than a reduced destruction rate.

Enhanced NS abundance in the compact ridge could arise from a higher than normal production rate. It is conceivable that this could result if there were a large abundance of nitrogen and sulfur available in the compact ridge region. In a model for the Orion(KL) region, Masson and Mundy (1988) proposed that the compact ridge emission arises from the compression and heating of the quiescent

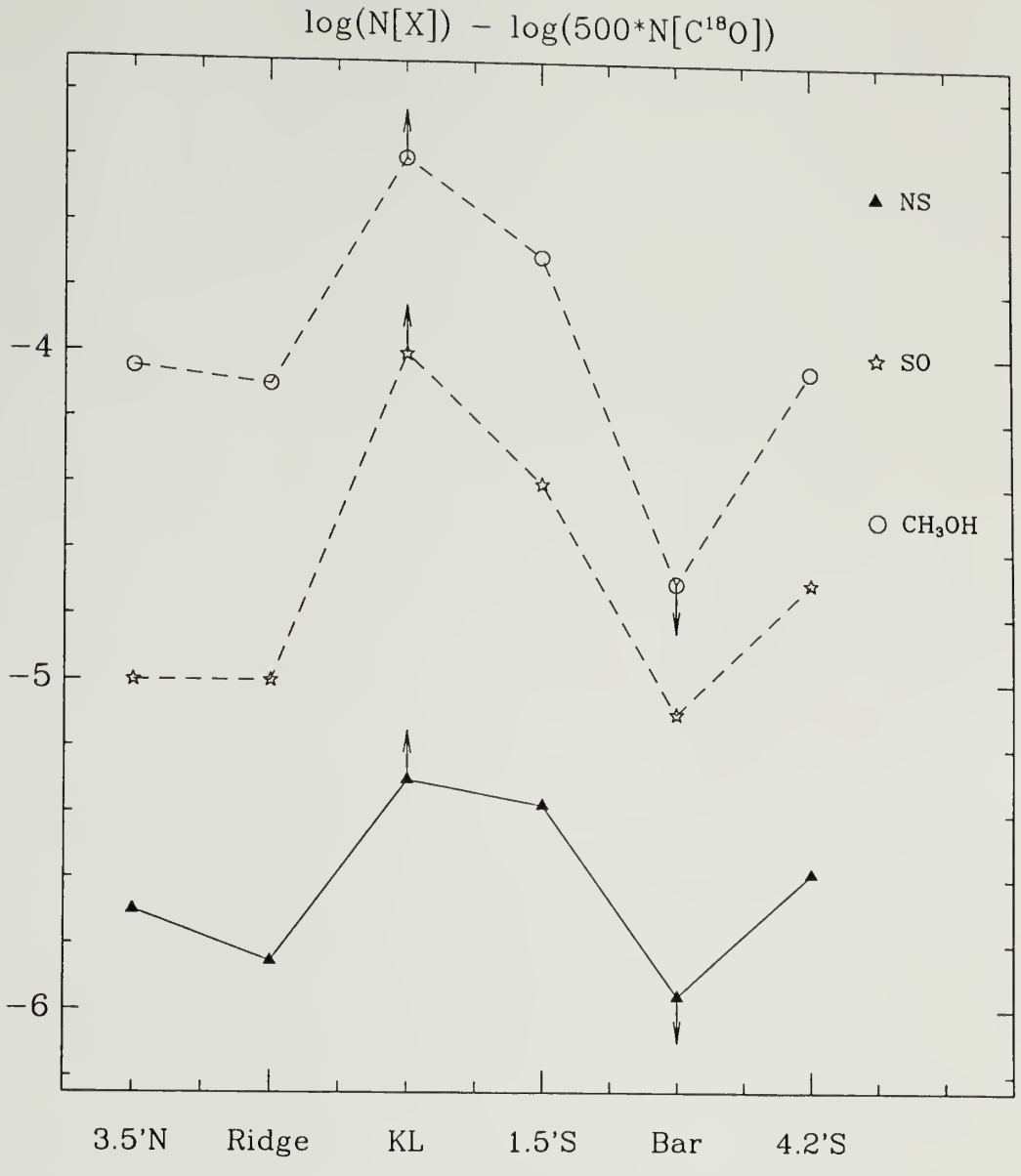

Figure 4.20. Column densities relative to $C^{18}O$ along the Orion Ridge for NS, SO, and CH_3OH. Downward pointing arrow indicate upper limits, while upward pointing arrows indicate lower limits. Data for SO and CH_3OH are taken from Bergin (1995).

8 km s^{-1} ridge cloud by the plateau gas outflowing from IRc 2. The plateau gas has significant amounts of sulfur containing molecules such as SO, SO_2, and H_2S (Ziurys and McGonagle, 1993; Minh *et al.*, 1990),while also containing nitrogen bearing molecules such as HC_3N and HCN (Blake *et al.*, 1987). We suggest that the enhanced abundance of NS may be a result of an enhanced production rate due to the constant supply of nitrogen and sulfur bearing molecules by the IRc 2 outflow into the compact ridge region.

A simpler explanation for the enhanced NS abundance may involve the grains. The chemistry models predict that a significant amount of the total NS produced will be accreted onto grains. Increased grain-grain collisions in regions were outflows interact with quiescent material may result in the grain-bound NS being released to the gas-phase and, thus, enhance the observed NS abundance. The enhanced abundance of CH_3OH in the compact ridge has been suggested to originate in evaporation from grains in material outflowing from IRc 2 (Millar, Herbst and Charnley 1991). This might seem unlikely in the case of an unsaturated species such as NS, in view of the evidence for hydrogenation of molecules under these conditions (Millar *et al.* 1988). Nevertheless, a possible link between outflows and enhanced NS abundance is further supported by the observed enhancement of NS towards the outflow source Orion(1.5S). Higher spatial resolution observations of NS towards Orion(KL) and Orion(1.5S), along with observations towards other outflow sources, will be necessary to determine if there is a link between outflows and enhanced NS abundance.

Chapter 5

A Search for HCCN

5.1 Summary

The first astronomical detection of HCCN, a member of a possible new interstellar carbon chain series ($HC_{2n}N$), has been at millimeter wavelengths reported towards the carbon star IRC+10216 (Guélin and Cernicharo 1991). We have conducted a deep search for HCCN towards TMC–1 and several GMC's via its $N(J)=1(2)\rightarrow 0(1)$ transition. HCCN was not detected in any of these sources, nor at this transition in IRC+10216. Upper limits for these sources have been calculated consistent with their respective baseline noise levels. Towards TMC–1, assuming optically thin emission, the HCCN total column density upper limit is $N_{HCCN} \leq 1-2\times10^{12}\,cm^{-2}$, which corresponds to a fractional abundance upper limit, with respect to molecular hydrogen, of $f_{HCCN} \leq 1\times10^{-10}$. We find the ratio of HCN:HCCN:HCCCN in TMC–1 to be $1 : <0.01 : 0.3$, which suggests that carbon-chain growth by the addition of single carbon atoms may not be efficient under dark cloud conditions. We estimate the HCCN total column density towards Sgr B2(NW), G34.3+0.2, and W51(H_2O) to be $N_{HCCN} \leq 4-10\times10^{13}\,cm\,s^{-1}$. Further, we offer an upper limit on the de-hydrogenation branching ratio due to electron recombination for the reaction $H_3C_2N^+ + e$.

5.2 Introduction

The possible existence of HCCN in molecular clouds was suggested by the detection of H_2C_2N (Irvine *et al.*, 1988) and H_2CN (Ohishi *et al.*, 1994). These authors suggest that H_2C_2N is formed by the dissociative recombination reaction,

$$H_3C_2N^+ + e \rightarrow H_2C_2N + H$$
$$\rightarrow HCCN + H_2, \qquad (5.1)$$

which has the potential to produce HCCN as shown in the second equation (cf. Bates 1989). The number of hydrogen atoms which dissociate during an electron recombination is typically unconstrained by experimental data. Measurements of the [HCCN]/[H_2C_2N] ratio in a dark cloud such as TMC–1 would provide important constraints on the theoretical models pertaining to dissociative recombination reactions. Thus, the time was right for a careful search in interstellar clouds for HCCN.

The presence of HCCN may also signal a new carbon-chain series, $HC_{2n}N$. The cyanopolyynes, $HC_{2n}CN$ (n = 1 – 5), and other related series such as CO and C_3O, CN and C_3N, and the radicals, C_nH (n = 1 – 6), are some of the more interesting products of ion-molecule chemistry. The predominance of species with carbon-carbon triple bonds suggests that these chains are formed through the addition of acetylenic units (Schiff and Bohme 1979; Herbst 1989). Another possibility, however, is that carbon atoms are added singly, as was suggested by Suzuki (1983). The latter suggestion would lead to the production of molecules such as CCO and HCCN in molecular clouds. In fact, both of these molecules have recently been detected astronomically. Ohishi *et al.* (1991) have confirmed the presence of CCO in the dark cloud TMC–1, while Guèlin and Cernicharo (1991) have reported detecting HCCN towards the carbon star, IRC+10216.

An unsuccessful search for a millimeter-wavelength transition of HCCN towards TMC–1 has been reported by Suzuki *et al.* (1985), but that transition may have been substantially subthermally excited. A tentative detection of HCCN in Sgr(B2) at 109.9 GHz was reported by Guélin and Cernicharo (1991), who also

suggest that unidentified lines previously reported by Goldsmith *et al.* (1983) and Turner (1989) in Orion-KL could correspond to HCCN. Furthermore, the HCCN line profile observed towards IRC+10216 suggests that the molecule is produced in the star's outer envelope by ion–molecule processes. The physical conditions in the outer envelopes of carbon stars are thought to be similar to the conditions found in molecular clouds.

Our primary target source was the quiescent dark cloud TMC–1. Detecting HCCN in this relatively simple and well studied source might lead to a better understanding of the chemical processes involved in production of carbon chain molecules. We included IRC+10216 in our survey, where the detection of a K-band line would provide a constraint on excitation. In addition to these two sources we also surveyed several regions of massive star formation. We report here the results of our search for HCCN.

5.3 Observations

HCCN is isoelectronic with C_2O, which has a $^3\Sigma^-$ ground electronic state. There is still a small uncertainty as to the molecular structure of HCCN. The dipole moment, μ, has been calculated by using the simple SCF method assuming both bent and linear structures: they find $\mu = 3.07$ D and 3.3 D, respectively (*see* Guélin and Cernicharo 1991). Recent laboratory spectroscopy work done by Endo and Ohshima (1993) suggests a nearly linear structure with a possibility of a large amplitude bending motion. To be consistent with Guélin and Cernicharo (1991), we have adopted a value of $\mu \sim 3.0$ D for the purpose of estimating HCCN abundance upper limits.

The HCCN hyperfine constants have very recently been measured by Endo and Ohshima (1993), which now allows for the determination of the hyperfine components relative line strengths. They adopted the coupling scheme $\vec{J} = \vec{N} + \vec{S}$,

Table 5.1. HCCN N(J) = 1(2) → 0(1)

F_1 (initial)	F	—	F_1 (final)	F	ν (MHz)	$S_{F1,F}$
2	2.5	—	1	1.5	21220.108	0.1680
3	2.5	—	2	1.5	21222.622	0.1692
3	3.5	—	2	2.5	21222.968	0.2686

$\vec{F_1} = \vec{J} + \vec{I}(N)$, and $\vec{F} = \vec{F_1} + \vec{I}(H)$. Table 5.1 lists the transition frequencies (Endo and Ohshima, 1993) and expected line strengths (Saito and Ohishi 1994, *private communication*) for the three strongest hyperfine components which fell in the our passband. The hyperfine line strengths listed in Table 5.1 have been normalized to unity across the N(J) = 1(2) → 0(1) transition.

Our observations were carried out in 1992 February at the NRAO Greenbank 42.7 m telescope using the K-Band maser receiver. The K-Band receiver is a dual polarization instrument. Both channels were employed to maximize sensitivity. The temperature scale was calibrated using a noise tube and is given in terms of antenna temperature T_A. The radiation temperature (T_R) was then approximated by, $T_R \approx T_A/\eta_B$, where $\eta_B \simeq 0.4$ is the beam efficiency. All temperatures quoted in this chapter are T_R. The HPBW was 1.4 arcmin at the observation frequency. Typical system temperatures were $T_{sys} \sim 55$ K(T_A scale).

Observations towards TMC–1 were carried out in frequency switching mode with $\Delta\nu = 0.55$ MHz. All other sources were observed in double beam switching mode, using a nutating secondary which provided an ±8 arcmin throw. The receiver was tuned to 21221.000 MHz for HCCN observations. During the TMC–1 integrations, the HC_5N, J = 8 → 7, rotational transition at 21301.262 MHz was periodically monitored in order to derive a gain curve (*see* § 5.4).

Table 5.2. HCCN Observations Source List

Source	α(1950)			δ(1950)			V_{LSR}
	hh	mm	ss.s	dd	mm	ss	(km s^{-1})
TMC–1	4	38	38.6	25	35	45	5.8
IRC+10216	9	45	14.8	13	30	39	-26.0
Sgr B2(NW)	17	44	6.1	28	21	20	62.0
G34.3+0.2	18	50	46.0	1	11	10	57.8
W51(H_2O)	19	21	26.2	14	24	43	53.0

An autocorrelation spectrometer was used for all observations. The spectrometer was configured for 512 channels with 9.77 kHz spacing for the TMC–1 observations. This corresponds to a 0.14 km s^{-1} velocity resolution at the observation frequency. W51(H_2O) was observed with 1024 channels on 78.1 kHz centers or 1.1 km s^{-1} resolution. Observations of the source G34.3+0.2 employed 1024 channels on 39 kHz centers for a velocity resolution of 0.55 km s^{-1}. Observations of Sgr B2(NW) and IRC+10216 were carried out using 512 channels with 156 kHz spacing which provided a velocity resolution of 2.2 km s^{-1}.

The source list with coordinates and V_{LSR} values is given in Table 5.2.

5.4 Results

HCCN was not detected towards any of the sources we observed. The baseline rms achieved towards each source is listed in Table 5.3. The TMC–1 data were corrected for elevation dependent gain variations. The gain curve is shown in Figure 5.1. The TMC–1 spectra were averaged together using (rms)$^{-2}$ weighting after correcting for gain variation.

In order to place an upper limit on the HCCN column density towards TMC–1, we have used the a 3σ upper limit for the HCCN radiation temperature

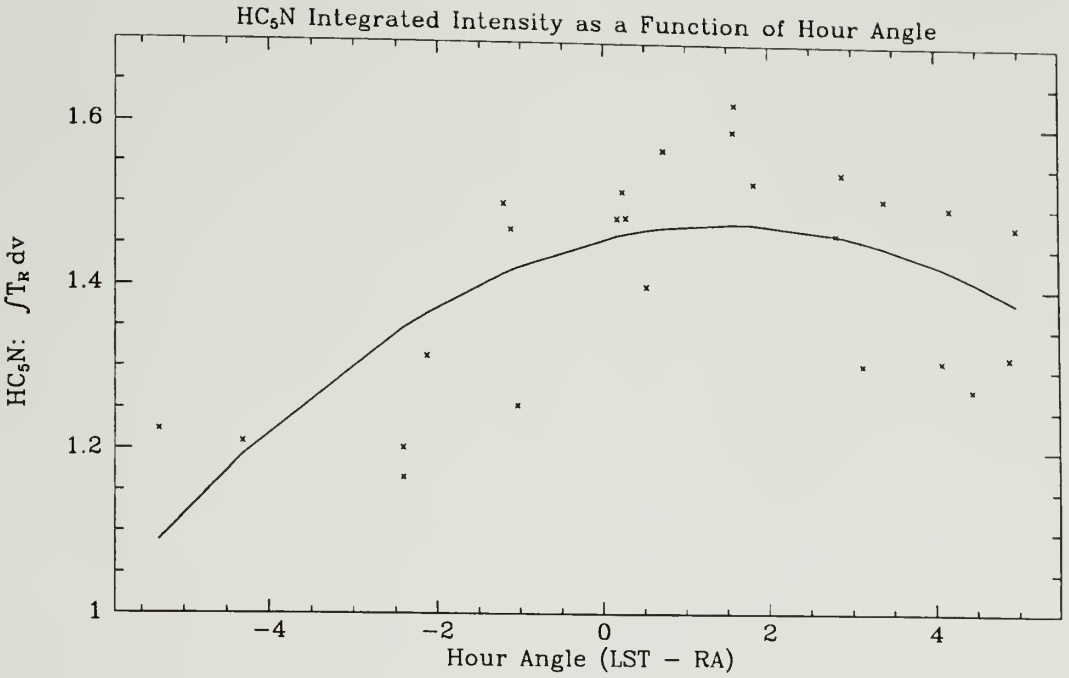

Figure 5.1. HC_5N $J = 8 \rightarrow 7$ integrated intensity towards TMC–1 as a function of hour angle using the NRAO Greenbank 140ft telescope. The spectra were made in frequency switching mode with a 3 minute integration time. Gaussian fits were made to each spectrum and the integrated line intensities were determined (crosses). The curve is a third order polynomial fit to the integrated intensities.(A gaussian fit to the weighted average of the HC_5N test spectra corrected for gain variation gives an amplitude of 2.42 K, and a FWHM of 0.61 km s^{-1} centered at 5.86 km s^{-1}).

(where σ is the baseline RMS smoothed to a velocity resolution equal to the adopted FWHM), T_R, and have adopted the FWHM value measured from the HC_5N test line. The upper level column density was calculated using the "standard" equation (Irvine, Goldsmith, and Hjalmarson 1987) which includes a correction for effects due to cosmic background radiation T_{BG},

$$\mathcal{N}_u = 10^5 \left(\frac{8\pi k\nu^2}{hc^3 A_u}\right) \left[1 - \frac{\exp(h\nu/kT_{EX}) - 1}{\exp(h\nu/kT_{BG}) - 1}\right]^{-1} \frac{1}{S_{F1,F}} \int T_R \, dv \; . \qquad (5.2)$$

In this expression $\int T_R \, dv$ is the total integrated line intensity (K km s^{-1}) of the observed transition, ν is the transition frequency, A_u is the Einstein coefficient, while $S_{F1,F}$ is the hyperfine component relative line strength. In addition, we have assumed relative intensities for the hyperfine components corresponding to their statistical weights, optically thin emission, an excitation temperature of $T_{EX} = 5 - 10$ K (cf. Matthews and Sears 1983), and that the hyperfine components are not blended.

The total HCCN column density upper limit was estimated assuming a Boltzmann distribution described by a rotational temperature, $T_{Rot} = T_{EX}$, using the expression,

$$N(HCCN) = \mathcal{N}_u / f_u \; , \qquad (5.3)$$

where,

$$f_u = \frac{g(J_u)\exp(-E[N_u(J_u)]/kT_{EX})}{\sum_N \sum_J g_J \exp(-E[N(J)]/kT_{EX})} \quad \text{where,} \quad \begin{array}{l} J = N-1,\ N,\ N+1 \text{ for} J \geq 0 \\ N = 0 \rightarrow \infty \end{array} \qquad (5.4)$$

Here, f_u is the fractional population of the upper level, and the denominator, the partition function, is a sum over all rotational energy levels. For the N(J)'th level, E[N(J)] is the energy above the ground state and the rotational transition statistical weight is $g(J) = 2J + 1$ (Bergman 1992). The partition function is formally calculated over all transitions out to infinity. In our case, the summation was calculated from N(J) = 0(1) to 21(20), which is sufficient to determine the

partition function for $T_{Rot} \leq 30$ K (energy levels provided by Saito and Ohishi, 1994, *private communication*).

HCCN column density upper limits were also estimated for IRC+10216 and the GMC's by essentially following the procedure outlined above. For the carbon star IRC+10216, the T_{EX} and FWHM values were taken from Guélin and Cernicharo (1991). For the GMC's, we have assumed that HCCN is thermalized such that $T_{EX} = T_K$. We have adopted gas kinetic temperatures of $T_K = 30$ K for Sgr B2(NW) (Cummins, Linke and Thaddeus 1986), $T_K = 55$ K for G34.3+0.2 (Henkel, Wilson, and Mauersberger 1987), and $T_K = 50$ K for W51(H_2O) (Scoville and Solomon 1973; Askne *et al.* 1984; Jaffe, Harris and Genzel 1987). The HCCN line widths were assumed to be similar to those observed for the nitrogen bearing molecules NO and NS. Since the F1(F)=3(3.5) $\rightarrow$2(2.5) and the F1(F)=3(2.5)$\rightarrow$2(1.5) hyperfine components are separated by only 4.9 km s^{-1}, we have assumed that these features are blended for IRC+10216, Sgr B2(NW), and W51(H_2O). Finally, for $T_{EX} > 30$ K we have used the high temperature limit partition function approximation (Powell and Lide 1964) to estimate the fractional population of the upper level,

$$f_u \simeq \frac{h\, B_o\, g_u}{3\, k T_{EX}} \exp\left[\frac{-E_u}{k\, T_{EX}}\right] . \qquad (5.5)$$

In this expression, $B_o = 10986.4052$ MHz is the HCCN rotation constant (Endo and Ohshima 1993). The upper limits for the HCCN total column densities towards the sources observed in this survey are listed in Table 5.3.

Two non-HCCN spectral features did appear in the passbands. One feature was detected towards W51(H_2O). A gaussian fit to the feature gives an amplitude of $T_R = 0.08$ K and a FWHM = 23 km s^{-1} centered at -31.9 km s^{-1}. Assuming a $V_{LSR} = 53.0$ km s^{-1} we calculate a rest frequency of 21228.0 MHz. We have tentatively identified this feature as the hydrogen recombination line, n = 120,

Table 5.3. HCCN Column Density Upper Limits

Source	Res. (kHz)	RMS (mK)	FWHM [a] ($km\,s^{-1}$)	$\int T_R\,dv$ ($mK\,km\,s^{-1}$)	$\Sigma S_{F1,F}$ [b] (K)	T_{Rot} [a] $[3/\mu]^2(cm^{-2})$	N(HCCN) [c]
TMC–1	10	8	0.61	<7	0.269	5 – 10	$<1-2\times10^{12}$
IRC+10216	156	2	20.0	<38	0.438	12	$<6\times10^{12}$
Sgr B2(NW)	156	8	20.0	<159	0.438	30	$<5\times10^{13}$
G34.3+0.2	39	28	4.00	<123	0.269	55	$<1\times10^{14}$
W51(H_2O)	78	8	10.0	<8	0.438	50	$<4\times10^{13}$

(a) Assumed, except FWHM for TMC–1 taken equal to observed value for HC_5N.

(b) Sum of blended hyperfine component relative line strengths. See text.

(c) Upper limit. See text for calculation details.

$(m - n) = 6$, $\nu_{m,n} = 21228.600$ MHz (list of H recombination lines provided by NRAO Green Bank).

The other feature was detected towards Sgr B2(NW). The line profile is asymmetric and may show a red shifted wing. A gaussian fit to this feature gives an amplitude of $T_R = 0.25$ K and a FWHM = 29 $km\,s^{-1}$ centered at -266.2 $km\,s^{-1}$. Assuming a $V_{LSR} = 62.0\,km\,s^{-1}$ we calculate a rest frequency of 21207.1 MHz. We have tentatively identified this feature as NH_2CHO, $J_{KK} = 1_{0,1} \rightarrow 0_{0,0}$, for which the rest frequency is 21207.432 MHz (Lovas, 1985).

5.5 Discussion

Estimated upper limits for HCCN column density towards TMC–1 were calculated for the temperature range $T_{EX} = 5 - 10$ K (cf. Matthews and Sears 1983). If higher energy levels are substantially subthermal in population, this will produce a conservatively large value for the upper limit. The column density limits thus derived for HCCN are $1 - 2\times10^{12}$ cm^{-2}, which indicates that the HCCN

abundance is relatively insensitive to the choice of $T_{EX} = T_{Rot}$ in this range of temperature. This column density correspond to a fractional abundance upper limit, relative to molecular hydrogen, of $f_{HCCN} \leq 2 \times 10^{-10}$ (using $N_{H_2} \sim 10^{22}$ cm^{-2}; Irvine, Goldsmith, and Hjalmarson 1987).

Comparing the TMC–1 HCCN fractional abundance upper limit with abundances for HCN and HCCCN, we find HCN:HCCN:HCCCN to be $1 : < 0.01 : 0.3$ (HCN and HCCCN fractional abundances for TMC–1 are taken from Ohishi, Irvine and Kaifu 1992). This result suggests that carbon-chain growth by the addition of single carbon atoms may not be an efficient way to produce HCCN. However, destruction pathways must also be examined before this suggestion can be considered established. Thus, the fact that the radical HCCN has an allenic structure, best approximated by $H-\dot{C}=C=\dot{N}$, may allow it to participate in reactions not available to the more stable, closed shell species HCN and HCCCN.

HCCN is isoelectronic with the interstellar molecule CCO. Our HCCN fractional abundance upper limit is only slightly less than the observed abundance of CCO (6×10^{-10}: Ohishi, Irvine and Kaifu 1992), which leaves open the possibility that HCCN may in fact be present in TMC–1.

Our search for HCCN has provided some constraints on the theoretical models pertaining to dissociative recombination reactions. Formula 5.1 describes a possible production path for HCCN where the ion, $H_3C_2N^+$, combines with an electron and in the process an H_2 molecule is split off leaving HCCN. This same reaction has also been proposed for the production of H_2C_2N, where in this case a single H atom is split off (Irvine *et al.*, 1988).

The most probable number of H atoms which are ejected in a electron dissociative recombination reaction is one of the important unknowns in gas phase

interstellar chemistry. The steps which lead to a dissociative recombination can be qualitatively described as follows (Bates 1986; Bates 1989):

1. A free electron encounters the attractive energy surface of the target ion and a radiationless transition occurs involving the free electron and one or more of the bound electrons in the ion.

2. The resultant neutral molecule will be weakened if the free electron takes up an antibonding orbital, simultaneously exciting another electron from a bonding orbital to an antibonding orbital.

3. The weakened neutral molecule finds itself on a repulsive energy surface. The molecule then fragments, and the excess energy possessed by the system is taken up by the energy of relative motion between the products.

4. The products move apart quickly before autoionization via inverse radiationless transition may occur.

The key to Bates analysis of dissociative recombination is the concept of "curve-crossing", where the crossing refers to the intersection between the initial attractive potential of the ion and the repulsive potential of the neutral molecule. In order for the dissociation of a neutral molecule to occur after an electron recombination, this repulsive potential must cross the initial attractive potential in or near the classically accessible region around the attractive potential minimum such that the radiationless transition between the free electron and one or more of the bound electrons might move the system onto the repulsive potential (Bates 1989). Thus, the greater the number of accessible potentials the higher the probability that a favorable dissociative potential crossing might exist.

Bates (1989) also points out that whether neutralization of the constituent ionized atom increases or decreases the number of valences plays an important role

in determining whether or not a molecular-ion is predisposed to dissociation after electron recombination. Ionized molecules can be grouped into two classes. In the first class, the ionized atom may be carbon or silicon, for example, and the number of valences increases on neutralization. The products of a dissociative recombination are both radicals which have many energetically accessible states, and thus there is a high probability that a favorable crossing may exist.

The second class of ions are those where the ionized constituent atom is nitrogen, oxygen, or sulfur. In this class, the number of valences decrease on neutralization and the products are all saturated, so there is only one energetically accessible state. The probability of there being a favorable dissociative crossing is small. However, there are molecules such as $CH_3N^+H_3$, $CH_3O^+H_2$, and H_3S^+ which are all known to have large dissociative recombination coefficients (Adams and Smith 1988a, b).

To try and account for the known large dissociative recombination coefficients for ions containing N, O, or S, Bates (1989) suggested that if two H atoms were to split off, a molecular radical would be formed. There would then be a modest increase in the number of available potentials and a subsequent increase in the possibility of a favorable dissociative crossing. The formation of H_2 might further improve the probability of a dissociative recombination reaction occurring owing to the weakness of the bond-bending force constants of H–H and the resultant large spread of energy that can be taken up by the H_2 molecule in the form of vibrational energy. However, the removal of two valence-bound hydrogen atoms in a dissociative process would require transitions involving twice as many molecular orbitals as would the removal of one H atom. The increased complexity of the reaction would decrease the probability of its occurrence (Bates 1986).

The proposed parent ion for the production of HCCN in formula 5.1 is $H_3C_2N^+$ which belongs to the second class of ions. The splitting off of a single H

atom results in the production of the molecule H_2C_2N which has been astronomically observed (Irvine *et al.* 1988). The formation of HCCN would require the splitting off of two H atoms. If we assume that formula 5.1 is indeed the primary production path for both these molecules, and furthermore, that their destruction rates are similar, then the abundance ratio of HCCN to H_2C_2N would tell us about the probability (P) of one H atom being ejected as opposed to two. Using the H_2C_2N column densities for TMC–1 as reported by Irvine *et al.* (1988), along with our upper limits for the HCCN column densities reported here, we find:

$$\frac{P(H_2)}{P(H)} \sim \frac{N(HCCN)}{N(H_2C_2N)} < 0.04 \qquad (5.6)$$

It would appear that this dissociative recombination reaction favors the splitting off of a single H atom in this case; however, uncertainty in the destruction rates for these molecules makes this result extremely tentative.

Chapter 6

Spectral Survey of Orion-KL: 160 – 170 GHz

6.1 Summary

A spectral survey of Orion–KL has been carried out in the 2 mm atmospheric window covering the frequency range 159.6 – 170.4 GHz, using the FCRAO 14 m radio telescope. The typical baseline RMS levels for the spectra in this survey are 20 – 60 mK. Over 235 spectral lines were detected, including $\sim$35 unidentified features. Sixteen known interstellar species were conclusively identified in Orion from this data, with the largest numbers of lines arising from ethyl cyanide, methyl formate, methanol, and dimethyl ether. Several other molecular species have been tentatively identified as producing emission lines in this band, including formamide, isothiocyanic acid, ethanol, and possibly AlCl. This survey supports earlier findings which suggests that there may be much chemical selectivity in the formation of large organic molecules. For example, this survey finds dimethyl ether to arise from the extended ridge component of OMC–1 while VyCN and EtCN appear to arise from the hot core. We also report on the tentative detection of a new interstellar molecular-ion, H_2COH^+. This survey provides further evidence that the 2 mm window is rich in spectral lines.

6.2 Introduction

This 2 mm band spectral line survey of Orion–KL is a continuation of the work begun by Ziurys and McGonagle (1993, hereafter ZM93), who conducted the first systematic spectral line survey towards Orion–KL in the 2 mm band. Their survey covered the frequency range 149.6 – 159.6 GHz. In this work, we have

extended the ZM93 survey to higher frequencies by observing the frequency range 159.6 – 170.4 GHz. Together, these surveys cover a frequency interval of ~20 GHz. Until now, most observations at millimeter wavelengths have been carried out in the atmospheric windows that contain transitions of carbon monoxide, namely, the 3, 1.2, and 0.8 mm bands.

Several spectral line surveys have been published for the 3, 1.2, and 0.8 mm windows. The Orion molecular cloud has been a popular target for such studies, which include the 3 mm surveys of Johansson *et al.* (1984) using the Onsala telescope and Turner (1991) who used the NRAO 11 m telescope, the Caltech 1.2 mm window observations by Sutton *et al.* (1985) and Blake *et al.* (1986), and the 0.8 mm band survey by Jewell *et al.* (1989) using the NRAO 12 m telescope. The only published survey of the 2 mm atmospheric window, prior to ZM93, was that of Cummins *et al.* (1986), who studied Sgr(OH) from 124 – 143 GHz using the Bell Labs 7 m telescope. Hollis and collaborators observed a small portion of the 2 mm window in the course of several line searches (Hollis *et al.* 1981, 1983).

The observations made by Cummins *et al.* and Hollis *et al.* suggested that the 2 mm band was potentially rich in spectral features, and showed evidence for a fair number of unidentified features or U–lines. This potential was realized in the ZM93 survey, which found ~180 spectral features over a 10 GHz interval. Of these 180 features, 45 were U–lines. In fact, the ZM93 survey was begun after the discovery of several U–lines while conducting a successful search for nitric oxide (NO) towards Orion–KL (Ziurys *et al.* 1991).

The 2 mm band is also of interest since this spectral region should contain the $J = 2 \rightarrow 1$ transitions of many 3–4 atom molecules comprised of cosmically abundant elements. Thus, information critical to the identification of unidentified lines in the 3, 1.2, and 0.8 mm windows may be present in the 2 mm band. In addition, the 2 mm band contains the fundamental transitions of several interstellar molecules

such as H_2S and NO. Recent detections of metal-bearing halides such as NaCl and AlCl, via their 2 mm band transitions (Cernicharo and Guélin 1987), provides further evidence of the importance of observations in this band.

From an observers perspective, working in the 2 mm band has several practical advantages. First, the system noise temperatures are not as critically affected by poor weather conditions as they are at 1.2 and 0.8 mm. This allows sensitive 2 mm data to be collected without having to be at the highest and driest sites. Second, the telescope beam size at 2 mm is significantly smaller than at 3 mm, which benefits modest aperture telescopes in observing complicated outflow sources or circumstellar envelopes.

In this 10 GHz region, we have detected $\sim$235 spectral features, including some 35 unidentified lines. For consistency, we have followed the same protocols in conducting the observations and in presenting the results as set out in ZM93.

6.3 Observations

The observations which comprise this spectral survey were taken during the months of March and October 1992, using the FCRAO 14 m telescope. In the frequency range observed ($\sim 160 - 170$ GHz) the average FWHM beamsize of the telescope was $\sim 35''$, while the average beam efficiency was $\eta_B \sim 0.40$. We used the FCRAO 2 mm single sideband receiver (Ziurys, Erickson, and Grosslein 1988), which employs a cooled Schottky diode mixer. The image sideband was terminated at 20 K. The rejection of the image sideband was 20–30 dB at the filter center and 15–20 dB at the edges for most of the frequency settings (*see* §6.5.10 for further discussion). The IF frequency was 1.391 GHz.

The temperature scale was determined by the chopper wheel method, which corrects for atmospheric and radome losses, and is given in terms of T_A^*. The radiation temperature is then defined as $T_R = T_A^*/\eta_B$, assuming the source fills the

main beam. Unfortunately, the weather during the two months of observations was mostly cloudy. Typical system temperatures on the sky at $\sim 42°$ elevation were $T_{sys} \sim 750 - 2000$ K. The baseline RMS noise level of this survey varied from 20 to 60 mK for the 1 MHz resolution filter bank (*see* Table 6.1).

The backends used were two 512 channel filter banks with 1 MHz (~ 1.82 km s^{-1}) and 250 kHz (~ 0.46 km s^{-1}) resolution, respectively. The spectra were taken in position-switching mode, with the reference position 30′ west in azimuth. Pointing was determined by observations of Jupiter, Venus and Mars. The position used for Orion–KL was $\alpha = 5^h\,32^m\,46.8^s$, and $\delta = -5°\,24'\,23.0''$ (1950.0).

The data were taken using 22 different frequency settings (*see* Table 6.1), which were chosen to allow at least 25 MHz of overlap at the edges of the 1 MHz filter bank, where the image rejection was not as dependable. Both the 1 MHz and 250 kHz filter banks were used simultaneously. The complete range of 159.6 – 170.4 GHz was covered in the 1 MHz filter bank. The 250 kHz filter banks covered the central 128 MHz of each passband. The selection of the signal sideband was dictated by the capabilities of the klystron-based LO system.

6.4 Results

The spectral survey is presented in Figure 6.1, which shows the complete data set in the 1 MHz filter bank. Figure 6.2 presents associated 250 kHz spectra which contain spectral features. The temperature scale is given in terms of T_A^* as determined by the chopper-wheel calibration method. The temperature scale has not been corrected for the beam efficiency, η_B. The rest frequency scale was set by assuming a $V_{LSR} = 9.0$ km s^{-1}.

The list of all detected spectral features is given in Table 6.2. In this table, the spectral features are listed in frequency order along with their identifications,

Table 6.1. Summary of Survey Spectra Parameters

Scan	Center Freq. (MHz)	Signal Sideband	1 MHz Resolution Start (MHz)	Stop (MHz)	RMS (K)	250 kHz Resolution Start (MHz)	Stop (MHz)	RMS (K)
1	159925	USB	159669	160181	0.021	159861	159989	0.037
2	160410	USB	160154	160666	0.021	160346	160474	0.031
3	160895	USB	160639	161151	0.022	160831	160959	0.035
4	161380	USB	161124	161636	0.022	161316	161444	0.048
5	161865	LSB	161609	162121	0.025	161801	161929	0.044
6	162350	LSB	162094	162606	0.023	162286	162414	0.045
7	162835	USB	162579	163091	0.020	162771	162899	0.032
8	163320	USB	163064	163576	0.034	163256	163384	0.053
9	163805	USB	163549	164061	0.027	163741	163869	0.051
10	164290	USB	164034	164546	0.036	164226	164354	0.069
11	164775	USB	164519	165031	0.041	164711	164839	0.075
12	165260	USB	165004	165516	0.049	165196	165324	0.108
13	165745	USB	165489	166001	0.033	165681	165809	0.075
14	166230	USB	165974	166486	0.034	166166	166294	0.064
15	166715	USB	166459	166971	0.037	166651	166779	0.077
16	167200	USB	166944	167456	0.037	167136	167264	0.077
17	167685	LSB	167429	167941	0.036	167621	167749	0.061
18	168170	USB	167914	168426	0.028	168106	168234	0.052
19	168655	USB	168399	168911	0.044	168591	168719	0.085
20	169140	USB	168884	169396	0.056	169076	169204	0.107
21	169625	USB	169369	169881	0.019	169561	169689	0.031
22	170110	USB	169854	170366	0.022	170046	170174	0.030

intensities, and the filter bank resolution by which they were observed. Most of the identifications were based on the spectral line list of Lovas (1985). When alternative sources for transition frequencies were used, they are noted in the accompanying tables. For the case of unidentified spectral features, the frequency listed in Table 6.2 was determined by assuming a $V_{LSR}=9.0$ km s^{-1}. Though the survey was carried out at 1 MHz resolution, about 10% of the lines were also detected in the 250 kHz filter banks. Whenever possible, line parameters were determined using the 250 kHz resolution data. In several cases, the 250 kHz data was boxcar smoothed to 500 kHz resolution in order to enhance the signal to noise level. The filter bank, or the effective spectral resolution, used in determining the line parameters is also listed in Table 6.2.

Tables 6.4 – 6.30 list the detected transitions by molecule, Table 6.31 gives the recombination lines, and Table 6.32 lists the unidentified lines. These tables list the observed LSR velocity, line widths, amplitudes, and the energy above the ground state of the *lower* level for each transition. The spectral resolution used in determining the line parameters are also listed in these tables when it is other than the standard 1 MHz (1.8 km s^{-1}).

Seven spectral features in this survey are due to strong emission lines in the image-sideband, which "leaked" past the sideband filter. These features are labeled (I) in Figure 6.1 and Table 6.2. The image-sideband emission lines which correspond to the I-lines are listed in Table 6.34. The steps taken to identify image-sideband features are discussed in §6.5.10.

The line parameters reported in this survey were all determined by Gaussian fits to the line profiles. In almost all cases the amplitude, line width, and line center velocity were all free variables. In a situation were several spectral features were blended, or the line profile indicated multiple velocity components, multiple independent Gaussians were fit to the spectral features simultaneously.

The molecules nitrogen sulfide (NS) and dimethyl ether ($(CH_3)_2O$) have closely spaced hyperfine and symmetry components, respectively. In these cases we have modeled a given rotational transition as a system of Gaussians with each Gaussian sharing a common $\Delta V_{1/2}$ and V_{LSR}, while the inter-Gaussian spacing was held fixed to the spacing determined by laboratory spectroscopy. The function used in modeling these molecules is given in the following expression,

$$f(x) = \sum_{j=0}^{n} A_j \exp\left[-C\left(\frac{x - V - H_j}{F}\right)^2\right] , \qquad (6.1)$$

were x is the LSR velocity, A_j is the component amplitude for the j-th component, V is the velocity with respect to the LSR as measured for the emission system's component with the largest intrinsic line strength, H_j is the frequency offset for the j-th component from the reference component expressed as a velocity shift (i.e. for the reference component, $H_0 = 0$), F_i is the emission systems full line width at half maximum, and $C = 4\ln(2)$. In all cases, the amplitude of each component was an independent fit parameter. The Levenberg-Marquardt method was used to fit Equation 6.1 to the data (*see* Press *et al.* 1988, §14.4).

The detection threshold, for spectral features found in this survey, is given by the expression,

$$T_A^* \Delta V_{1/2} > N \sqrt{\frac{\Delta V_{1/2}}{dv}}\, \sigma\, dv , \qquad (6.2)$$

were T_A^* and $\Delta V_{1/2}$ are the Gaussian fit amplitude and full width at half maximum, respectively, dv is the filter bank channel width in velocity units, and σ is the spectral baseline RMS. The value N was set equal to 3 for spectral features which were coincident with known spectral lines, or to 4 in the cases of unidentified features.

Figure 6.1. Spectrum of Orion–KL at from 159.7 to 170.4 GHz, observed with the FCRAO telescope. The filter resolution is 1 MHz ($\sim$ 1.8 km s^{-1}). The spectra overlap $\sim$ 25 MHz at the filter bank edges. The data were taken in single sideband mode, with a 20–30 dB image rejection filter. The frequency scale assumes $V_{LSR} = 9.0$ km s^{-1}. The lower two panels of each figure set are an enlargment of the top spectrum. Lines labeled as U are unidentified. Features marked I are due to strong lines in the image sideband.

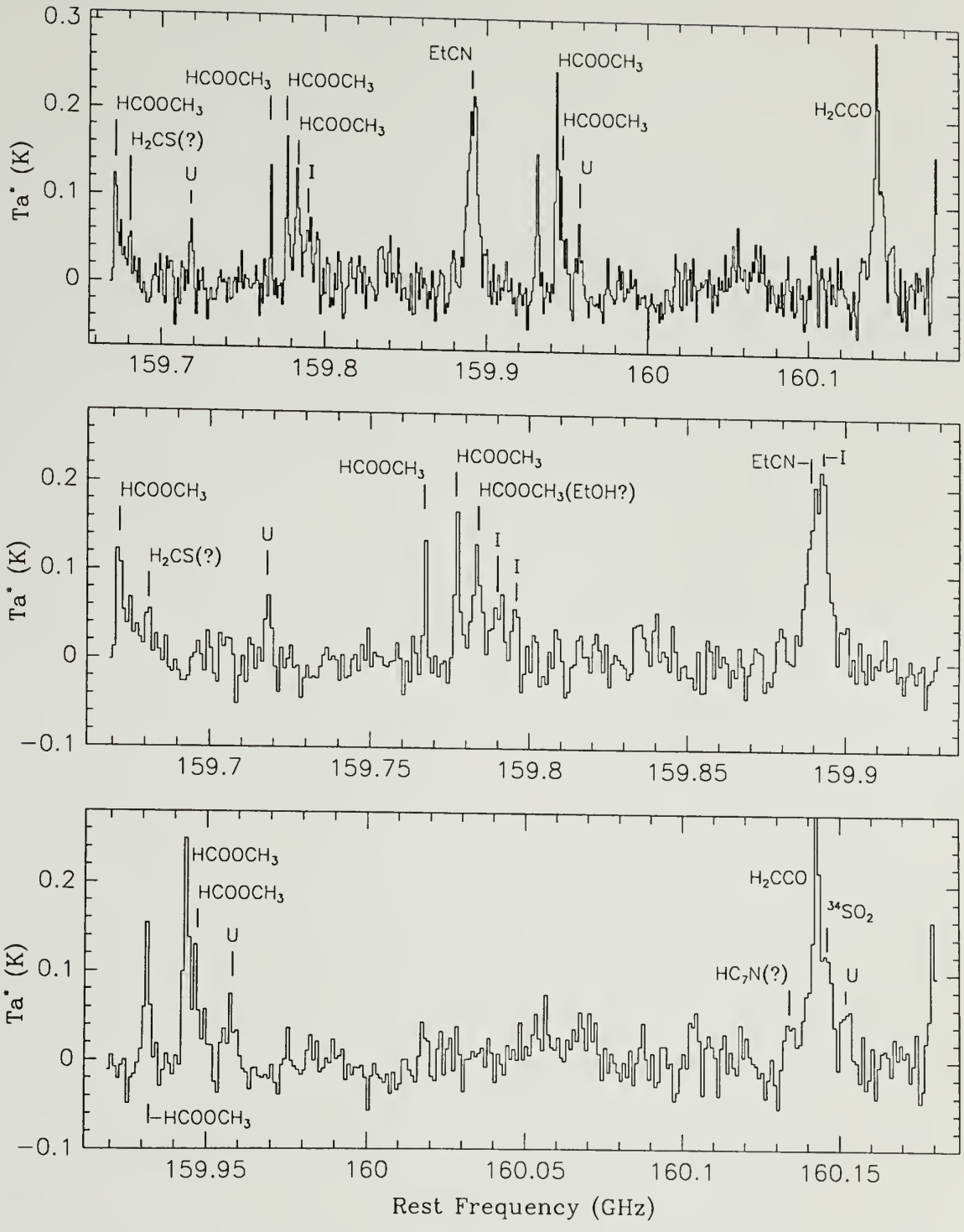

Continued, next page.

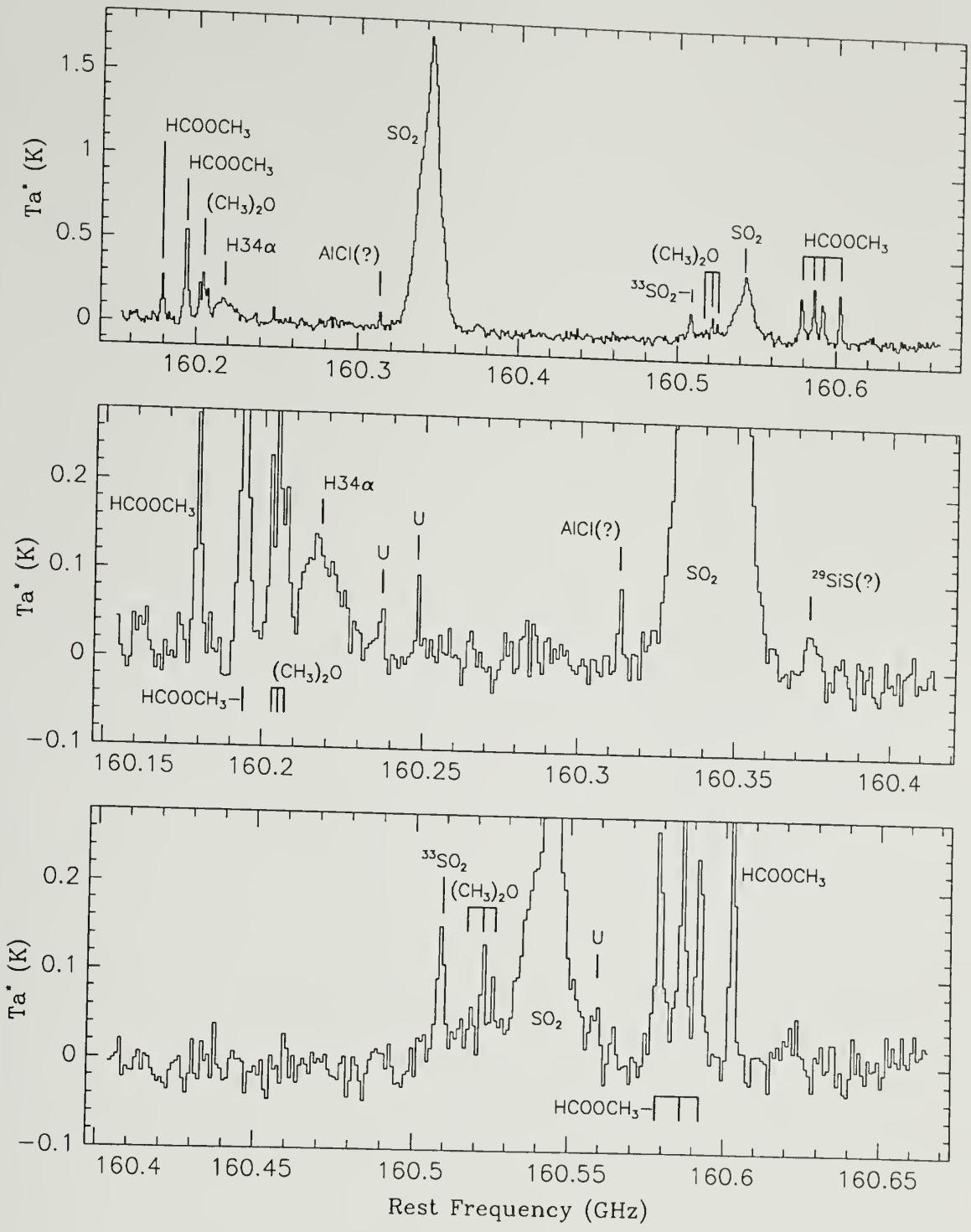

Figure 6.1. continued

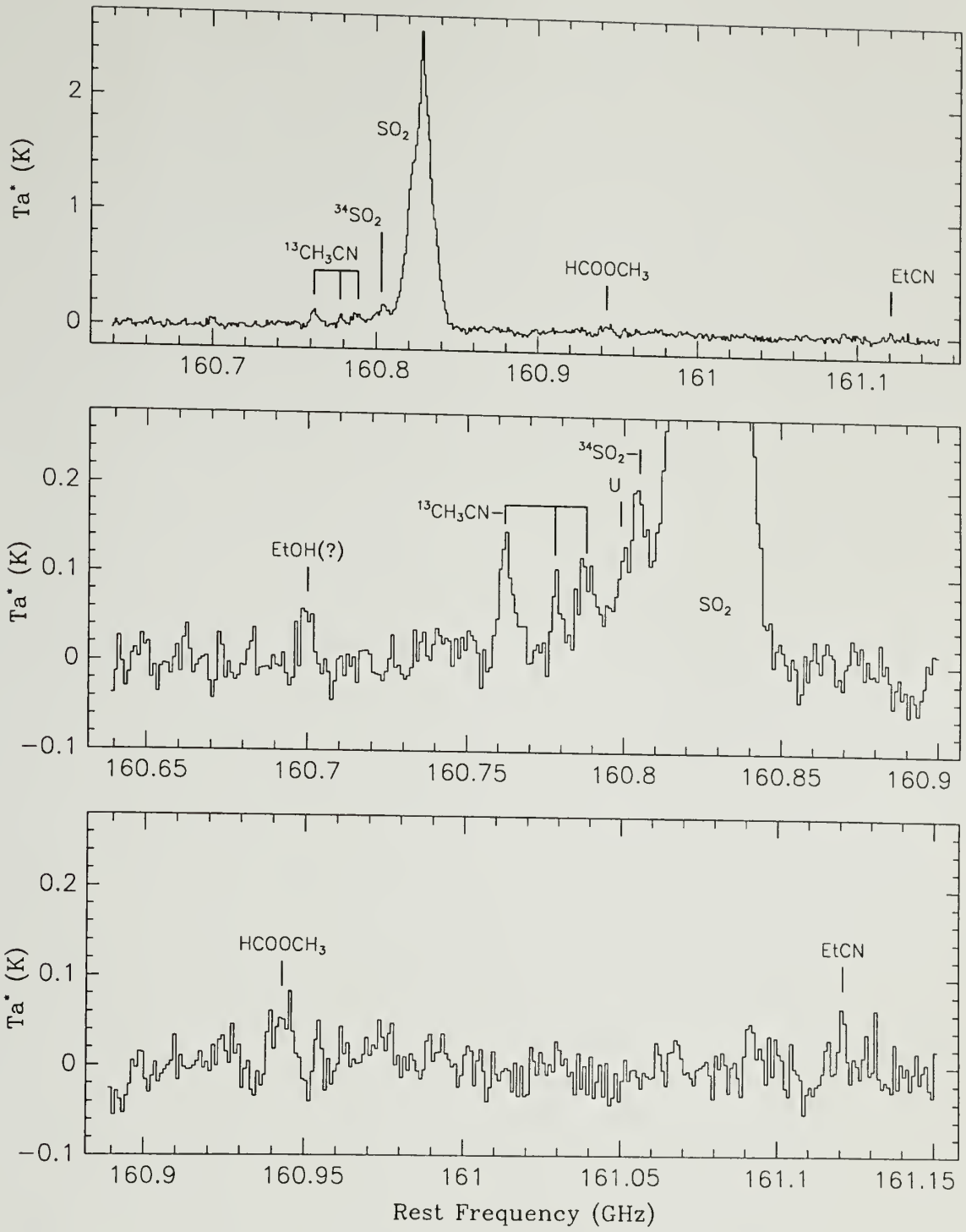

Figure 6.1. continued

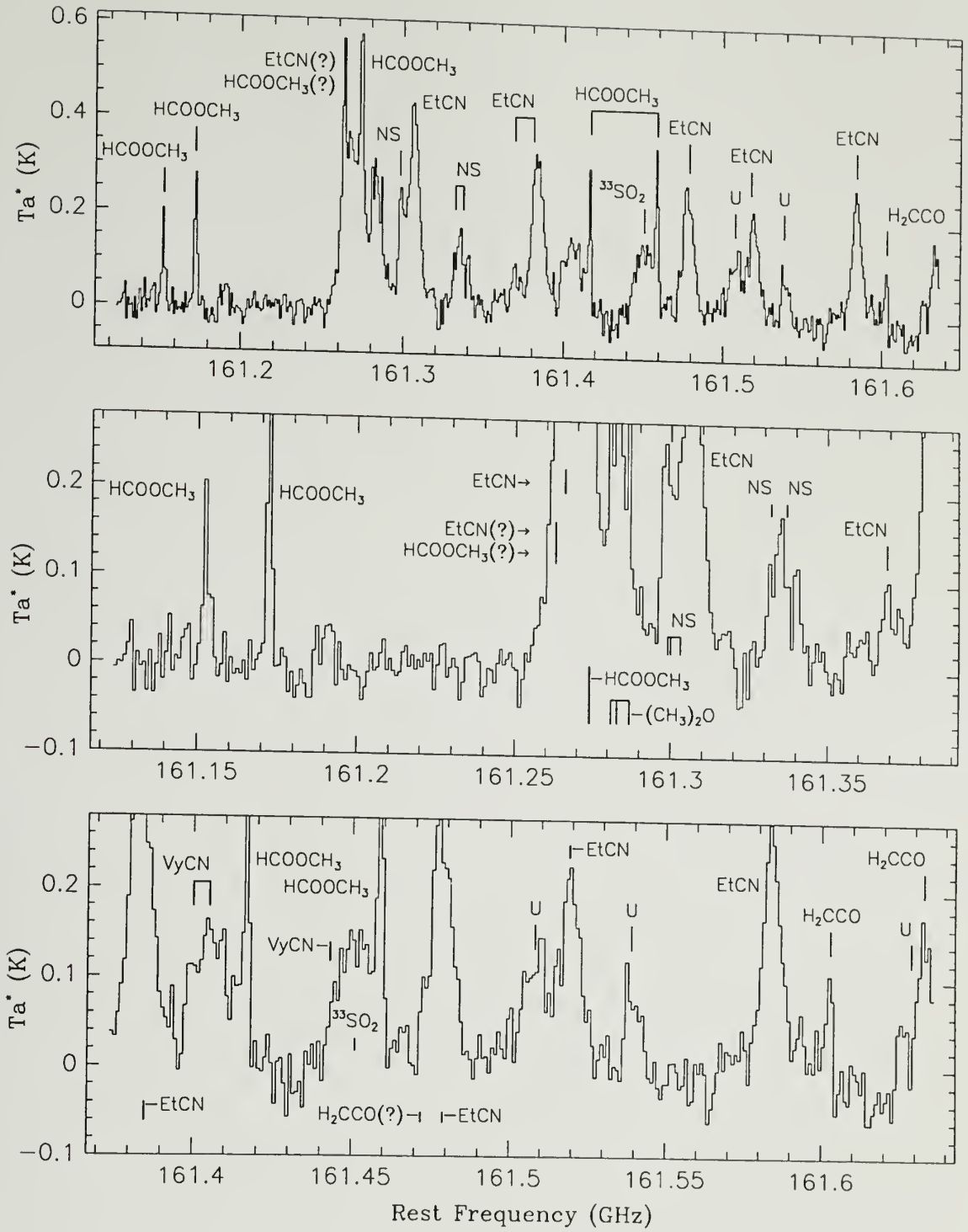

Figure 6.1. continued

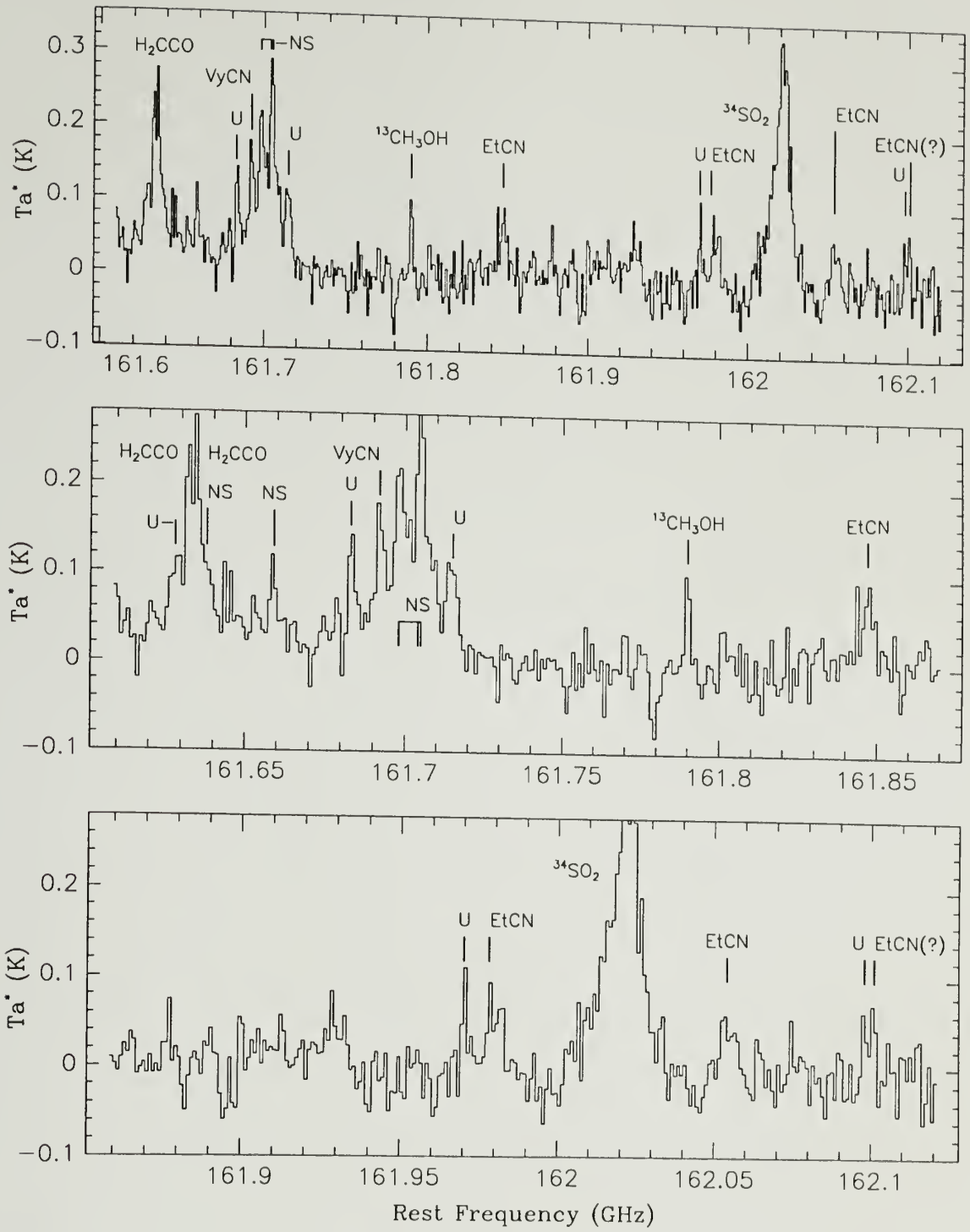

Figure 6.1. continued

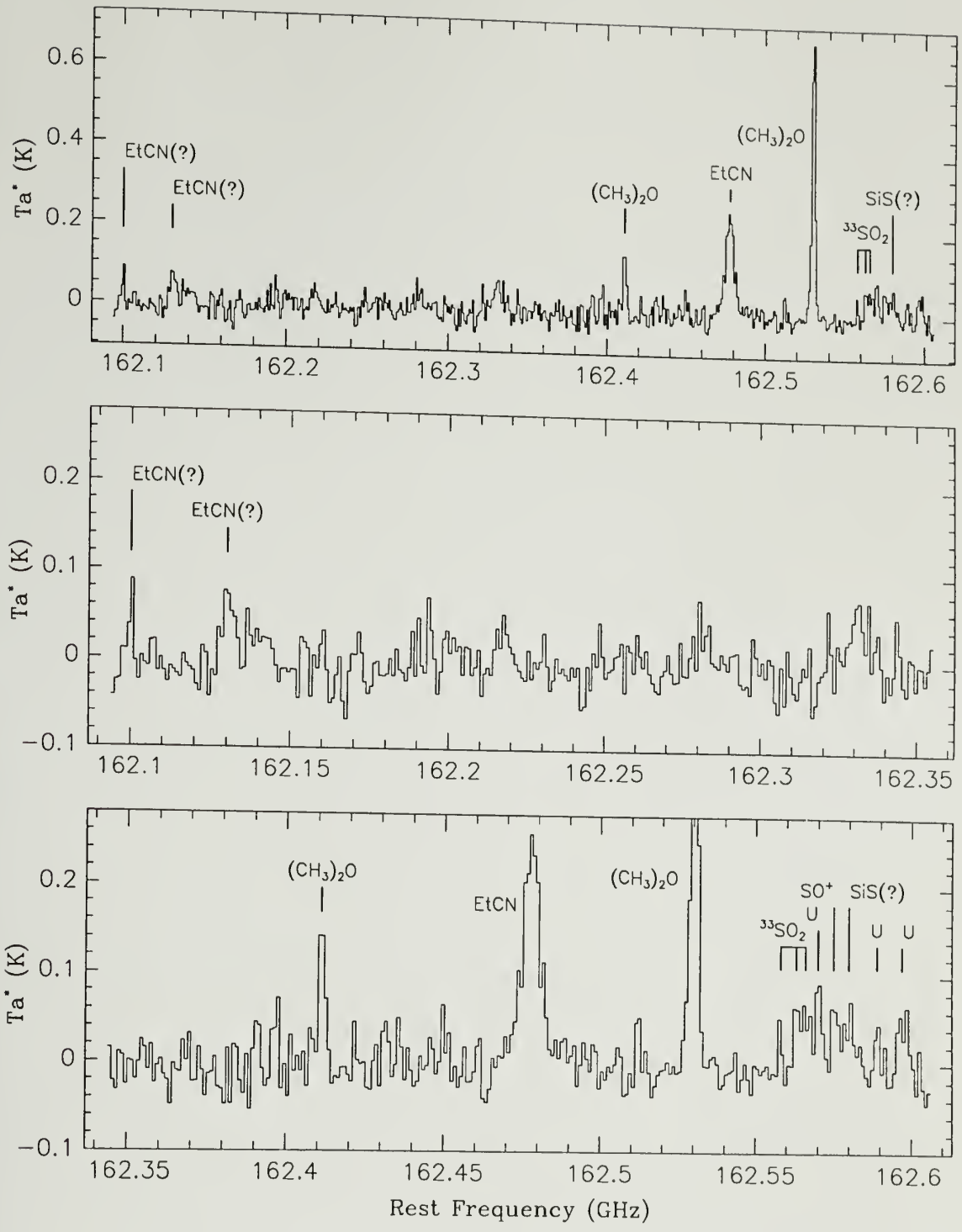

Figure 6.1. continued

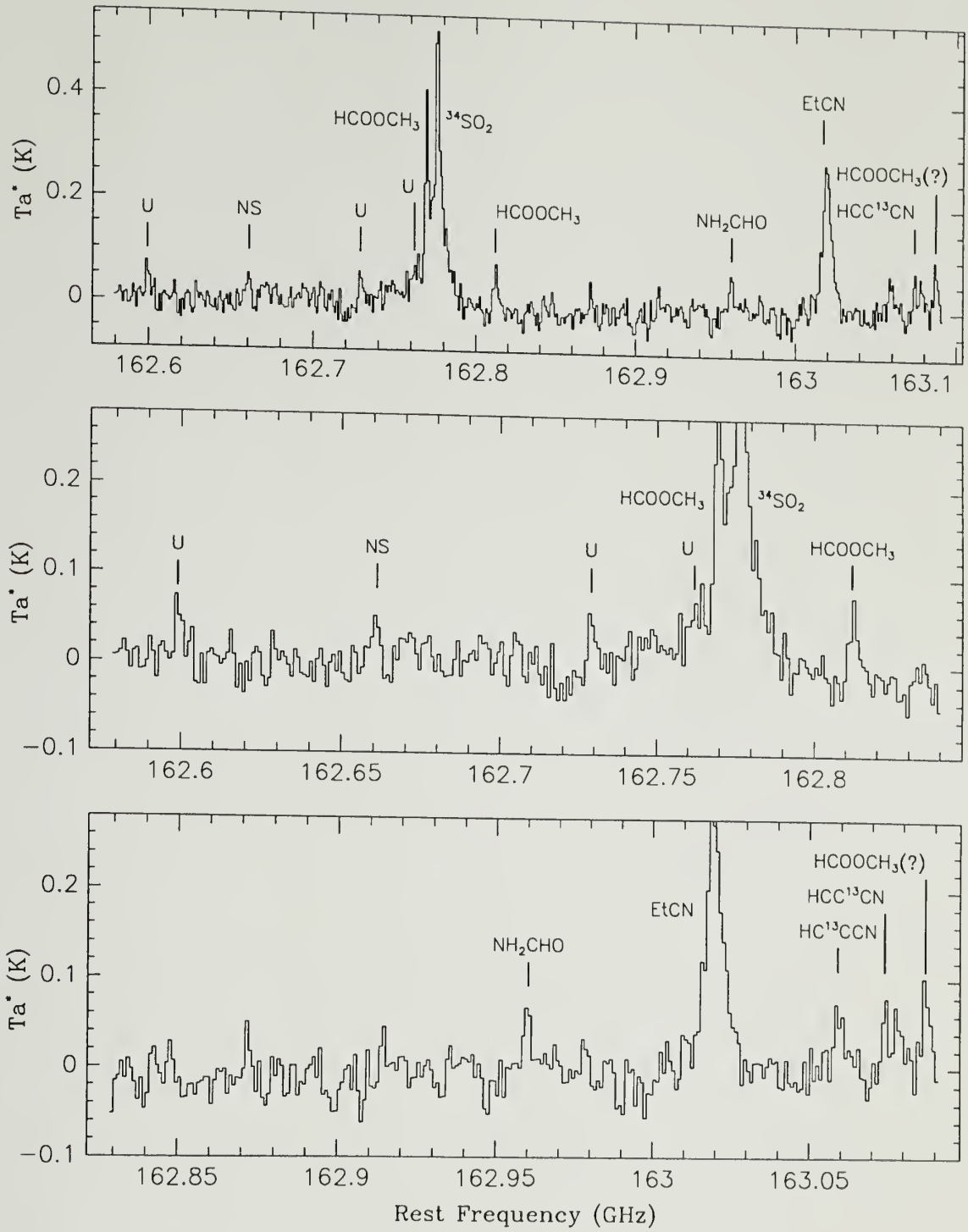

Figure 6.1. continued

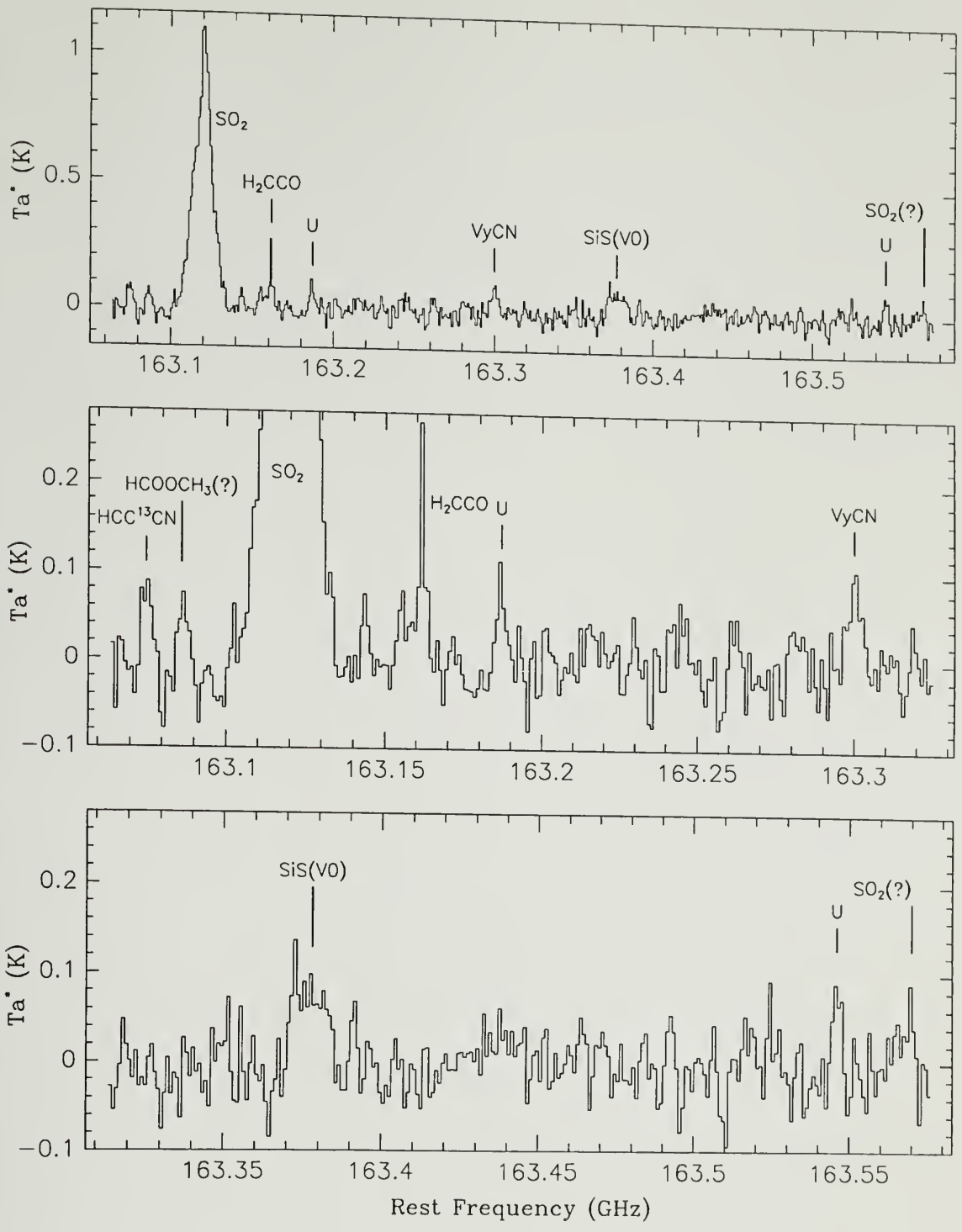

Figure 6.1. continued

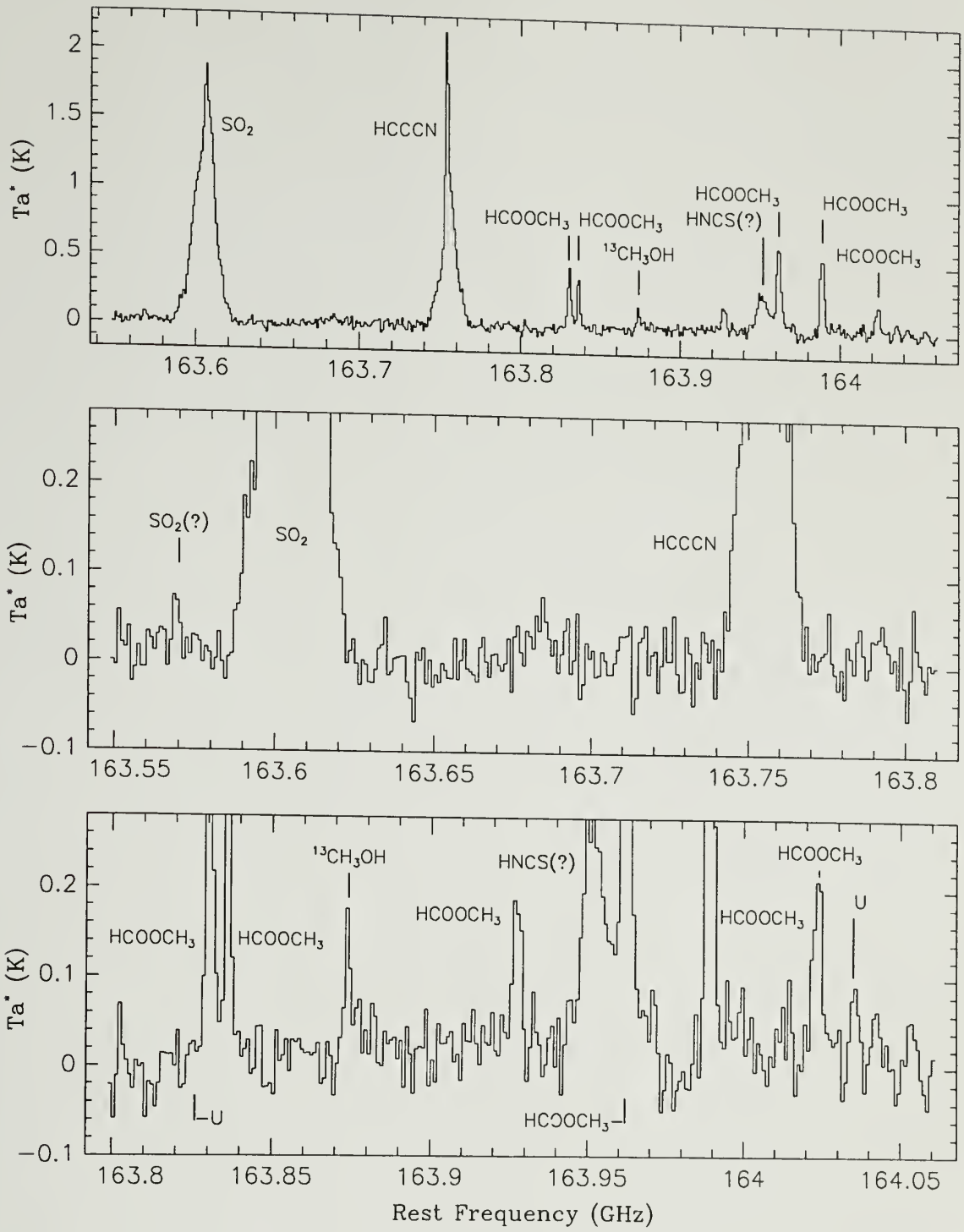

Figure 6.1. continued

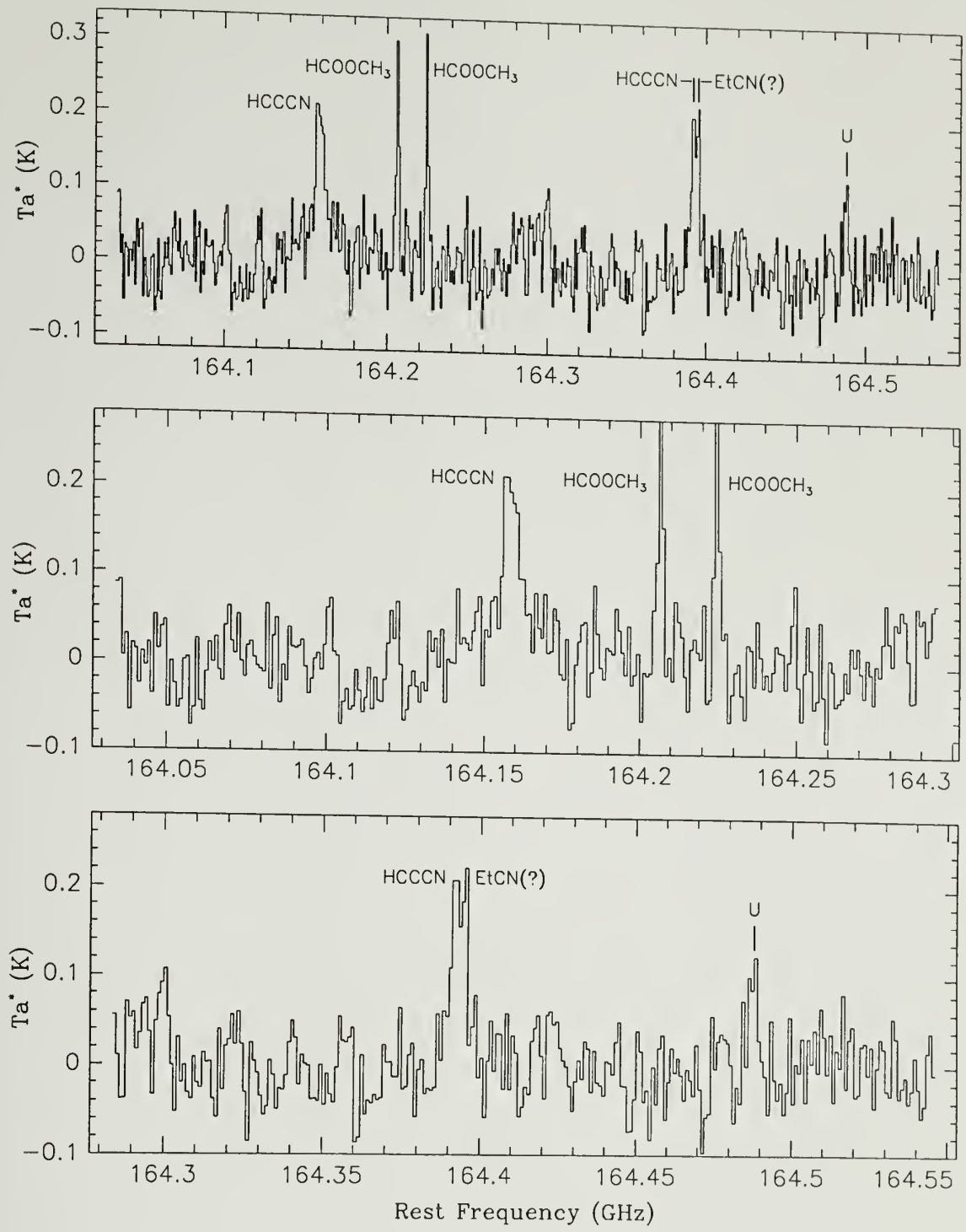

Figure 6.1. continued

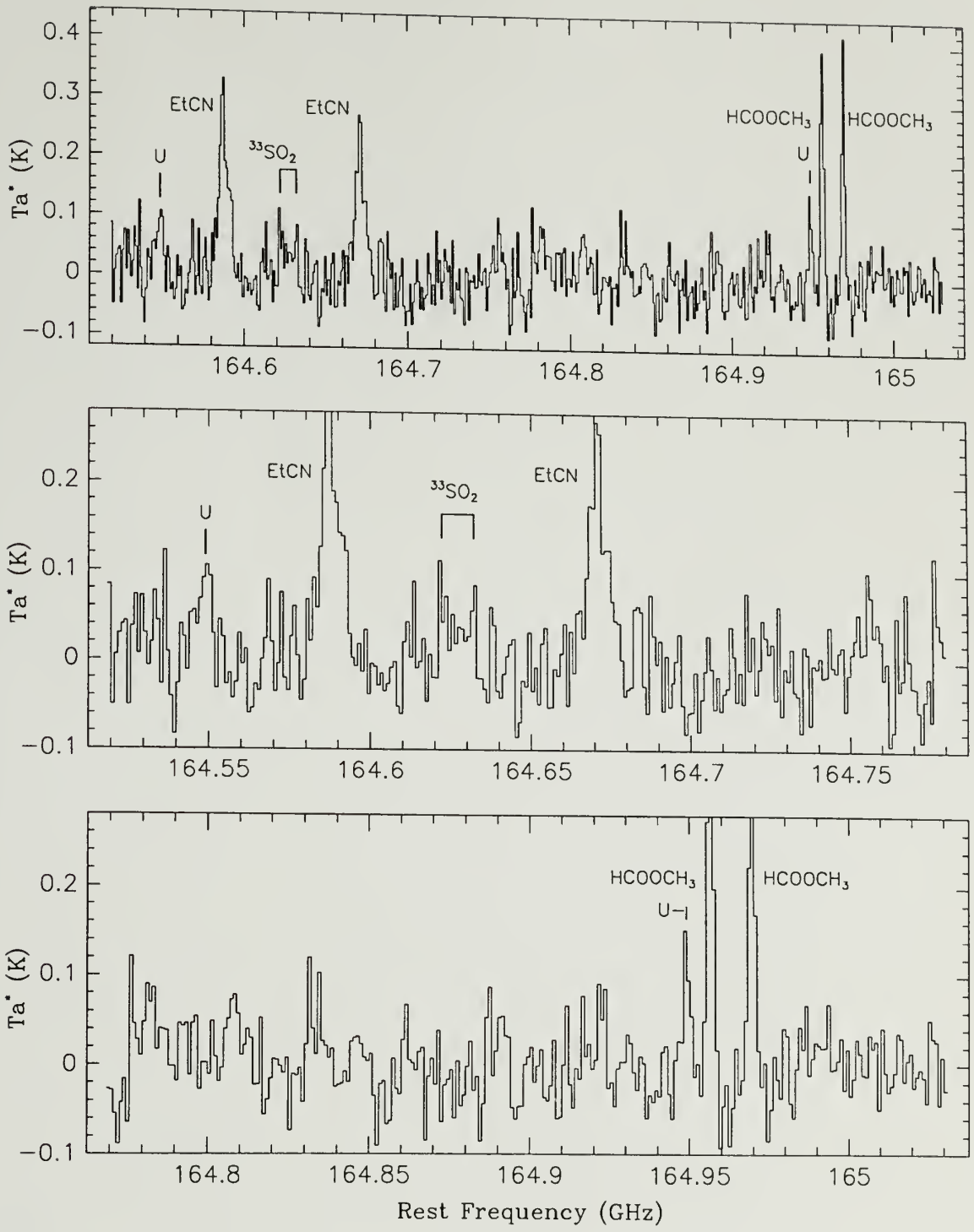

Figure 6.1. continued

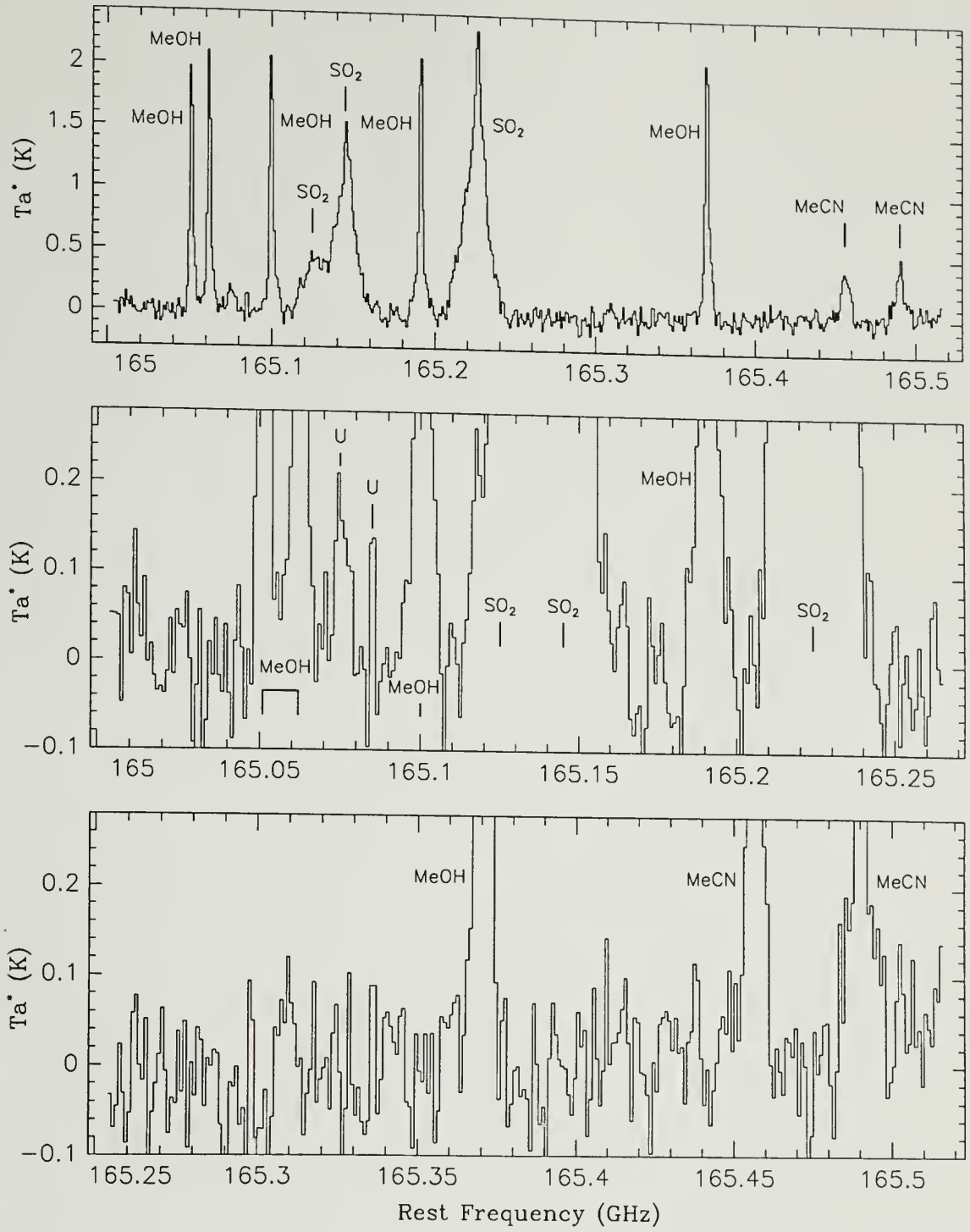

Figure 6.1. continued

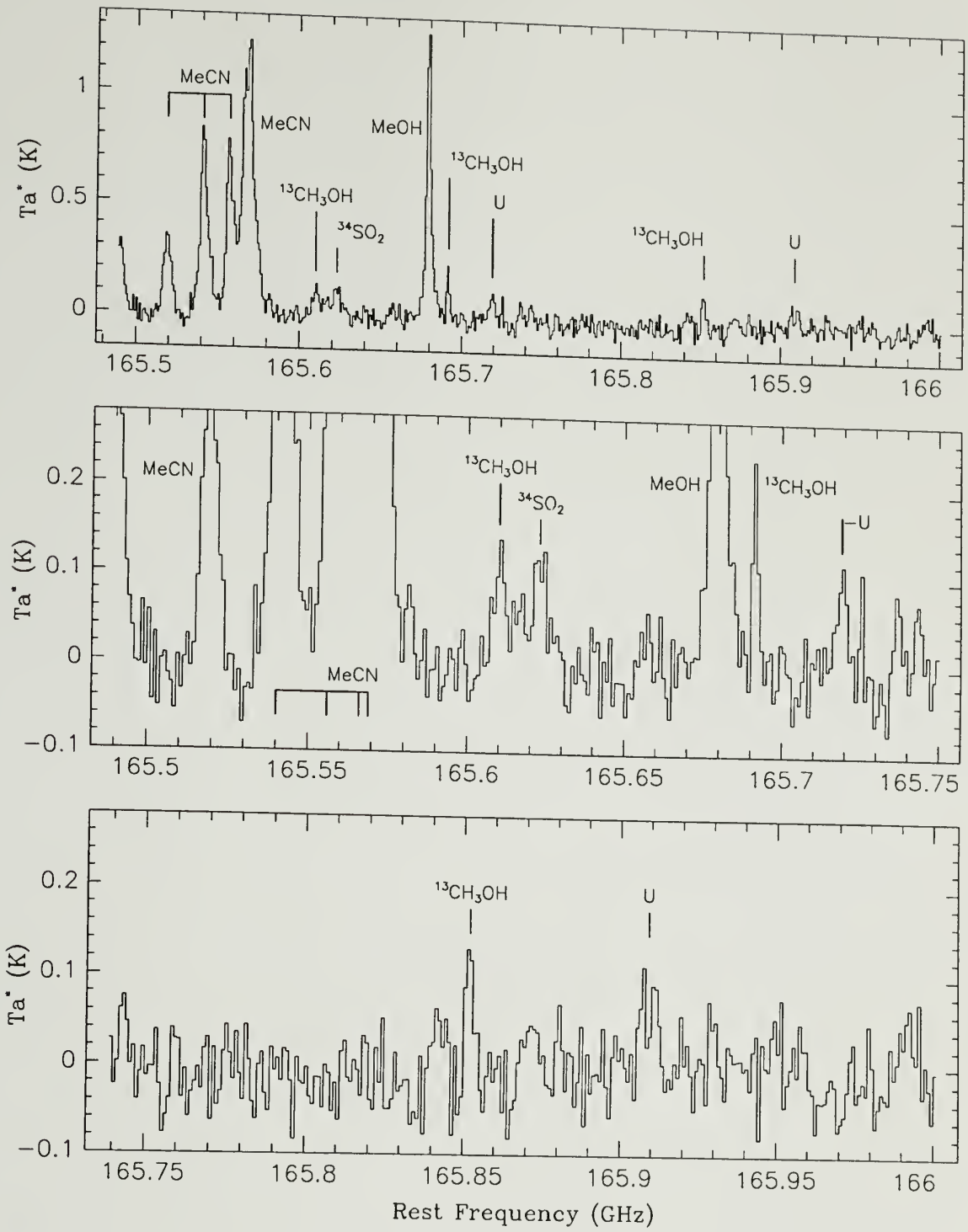

Figure 6.1. continued

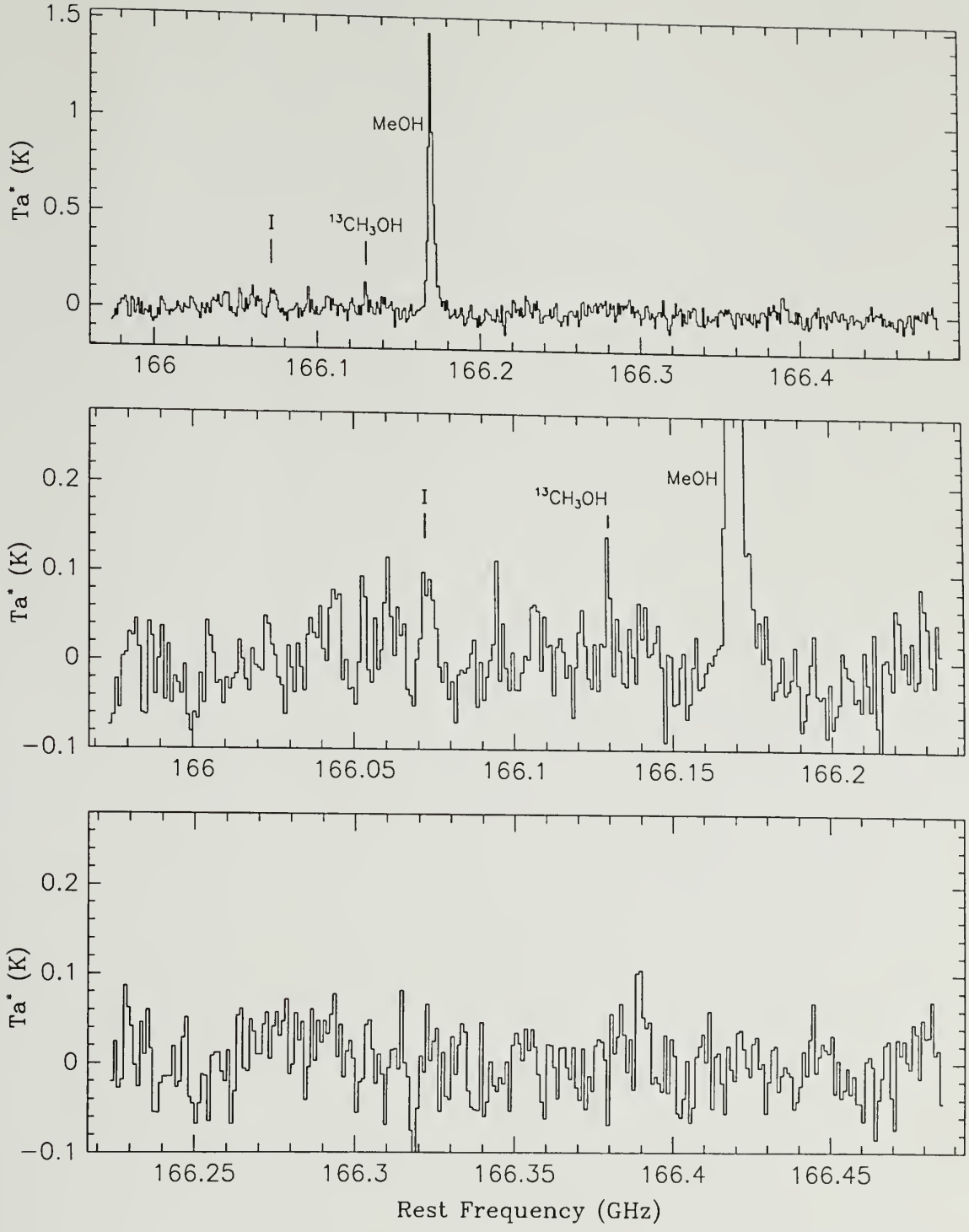

Figure 6.1. continued

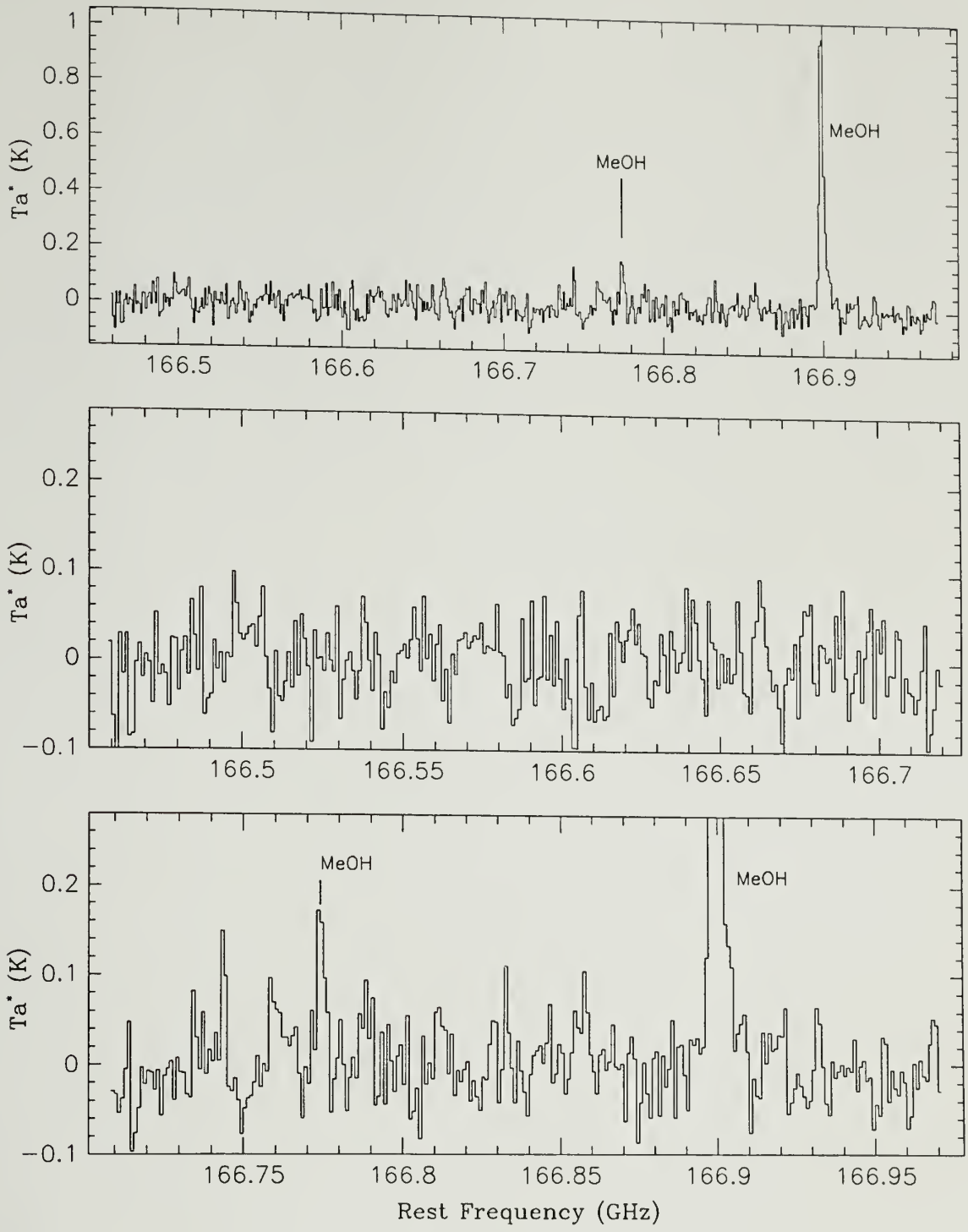

Figure 6.1. continued

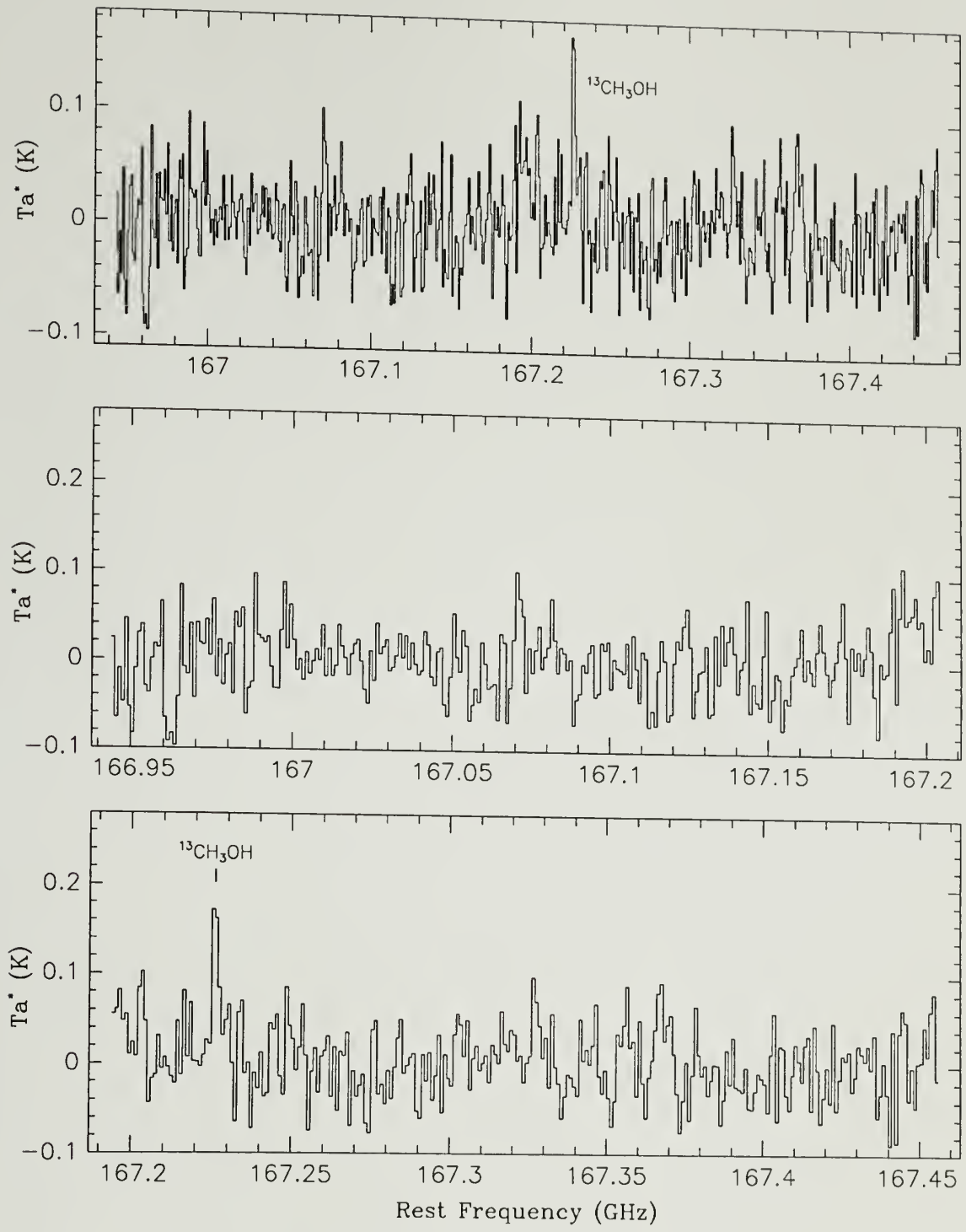

Figure 6.1. continued

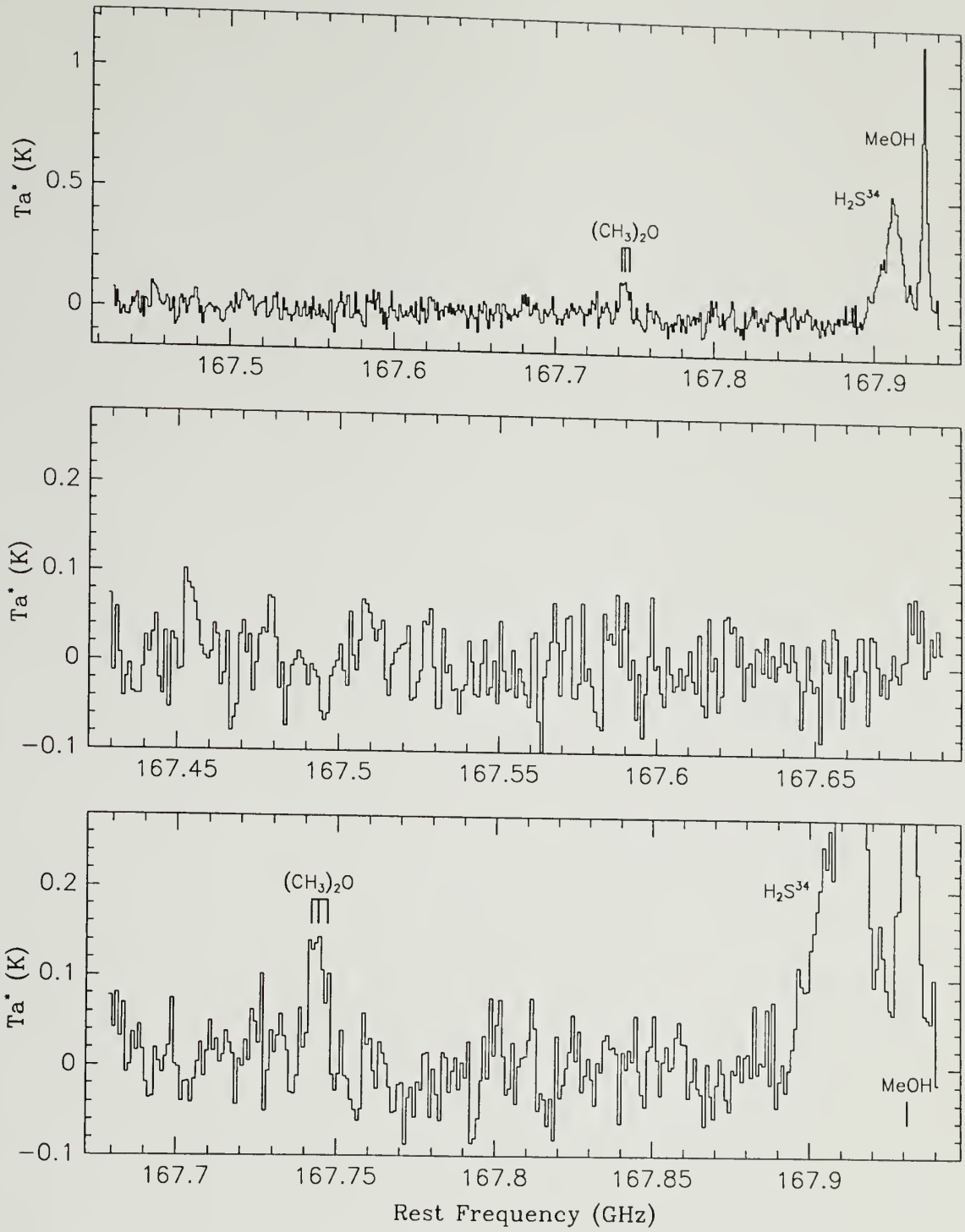

Figure 6.1. continued

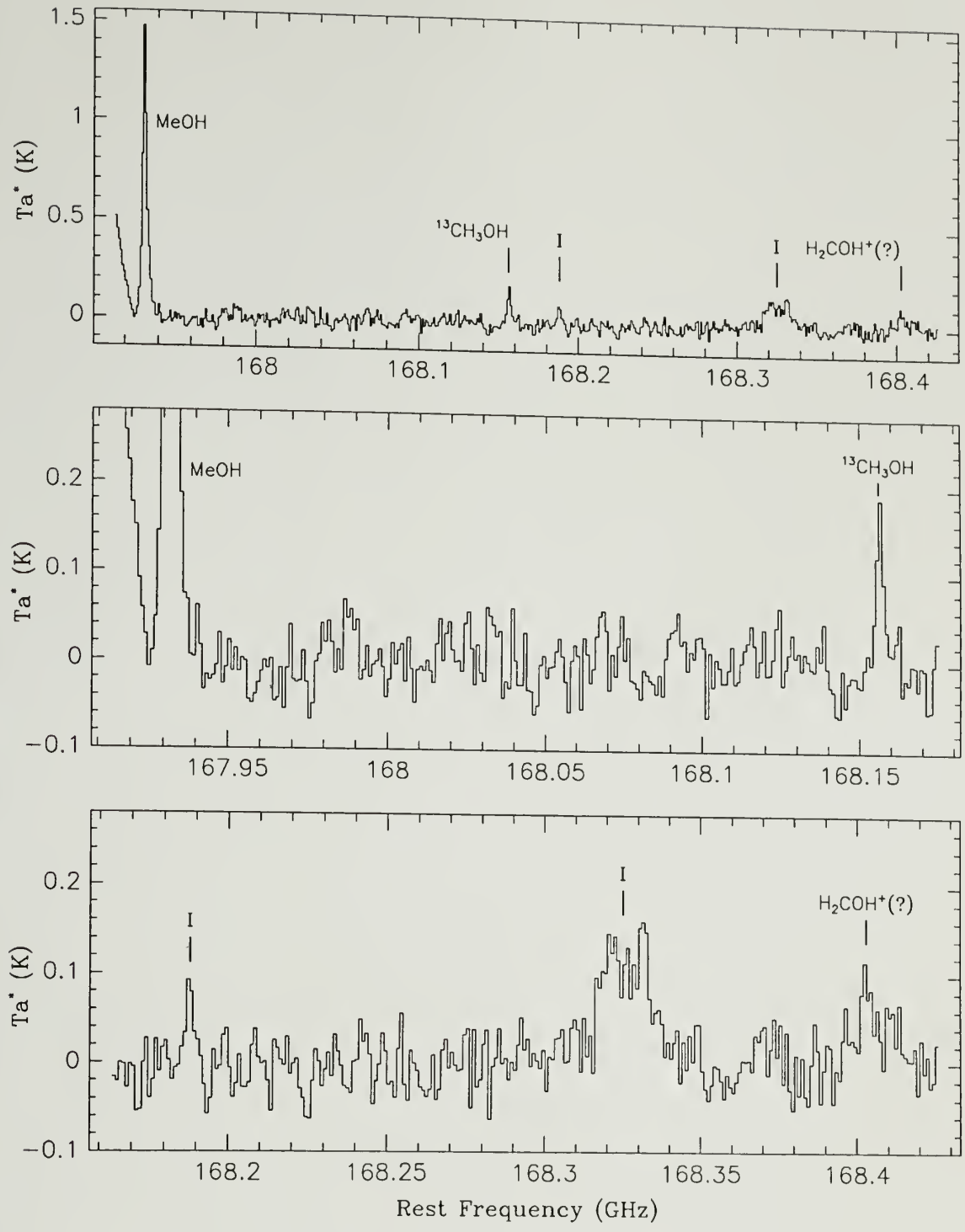

Figure 6.1. continued

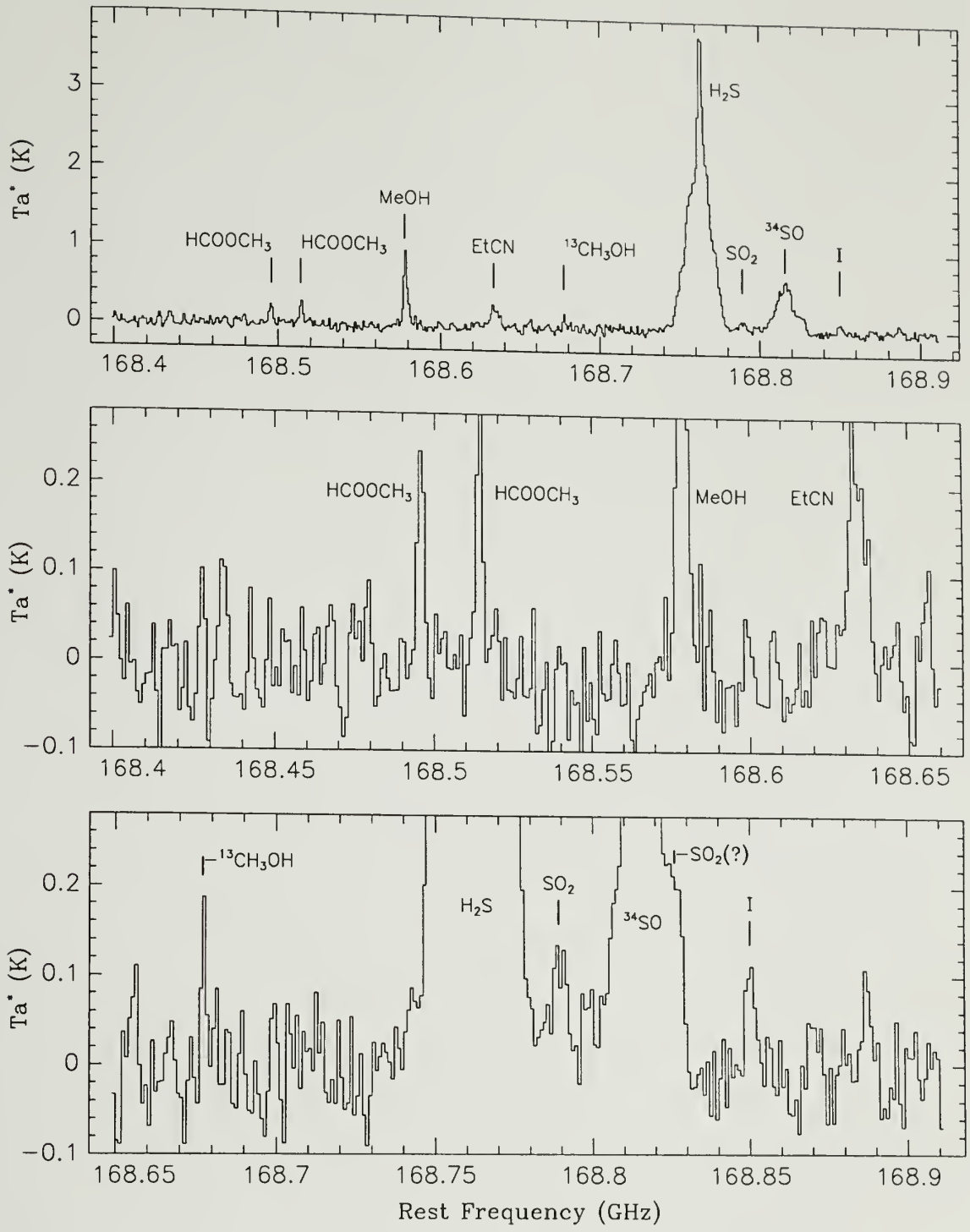

Figure 6.1. continued

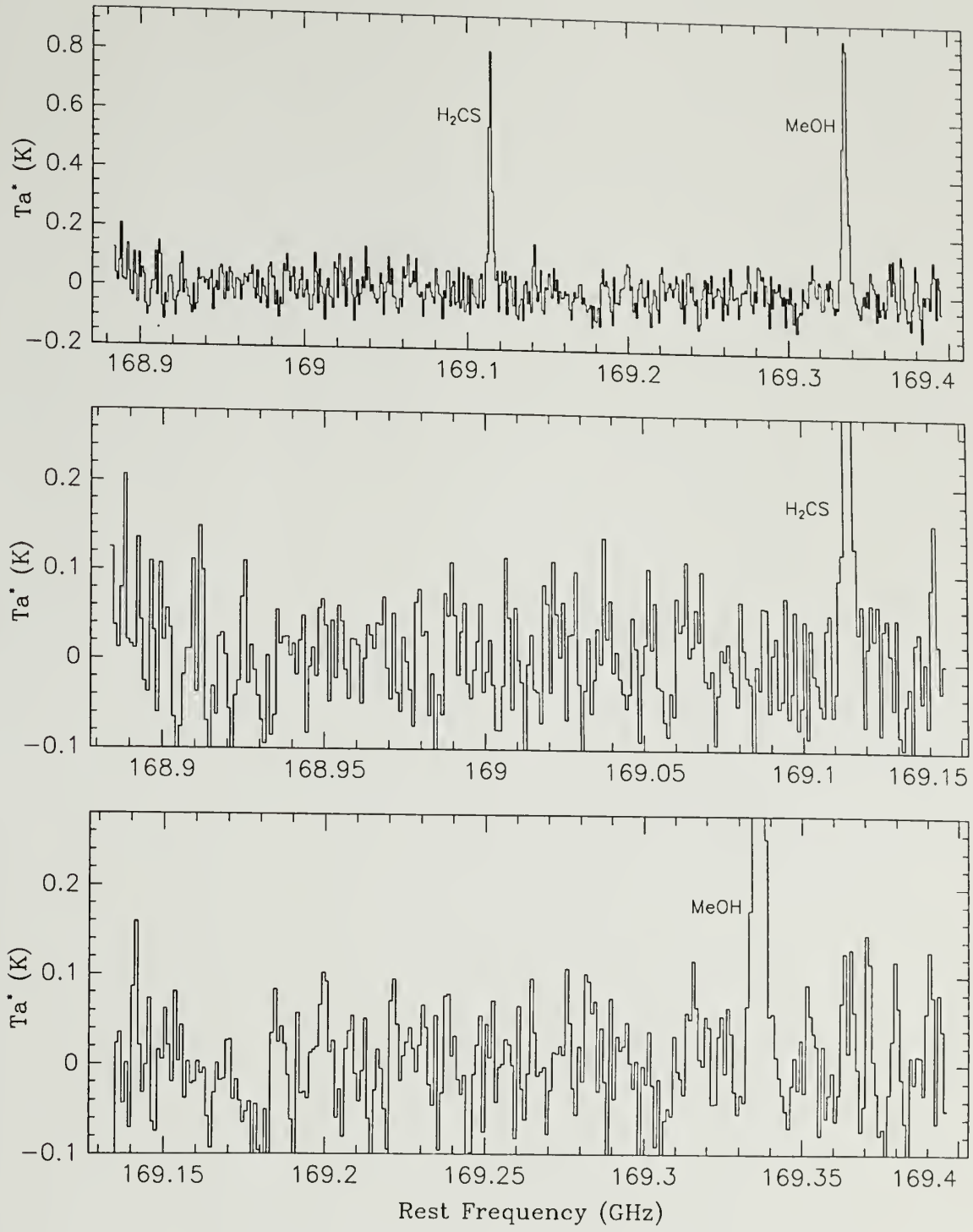

Figure 6.1. continued

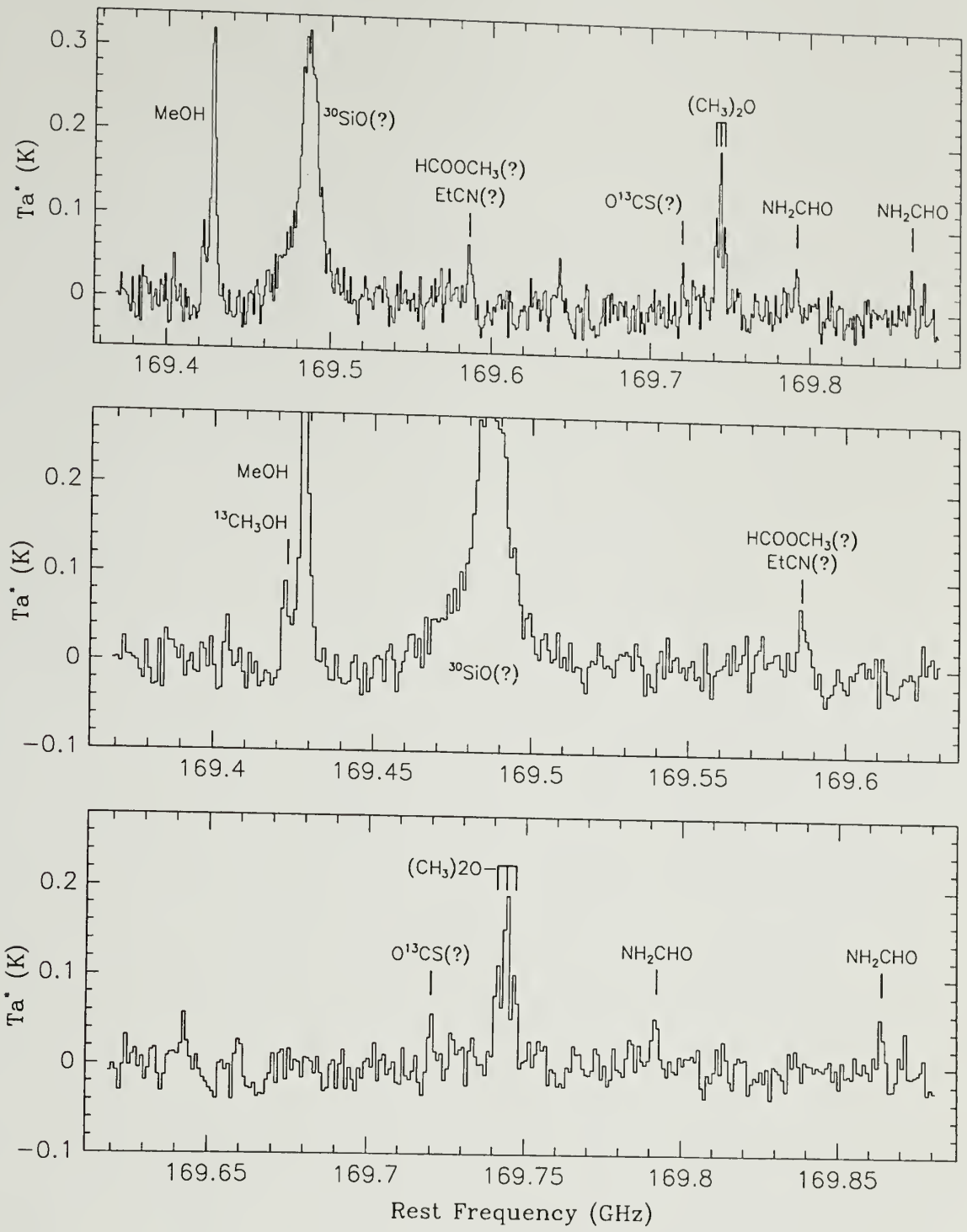

Figure 6.1. continued

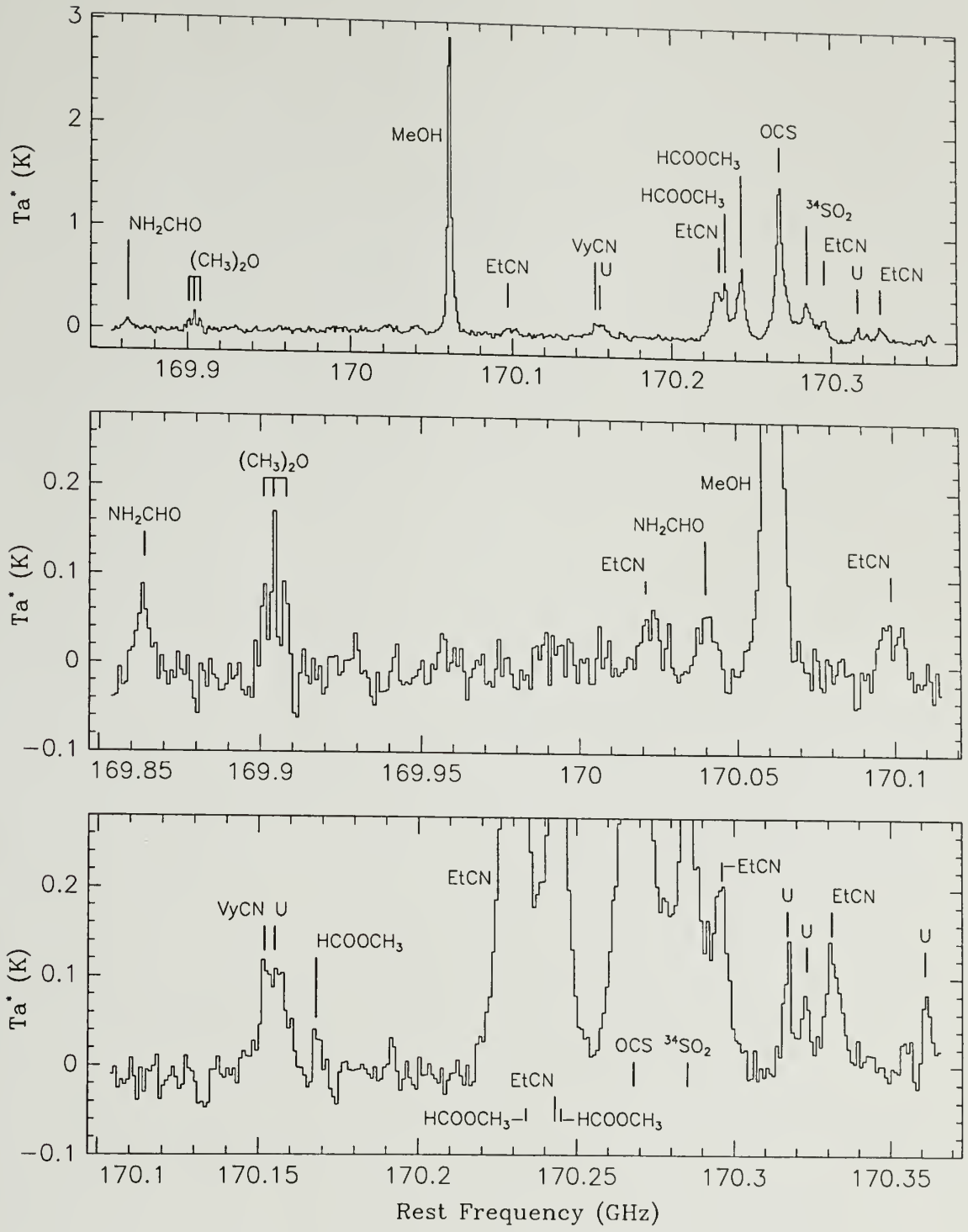

Figure 6.1. continued

Figure 6.2. Selected 250 kHz resolution spectra of Orion–KL. These spectra cover the central 128 MHz of scans 1, 4, 7, 9, 12, 14, 18, 19, 20, 21, and 22 (*see* Table 6.1). The data were taken in single sideband mode, with a 20–30 dB image rejection filter. The frequency scale assumes $V_{LSR} = 9.0$ km s^{-1}. Lines labeled as U are unidentified. Features marked I are due to strong lines in the image sideband.

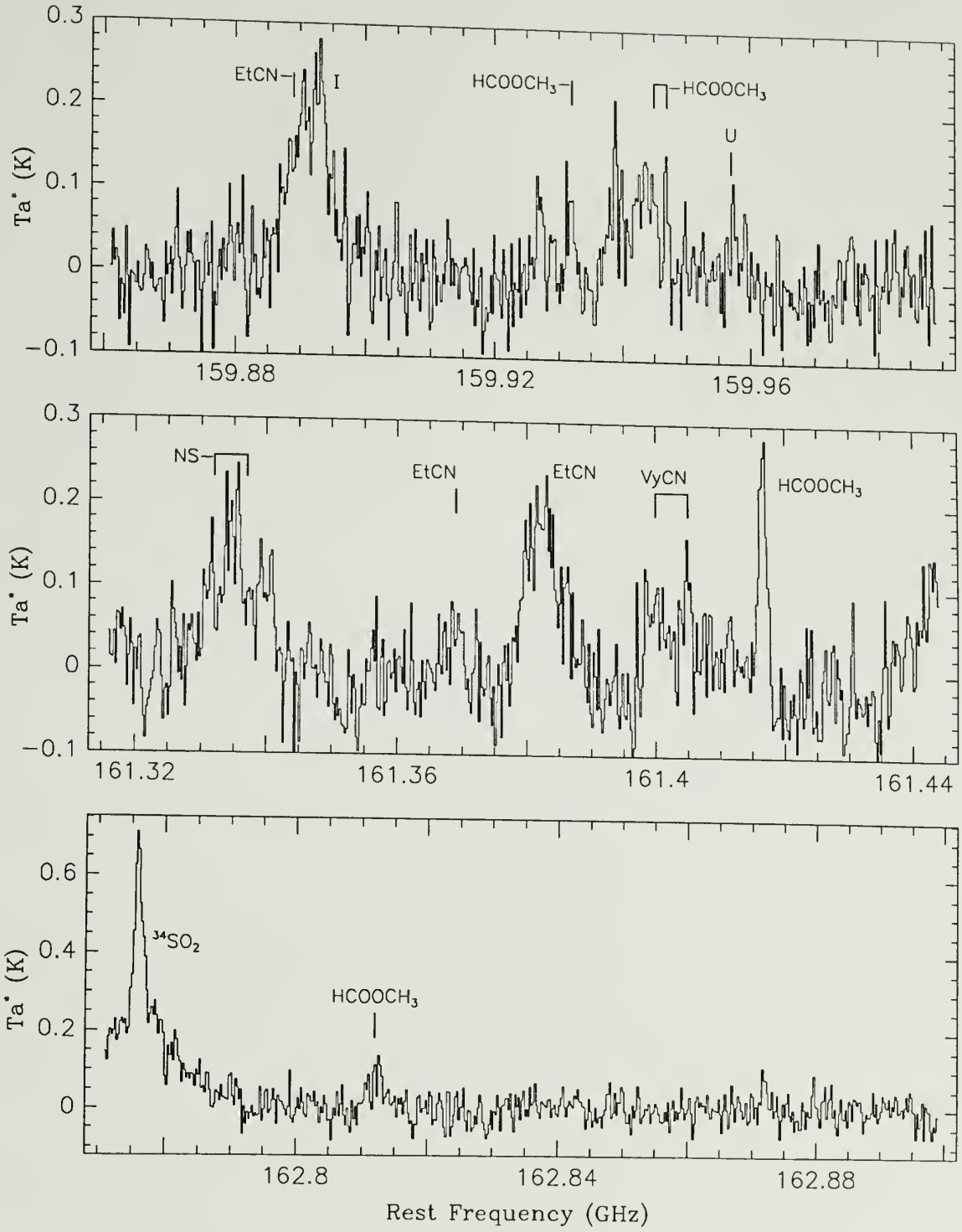

Continued, next page.

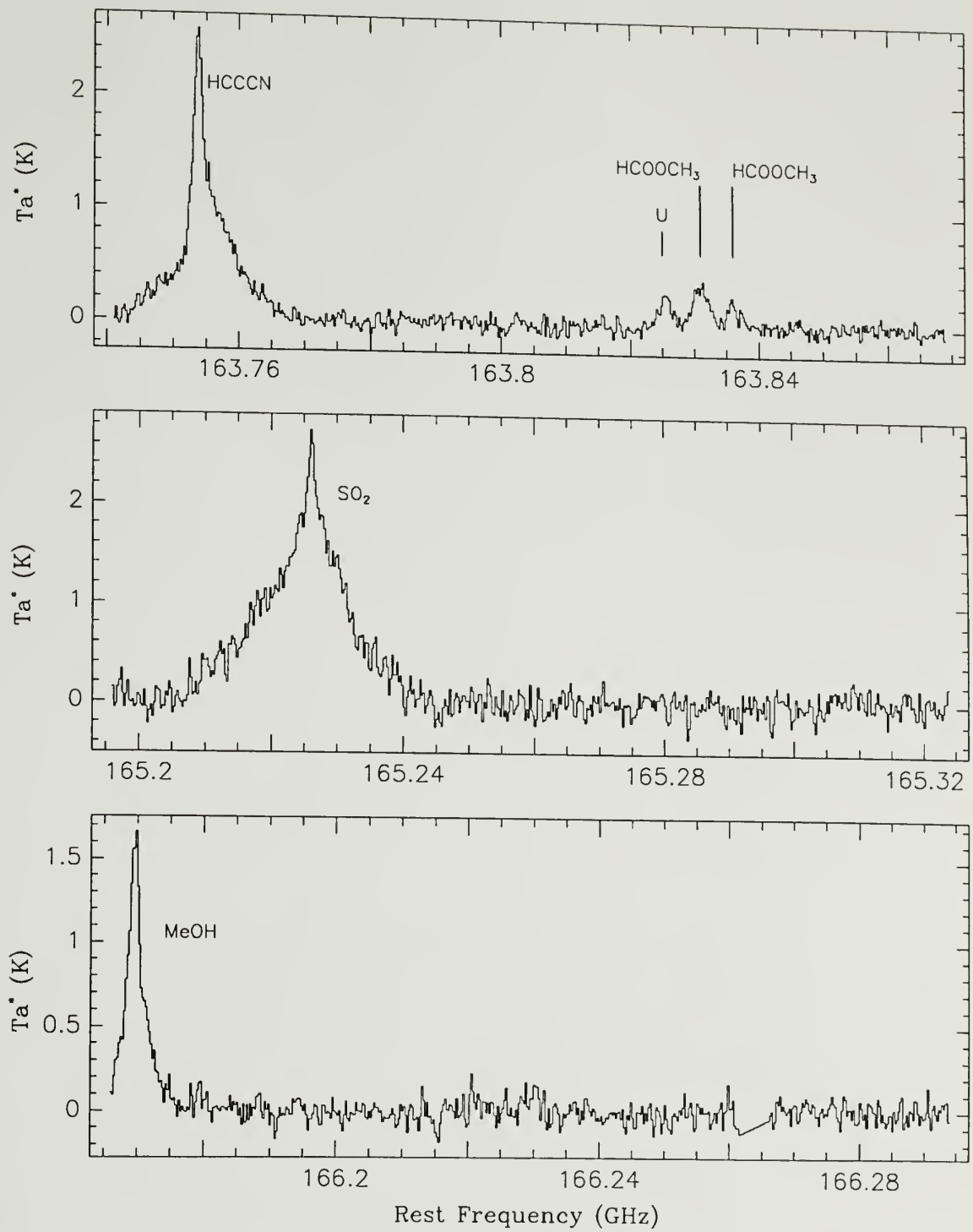

Figure 6.2. continued

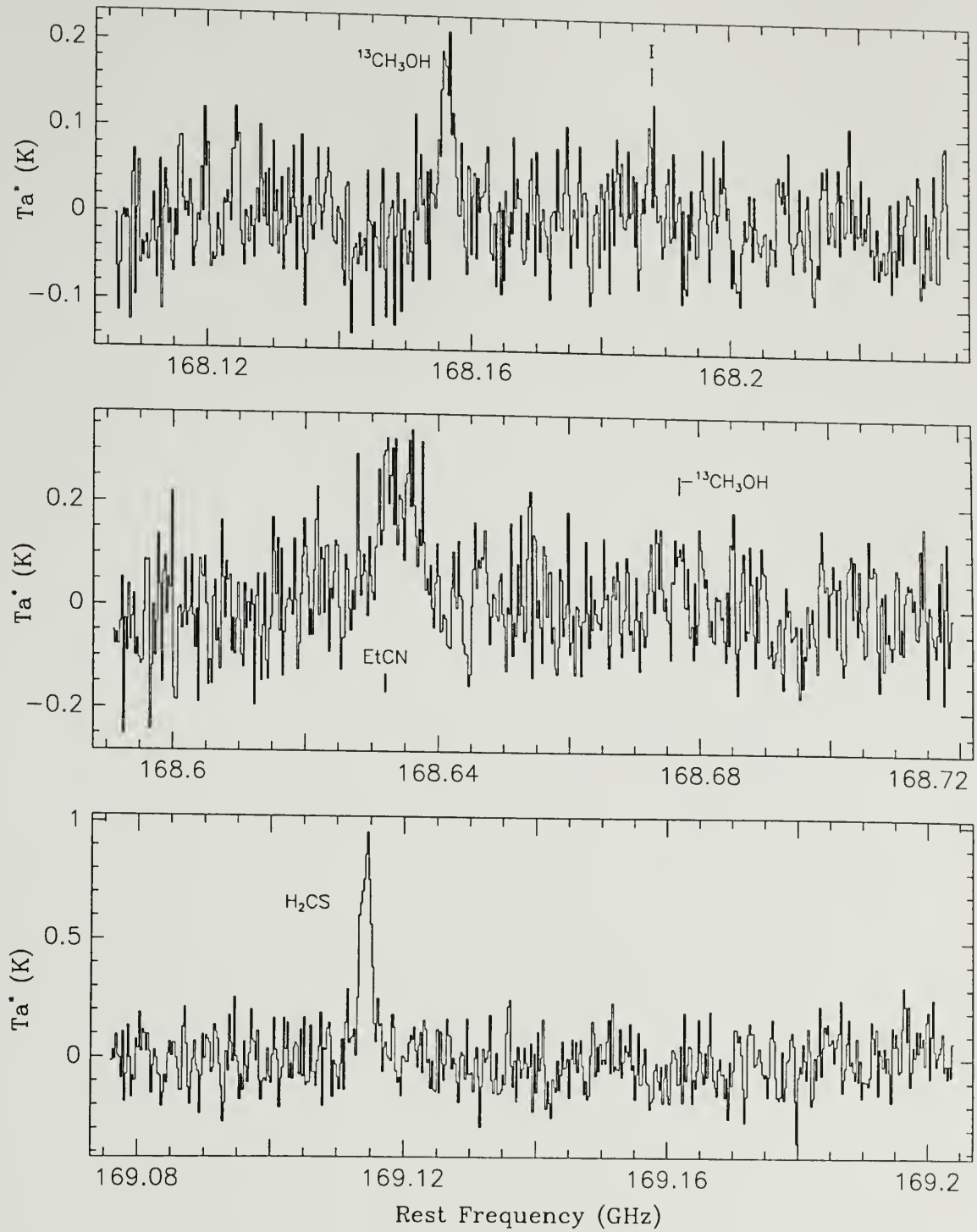

Figure 6.2. continued

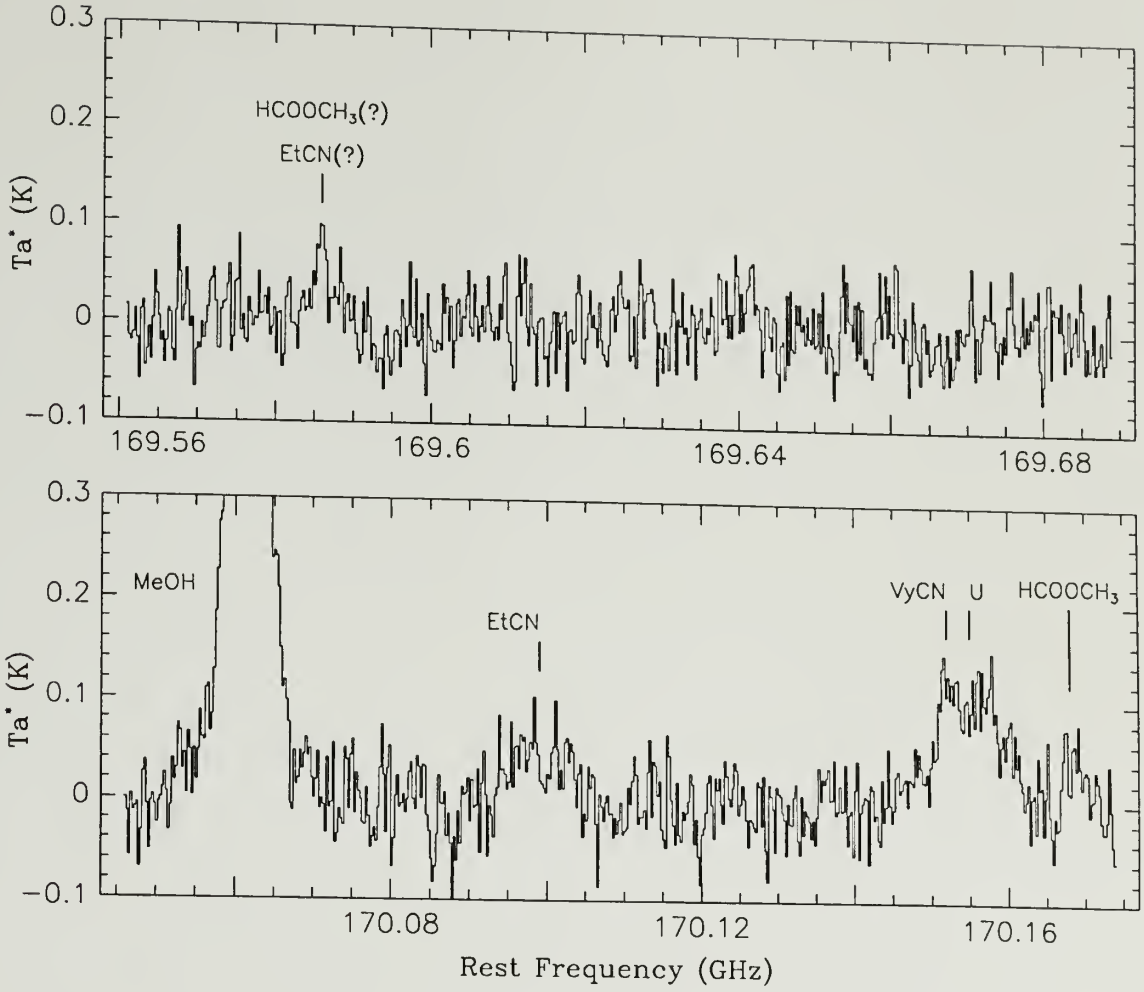

Figure 6.2. continued

Table 6.2. Spectral Lines Observed Toward Orion–KL at 2 Millimeters

Frequency (MHz)	Species	Transition	Peak T_A^* (K)	Filter Bank
~159671.2	$HCOOCH_3$	13(10,4)–12(10,3)E	~0.1	1 MHz
~159682.1	H_2CS(?)	17(1,16)–17(1,17)	~0.05	1 MHz
159718	U	...	0.08	1 MHz
159766.8	$HCOOCH_3$	13(9,4)–12(9,3)E	0.15	1 MHz
159777.4	$HCOOCH_3$	13(9,4)–12(9,3)A 13(9,5)–12(9,4)A	0.17	1 MHz
~159781.8	EtOH(?)	5(2,4)–4(1,3)	~0.12	1 MHz
159783.0	$HCOOCH_3$	13(9,5)–12(9,4)E	0.12	1 MHz
159790	I	...	~0.06	1 MHz
159796	I	...	0.07	1 MHz
~159888.9	EtCN	18(2,17)–17(2,16)	0.19	250 kHz
159893	I	...	0.09	250 kHz
159930.6	$HCOOCH_3$	13(8,5)–12(8,4)E	0.15	1 MHz
~159942.9	$HCOOCH_3$	13(8,6)–12(8,5)A 13(8,5)–12(8,4)A	~0.1	1 MHz
159946.2	$HCOOCH_3$	13(8,6)–12(8,5)E	0.13	1 MHz
159958	U	...	0.05	1 MHz
160132.5	HC_7N(?)	J = 142 → 141	~0.05	1 MHz
~160142.2	H_2CCO	8(1,8)–7(1,7)	~0.2	1 MHz
160143.6	$^{34}SO_2$	5(2,4)–5(1,5)	0.12	1 MHz
160152	U	...	0.06	1 MHz
160178.9	$HCOOCH_3$	13(7,6)–12(7,5)E	0.27	1 MHz
160193.0 160193.5 160193.7	$HCOOCH_3$	13(7,7)–12(7,6)A 13(7,6)–12(7,5)A 13(7,7)–12(7,6)E	0.61	1 MHz
160201.6 160201.7	$(CH_3)_2O$	4(2,3)–3(1,2)EA 4(2,3)–3(1,2)AE	0.21	1 MHz
160204.1	$(CH_3)_2O$	4(2,3)–3(1,2)EE	0.28	1 MHz
160206.6	$(CH_3)_2O$	4(2,3)–3(1,2)AA	0.17	1 MHz
160211.6	H34α	...	~0.1	1 MHz
160237	U	...	0.06	1 MHz
160248	U	...	0.10	1 MHz
~160312.1	AlCl(?)	J = 11 → 10	0.09	1 MHz
160343.0	SO_2	18(2,16)–18(1,17)	1.75	1 MHz

Continued, next page.

Table 6.2 continued

Frequency (MHz)	Species	Transition	Peak T_A^* (K)	Filter Bank
~160375.0	$^{29}Si^{32}S$(?)	J = 9 → 8, v = 0	~0.04	1 MHz
160508.7	$^{33}SO_2$	18(2,16) − 18(1,17)	0.15	1 MHz
~160518.6	$(CH_3)_2O$	15(2,14) − 15(1,15)AE 15(2,14) − 15(1,15)EA	0.07	1 MHz
~160521.7	$(CH_3)_2O$	15(2,14) − 15(1,15)EE	0.13	1 MHz
~160524.9	$(CH_3)_2O$	15(2,14) − 15(1,15)AA	0.09	1 MHz
160543.1	SO_2	4(3,1) − 5(2,4)	0.39	1 MHz
160559	U	...	0.05	1 MHz
160578.3	$HCOOCH_3$	13(6,7) − 12(6,6)E	0.24	1 MHz
160585.8	$HCOOCH_3$	13(6,8) − 12(6,7)A	0.28	1 MHz
160591.3	$HCOOCH_3$	13(6,8) − 12(6,7)E	0.24	1 MHz
160602.2	$HCOOCH_3$	13(6,7) − 12(6,6)A	0.30	1 MHz
~160699.0	EtOH(?)	10(0,10) − 9(1,9)	~0.06	1 MHz
160761.8	$^{13}CH_3CN$	9(3) − 8(3)	0.13	1 MHz
160776.8	$^{13}CH_3CN$	9(2) − 8(2)	0.10	1 MHz
160785.9 160789.0	$^{13}CH_3CN$	9(1) − 8(1) 9(0) − 8(0)	0.10	1 MHz
160799	U	...	0.08	1 MHz
~160802.6	$^{34}SO_2$	18(2,16) − 18(1,17)	0.16	1 MHz
160827.8	SO_2	10(0,10) − 9(1,9)	2.60	1 MHz
~160944.9	$HCOOCH_3$	14(1,13) − 13(2,12)E	~0.06	1 MHz
161122.0	EtCN	9(2,7) − 8(1,8)	~0.07	1 MHz
161152.5	$HCOOCH_3$	13(5,9) − 12(5,8)A	0.20	1 MHz
161171.4	$HCOOCH_3$	13(5,9) − 12(5,8)E	0.29	1 MHz
~161261.1	EtCN(?)	18(8,10) − 17(8,9) 18(8,11) − 17(8,10)	~0.5	1 MHz
~161262.4	$HCOOCH_3$(?)	13(4,10) − 12(4,9)E	~0.5	1 MHz
~161265.7	EtCN	18(9,9) − 17(9,8) 18(9,10) − 17(9,9)	~0.36	1 MHz
~161273.3	$HCOOCH_3$	13(4,10) − 12(4,9)A	~0.5	1 MHz
~161279.8	$(CH_3)_2O$	14(3,12) − 14(2,13)AE 14(3,12) − 14(2,13)EA	0.33	1 MHz
~161282.8	$(CH_3)_2O$	14(3,12) − 14(2,13)EE	0.40	1 MHz
~161285.8	$(CH_3)_2O$	14(3,12) − 14(2,13)AA	0.32	1 MHz

Table 6.2 continued

Frequency (MHz)	Species	Transition	Peak T_A^* (K)	Filter Bank
161297.2	NS $^2\Pi_{1/2}$	J=7/2→5/2 F=9/2→7/2 e	0.16	1 MHz
161298.4	NS $^2\Pi_{1/2}$	J=7/2→5/2 F=7/2→5/2 e	0.10	1 MHz
~161301.7	NS $^2\Pi_{1/2}$	J=7/2→5/2 F=5/2→3/2 e	~0.14	1 MHz
~161303.5	EtCN	18(11,8)−17(11,7)	0.42	1 MHz
~161303.5		18(11,7)−17(11,6)		
~161304.9		18(6,13)−17(6,12)		
~161304.9		18(6,12)−17(6,11)		
161330.1	NS $^2\Pi_{1/2}$	J=7/2→5/2 F=5/2→5/2 e	~0.10	1 MHz
161335.8	NS $^2\Pi_{1/2}$	J=7/2→5/2 F=7/2→7/2 e	~0.10	1 MHz
161367.3	EtCN	18(13,5)−17(13,4)	~0.06	500 kHz
		18(13,6)−17(13,5)		
161379.8	EtCN	18(5,14)−17(5,13)	0.21	500 kHz
161381.9		18(5,13)−17(5,12)		
161397.0	VyCN	17(6,12)−16(6,11)	0.11	500 kHz
161397.1		17(6,11)−16(6,10)		
161402.6	VyCN	17(5,13)−16(5,12)	0.12	500 kHz
		17(5,12)−16(5,11)		
~161416.2	$HCOOCH_3$	13(5,8)−12(5,7)E	~0.3	500 kHz
~161445.4	VyCN	17(4,14)−16(4,13)	~0.04	1 MHz
161452.7	$^{33}SO_2$	10(0,10)−9(1,9)	~0.14	1 MHz
161457.6	$HCOOCH_3$	20(2,18)−20(1,19)A	0.30	1 MHz
161458.2		13(5,8)−12(5,7)A		
~161471.6	H_2CCO(?)	8(5,3)−7(5,2)	~0.07	1 MHz
		8(5,4)−7(5,3)		
161475.2	EtCN	18(3,16)−17(3,15)	0.29	1 MHz
161509	U	...	0.12	1 MHz
~161516.7	EtCN	18(4,15)−17(4,14)	0.24	1 MHz
161539	U	...	0.10	1 MHz
161581.2	EtCN	18(4,14)−17(4,13)	0.25	1 MHz
161602.3	H_2CCO	8(3,6)−7(3,5)	0.12	1 MHz
		8(3,5)−7(3,4)		
161629	U	...	0.08	1 MHz
~161631.6	H_2CCO	8(2,7)−7(2,6)	~0.2	1 MHz

Table 6.2 continued

Frequency (MHz)	Species	Transition	Peak T_A^* (K)	Filter Bank
~161634.0	H_2CCO	8(0,8)−7(0,7)	~0.2	1 MHz
~161636.5	NS $^2\Pi_{1/2}$	J=7/2→5/2 F=7/2→7/2 f	~0.08	1 MHz
161657.8	NS $^2\Pi_{1/2}$	J=7/2→5/2 F=5/2→5/2 f	0.06	1 MHz
161683	U	...	0.13	1 MHz
161689.8	VyCN	17(3,14)−16(3,13)	0.14	1 MHz
161697.3	NS $^2\Pi_{1/2}$	J=7/2→5/2 F=9/2→7/2 f	0.24	1 MHz
161703.4	NS $^2\Pi_{1/2}$	J=7/2→5/2 F=7/2→5/2 f	0.19	1 MHz
~161704.0	NS $^2\Pi_{1/2}$	J=7/2→5/2 F=5/2→3/2 f	~0.12	1 MHz
161714	U	...	0.11	1 MHz
161789.2	$^{13}CH_3OH$	4(1)−3(2)E	0.12	1 MHz
161845.6	EtCN	17(4,14)−17(3,15)	~0.09	1 MHz
161970	U	...	0.12	1 MHz
161978.0	EtCN	10(4,6)−10(3,7)	~0.07	1 MHz
161978.3		19(4,16)−19(3,17)		
162020.4	$^{34}SO_2$	10(0,10)−9(1,9)	0.33	1 MHz
162053.3	EtCN	11(4,8)−11(3,9)	~0.06	1 MHz
162098	U	...	0.18	1 MHz
162098.6	EtCN(?)	10(4,7)−10(3,8)	~0.1	1 MHz
162132.9	EtCN(?)	20(4,17)−20(3,18)	0.08	1 MHz
162134.9		8(4,4)−8(3,5)		
162409.5	$(CH_3)_2O$	22(3,19)−22(4,18)AE	0.16	1 MHz
162409.5		22(3,19)−22(4,18)EA		
162410.8		22(3,19)−22(4,18)EE		
162412.0		22(3,19)−22(4,18)AA		
162475.0	EtCN	18(3,15)−17(3,14)	0.26	1 MHz
162529.0	$(CH_3)_2O$	8(1,8)−7(0,7)AE	0.74	1 MHz
162529.0		8(1,8)−7(0,7)EA		
162529.6		8(1,8)−7(0,7)EE		
162530.3		8(1,8)−7(0,7)AA		
~162558.4	$^{33}SO_2$	5(2,4)−5(1,5) F=11/2→11/2	0.04	1 MHz
~162558.4		F=9/2→11/2		
~162558.5		F=13/2→11/2		
~162564.5	$^{33}SO_2$	5(2,4)−5(1,5) F=9/2→13/2	0.08	1 MHz
~162564.7		F=13/2→13/2		

Table 6.2 continued

Frequency (MHz)	Species	Transition	Peak T_A^* (K)	Filter Bank
~162566.3 ~162566.4	$^{33}SO_2$	5(2,4)−5(1,5) F=9/2→7/2 F=7/2→7/2	0.08	1 MHz
162570	U	...	0.11	1 MHz
162574.1	SO^+ $^2\Pi_{1/2}$	J=7/2 →5/2 f	~0.08	1 MHz
~162581.6	$^{28}Si^{32}S$(?)	J=9→8, v=1	~0.06	1 MHz
162589	U	...	0.07	1 MHz
162598	U	...	0.07	1 MHz
~162658.5	NS $^2\Pi_{3/2}$(?)	J=7/2→5/2 F=9/2→7/2 e,f	~0.05	1 MHz
162729	U	...	0.06	1 MHz
162762	U	...	0.05	1 MHz
162768.8	$HCOOCH_3$	14(2,13)−13(2,12)E	0.31	1 MHz
162775.9	$^{34}SO_2$	7(1,7)−6(0,6)	0.72	250 kHz
162812.8	$HCOOCH_3$	22(4,19)−22(3,20)A	0.08	250 kHz
162958.7	NH_2CHO	8(1,8)−7(1,7)	~0.07	1 MHz
163016.8	EtCN	18(1,17)−17(1,16)	0.29	1 MHz
163058.7	$HC^{13}CCN$	J=18→17	0.06	1 MHz
163074.5	$HCC^{13}CN$	J=18→17	0.09	1 MHz
~163084.1	$HCOOCH_3$(?)	20(3,18)−20(1,19)A	~0.08	1 MHz
163119.4	SO_2	18(2,16)−17(3,15)	1.10	1 MHz
~163160.8	H_2CCO	8(1,7)−7(1,6)	0.27	1 MHz
163187	U	...	0.10	1 MHz
163298.0	VyCN	17(2,15)−16(2,14)	0.10	1 MHz
163376.6	$^{28}Si^{32}S$	J=9→8, v=0	0.11	1 MHz
163546	U	...	0.09	1 MHz
~163567.6	SO_2(?)	30(8,22)−31(7,25)	~0.06	1 MHz
163605.5	SO_2	14(1,13)−14(0,14)	1.88	1 MHz
163753.4	HCCCN	J=18→17	2.56	250 kHz
163826	U	...	0.28	250 kHz
163829.6	$HCOOCH_3$	14(1,13)−13(1,12)E	0.38	250 kHz
163835.4	$HCOOCH_3$	14(1,13)−13(1,12)A	0.21	250 kHz
163872.9	$^{13}CH_3OH$	7(0)−6(1)E	0.16	1 MHz
163925.8 163927.2	$HCOOCH_3$	15(0,15)−14(1,14)E 15(0,15)−14(1,14)A	0.17	1 MHz
~163953.0	HNCS(?)	14(1,14)−13(1,13)	0.25	1 MHz

Table 6.2 continued

Frequency (MHz)	Species	Transition	Peak T_A^* (K)	Filter Bank
163960.4 163961.7	$HCOOCH_3$	15(1,15)−14(1,14)E 15(1,15)−14(1,14)A	0.55	1 MHz
163987.4 163988.8	$HCOOCH_3$	15(0,15)−14(0,14)E 15(0,15)−14(0,14)A	0.58	1 MHz
164022.0 164023.3	$HCOOCH_3$	15(1,15)−14(0,14)E 15(1,15)−14(0,14)A	0.20	1 MHz
164035	U	...	0.09	1 MHz
164155.6	HCCCN	J=18→17 v7:1e	0.20	1 MHz
164206.0	$HCOOCH_3$	13(4,9)−12(4,8)E	0.30	1 MHz
164223.8	$HCOOCH_3$	13(4,9)−12(4,8)A	0.31	1 MHz
~164390.7	HCCCN	J=18→17 v7:1f	0.20	1 MHz
~164394.6	EtCN(?)	25(4,22)−25(3,23)	0.20	1 MHz
164488	U	...	0.12	1 MHz
164549	U	...	0.09	1 MHz
164584.7	EtCN	19(0,19)−18(0,18)	0.33	1 MHz
164619.5 164620.5	$^{33}SO_2$	14(1,13)−14(0,14) F=29/2→29/2 F=27/2→27/2	0.11	1 MHz
164629.5 164630.5	$^{33}SO_2$	14(1,13)−14(0,14) F=31/2→31/2 F=25/2→25/2	0.09	1 MHz
164668.0	EtCN	18(2,16)−17(2,15)	0.27	1 MHz
164949	U	...	0.15	1 MHz
164955.7	$HCOOCH_3$	13(2,11)−12(2,10)E	0.41	1 MHz
164968.6	$HCOOCH_3$	13(2,11)−12(2,10)A	0.42	1 MHz
165050.2	MeOH	1(1)−1(0)E	1.98	1 MHz
165061.1	MeOH	2(1)−2(0)E	2.12	1 MHz
165075	U	...	0.19	1 MHz
165085	U	...	0.30	1 MHz
165099.3	MeOH	3(1)−3(0)E	2.10	1 MHz
165123.7	SO_2	9(4,6)−10(3,7)	0.43	1 MHz
165144.7	SO_2	5(2,4)−5(1,5)	1.58	1 MHz
165190.5	MeOH	4(1)−4(0)E	2.11	1 MHz
165225.4	SO_2	7(1,7)−6(0,6)	2.75	250 kHz
165369.4	MeOH	5(1)−5(0)E	2.08	1 MHz
165454.4	MeCN	9(6)−8(6)	0.39	1 MHz
165489.4	MeCN	9(5)−8(5)	0.40	1 MHz

Table 6.2 continued

Frequency (MHz)	Species	Transition	Peak T_A^* (K)	Filter Bank
165517.9	MeCN	9(4)−8(4)	0.34	1 MHz
165540.3	MeCN	9(3)−8(3)	0.84	1 MHz
165556.2	MeCN	9(2)−8(2)	0.78	1 MHz
165565.7	MeCN	9(1)−8(1)	1.10	1 MHz
165569.0	MeCN	9(0)−8(0)	1.24	1 MHz
165609.4	$^{13}CH_3OH$	3(1)−3(0)E	0.12	1 MHz
165620.7	$^{34}SO_2$	14(1,13)−14(0,14)	0.13	1 MHz
165678.8	MeOH	6(1)−6(0)E	1.29	1 MHz
165691.0	$^{13}CH_3OH$	4(1)−4(0)E	0.24	1 MHz
165719	U	...	0.12	1 MHz
165851.2	$^{13}CH_3OH$	5(1)−5(0)E	0.14	1 MHz
165909	U	...	0.08	1 MHz
166073	I	...	0.10	1 MHz
166128.8	$^{13}CH_3OH$	6(1)−6(0)E	0.16	1 MHz
166169.2	MeOH	7(1)−7(0)E	1.66	250 kHz
166773.3	MeOH	7(1)−8(2)A^+, $v_t=1$	~0.18	1 MHz
166898.6	MeOH	8(1)−8(0)E	1.00	1 MHz
167225.6	$^{13}CH_3OH$	8(1)−8(0)E	0.18	1 MHz
167741.5 / 167741.6	$(CH_3)_2O$	4(2,2)−3(1,3)AE / 4(2,2)−3(1,3)EA	0.14	1 MHz
167744.1	$(CH_3)_2O$	4(2,2)−3(1,3)EE	0.15	1 MHz
167746.6	$(CH_3)_2O$	4(2,2)−3(1,3)AA	0.08	1 MHz
167910.5	$H_2{}^{34}S$	1(1,0)−1(0,1)	0.53	1 MHz
167931.1	MeOH	9(1)−9(0)E1	1.16	1 MHz
168155.4	$^{13}CH_3OH$	9(1)−9(0)E	0.19	250 kHz
168188	I	...	0.09	1 MHz
168326	I	...	~0.1	1 MHz
168401.1	H_2COH^+(?)	1(1,0)−1(0,1)	~0.07	1 MHz
168495.1	$HCOOCH_3$	13(3,10)−12(3,9)E	0.25	1 MHz
168513.7	$HCOOCH_3$	13(3,10)−12(3,9)A	0.30	1 MHz
168577.9	MeOH	4(1)−3(2)E	0.96	1 MHz
168630.7	EtCN	19(2,18)−18(2,17)	0.24	500 kHz
168676.5	$^{13}CH_3OH$	3(2)−2(1)E	0.19	1 MHz
168762.8	H_2S	1(1,0)−1(0,1)	3.80	1 MHz
168789.9	SO_2	24(2,22)−25(1,25)	0.12	1 MHz
168815.1	$^{34}S^{16}O$	4(4)−3(3)	0.66	1 MHz

Table 6.2 continued

Frequency (MHz)	Species	Transition	Peak T_A^* (K)	Filter Bank
168826.2	SO_2(?)	...	0.17	1 MHz
168850	I	...	0.12	1 MHz
169113.8	H_2CS	5(1,5)−4(1,4)	0.90	250 kHz
169335.3	MeOH	10(1)−10(0)E	0.91	1 MHz
169421.6	$^{13}CH_3OH$	10(1)−10(0)E	0.09	1 MHz
169427.2	MeOH	7(1)−8(2)A$^-$, $v_t=1$	0.32	1 MHz
~169486.6	$^{30}Si^{16}O$	J=4→3, v=0	0.32	1 MHz
~169584.1	$HCOOCH_3$(?)	20(7,13)−20(6,14)E	~0.06	1 MHz
~169584.4	EtCN(?)	26(2,24)−25(3,23)	~0.06	1 MHz
~169719.6	$O^{13}CS$(?)	J=14→13	~0.06	1 MHz
169740.6	$(CH_3)_2O$	16(2,15)−16(3,14)AE 16(2,15)−16(3,14)EA	0.12	1 MHz
169743.4	$(CH_3)_2O$	16(2,15)−16(3,14)EE	0.21	1 MHz
169746.1	$(CH_3)_2O$	16(2,15)−16(3,14)AA	0.11	1 MHz
169790.9	NH_2CHO	8(6,3)−7(6,2) 8(6,2)−7(6,1)	~0.06	1 MHz
169861.5 169862.5	NH_2CHO	8(4,5)−7(4,4) 8(4,4)−7(4,3)	0.09	1 MHz
169900.2	$(CH_3)_2O$	16(1,16)−16(2,15)AE 16(1,16)−16(2,15)EA	0.10	1 MHz
169903.6	$(CH_3)_2O$	16(1,16)−16(2,15)EE	0.17	1 MHz
169907.0	$(CH_3)_2O$	16(1,16)−16(2,15)AA	0.11	1 MHz
170020.9	EtCN	20(0,20)−19(1,19)	~0.05	1 MHz
~170039.1	NH_2CHO	8(3,5)−7(3,4)	~0.06	1 MHz
170060.6	MeOH	3(2)−2(1)E	3.69	250 kHz
170096.1	EtCN	29(10,19)−30(9,22) 29(10,20)−30(9,21)	~0.06	250 kHz
170150.3	VyCN	18(2,17)−17(2,16)	0.09	250 kHz
170157	U	...	0.11	250 kHz
170161.9 170168.8	$HCOOCH_3$	6(4,3)−5(3,2)E 26(4,22)−26(3,23)A	~0.06	250 kHz
~170225.2 ~170225.2 ~170227.2 ~170227.2	EtCN	19(8,11)−18(8,10) 19(8,12)−18(8,11) 19(9,10)−18(9,9) 19(9,11)−18(9,10)	0.47	1 MHz

Table 6.2 continued

Frequency (MHz)	Species	Transition	Peak T_A^* (K)	Filter Bank
~170233.2	$HCOOCH_3$	14(3,12)−13(3,11)E	~0.4	1 MHz
~170240.2	EtCN	19(7,13)−18(7,12)	0.38	1 MHz
~170240.2	EtCN	19(7,12)−18(7,11)	0.38	1 MHz
~170240.9	EtCN	19(10,9)−18(10,8)	0.38	1 MHz
~170240.9	EtCN	19(10,10)−18(10,9)	0.38	1 MHz
~170243.9	$HCOOCH_3$	14(3,12)−13(3,11)A	~0.3	1 MHz
~170267.5	OCS	J = 14 → 13	1.50	1 MHz
170284.9	$^{34}SO_2$	3(3,1)−4(2,2)	0.32	1 MHz
170293.1	EtCN	19(12,8)−18(12,7)	0.19	1 MHz
170293.1	EtCN	19(12,7)−18(12,6)	0.19	1 MHz
170317	U	...	0.13	1 MHz
170323	U	...	0.08	1 MHz
170328.7	EtCN	19(13,6)−18(13,5)	0.12	1 MHz
170328.7	EtCN	19(13,7)−18(13,6)	0.12	1 MHz
170362	U	...	0.09	1 MHz

6.5 Discussion

6.5.1 The Source

The Orion-A giant molecular cloud (OMC–1) is nearby, at a distance of only ~ 450 pc (Genzel and Stutzki 1989), and is a site of ongoing massive star formation. At the center of this complex is the Becklin-Neugebauer/Kleinmann-Low (hereafter denoted BN and KL) infrared cluster. For the molecular emission observed towards Orion(KL), there are four generally accepted kinematic components: the "extended ridge", "hot core", "plateau", and the "compact ridge". The extended ridge is made up of quiescent gas which extends NE to SW through Orion(KL) and is characterized by V_{LSR} in the range 7–10 km s^{-1} (Johansson *et al.* 1984; Blake *et al.* 1986; Irvine, Goldsmith

Hjalmarson 1987), line widths of 2–4 $km\,s^{-1}$, and gas kinetic temperatures of 50–60 K (Minh 1990; Askne *et al.* 1984). In the vicinity of the KL nebula, the extended ridge velocity makes a sudden shift from ~ 8 $km\,s^{-1}$ in the SW to ~ 10 $km\,s^{-1}$ towards the NE.

The "hot core" component is thought to be a left over molecular clump from the formation of the highly luminous infrared star, IRc 2. Most of the luminosity of the BN/KL region may arise from IRc 2, about $10^4 - 10^5$ $L_\odot$, with the rest coming from BN which is itself a BO star. It is currently thought that IRc 2 is surrounded by a torus or circumstellar disk. Radiative heating from IRc 2 is thought to induce gas kinetic temperatures ~ 300 K. The lines emanating from the hot core characteristically have V_{LSR} in the range 3–5 $km\,s^{-1}$ and FWHM of 10–15 $km\,s^{-1}$ (Blake *et al.* 1987). Many of the emission lines which arise from this small, hot and dense region belong to molecules which require high excitation rates, due to their large permanent dipole moment, such as: HNCO, CH_2CHCN, CH_3CH_2CN, CH_3CN, and vibrationally excited HC_3N (Johansson *et al.*, 1984; Goldsmith *et al.*, 1982).

The "plateau" component is most notable for the broad line widths, FWHM 20–30 $km\,s^{-1}$, and is dominated by sulfur and silicon containing species. Broad IR emission arising from highly excited molecular hydrogen as well as from high levels of CO ($J \sim 30$) have been detected over an extended region ($> 1'$) approximately centered on BN/KL and aligned SE–NW. This emission has been interpreted as evidence of shock heating of the surrounding cloud (Beckwith *et al.*, 1978; Storey *et al.*, 1981; Beck *et al.*, 1982). The H_2 emission shows pronounced velocity structure over the cloud (Scoville *et al.*, 1982), which is also seen in the similarly extended HCO^+ ($J = 1 \rightarrow 0$) moderate velocity flow (Olofsson *et al.*, 1982). The spatially confined SiO ($\nu = 0$, $J = 2 \rightarrow 1$) as well as CO ($J = 1 \rightarrow 0$ and $J = 3 \rightarrow 2$) line profiles show definite position displacements between the blue- and read-shifted

wings, which is approximately aligned with the H_2 and HCO^+ flows (Olofsson *et al.*, 1981, 1982; Erickson *et al.*, 1982). In contrast, the SO $(2_2 - 1_1)$ emission line profiles observed towards the central part of this region exhibit small scale structures in an orthogonal direction (SW–NE; Plambeck *et al.*, 1982), which suggests a disk-confined bipolar outflow (Johansson *et al.*, 1984). Shocks, driven by outflows from IRc 2, appear to dominate the plateau chemistry ($T_K \sim 100-200$ K). Like the extended ridge, the plateau lines have a V_{LSR} in the range 7–10 km s^{-1} (Blake *et al.* 1987).

The "compact ridge" component is the position where most of the large, oxygen-rich molecules found in Orion have their peak intensity (Blake *et al.*, 1987). The compact ridge emission is thought to arise from the interaction of the plateau gas when it encounters the 8 km s^{-1} quiescent ridge material, and is characterized by $V_{LSR} \sim 7 - 8$ km s^{-1}, FWHM $\sim 3 - 5$ km s^{-1} (Blake *et al.*, 1987). Studies of CH_3OH emission from the compact ridge by Johansson *et al.* (1984) and Blake *et al.* (1987) indicates that though the line parameters are fairly uniform, there does appear to be a line width dependence as a function of the transition's energy above the ground state.

Recent VLA observations carried out by Menten and Reid (1995) call into question the role of IRc2 in the morphology and chemistry of Orion(KL). In fact, Menten and Reid suggest that IRc2 may not even be a self luminous body. In the model for the KL region outlined by Menten an Reid, the infrared source n (Lonsdale *et al.* 1982; Wynn-Williams *et al.* 1984) is at the center of the dense molecular "hot core" and may be a significant source of power in the KL region. Since this source is not prominent at wavelengths longer than 3.8 μm, it had not been included in most discussions of the KL region's energetics.

6.5.2 The Overall Survey

In the 10 GHz region surveyed here, 16 known interstellar species were observed, along with their isotopic variants. These include the sulfur-bearing molecules NS, SO, SO_2, OCS, H_2S, and H_2CS, silicon compounds SiS and SiO, and the large organics MeCN, MeOH, VyCN, EtCN, $HCOOCH_3$, and $(CH_3)_2O$. The molecules which appear to dominate the survey by numbers of spectral features are ethyl cyanide and methyl formate. Next would come methanol, sulfur dioxide, and methyl cyanide, respectively. These findings are consistent with those of ZM93. The strongest transitions, in terms of peak antenna temperature, arise from methanol as was also the case in ZM93.

Some spectral features coincided with molecules having only one or two transitions in the frequency range surveyed, or with molecules for which there were *missing* favorable transitions and, thus, could not be conclusively identified. Some of these tentative identifications include the molecules HC_7N, HNCS (also tentatively identified in ZM93), NH_2CHO, EtOH, and AlCl. Aluminum chloride is an example of a molecule with only one transition in the spectral range surveyed which happened to coincide with an observed spectral feature. Formamide (NH_2CHO) has four detected transitions but is missing several other favorable transitions.

In Table 6.3 we list the molecular species observed in this survey along with the emission regions in Orion–KL from which they appear to arise. Solid dots indicate that characteristic line center velocities and line widths for a given emission region was clearly evident in the line fits, while a circle indicates a tentative classification.

In the following sections we discuss each of the molecular species identified in this survey. In Tables 6.4 – 6.30 we list the favorable transitions covered by the survey, whether they were observed or not. In the case of missing transitions we have assigned an upper-limit, which is defined as three times the baseline RMS as

Table 6.3. Summary of Observed Molecules and Emission Sources

Molecule	Emission Source: Hot Core	Plateau	Extended Ridge	Compact Ridge
H_2CCO				●
HCCCN	●	●	●	
NS				●
$^{34}S^{16}O$	●	●		
SO_2	●	●	●	
OCS		●	○	○
H_2S	●	●	●	
H_2CS				●
SiO		●		
SiS		●		
MeCN	●		●	
MeOH	●			●
VyCN	●			
$HCOOCH_3$				●
EtCN	●			○
$(CH_3)_2O$				●

listed in Table 6.1 for the relevant spectrum. In the cases where spectral features were blended, thus introducing uncertainties into the results of the spectral line fits, this is indicated in the tables by reducing the number of significant figures reported for the line parameters, or by adding the prefix (∼).

6.5.3 Simple Carbon-Bearing Species

6.5.3.1 H_2CCO

The $J=8\rightarrow 7$ transitions of ketene (H_2CCO) occur in the spectral region surveyed, as shown in Table 6.4. Six transitions with $\Delta E<80$ K were detected, though five of these transitions were partially blended with other spectral features. The ketene lines have typically $T_A^* \sim 0.2$ K, $V_{LSR}=8$ km s^{-1}, and $\Delta V_{1/2}=3$ km s^{-1}.

The 8(2,6)–7(2,5) transition was not detected even though it shares the same energy above the ground state and statistical weight as the tentatively detected 8(2,7)–8(2,6) transition. The 8(2,7)–8(2,6) transition is itself blended with the lower energy 8(0,8)–7(0,7) transition and it may be that what appears to be two blended features in the spectra may actually be the lower energy 8(0,8)–7(0,7) transition. Since most of our features were blended, thus making the line widths and line center velocities uncertain, its difficult to discern whether this emission belongs to the extended or compact ridge. Johansson *et al.* (1984) assigned H_2CCO to the compact ridge. Furthermore, Turner (1991) and Blake *et al.* (1987) applied LTE "rotation diagram" to ketene transitions observed towards Orion–KL, and estimated $T_{Rot} \sim 84 - 110$ K which is consistent with $T_{kin} \sim 95$ K for the compact ridge (Mangum *et al.* 1990).

6.5.3.2 H_2COH^+

The millimeter-wave spectrum of protonated formaldehyde, H_2COH^+ has recently been measured in the laboratory (Chomiak, Taleb-Bendiab and Amano 1994). Two b–type transitions were present in the survey region (*see* Table 6.5). It is thought that the b–dipole moment is slightly larger than the a–dipole moment, though this has yet to be confirmed. H_2COH^+ is of interest to astro-chemists since it is thought to be a precursor of H_2CO. Ohishi *et al.* are conducting a survey of protonated formaldehyde in GMC's and quiescent dark clouds (1995 *private communications*). A weak feature observed in this survey, which is coincident with the favorable 1(1,0)–1(0,1) transition, has been tentatively identified as arising from H_2COH^+. The detection of an emission feature towards Orion(KL) coincident with the H_2COH^+ 1(1,0)–1(0,1) transition has recently been confirmed by Ziurys *et al.* using the NRAO 12-m radio telescope (1995, private communications). The higher energy level 14(4,11)–15(3,12) transition was not

Table 6.4. Transitions of H_2CCO

Transition $J(K_{-1},K_{+1})$	Freq. (MHz)	T_A^* (K)	V_{LSR} ($km\,s^{-1}$)	$\Delta V_{1/2}$ ($km\,s^{-1}$)	ΔE (cm^{-1})	Comments
8(1,8)−7(1,7)	160142.2	∼0.2	∼8	∼3	27.8	Blend with $^{34}SO_2$.
8(7,1)−7(7,0) 8(7,2)−7(7,1)	161267.9	...	...	...	464.3	Obscured by EtCN & $HCOOCH_3$
8(6,2)−7(6,1) 8(6,3)−7(6,2)	161379.7	...	...	...	346.1	Obscured by EtCN.
8(5,3)−7(5,2) 8(5,4)−7(5,3)	161471.6	∼0.07	∼8	∼3.6	246.1	Tentative, Blend with EtCN.
8(4,4)−7(4,3) 8(4,5)−7(4,4)	161545.1	...	...	...	164.3	Obscured by U-line.
8(3,6)−7(3,5) 8(3,5)−7(3,4)	161602.3	0.12	8.5	3.72	100.7	...
8(2,7)−7(2,6)	161631.6	∼0.2	∼8	∼2.3	55.2	Blend with H_2CCO.
8(0,8)−7(0,7)	161634.0	∼0.2	∼8	∼4.3	18.9	Blend with H_2CCO.
8(2,6)−7(2,5)	161664.4	<0.07	...	...	55.2	...
8(1,7)−7(1,6)	163160.8	0.27	∼8	∼2.9	28.1	Blend with U-line.

detected in our survey. Further observations of other protonated formaldehyde transitions will be necessary to confirm the presence of this molecule in Orion.

6.5.4 Carbon-Chain Molecules

6.5.4.1 HCCCN

The nitrogen bearing molecule cyanoacetylene (HCCCN) was clearly detected in this survey by its $J = 18 \rightarrow 17$ transition (*see* Table 6.6). The line was captured in the 250 kHz resolution spectrometer, which shows an asymmetric line profile with hot core, ridge, and plateau velocity components. The multiple velocity components of the HCCCN $J = 18 \rightarrow 17$ transition observed in this survey are consistent with the observations of the HCCCN $J = 17 \rightarrow 16$ transition reported by

Table 6.5. Transition of H_2COH^+ [a]

Transition $J(K_{-1},K_{+1})$	Freq. (MHz)	T_A^* (K)	V_{LSR} ($km\,s^{-1}$)	$\Delta V_{1/2}$ ($km\,s^{-1}$)	ΔE (cm^{-1})	Comments
$1(1,0)-1(0,1)$?	168401.1	~ 0.07	6.4	4.2	2.1	Tentative.
$15(3,12)-14(4,11)$	168661.2	< 0.13	...	...	305.7	...

(a) Frequency from Amano, private communication (1995).

ZM93. The main isotope line profile, along with the three-component gaussian fit, is displayed in Figure 6.3.

The $J=18\rightarrow 17$ transition in the $\nu 7$ vibrational mode of HCCCN was also detected in this survey. The $\nu 7$ mode was first observed by Goldsmith, Krotkov, and Snell (1985) and has been observed towards Orion by Jewell *et al.* (1989), Turner (1991), as well as others. The vibrational mode is split by l-type doubling. In this survey, the 1e–1e doublet member was detected with $V_{LSR}=4$ km s^{-1} and $\Delta V_{1/2}=14$ km s^{-1}. The line center velocity is slightly lower than the $5-6$ km s^{-1} found by ZM93; however, the line shape is not particularly Gaussian, which could account for the apparent lower velocity measured in the present work. The broad line width, though, is consistent with the findings of ZM93, who found the $J=17\rightarrow 16$ 1e–1e line to have $\Delta V_{1/2}=19$ km s^{-1}, which is twice the width they observed for the 1f–1f transition. Unfortunately, in our survey the 1f–1f line is obscured by a transition of $HCOOCH_3$, so we are unable to further investigate the anomalous observations reported by ZM93. No transitions from other vibrational modes were detected in this survey.

Two isotopic variants, $HC^{13}CCN$ and $HCC^{13}CN$, were also detected, and the results of the gaussian fits to the line profiles are reported in Table 6.6.

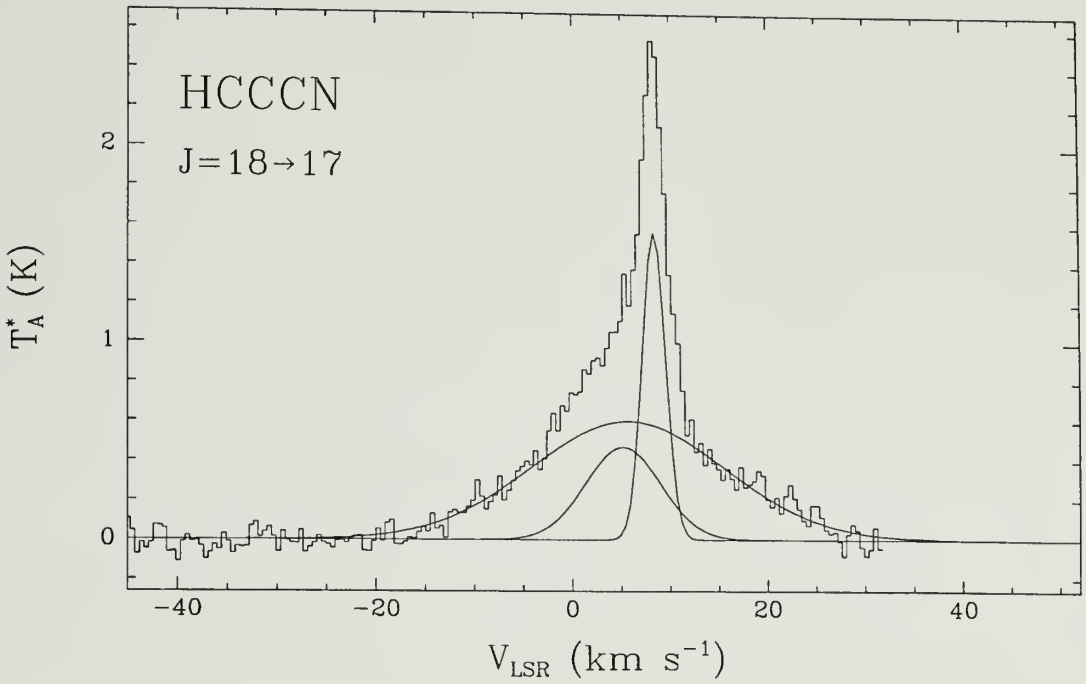

Figure 6.3. Spectrum of the HCCCN main isotope $J = 18 \rightarrow 17$ transition, which shows hot core, ridge, and plateau velocity components (solid curves). The spectral resolution is 250 kHz (0.45 km s^{-1}).

Table 6.6. Transitions of HCCCN

Transition (J)	Freq. (MHz)	T_A^* (K)	V_{LSR} (kms^{-1})	$\Delta V_{1/2}$ (kms^{-1})	ΔE (cm^{-1})	Comments
HCCCN						
18→17	163753.4	1.57	8.4	2.79	...	250 kHz Res.
		0.60	5.7	23.38		
		0.47	5.2	9.02		
18→17 v6:1e	164022.4	...	...	...	...	Obscured by $HCOOCH_3$.
18→17 v7:1e	164155.6	0.20	4.0	14.43	...	...
18→17 v7:1f	164390.7	0.20	5.7	9.24	...	Blend with EtCN.
18→17 v6:1f	164450.6	<0.11	...	...	...	...
$HC^{13}CCN$						
18→17	163058.7	0.06	7.6	7.01	...	...
$HCC^{13}CN$						
18→17	163074.5	0.09	8.8	4.29	...	...
$HCCCN^{15}$						
19→18	167882.6	<0.11	...	...	...	...

6.5.4.2 HC_5N and HC_7N

There were three cyanodiacetylene (HC_5N) transitions present in the survey region and they are listed in Table 6.7. The carbon chain HC_5N has been detected towards Orion by Ziurys (1988) and Turner (1991); however, transitions associated with HC_5N were not detected in this work.

There were 10 cyanotriacetylene (HC_7N) transitions present in the survey region (*see* Table 6.7). These transitions all lie $\Delta E > 540$ K above the ground state; the three lowest energy transitions are listed in Table 6.7. There is a weak ($T_A^* \sim 50$ mK) spectral feature which is coincident with the HC_7N J = 142→141 transition; the lowest energy level transition covered by this survey. In the absence of any HC_5N detections, however, we believe that this feature is most likely a

Table 6.7. Transitions of HC_5N and HC_7N

Transition J	Freq. (MHz)	T_A^* (K)	V_{LSR} (kms^{-1})	$\Delta V_{1/2}$ (kms^{-1})	ΔE (cm^{-1})	Comments
HC_5N						
61→60	162395.3	<0.07	...	...	162.5	...
62→61	165056.6	<0.15	...	...	167.9	...
63→62	167717.8	<0.11	...	...	173.4	...
HC_7N						
142→141	160132.5	~0.05	5.9	5.30	376.6	Tentative identification probable U-line
143→142	161259.6	...	...	...	382.0	Obscured by EtOH
144→143	162386.7	<0.06	...	...	387.3	...

U-line. Given that the rotational transitions of these molecules at 2 mm involve levels J > 60 in the case of HC_5N and J > 140 for HC_7N, it is not surprising that these species are difficult to detect since the transitions are high in energy and their populations will be spread out over many closely spaced transitions.

6.5.5 Nitrogen-Bearing Molecules

6.5.5.1 NS

Nitrogen sulfide (NS) was observed by the ten hyperfine components of the $^2\Pi_{1/2}$, J = 9/2 → 7/2 parity-e,f transitions (see Table 6.8). For most of the molecules discussed in this survey, each spectral feature was fit with gaussians independently of fits to other features belonging to the same species. For NS, we used the results of laboratory spectroscopy (Lee, Ozeki, and Saito 1995) to create a function which modeled the NS hyperfine structure for a given rotational level and parity (*see* Equation 6.1). In this model, the inter-gaussian spacing was held fixed at the laboratory values, and the fit parameters were the peak T_A^* for each

component, and a shared $\Delta V_{1/2}$ and V_{LSR}. For a more detailed discussion of the NS emission model, see Chapter 4.

The NS $J=9/2\rightarrow 7/2$ transition hyperfine components are severely blended with other spectral features such as EtCN and VyCN, which made measuring the line parameters difficult. We attempted to subtract from the spectra these EtCN and VyCN features. Unfortunately, no good method was found to do this, and, as a result, the values quoted in Table 6.8 for the NS $^2\Pi_{1/2}$ ladder transitions are highly suspect. The greatest uncertainties were in determining the line widths. To avoid this problem we chose to fix $\Delta V_{1/2}=5.7$ km s^{-1}, which is the line width of the NS $J=5/2\rightarrow 3/2$ transition hyperfine components observed towards OMC–1 (*see* Chapter 4). Using these assumptions, we find that the NS V_{LSR} is typically 7 km s^{-1}. By comparing the NS integrated intensity for several rotational transitions towards OMC–1, McGonagle and Irvine (1995) found that NS emission arises from the spatially confined, compact ridge source.

In addition to observing lines from the $^2\Pi_{1/2}$ ladder, we have tentatively detected the first NS transition from the higher energy ($\Delta E\sim 322$ K) $^2\Pi_{3/2}$ ladder (see Table 6.8).

Table 6.8. Transitions of NS [a]

Transition (F parity)	Freq. (MHz)	T_A^* (K)	V_{LSR} ($km\,s^{-1}$)	$\Delta V_{1/2}$ ($km\,s^{-1}$)	ΔE (cm^{-1})	Comments
$J = 7/2 \rightarrow 5/2,\ ^2\Pi_{1/2}$						
$F = 9/2 \rightarrow 7/2$ e	161297.2	0.16	7.3	5.7	6.3	...
$F = 7/2 \rightarrow 5/2$ e	161298.4	0.10	7.3	5.7	6.3	...
$F = 5/2 \rightarrow 3/2$ e	161301.7	$\sim$0.14	7.3	5.7	6.3	Blend with EtCN.
$F = 5/2 \rightarrow 5/2$ e	161330.1	$\sim$0.10	7.3	5.7	6.3	...
$F = 7/2 \rightarrow 7/2$ e	161335.8	$\sim$0.10	7.3	5.7	6.3	...
$F = 7/2 \rightarrow 7/2$ f	161636.5	$\sim$0.08	7.0	5.7	6.3	Blend with H_2CCO.
$F = 5/2 \rightarrow 5/2$ f	161657.8	0.06	7.0	5.7	6.3	...
$F = 9/2 \rightarrow 7/2$ f	161697.3	0.24	7.0	5.7	6.3	...
$F = 7/2 \rightarrow 5/2$ f	161703.4	0.19	7.0	5.7	6.3	...
$F = 5/2 \rightarrow 3/2$ f	161704.0	$\sim$0.12	7.0	5.7	6.3	Blend with VyCN.
$J = 7/2 \rightarrow 5/2,\ ^2\Pi_{3/2}$						
$F = 9/2 \rightarrow 7/2$ e,f	162658.5	$\sim$0.05	5.3	5.3	331	Tentative.
$F = 7/2 \rightarrow 5/2$ e,f	162668.2	$<$0.06	...	...	331	...
$F = 5/2 \rightarrow 3/2$ e,f	162674.2	$<$0.06	...	...	331	...

(a) Frequencies are quoted from Lee, Ozeki, and Saito (1995). See text for details of Gaussian fits to the NS spectral features.

Table 6.9. Transitions of HNCS

Transition $J(K_{-1},K_{+1})$	Freq. (MHz)	T_A^* (K)	V_{LSR} ($km\,s^{-1}$)	$\Delta V_{1/2}$ ($km\,s^{-1}$)	ΔE (cm^{-1})	Comments
$14(1,14)-13(1,13)$	163953.0	0.25	12	12.9	...	Tentative identification; possible U-line
$14(0,14)-13(0,13)$	164193.5	<0.11	...	...	...	...
$14(4,10)-13(4,9)$	164250.7	<0.11	...	...	...	...
$14(3,11)-13(3,10)$	164272.8	<0.11	...	...	...	...
$14(1,13)-13(1,12)$	164482.6	<0.11	...	...	...	Near U164488

6.5.5.2 HNCS

Five transitions of isothiocyanic acid (HNCS) were present in the survey region, as shown in Table 6.9. A strong feature was detected at the frequency of the $14(1,14)-13(1,13)$ transition with $T_A^* = 0.25$ K. The calculated line velocity of $V_{LSR} = 12\ km\,s^{-1}$ is somewhat high for OMC–1; however, the line is partially blended with $HCOOCH_3$, which may have effected the velocity measurement. More troubling is the fact that no other HNCS transitions were observed, which leads us to believe that this feature is probably a U-line. The presence or absence of HNCS in Orion has been difficult to establish. Johannson *et al.* (1984), Sutton *et al.* (1985), and Jewell *et al.* (1989) did not detect HNCS in their respective spectral surveys of Orion–KL. Turner (1991) reported detecting 5 HNCS transitions, though only one of these putative detections was thought to be "reliable". ZM93 covered 6 transitions of HNCS in their survey, but only tentatively identified one weak spectral feature as arising from the $13(1,13)-12(1,12)$ transition of HNCS. As ZM93 concluded, the presence of HNCS in Orion is still uncertain.

6.5.5.3 NH_2CHO

There are 20 formamide (NH_2CHO) transitions with $\Delta E < 165$ K above the ground state present in the spectral region surveyed, and these are presented in Table 6.10. Four spectral features have been tentatively identified as arising from seven NH_2CHO transitions with energy levels ranging $\Delta E = 30 - 135$ K. Unfortunately, all these spectral features have amplitudes only three times the spectral baseline RMS, and several probable transitions with $\Delta E < 135$ K were not detected; hence, we are only tentatively identifying these spectral features as belonging to formamide. The spectral features have typically $V_{LSR} = 7$ km s^{-1} and $\Delta V_{1/2} = 5$ km s^{-1}, which would suggest that NH_2CHO resides in the compact ridge component. Formamide was first observed towards Orion–KL by Turner (1991) who observed 16, 3mm band transitions. Since the 72–90 GHz Onsala survey (Johansson *et al.* 1984) did not detect NH_2CHO, Turner suggests that formamide occurs in the extended ridge component and has a relatively low surface brightness. NH_2CHO was not detected by ZM93 in their 150–160 GHz spectral survey of Orion–KL.

Table 6.10. Transitions of NH_2CHO

Transition $J(K_{-1},K_{+1})$	Freq. (MHz)	T_A^* (K)	V_{LSR} ($km\,s^{-1}$)	$\Delta V_{1/2}$ ($km\,s^{-1}$)	ΔE (cm^{-1})	Comments
$15(2,13)-15(1,14)$	159739.1	<0.06	...	...	89.4	...
$9(2,7)-9(2,8)$	161899.8	<0.07	...	...	35.0	...
$6(3,3)-7(2,6)$	162825.3	<0.06	...	...	28.1	...
$8(1,8)-7(1,7)$	162958.7	~0.07	7.0	4.3	21.1	Near H48γ
$16(2,14)-16(1,15)$	163891.9	<0.08	...	...	100.9	...
$3(2,1)-4(0,4)$	164177.2	<0.11	...	...	7.1	...
$8(2,6)-8(1,7)$	165176.8	<0.15	...	...	28.4	...
$12(3,9)-13(1,12)$	166828.9	<0.11	...	...	68.4	...
$8(0,8)-7(0,7)$	167320.7	<0.11	...	...	19.7	...
$7(2,5)-7(1,6)$	168741.4	...	...	...	22.6	Obscured by H_2S
$8(2,7)-7(2,6)$	169299.2	<0.17	...	...	28.1	...
$17(2,15)-17(1,16)$	169683.0	<0.06	...	...	113.1	...
$8(6,3)-7(6,2)$ $8(6,2)-7(6,1)$	169790.9	~0.06	7.1	4.4	94.3	...
$8(5,4)-7(5,3)$ $8(5,3)-7(5,2)$	169810.7	<0.06	...	...	71.6	...
$8(4,5)-7(4,4)$	169861.5	~0.08	6.3	6.8	53.0	...
$8(4,4)-7(4,3)$	169862.5					
$8(3,6)-7(3,5)$	169955.8	<0.06	...	...	38.5	...
$8(3,5)-7(3,4)$	170039.1	~0.06	6.7	9.1	38.5	Coincides with $^{13}CH_3OH$

6.5.6 Sulfur-Bearing Molecules

6.5.6.1 SO

There were no sulfur monoxide (SO) main isotope transitions present in the spectral region surveyed here. However, there were two $^{34}S^{16}O$ and one $^{32}S^{18}O$ isotope transitions (*see* Table 6.11). These transitions lie between $\Delta E = 14-43$ K above the ground state. Of the two $^{34}S^{16}O$ transitions only the $N(J) = 4(4) \rightarrow 3(3)$ transition was detected. This transition appears to be partially blended with a U-line (tentatively identified as a $\nu 2$ mode transition of SO_2). However, there do appear to be at least two components to the $^{34}S^{16}O$ emission, corresponding to a plateau and hot core component. The plateau component has a $V_{LSR} = 11$ km s^{-1} and $\Delta V_{1/2} = 24$ km s^{-1}, while the hot core has $V_{LSR} = 5$ km s^{-1} and $\Delta V_{1/2} = 12$ km s^{-1}. This spectrum is displayed in Figure 6.4. Evidence for multiple SO velocity components have been found by Blake *et al.* (1987) and Johannson *et al.* (1984). Observations of a main SO isotope transition by ZM93 found that, though the plateau component dominates the line profile, the hot core and ridge components are not negligible. Our observation of $^{34}S^{16}O$ supports these findings. This transition has previously been detected towards Orion-KL by Hollis *et al.* (1981); however, they refer to it as the $4(3)-3(3)$ transition where as we have taken our identification from the Lovas spectral line catalog (1985) which lists the transition as the $4(4)-3(3)$. The $6(7)-6(6)$ transition was not detected; however, this transition has a weak intrinsic line strength and, based on the amplitude of the observed transition, would not be detectable at the sensitivity of the spectra. The $^{32}S^{18}O$ isotopomer $5(4)-4(3)$ transition, which lies at $\Delta E = 15$ K, was not detected to a level of $T_a^* < 0.1$ K (*see* Table 6.11).

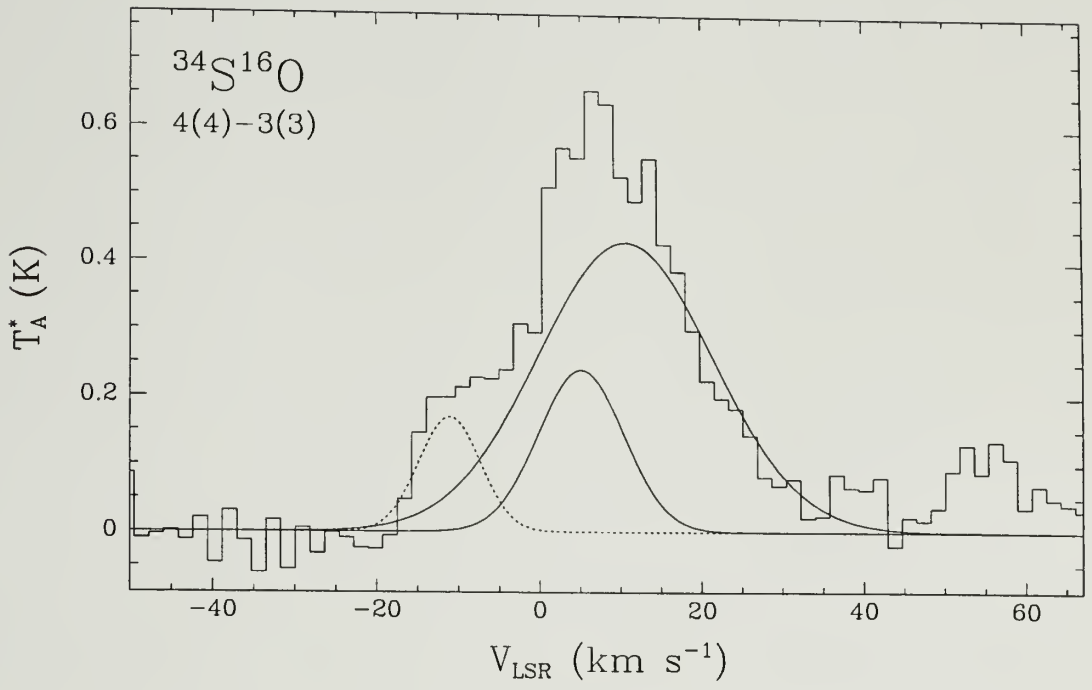

Figure 6.4. Spectrum of the $^{34}S^{16}O$ $4(4)-3(3)$ transition observed in the 2 mm survey, which indicates the presence of hot core and plateau velocity components. Gaussian fits to the spectrum are represented by the solid curves. The fit results are listed in Table 6.11. The dashed curve is a U-line tentatively identified as a $\nu 2$ mode transition of $^{32}SO_2$. Spectral resolution is 1 MHz.

Table 6.11. Transitions of SO

Transition N(J)	Freq. (MHz)	T_A^* (K)	V_{LSR} ($km\,s^{-1}$)	$\Delta V_{1/2}$ ($km\,s^{-1}$)	ΔE (cm^{-1})	Comments
$^{34}S^{16}O$						
4(4)−3(3)	168815.1	0.43	10.6	24.2	17.6	Blend with U-line
		0.24	5.1	12.4		
6(7)−6(6)	169787.5	<0.06	...	...	38.7	...
$^{32}S^{18}O$						
5(4)−4(3)	166285.3	<0.10	...	...	10.4	...

6.5.6.2 SO^+

Only in recent years has confirmation for the existence of interstellar SO^+ come from observational work by Turner (1992) and the work of R.C. Woods and E. Churchwell (University of Wisconsin) and D. McGonagle and W.M. Irvine (University of Massachusetts). Woods, Churchwell and Irvine combined their observations with data taken for the 2 mm spectral survey, and detected the two Λ–doublet members of the $J = 7/2 \rightarrow 5/2$ transition of SO^+ centered about 162.38 GHz (*see* McGonagle and Irvine, 1993; Irvine, 1995). Since then, Turner (1994) has identified SO^+ by multiple transitions towards Orion(KL) as well as other GMC's.

In the survey data, only the parity–f Λ–doublet member at 162574.068 MHz (Amano, Amano and Warner 1991) is evident. This feature has a $T_a^* \sim 0.08$ K, FWHM $\sim 4\ km\,s^{-1}$ and $V_{LSR} \sim 7\ km\,s^{-1}$. The line appears to be partially blended with a feature tentatively identified as SiS.

6.5.6.3 SO_2

There are 13 transitions with $\Delta E < 500$ cm^{-1} (720 K) of the sulfur dioxide (SO_2) main isotope present in the surveyed region, as shown in Table 6.12. Eleven transitions were detected, of which six show evidence of ridge and hot core emission, as well as plateau emission (*see* Figure 6.5). The typical fit parameters for the three emission components are: ridge $V_{LSR} = 8$ km s^{-1}, $\Delta V_{1/2} = 4$ km s^{-1}; hot core $V_{LSR} = 4$ km s^{-1}, $\Delta V_{1/2} = 7$ km s^{-1}; plateau $V_{LSR} = 10$ km s^{-1}, $\Delta V_{1/2} = 30$ km s^{-1}. These results are consistent with the findings of ZM93. The identification of SO_2 hot core emission is also supported by Johansson *et al.* (1984). Two of the eleven transitions, $5(2,4)-5(1,5)$ and $9(4,6)-10(3,7)$, are partially blended together, which makes it difficult to resolve the velocity structure of these two lines. The line shapes of three other lines could not be determined because they where too weak or partially blended with other spectral features.

The highest energy transition positively detected was the $24(2,22)-25(1,25)$ transition, which lies ~ 285 K above the ground state. The $30(8,22)-31(7,25)$ transition, which lies ~ 577 K above the ground state, was tentatively detected. A feature blended with a $^{34}S^{16}O$ line corresponds to the vibrationally excited ($\nu 2 = 1$) $5(2,4)-5(1,5)$ transition of SO_2; a transition which was detected in its ground vibrational state. Jewell *et al.* (1989) found that the conditions in Orion-KL were adequate to populate the high energy levels of SO_2 and reported the detection of two ($\nu_2 = 1$) type transitions. However, given that this transition lies ~ 760 K above the absolute ground state and considering the uncertainties introduced by its blend with another feature, we have decided to make this a tentative identification.

The two transitions of SO_2 that were not detected in this survey lay above $\Delta E < 570$ K and were coincident with spectral features arising from other species.

Table 6.12. Transitions of $^{32}SO_2$

Transition $J(K_{-1},K_{+1})$	Freq. (MHz)	T_A^* (K)	V_{LSR} (km s^{-1})	$\Delta V_{1/2}$ (km s^{-1})	ΔE (cm^{-1})	Comments
18(2,16)−18(1,17)	160343.0	1.35	10	29.8		
		0.42	8	5.5	113.3	...
		0.28	3	4.6		
4(3,1)−5(2,4)	160543.1	0.24	11	29.1		
		0.14	8	5.3	16.4	...
		0.08	3	6.3		
10(0,10)−9(1,9)	160827.8	1.80	10	31.4		
		0.79	8	4.4	29.2	...
		0.36	3	5.3		
18(2,16)−17(3,15)	163119.4	0.77	9	26.7		
		0.29	8	3.1	113.2	...
		0.25	4	6.3		
30(8,22)−31(7,25)	163567.6	∼0.06	6.4	3.4	400.8	Tentative
14(1,13)−14(0,14)	163605.5	1.28	10	28.3		
		0.58	8	4.1	65.3	...
		0.37	2	6.6		
37(5,33)−36(6,30)	163924.9	...	...	...	488.5	Obscured by $HCOOCH_3$
9(4,6)−10(3,7)	165123.7	0.43	6	25.6	50.5	Blend with SO_2
5(2,4)−5(1,5)	165144.7	0.99	9	29.3	10.9	Blend with SO_2
		0.50	7	7.5		
7(1,7)−6(0,6)	165225.4	1.21	11.4	33.9		
		0.78	7.8	1.8	13.3	250 kHz Res
		0.76	6.5	11.8		
24(2,22)−25(1,25)	168789.9	0.12	9.9	9.50	197.8	...
5(2,4)−5(1,5)	168826.2	0.17	8.8	8.88	529.9	$V_2=1$ Unlikely transition, blend with $^{34}S^{16}O$, probably U-line.
34(3,31)−35(2,34)	170293.5	...	...	...	398.8	Obscured by EtCN

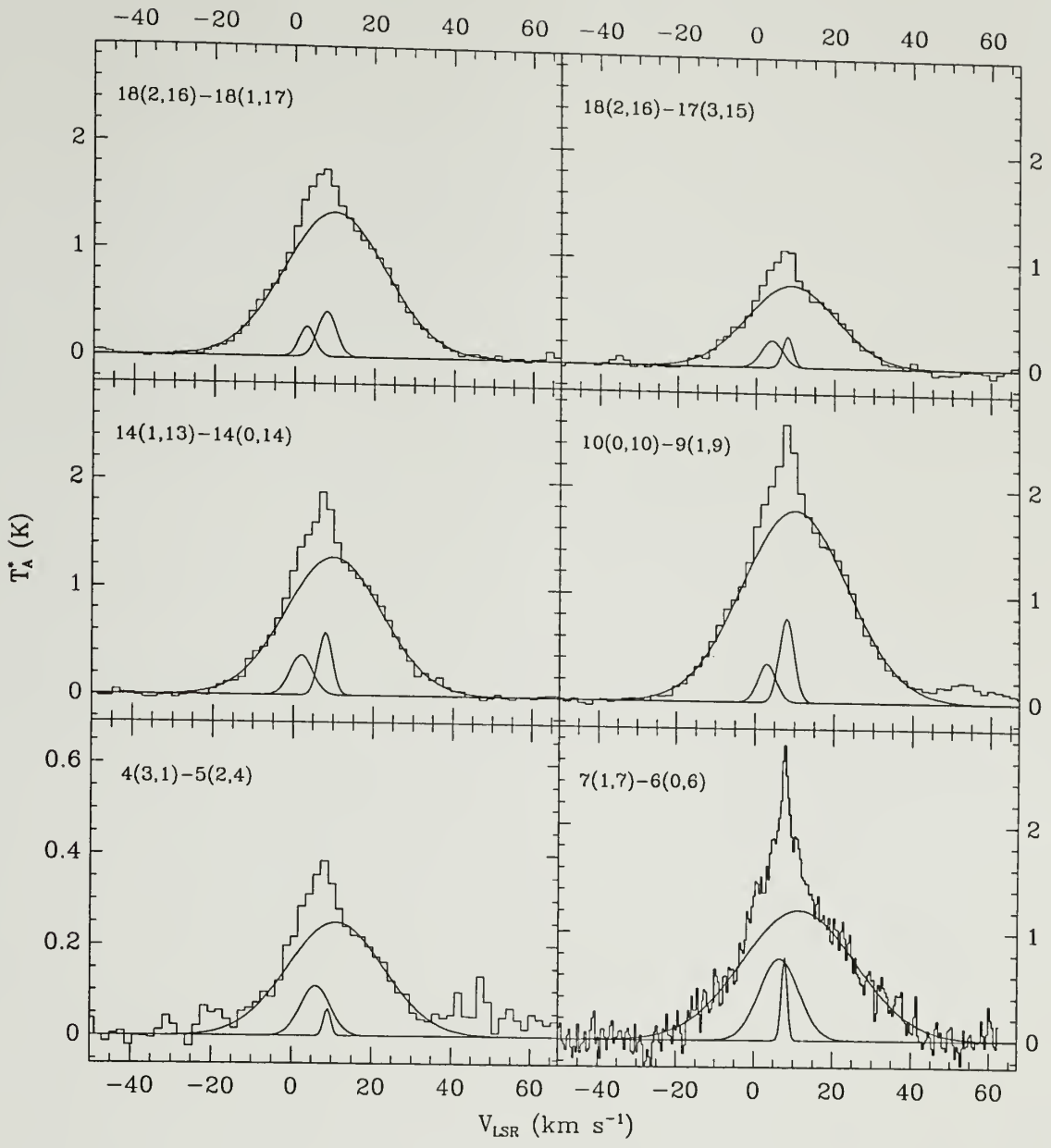

Figure 6.5. Spectra of selected SO_2 transitions observed in the 2 mm survey, which indicate the presence of hot core, ridge, and plateau velocity components. The spectra are ordered by decreasing energy above the ground state (left to right, top to bottom: 163K, 163K, 94K, 42K, 23K, 19K). The ridge component has typically $V_{LSR}=8$ km s^{-1} and $\Delta V_{1/2}=4$ km s^{-1}, the hot core component has $V_{LSR}=4$ km s^{-1} and $\Delta V_{1/2}=7$ km s^{-1}, while the plateau component parameters are typically $V_{LSR}=10$ km s^{-1} and $\Delta V_{1/2}=30$ km s^{-1}. Resolution 1 MHz except lower right spectrum, which is 250 kHz.

$^{33}SO_2$: There are eleven rotational transitions of $^{33}SO_2$ with $\Delta E < 500$ cm^{-1} in the region surveyed (*see* Table 6.13). Transitions with $\Delta E < 150$ K were readily detected. The highest energy transition detected was $18(2,16)-18(1,17)$, which lies ~ 163 K above the ground state. The $^{33}SO_2$ transitions have typically $V_{LSR} = 8.4$ km s^{-1} and $\Delta V_{1/2} = 3.8$ km s^{-1}, which suggest that the emission originates from the ridge component. The ^{33}S atom has non-zero nuclear spin angular momentum, which couples with the molecules rotational angular momentum resulting in the splitting of the rotational levels into hyperfine components. The hyperfine components' separation is often less than the spectral resolution of this survey. However, clusters of hyperfine components could be resolved for the $5(2,4)-5(1,5)$ and $14(1,13)-14(0,14)$ transitions.

$^{34}SO_2$: Seven transitions of $^{34}SO_2$ with $\Delta E < 500$ cm^{-1} are present in the surveyed region (*see* Table 6.14) of which six were detected. As was the case in ZM93 and for $^{33}SO_2$ in this survey, transitions with $\Delta E < 150$ K were readily detected. Most of the lines are either blended or obscured by other spectral features so it is difficult to asses if there are multiple velocity components comprising the $^{34}SO_2$ line profile. However, one particularly strong line, $10(0,10)-9(1,9)$, appears to be assymetric and is consistent with a superposition of hot core and plateau emission (*see* Figure 6.6). The $^{34}SO_2$ emission has typically $V_{LSR} = 5 - 10$ km s^{-1} and $\Delta V_{1/2} = 6 - 30$ km s^{-1}.

Table 6.13. Transitions of $^{33}SO_2$

Transition $J(K_{-1},K_{+1})$	Freq. (MHz)	T_A^* (K)	V_{LSR} (kms^{-1})	$\Delta V_{1/2}$ (kms^{-1})	ΔE (cm^{-1})	Comments
$18(2,16)-18(1,17)$	160508.7	0.15	9.2	6.03	113.2	...
$33(4,30)-32(5,27)$	161064.2	<0.06	...	...	380.8	...
$10(0,10)-9(1,9)$	161452.7	~0.14	10	21.9	29.1	Blend with VyCN and $HCOOCH_3$
$5(2,4)-5(1,5)$						
$F=11/2\rightarrow11/2$	162558.4	0.04	10.2	~4	10.8	...
$F=9/2\rightarrow11/2$	162558.4					
$F=13/2\rightarrow11/2$	162558.5					
$F=11/2\rightarrow9/2$	162560.1	<0.06	...	...	10.8	...
$F=9/2\rightarrow9/2$	162560.1					
$F=7/2\rightarrow9/2$	162560.3					
$F=9/2\rightarrow13/2$	162564.5	0.08	9.2	~4	10.8	...
$F=13/2\rightarrow13/2$	162564.7					
$F=9/2\rightarrow7/2$	162566.3	0.08	9.4	~4	10.8	...
$F=7/2\rightarrow7/2$	162566.4					
$14(5,9)-15(4,12)$	162743.6	<0.06	...	...	103.5	...
$7(1,7)-6(0,6)$	163964.9	...	...	...	13.3	Obscured by HNCS and $HCOOCH_3$
$14(1,13)-14(0,14)$						
$F=29/2\rightarrow29/2$	164619.5	0.11	6	3	65.2	...
$F=27/2\rightarrow27/2$	164620.5					
$F=31/2\rightarrow31/2$	164629.5	0.09	5	3	65.2	...
$F=25/2\rightarrow25/2$	164630.5					
$19(6,14)-20(5,15)$	165263.3	<0.15	...	...	176.1	...
$24(7,17)-25(6,20)$	167949.9	<0.08	...	...	268.0	...
$18(2,16)-17(3,15)$	169162.5	<0.17	...	...	112.9	...
$29(8,22)-30(7,23)$	170171.5	...	...	...	379.2	Obscured by $HCOOCH_3$

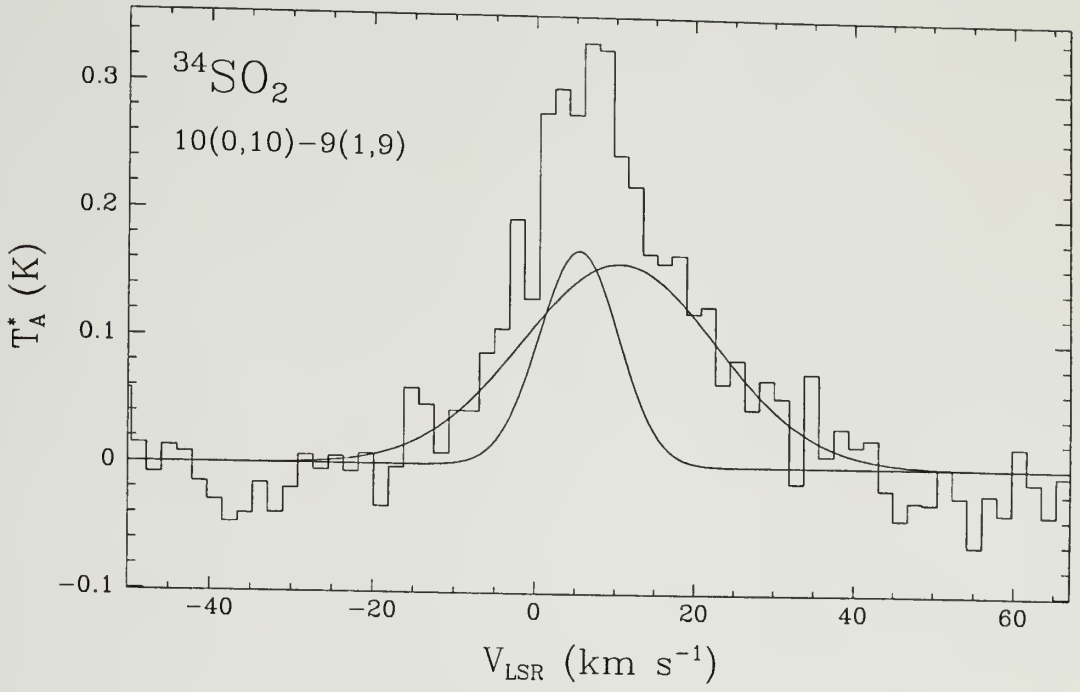

Figure 6.6. Spectra of the $^{34}SO_2$ $10(0,10)-9(1,9)$ transition observed in the 2 mm survey, which indicates the presence of hot core and plateau velocity components. Gaussian fits to the spectrum are represented by the solid curves. The fit results are listed in Table 6.14. Spectral resolution is 1 MHz.

Table 6.14. Transitions of $^{34}SO_2$

Transition $J(K_{-1},K_{+1})$	Freq. (MHz)	T_A^* (K)	V_{LSR} ($km\,s^{-1}$)	$\Delta V_{1/2}$ ($km\,s^{-1}$)	ΔE (cm^{-1})	Comments
5(2,4)−5(1,5)	160143.6	0.11	11	13	10.8	Blend with H_2CCO
		0.09	4	7		
18(2,16)−18(1,17)	160802.6	0.16	∼5	∼12	113.0	Blend with $H^{12}COOH$ and SO_2
10(0,10)−9(1,9)	162020.4	0.16	10.5	28.9	29.0	...
		0.17	5.4	11.7		
7(1,7)−6(0,6)	162775.9	0.44	9	3	13.3	Blend with $HCOOCH_3$ 250 kHz Res.
		0.24	9	21		
33(4,30)−32(5,27)	164323.4	<0.1	...	...	380.0	...
14(1,13)−14(0,14)	165620.7	0.07	16.8	6.00	65.0	...
		0.12	4.7	9.34		
3(3,1)−4(2,2)	170284.9	0.32	8.9	16.02	13.0	Blend with OCS and U-line

6.5.6.4 OCS

There are three $J=14\rightarrow13$ transitions of carbonyl sulfide (OCS), each associated with a different isotopic variant, present in the spectral region surveyed (see Table 6.15). The main isotope line profile appears to be comprised of a narrow ($\Delta V_{1/2}\sim5$ km s^{-1}) and a broad component ($\Delta V_{1/2}\sim19$ km s^{-1}). These findings are fairly consistent with the OCS $J=13\rightarrow12$ line parameters measured by ZM93. The major difference is that the $J=13\rightarrow12$ plateau component has $\Delta V_{1/2}\sim30$ km s^{-1}, which is larger than what we measure for the $J=14\rightarrow13$ transition. However, our smaller line width may be due to a partial blending of the OCS line with a spectral feature arising from $^{34}SO_2$, which makes it particularly difficult to determine their relative line widths. Blake *et al.* (1986) classified the narrow component as coming from the compact ridge with a velocity of 7.8 km s^{-1}. Unfortunately, the 1 MHz resolution of our spectrum does not allow us to

Table 6.15. Transitions of OCS

Transition J	Freq. (MHz)	T_A^* (K)	V_{LSR} ($km\,s^{-1}$)	$\Delta V_{1/2}$ ($km\,s^{-1}$)	ΔE (cm^{-1})	Comments
OCS						
$14 \rightarrow 13$	170267.5	0.91	8	5	36.9	Blend with $^{34}SO_2$.
		0.64	7	19		
$O^{13}CS$						
$14 \rightarrow 13$	169719.6	~ 0.06	7.8	2.9	36.8	Tentative.
$OC^{34}S$						
$14 \rightarrow 13$	166105.8	< 0.10	...	...	36.0	...

distinguish whether the narrow component arises from the compact or extended ridge.

$O^{13}CS$: A narrow, weak feature has been tentatively identified as the $J = 14 \rightarrow 13$ transition of $O^{13}CS$. ZM93 observed the $O^{13}CS$ $J = 13 \rightarrow 12$ transition towards OMC–1 and the two lines share similar amplitudes and V_{LSR}'s.

$OC^{34}S$: ZM93 reported detecting $OC^{34}S$ with an amplitude of $T_A^* \sim 0.2$ K, which was blended with EtCN. We did not detect the $J = 14 \rightarrow 13$ transition to an upper limit of $T_A^* < 0.1$ K.

6.5.6.5 H_2S

Two hydrogen sulfide (H_2S) transitions are present in the spectral region surveyed (*see* Table 6.16). The low energy level $1(1,0) - 1(0,1)$ transition has an asymmetric line profile which we fit with three gaussians. The spectra is displayed in Figure 6.7. The results of these fits confirm the findings of Minh *et al.* (1990) that H_2S emission arises from the plateau, hot core and ridge components of OMC–1. In this work, we found the plateau component line parameters to be

$V_{LSR} = 10$ km s^{-1} and $\Delta V_{1/2} = 32$ km s^{-1}, the hot core were $V_{LSR} = 4$ km s^{-1} and $\Delta V_{1/2} = 7$ km s^{-1}, and the ridge were $V_{LSR} = 9$ km s^{-1} and $\Delta V_{1/2} = 4$ km s^{-1}. Minh *et al.* (1990) found the abundance of H_2S to be enhanced by a factor of 1000 in the Orion hot core and plateau emission ($f(H_2S) \sim 10^{-6}$) relative to quiescent dark clouds such as TMC–1 and L134N. They suggested that the large abundance of H_2S towards the hot core may be the result of grain mantel evaporation, while the enhanced abundance in the plateau may be the result of high-temperature gas phase chemistry. The $7(3,4)-8(2,7)$ line, the other main isotope transition covered by this survey, lies $\Delta E \sim 650$ K above the ground state and was not detected.

$H_2{}^{34}S$: The $1(1,0)-1(0,1)$ transition of $H_2{}^{34}S$ was detected and it appears to have only a plateau and hot core component (*see* Figure 6.7). This result is consistent with the findings of Minh *et al.* (1990). However, the somewhat low SNR and the presence of a nearby MeOH line makes fitting the line profile difficult; thus, the presence of ridge emission can not be ruled out.

HDS : Two transitions of HDS are present in the spectral region surveyed; however, neither was detected. Both transitions have energies above the ground state of $\Delta E > 136$ K.

Table 6.16. Transitions of H_2S

Transition $J(K_{-1},K_{+1})$	Freq. (MHz)	T_A^* (K)	V_{LSR} (kms^{-1})	$\Delta V_{1/2}$ (kms^{-1})	ΔE (cm^{-1})	Comments
H_2S						
$7(3,4)-8(2,7)$	161438.4	<0.06	...	...	452.5	...
$1(1,0)-1(0,1)$	168762.8	2.18	10.1	31.86		
		1.74	8.7	4.14	13.7	...
		0.38	3.5	7.08		
$H_2{}^{34}S$						
$1(1,0)-1(0,1)$	167910.5	0.26	10.0	33.34		
		0.26	3.9	13.39	~ 14	...
HDS						
$3(3,0)-4(1,3)$	169830.4	<0.06	...	...	94.5	...
$8(5,4)-7(6,1)$	169949.5	<0.06	...	...	432.3	...

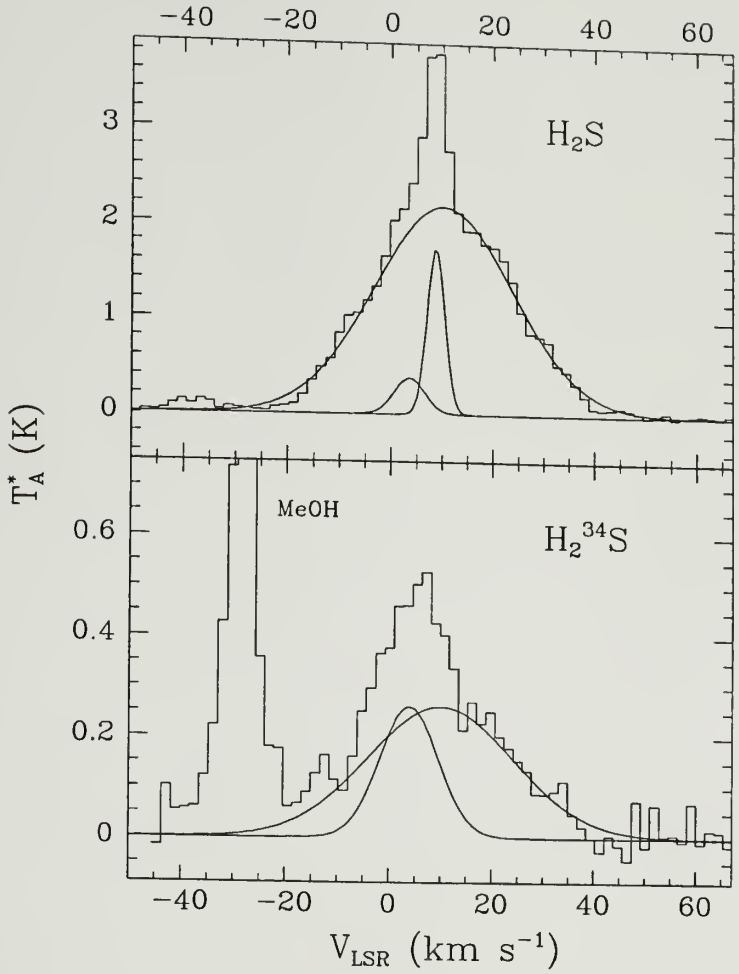

Figure 6.7. Spectra of the H_2S and $H_2{}^{34}S$, $1(1,0)-1(0,1)$ transition observed in the 2 mm survey. These spectra clearly show that H_2S is present in the plateau, hot core, and ridge components of OMC–1. The spectral resolution is 1 MHz. Line parameters are listed in Table 6.16.

6.5.6.6 H_2CS

Two transitions of the thioformaldehyde (H_2CS) main isotopomer were present in the spectral region surveyed and are listed in Table 6.17. The 5(1,5)–4(1,4) transition, with $\Delta E = 29$ K, was clearly detected. The line was observed with a spectral resolution of 250 kHz, and has a $V_{LSR} = 8.0$ km s^{-1} and $\Delta V_{1/2} = 3.52$ km s^{-1}, which suggests that H_2CS may arise from the compact ridge component or, perhaps, the quiescent extended ridge gas. Minh, Irvine and Brewer (1991) conducted an LVG analysis on H_2CS ortho and para emission lines which were observed towards Orion(KL). They found that the observed line strengths were best fit when a source size of $\sim 30''$ was assumed. This finding, coupled with their observed line widths and velocities, which are consistent with those measured in this work, led them to concluded that the H_2CS emission observed towards Orion(KL) arises from the compact ridge component.

The other transition present in the survey region, 17(1,16)–17(1,17), lies $\Delta E \sim 260$ K above the ground state. A weak feature, which is near the edge of a spectrum and is thus suspect, has been tentatively identified as the 17(1,16)–17(1,17) transition of H_2CS.

Nine transitions belonging to the isotopic variant $H_2{}^{13}CS$ are present in the survey region with $\Delta E < 227$ K (*see* Table 6.17). Half of these lines were obscured by other spectral features and none of the remaining transitions were detected.

6.5.7 Silicon-Bearing Molecules

6.5.7.1 SiO

One new transitions of SiO were observed in this survey. The isotopic species $^{30}Si^{16}O$ was observed by its $J = 4 \rightarrow 3$ ground vibrational state transition (see Table 6.18). The transition lies $\Delta E \sim 12$ K above the ground state. The line profile displays broad wings, which suggests that $^{30}Si^{16}O$ is part of the high-velocity

Table 6.17. Transitions of H_2CS

Transition $J(K_{-1},K_{+1})$	Freq. (MHz)	T_A^* (K)	V_{LSR} ($km\,s^{-1}$)	$\Delta V_{1/2}$ ($km\,s^{-1}$)	ΔE (cm^{-1})	Comments
H_2CS						
$17(1,16)-17(1,17)$	159682.1	~ 0.05	~ 11	~ 6	181.6	Unlikely, possible U-line. Blend with $HCOOCH_3$.
$5(1,5)-4(1,4)$	169113.8	0.90	8.0	3.52	20.4	250 kHz Res.
$H_2{}^{13}CS$						
$5(1,5)-4(1,4)$	162706.6	<0.06	...	...	20.0	...
$5(4,2)-4(4,1)$ $5(4,1)-4(4,0)$	165067.4	<0.15	...	...	157.4	...
$5(0,5)-4(0,4)$	165090.0	...	...	...	11.0	Obscured by MeOH.
$5(3,3)-4(3,2)$ $5(3,2)-4(3,1)$	165105.2 165105.3	...	...	...	93.4	Obscured by MeOH.
$5(2,4)-4(2,3)$	165115.7	...	...	...	47.7	Blend with SO_2.
$5(2,3)-4(2,2)$	165166.6	...	...	...	47.7	Blend with SO_2.
$5(1,4)-4(1,3)$	167543.4	<0.11	...	...	20.3	...

molecular outflow in Orion. Observations by Wright *et al.* (1983) of the SiO $v=0$, $J=2\rightarrow 1$ transition showed the high-velocity outflow to be bipolar and to originate within a few arc seconds of the infrared source IRc2. They found that the red-shifted wing was strongest to the east of IRc2, while the blue-shifted wing was strongest to the north. Erickson *et al.* (1982) had drawn similar conclusions from observations of CO $J=3\rightarrow 2$ emission. In our spectrum of SiO, the wings appear to be asymmetric with the red-shifted wing being the strongest (see Figure 6.8). We have fit this feature with two gaussians; one for the core of the profile and the other for the pedestal or wings. The line core has a $V_{LSR}=8$ $km\,s^{-1}$ and a $\Delta V_{1/2}=18$ $km\,s^{-1}$, which most closely matches plateau emission. The pedestal has a $\Delta V_{1/2}=53$ $km\,s^{-1}$ and is shifted, relative to the line core, by approximately

Table 6.18. Transitions of $^{30}Si^{16}O$

Transition J	Freq. (MHz)	T_A^* (K)	V_{LSR} ($km\,s^{-1}$)	$\Delta V_{1/2}$ ($km\,s^{-1}$)	ΔE (cm^{-1})	Comments
$4 \rightarrow 3$, v=0	169486.6	0.09	14	53.5	8.5	Broad line wings.
		0.24	8.0	17.2		

+6 $km\,s^{-1}$. The results of the fits are to be considered a crude estimate since the line wings can not be modeled as a single gaussian.

6.5.7.2 SiS

There are three transitions of silicon sulfide (SiS) present in the spectral region surveyed, belonging to two isotopic species (see Table 6.19). Two of these transitions belong to the primary isotopomer $^{28}Si^{32}S$ $J=9\rightarrow 8$ ground and first vibrational state. The ground vibrational transition lies $\Delta E \sim 30$ K above the ground state and has a line profile which suggests plateau emission. The $J=9\rightarrow 8$, v=1 transition lies $\Delta E \sim 1100$ K above the ground vibrational state. There appears to be a spectral feature at this frequency; however, the feature is weak and crowded by other emission features. Thus, we have made this a tentative identification. The SiS $J=9\rightarrow 8$, v=1 transition has been observed towards the carbon-star IRC+10216 by Guélin *et al.* (1987).

The remaining SiS transition covered by this survey belongs to the isotopic variant, $^{29}Si^{32}S$ (see Table 6.19). A weak spectral feature has been tentatively identified as belonging to the $^{29}Si^{32}S$ $J=9\rightarrow 8$, v=0 transition, which lies $\Delta E \sim 31$ K above the ground state.

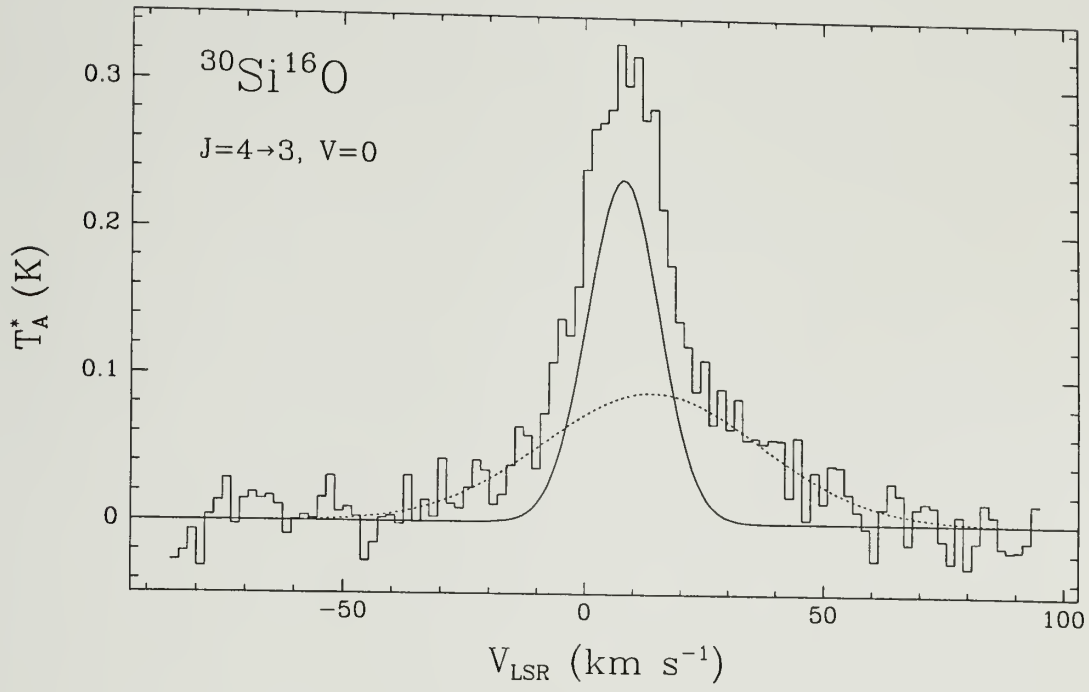

Figure 6.8. Spectrum of the $^{30}Si^{16}O$ J=4→3, ground vibrational state transition, which appears to have broad line wings indicative of the Orion-KL high-velocity molecular outflow. The plateau component is indicated by the solid curve, while the gaussian fit to the wings is traced out by the dashed curve. The line fitting is discussed in the text. The spectral resolution is 1 MHz.

Table 6.19. Transitions of SiS

Transition J	Freq. (MHz)	T_A^* (K)	V_{LSR} ($km\,s^{-1}$)	$\Delta V_{1/2}$ ($km\,s^{-1}$)	ΔE (cm^{-1})	Comments
$^{28}Si^{32}S$						
$9 \rightarrow 8$, v=1	162581.6	~0.06	~12	~11	766.2	Tentative.
$9 \rightarrow 8$, v=0	163376.6	0.11	9	20	21.8	...
$^{29}Si^{32}S$						
$9 \rightarrow 8$, v=0	160375.0	~0.04	~10	~7	21.4	Tentative.

6.5.8 Large Organic Species

6.5.8.1 CH_3CN

Methyl cyanide (MeCN) was observed in this survey by its $J=9 \rightarrow 8$ transitions. The results are reported in Table 6.20. The transitions with $\Delta E < 100$ K are each comprised of two components, which we have classified as arising from the hot-core and compact-ridge.

The $J_K = 9_0 \rightarrow 8_0$ transition was severely blended with the $J_K = 9_1 \rightarrow 8_1$ transition, and partially blended with the $J_K = 9_2 \rightarrow 8_2$ transition. The $J_K = 9_3 \rightarrow 8_3$ transition is not blended with any other feature. We simultaneously fit Gaussians to all four features. Initially, each line was fit with a single Gaussian, which left significant residuals. We then added a second Gaussian, which greatly enhanced the goodness of fit. Since all of the fit parameters were free variables, the fact that each component shows the same pattern of line center velocities and line widths suggests that these transitions do indeed arise from two velocity components attributed to MeCN.

The next three transitions, with $\Delta E \sim 100-275$ K, appear to have only a hot-core component, though all three of these transitions have irregular line

Table 6.20. Transitions of CH_3CN (MeCN)

Transition J(K)	Freq. (MHz)	T_A^* (K)	V_{LSR} ($km\,s^{-1}$)	$\Delta V_{1/2}$ ($km\,s^{-1}$)	ΔE (cm^{-1})	Comments
9(8)−8(8)	165365.3	<0.15	...	...	337.9	...
9(7)−8(7)	165413.0	<0.15	...	...	263.9	...
9(6)−8(6)	165454.4	0.39	5.4	11.27	199.8	...
9(5)−8(5)	165489.4	0.40	7.7	11.73	145.5	...
9(4)−8(4)	165517.9	0.34	6.8	9.74	101.1	...
9(3)−8(3)	165540.3	0.48	8.5	5.00	66.5	...
		0.42	5.5	14.59		
9(2)−8(2)	165556.2	0.36	8.8	4.10	41.8	...
		0.50	6.1	10.48		
9(1)−8(1)	165565.7	0.49	8.3	4.50	27.0	...
		0.42	5.4	16.72		
9(0)−8(0)	165569.0	0.56	8.6	3.87	22.1	...
		0.34	6.5	19.54		

shapes. The two remaining highest energy level transitions ($\Delta E \geq 275$ K) were not detected. The mean hot-core component line center velocity and line width are $V_{LSR} = 6\ km\,s^{-1}$ and $\Delta V_{1/2} = 13.4\ km\,s^{-1}$, respectively. The compact-ridge component mean center velocity is $V_{LSR} = 8\ km\,s^{-1}$ and the mean line width is $\Delta V_{1/2} = 4.4\ km\,s^{-1}$. All the observed transitions have similar line intensities, which suggests that MeCN is optically thick for both the hot-core emission and the compact-ridge.

$^{13}CH_3CN$: The four $^{13}CH_3CN$ $J = 9 \rightarrow 8$ components covered by this survey, and with $\Delta E < 100$ K, are listed in Table 6.21. All four components were detected, though two were blended. All four transitions lie on the red shifted wing of a broad SO_2 feature, which increased the uncertainty of the measured line parameters. The $^{13}CH_3CN$ mean line width and line center velocity are $\Delta V_{1/2} = 8\ km\,s^{-1}$ and $V_{LSR} = 7\ km\,s^{-1}$.

Table 6.21. Transitions of $^{13}CH_3CN$

Transition J(K)	Freq. (MHz)	T_A^* (K)	V_{LSR} (km s^{-1})	$\Delta V_{1/2}$ (km s^{-1})	ΔE (cm^{-1})	Comments
9(3)−8(3)	160761.8	0.13	7.8	10.37	66.3	Blend with VyCN
9(2)−8(2)	160776.8	0.10	6.1	5.65	41.4	...
9(1)−8(1)	160785.9	0.10	8.0	14.44	26.4	Blended
9(0)−8(0)	160789.0				21.4	

6.5.8.2 CH_3OH

There were 14 favorable transitions of methanol (MeOH) in this survey, and all were detected. The (E) torsional substate transitions are listed in Table 6.22, and the (A) torsional substates in Table 6.23. The energy levels quoted in these two tables were calculated by Anderson, De Lucia, and Herbst (1990). All of the (E) transitions belong to the ground torsionally excited state ($v_t = 0$), while the (A) transitions have $v_t = 1$. Several of the MeOH transitions are among the strongest lines observed in this survey, with the strongest MeOH transition having a peak temperature of $T_A^* \sim 3$ K. The (E) substate transition line profiles were found to be asymmetric and were fit with two gaussians, with all fit parameters allowed to be free variables. The weaker (A) substate transitions were fit with a single gaussian. The dominant components of all the MeOH lines observed in this survey are moderately narrow, with typical line widths of $\Delta V_{1/2} = 2-4$ km s^{-1}, and have an average velocity of $V_{LSR} = 8.3$ km s^{-1}. These results are consistent with ZM93, and further strengthens the likely association of MeOH with the compact-ridge source found by other surveys (e. g., Blake *et al.* 1987; Turner 1991). The broader, MeOH components have typical line widths of $\Delta V_{1/2} = 9$ km s^{-1}, and an average velocity of $V_{LSR} = 7.3$ km s^{-1}, which are consistent with hot-core emission and are

again in good agreement with the results of ZM93. This finding, that MeOH may be a constituent of the hot-core as well as the compact-ridge, finds further support by the presence of CH_3OD in the hot-core, as pointed out by Turner (1991). In addition, ZM93 found that some of the MeOH features, with line profiles similar to hot-core emission, had energy levels above the ground state of $\Delta E \sim 200$ K. Observations of such high-lying transitions were yet another indicator of MeOH residing in the hot-core. In this survey we, too, have detected weak, high-lying transitions $\Delta E \sim 350-543$ K, whose line parameters suggest that they may arise from the hot-core. Using the Nobeyama Millimeter Array, Minh *et al.* (1993) found the $15(3) - 14(4)A^-$ MeOH emission to have an ellipsoidal shape between IRc2 and the compact ridge, peaking towards the compact ridge. Minh *et al.* suggest that there may be a relation between methanol and the outflow from IRc2.

Table 6.22. Transitions of CH_3OH (MeOH)in the E Torsional Substate [a]

Transition J(K)	Freq. (MHz)	T_A^* (K)	V_{LSR} ($km\,s^{-1}$)	$\Delta V_{1/2}$ ($km\,s^{-1}$)	ΔE (cm^{-1})	Comments
1(1)−1(0)E	165050.2	1.62	7.9	3.10	10.1	...
		0.60	6.8	7.52		
2(1)−2(0)E	165061.1	1.80	7.9	3.21	13.3	...
		0.44	7.0	10.40		
3(1)−3(0)E	165099.3	1.88	8.3	4.24	18.1	...
		0.33	6.1	13.33		
4(1)−4(0)E	165190.5	1.88	8.0	3.56	24.6	...
		0.44	8.0	15.18		
5(1)−5(0)E	165369.4	1.60	8.2	3.48	32.7	...
		0.71	7.6	10.07		
6(1)−6(0)E	165678.8	1.00	8.4	4.21	42.3	...
		0.35	7.1	12.39		
7(1)−7(0)E	166169.2	0.96	8.4	2.51	53.6	250 kHz Res.
		0.68	7.8	9.46		
8(1)−8(0)E	166898.6	0.90	8.4	4.12	66.5	...
		0.24	5.4	11.60		
9(1)−9(0)E1	167931.1[b]	0.81	8.3	3.42	81.0	...
		0.52	8.0	10.29		
4(1)−3(2)E	168577.9	0.65	8.6	1.76	24.5	...
		0.54	7.5	6.33		
10(1)−10(0)E	169335.3[c]	0.91	7.9	5.83	97.1	...
3(2)−2(1)E	170060.6	3.00	8.4	2.93	18.8	250 kHz Res.
		0.80	7.5	10.04		

(a) Anderson, De Lucia, & Herbst (1990), all $v_t = 0$.

(b) Lovas (1992).

(c) Predicted frequency.

Table 6.23. Transitions of CH_3OH (MeOH) in the A Torsional Substate

Transition J(K)	Freq. (MHz)	T_A^* (K)	V_{LSR} ($km\,s^{-1}$)	$\Delta V_{1/2}$ ($km\,s^{-1}$)	ΔE (cm^{-1})	Comments
$7(1)-8(2)A^+$	166773.3[a]	~ 0.18	7.3	4.96	265.4	$v_t=1$
$7(1)-8(2)A^-$	169427.2[a]	0.32	7.3	5.64	265.4	$v_t=1$, Blended with $^{13}CH_3OH$

(a) Frequency from Anderson, De Lucia, & Herbst (1990).

$^{13}CH_3OH$: There were 16 $^{13}CH_3OH$ transitions with $\Delta E < 130$ K within this survey, of which 7 were detected (*see* Table 6.24). Three of the remaining nine transitions were obscured by other spectral features: one was obscured by an SO_2 line, two others by MeCN. Another line, $9(2)-8(3)A^+$, coincides with a favorable transition of NH_2CHO. The remaining three undetected transitions have upper limits which are similar to the line strengths of the observed $^{13}CH_3OH$ transitions. These latter features were fit with single gaussians, which gave average values of $\Delta V_{1/2}=4$ km s^{-1} and $V_{LSR}=7.6$ km s^{-1}.

CH_3OD: Six transitions of CH_3OD are present in this survey; however, none were detected. Upper limits for these transitions are given in Table 6.25.

Table 6.24. Transitions of $^{13}CH_3OH$ [a]

Transition J(K)	Freq. [a] (MHz)	T_A^* (K)	V_{LSR} (kms^{-1})	$\Delta V_{1/2}$ (kms^{-1})	ΔE (cm^{-1})	Comments
$2(1)-3(0)A^+$	160507.8	...	...	...	9.4	Obscured by SO_2
$4(1)-3(2)E$	161789.2	0.12	7.8	3.00	25.0	...
$7(0)-6(1)E$	163872.9	0.16	7.5	3.32	47.7	...
$6(2)-7(1)A^+$	165280.5	<0.15	...	...	53.9	...
$1(1)-1(0)E$	165566.1	...	...	...	10.7	Obscured by MeCN
$2(1)-2(0)E$	165575.6	...	...	...	13.9	Obscured by MeCN
$3(1)-3(0)E$	165609.4	0.12	7.5	7.77	18.6	Blended with $^{34}SO_2$
$4(1)-4(0)E$	165691.0	0.24	8.1	3.44	24.9	...
$5(1)-5(0)E$	165851.2[b]	0.14	7.9	4.48	32.1	...
$6(1)-6(0)E$	166128.8	0.16	7.2	2.52	42.2	...
$7(1)-7(0)E$	166569.5	<0.11	...	...	53.2	...
$8(1)-8(0)E$	167225.6	0.18	8.1	4.45	65.8	...
$9(1)-9(0)E$	168155.4	0.19	7.3	3.85	79.9	250 kHz Res.
$9(4)-10(3)A^-$	168510.4[b]	<0.13	...	...	121.4	...
$9(4)-10(3)A^+$	168537.5[b]	<0.13	...	...	121.4	...
$3(2)-2(1)E$	168676.5	0.19	7.4	2.82	19.4	...
$9(2)-8(3)A^-$	169356.8[b]	<0.17	...	...	91.5	...
$10(1)-10(0)E$	169421.6[b]	0.09	7.3	4.11	94.9	Blend with CH_3OH
$9(2)-8(3)A^+$	170041.0[b]	...	...	...	91.5	Obscured by NH_2CHO

(a) Frequencies from Anderson, Herbst & De Lucia (1987).

(b) Anderson, Herbst, & De Lucia (1990).

Table 6.25. Transitions of CH_3OD [a]

Transition J(K)	Freq. (MHz)	T_A^* (K)	V_{LSR} (kms^{-1})	$\Delta V_{1/2}$ (kms^{-1})	ΔE (cm^{-1})	Comments
4(0)−3(−1)E	162185.7	< 0.07	...	...	12.3	...
9(−4)−10(−3)E	165348.8[b]	<0.15	...	...	112.4	...
9(1)−9(0)A∓	166505.7	<0.11	...	...	67.9	...
10(4)−11(3)E	166920.6[b]	<0.11	...	...	126.2	...
10(−1)−9(−2)E	168482.4[b]	<0.13	...	...	80.4	...
8(1)−7(2)E	169994.8[b]	<0.06	...	...	55.2	...

(a) Frequencies from Anderson *et al.* (1988).

(b) Predicted Frequencies.

6.5.8.3 CH_2CHCN

Some 47 favorable transitions of vinyl cyanide (CH_2CHCN: VyCN) were present in the surveyed region (*see* Table 6.26). These include both a-type and b-type transitions, where the a-type are the strongest. Seven a-type transitions were detected. However, all except one transition were blended with other spectral features. The one clearly detected transition was $17(2,15)-16(2,14)$ which lies $\Delta E = 71$ K above the ground state and has an intensity of $T_A^* = 0.1$ K, a line width of $\Delta V_{1/2} = 8.4$ km s^{-1}, and velocity $V_{LSR} = 5$ km s^{-1}. Two other a-type transition pairs, $17(6,12)-16(6,11)$ and $17(6,11)-16(6,10)$, and $17(5,13)-16(5,12)$ and $17(5,12)-16(5,11)$, are partially blended together, and were fit with a single gaussian. Each pair has $T_A^* \sim 0.1$ K, $V_{LSR} \sim 5$ km s^{-1}, and $\Delta V_{1/2} \sim 6$ km s^{-1}. Finally, $18(2,17)-17(2,16)$, which is blended with an unidentified feature, has an intensity $T_A^* \sim 0.1$ K, $\Delta V_{1/2} \sim 7$ km s^{-1}, and $V_{LSR} \sim 7$, which makes it consistent with the other observed a-type transitions. The a-type transitions all lie in the range $\Delta E = 71 - 140$ K. There are three a-type transitions ($\Delta E \sim 70$ K) which were not detected and which were not otherwise obscured. These transitions, $17(1,16)-16(1,15)$, $18(1,18)-17(1,17)$, and $18(0,18)-17(0,17)$, were all in spectra with relatively large baseline noise levels so the upper limits on these lines, typically $T_A^* < 0.11$ K, are consistent with the intensities of the observed a-type transitions. With additional integration, these lines would most likely be detected.

As is the case with the other asymmetric tops observed in this survey, the expected intensity of the VyCN b-type transition is very weak, $T_A^* \sim 0.06$ K. This would place the b-type transitions at the 3σ level for most of this survey, which accounts for our not observing any b-type transitions.

Our results for VyCN, albeit meager, are consistent with the findings of ZM93. The lines detected here typically have $V_{LSR} \sim 5 - 7$ km s^{-1}, and line width of $\Delta V_{1/2} \sim 7 - 10$ km s^{-1}, indicating that the emission arises from the hot-core.

Table 6.26. Transitions of CH_2CHCN (VyCN)

Transition $J(K_{-1},K_{+1})$	Freq. (MHz)	T_A^* (K)	V_{LSR} (kms^{-1})	$\Delta V_{1/2}$ (kms^{-1})	ΔE (cm^{-1})	Comments
26(1,25)−26(0,26)	159753.9	<0.06	...	...	109.2	...
14(2,13)−14(1,14)	159788.2	<0.06	...	...	33.9	...
34(6,29)−35(5,30)	159895.6	...	...	...	237.2	Obscured by I-line
17(2,16)−16(2,15)	160758.8	...	...	...	49.0	Obscured by $^{13}CH_3CN$
17(6,12)−16(6,11)	161397.0	0.11	4	6	97.1	Blend with VyCN 500 kHz
17(6,11)−16(6,10)	161397.1					
17(5,13)−16(5,12)	161402.6	∼0.10	∼5	∼5	80.6	Blend with VyCN 500 kHz
17(5,12)−16(5,11)						
17(7,10)−16(7,9)	161412.4	∼0.08	...	...	116.6	Obscured by $HCOOCH_3$
17(7,11)−16(7,10)						
17(8,9)−16(8,8)	161441.3	...	...	...	139.0	Obscured by $^{33}SO_2$
17(8,10)−16(8,9)						
17(4,14)−16(4,13)	161445.4	∼0.04	∼9	∼10	67.1	...
17(4,13)−16(4,12)	161450.4	...	...	...	67.1	Obscured by $^{33}SO_2$
17(9,8)−16(9,7)	161480.2	...	...	...	164.4	Obscured by EtCN
17(9,9)−16(9,8)						
17(3,15)−16(3,14)	161502.3	<0.06	...	...	56.6	Close to U-line
17(10,8)−16(10,7)	161527.5	<0.06	...	...	192.7	...
17(10,7)−16(10,6)						
17(11,7)−16(11,6)	161582.1	...	...	...	223.9	Obscured by EtCN
17(11,6)−16(11,5)						
17(12,6)−16(12,5)	161643.3	<0.07	...	...	258.0	...
17(12,5)−16(12,4)						
17(3,14)−16(3,13)	161689.8	0.14	4.5	9.5	56.6	Blend with NS
17(13,5)−16(13,4)	161710.7	...	...	...	294.9	Obscured by NS
17(13,4)−16(13,3)						
17(14,4)−16(14,3)	161784.0	<0.07	...	...	334.7	...
17(14,3)−16(14,2)						
17(15,3)−16(15,2)	161863.0	<0.07	...	...	377.3	...
17(15,2)−16(15,1)						

Continued, next page.

Table 6.26 continued

Transition $J(K_{-1},K_{+1})$	Freq. (MHz)	T_A^* (K)	V_{LSR} ($km\,s^{-1}$)	$\Delta V_{1/2}$ ($km\,s^{-1}$)	ΔE (cm^{-1})	Comments
17(16,1)−16(16,0) 17(16,2)−16(16,1)	161947.5	<0.07	...	...	422.7	...
3(2,2)−2(1,1)	163056.4	<0.06	...	...	2.5	Close to $HC^{13}CCN$
17(2,15)−16(2,14)	163298.0	0.10	5.3	8.36	49.3	...
15(2,14)−15(1,15)	163338.4	<0.09	...	...	38.5	Close to VyCN
33(2,31)−32(3,30)	163491.0	<0.09	...	...	180.8	...
15(1,15)−14(0,14)	164228.3	<0.10	...	...	33.0	Close to $HCOOCH_3$
17(1,16)−16(1,15)	164287.2	<0.10	...	...	45.5	...
3(2,1)−2(1,2)	164445.6	<0.10	...	...	2.4	...
18(1,18)−17(1,17)	165866.4	<0.10	...	...	48.6	...
25(1,24)−24(2,23)	165891.8	<0.10	...	...	100.6	...
35(2,33)−35(1,34)	166177.3	...	...	...	203.0	Obscured by MeOH
16(2,15)−16(1,16)	167133.7	<0.11	...	...	43.4	...
18(0,18)−17(0,17)	167728.4	<0.11	...	...	48.0	...
27(1,26)−27(0,27)	169436.9	<0.06	...	...	117.4	...
20(0,20)−19(1,19)	169569.8	<0.06	...	...	60.0	...
18(2,17)−17(2,16)	170150.3	0.09	6.5	6.8	54.4	Blend with U-line 250 kHz Res.

6.5.8.4 $HCOOCH_3$

Approximately 62 favorable transitions of methyl formate with $\Delta E < 145$ K were present in the surveyed region (*see* Table 6.27). Of those transitions which were not otherwise obscured by other spectral features, only 10 were not detected. These "missing" lines are readily accounted for since in all cases they are relatively weak transitions; $S_{ij} < 10$ where S_{ij} is the standard line strength parameter (Townes and Schawlow 1975). The strongest transitions ($S_{ij} \geq 10$) showed intensities of $T_A^* \sim 0.1-0.6$ K, for a mean value of 0.3 ± 0.1 K. The weaker lines would then have $T_A^* \sim 50$ mK, which is at the limit of detection for most of this survey given the RMS noise level of the spectra, which is typically 30 mK. Both a-type and b-type

transitions were observed, the a-type being the stronger, for both (A) and (E) torsional substates. In fact, all a-type transitions were either directly observed or were obscured by intervening spectral features due to other species. In general, transitions up to $\Delta E = 75$ cm^{-1} (~ 110 K) were readily detected.

Methyl formate in this survey was found to have an average velocity $V_{LSR} = 7.9 \pm 0.7$ km s^{-1} and on average line width of $\Delta V_{1/2} = 4.4 \pm 1$ km s^{-1}, which is in good agreement with the findings of ZM93. In determining the mean line parameters, we included only those methyl formate features which were not blended with other species. As ZM93 concluded, we find that methyl formate most probably arises from the compact-ridge source. This is consistent with the results of Blake *et al.* (1987) who found that the compact-ridge appeared to be the position where oxygen rich molecules have their peak intensities, and with the high spatial resolution ($\sim 5''$) observations carried out by Minh *et al.* (1993), which show $HCOOCH_3$ to be well concentrated towards the compact ridge position.

Table 6.27. Transitions of $HCOOCH_3$ [a]

Transition $J(K_{-1},K_{+1})$	Freq. (MHz)	T_A^* (K)	V_{LSR} (km s^{-1})	$\Delta V_{1/2}$ (km s^{-1})	ΔE (cm^{-1})	Comments
13(10,4)−12(10,3)E	159671.2	∼0.1	∼8	∼8	83	Edge of spectrum
13(9,4)−12(9,3)E	159766.8	0.15	8.1	1.88	75	...
13(9,4)−12(9,3)A 13(9,5)−12(9,4)A	159777.4	0.17	9.0	3.23	69.3	...
13(9,5)−12(9,4)E	159783.0	0.12	8.0	6.16	75	Coincides with EtOH
13(8,5)−12(8,4)E	159930.6	0.15	7.3	3.25	67	...
13(8,6)−12(8,5)A 13(8,5)−12(8,4)A	159942.9	∼0.1	∼8	∼18	61.5	Blend with U-line
13(8,6)−12(8,5)E	159946.2	0.13	8.3	3.29	67	...
39(8,31)−39(7,32)A	159981.0	<0.06	...	...	352.7	...
13(7,6)−12(7,5)E	160178.9	0.27	7.9	3.75	60	...
13(7,7)−12(7,6)A 13(7,6)−12(7,5)A 13(7,7)−12(7,6)E	160193.0 160193.5 160193.7	0.61	7.1	4.51	54.6 54.6 60	...
13(6,7)−12(6,6)E	160578.3	0.24	7.8	5.60	54	...
13(6,8)−12(6,7)A	160585.8	0.28	7.8	4.75	48.6	...
13(6,8)−12(6,7)E	160591.3	0.24	8.0	4.62	54	...
13(6,7)−12(6,6)A	160602.2	0.30	7.9	3.50	48.6	...
14(1,13)−13(2,12)E	160944.9	∼0.06	∼12	∼11.4	43	...
14(1,13)−13(2,12)A	160953.0	<0.06	...	...	38.1	...
13(5,9)−12(5,8)A	161152.5	0.20	9.0	3.49	43.6	...
13(5,9)−12(5,8)E	161171.4	0.29	7.3	3.59	49	...
13(4,10)−12(4,9)E	161262.4	<0.5	∼8	<7	45	Coincides with EtCN
13(4,10)−12(4,9)A	161273.3	∼0.5	∼8	∼9	39.5	Blend with H_2CCO
20(2,18)−20(2,19)A	161374.1	...	...	...	83.5	Coincides with EtCN
20(2,18)−20(1,19)E	161380.3	...	...	...	89	Coincides with EtCN
13(5,8)−12(5,7)E	161416.2	∼0.3	∼8	∼2.6	49	Blend with U-line 500 kHz
20(2,18)−20(1,19)A 13(5,8)−12(5,7)A	161457.6 161458.2	0.30	8.2	3.71	83.5 43.6	...
32(6,26)−32(5,27)A	161515.6	...	...	...	234.8	Obscured by $H^{13}COOH$
22(7,15)−22(6,16)A	162058.8	<0.07	...	...	121.6	...
22(7,15)−22(6,16)E	162063.3	<0.06	...	...	127	...
18(1,17)−18(1,18)A	162085.3	<0.06	...	...	63.4	...
18(1,17)−18(0,18)A	162091.1	<0.06	...	...	63.4	...

Continued, next page.

Table 6.27 continued

Transition $J(K_{-1},K_{+1})$	Freq. (MHz)	T_A^* (K)	V_{LSR} (kms^{-1})	$\Delta V_{1/2}$ (kms^{-1})	ΔE (cm^{-1})	Comments
$25(6,20)-25(5,21)$E	162096.6	<0.06	...	...	151	...
$25(6,20)-25(5,21)$A	162127.8	<0.06	...	...	145.9	...
$18(2,17)-18(1,18)$A	162329.8	<0.10	...	...	63.4	...
$35(10,26)-34(11,23)$A	162405.0	<0.06	...	...	301.0	...
$22(4,19)-22(3,20)$E	162747.6	<0.06	...	...	111	...
$14(2,13)-13(2,12)$E	162768.8	0.31	7.9	3.22	43	...
$14(2,13)-13(2,12)$A	162775.1	...	...	...	38.1	Obscured by $^{34}SO_2$
$22(4,19)-22(3,20)$A	162812.8	0.08	9.6	5.32	105.8	250 kHz Res.
$20(3,18)-20(2,19)$E	162926.0	<0.06	...	...	89	...
$20(3,18)-20(2,19)$A	163000.7	<0.06	...	...	83.5	...
$20(3,18)-20(1,19)$A?	163084.1	~0.08	~4	~5.2	83.5	Edge of spectrum
$24(5,20)-24(4,21)$E	163464.5	<0.09	...	...	136	...
$24(5,20)-24(4,21)$A	163516.3	<0.09	...	...	130.1	...
$14(1,13)-13(1,12)$E	163829.6	0.38	6.4	5.61	43	250 kHz Res.
$14(1,13)-13(1,12)$A	163835.4[b]	0.21	7.6	5.02	38.0	250 kHz Res.
$15(0,15)-14(1,14)$E	163925.8	0.17	7.7	5.26	45	...
$15(0,15)-14(1,14)$A	163927.2[b]				39.4	
$15(1,15)-14(1,14)$E	163960.4	0.55	7.4	5.28	45	Blend with $^{33}SO_2$
$15(1,15)-14(1,14)$A	163961.7				39.4	
$15(0,15)-14(0,14)$E	163987.4	0.58	8.8	5.47	45	...
$15(0,15)-14(0,14)$A	163988.8				39.4	
$15(1,15)-14(0,14)$E	164022.0	0.20	8.5	6.5	45	...
$15(1,15)-14(0,14)$A	164023.3				39.4	
$35(10,25)-34(11,24)$A	164064.1	<0.10	...	...	301.0	...
$30(8,22)-29(9,21)$A	164073.6	<0.10	...	...	216.8	...
$29(5,24)-29(5,25)$E	164151.7	...	...	...	196	Obscured by HCCN
$13(4,9)-12(4,8)$E	164206.0	0.30	7.9	3.50	45	...
$13(4,9)-12(4,8)$A	164223.8	0.31	7.5	3.06	39.6	...
$29(5,24)-29(5,25)$A	164236.1	<0.10	...	...	190.6	...
$13(2,11)-12(2,10)$E	164955.7	0.41	7.8	3.95	41	...
$13(2,11)-12(2,10)$A	164968.6	0.42	7.5	3.55	35.2	...
$36(9,27)-36(8,28)$A	165047.6	...	...	...	308.5	Obscured by MeOH
$9(3,7)-8(2,6)$E	165276.0	<0.12	...	...	17.1	...
$9(3,7)-8(2,6)$A	165295.3	<0.15	...	...	17.1	...

Table 6.27 continued

Transition $J(K_{-1},K_{+1})$	Freq. (MHz)	T_A^* (K)	V_{LSR} (km s^{-1})	$\Delta V_{1/2}$ (km s^{-1})	ΔE (cm^{-1})	Comments
14(2,13)−13(1,12)E	165653.5	<0.09	...	...	43	Obscured by MeCN
14(2,13)−13(1,12)A	165657.5				38.0	
19(4,15)−18(5,14)A	166029.8	<0.09	...	...	82.2	...
21(7,14)−21(6,15)A	166293.3	<0.09	...	...	112.3	...
21(7,14)−21(6,15)E	166297.1				118	
33(9,25)−32(10,22)A	166350.6	<0.09	...	...	263.9	...
29(8,21)−29(7,22)A	167351.1				204.1	
23(3,20)−23(3,21)A	167381.3	<0.09	...	...	114.8	...
29(8,21)−29(7,22)E	167392.6	<0.09	...	...	210	...
23(3,20)−23(2,21)E	167685.3	<0.09	...	...	120	...
26(6,21)−26(5,22)E	167691.4	<0.09	...	...	162	...
26(6,21)−26(5,22)A	167725.8	<0.09	...	...	156.5	...
23(3,20)−23(2,21)A	167761.4	<0.09	...	...	114.8	...
29(5,24)−29(4,25)E	167850.8	<0.09	...	...	196	...
29(5,24)−29(4,25)A	167926.3	...	...	...	190.5	Obscured by MeOH
36(7,29)−36(6,30)A	168348.0	<0.08	...	...	298.5	...
13(3,10)−12(3,9)E	168495.1	0.25	7.9	4.18	43	...
40(12,28)−39(13,27)A	168505.1	<0.12	...	...	399.1	...
13(3,10)−12(3,9)A	168513.7	0.30	8.1	3.84	37.0	...
26(4,22)−26(4,23)E	168788.4	...	...	...	156	Obscured by SO_2
26(4,22)−26(4,23)A	168867.2	<0.12	...	...	150.5	...
15(2,13)−14(3,12)E	168914.8	<0.15	...	...	53	...
15(2,13)−14(3,12)A	168934.2	<0.15	...	...	47.1	...
20(7,13)−20(6,14)A	169571.5	<0.06	...	...	103.5	...
20(7,13)−20(6,14)E?	169584.1	∼0.06	6	5	109	Coincides with EtCN
26(4,22)−26(3,23)E	170093.1	<0.06	...	...	156	...
6(4,3)−5(3,2)E	170161.9	∼0.06	9	5.2	10.3	250 khz Res.
26(4,22)−26(3,23)A	170168.8				150.4	
14(3,12)−13(3,11)E	170233.2	∼0.4	∼8	∼4	47	Blend with $HCOOCH_3$
14(3,12)−13(3,11)A	170243.9	∼0.3	∼8	∼4	41.4	Blend with $HCOOCH_3$

(a) Frequencies for E-state transitions are from Plummer *et al.* (1986).

(b) Frequencies from Lovas (1992).

6.5.8.5 CH_3CH_2CN

Moderately strong lines of ethyl cyanide (EtCN) were observed in the survey region, most originating from the $J=18\rightarrow 17$ and $J=19\rightarrow 18$ transitions. As illustrated in Table 6.28, 52 a-type transitions with reasonable line strengths and $\Delta E<385$ K were observed. However, only 5 transitions were cleanly detected. Four a-type transitions with $\Delta E>340$ K were not detected. All of the remaining a-type transitions, with $\Delta E<340$ K, were either partially blended or totally obscured by other spectral features.

Previous spectral line surveys of Orion–KL have assigned ethyl cyanide to the hot core (*see* ZM93; Turner 1991; Blake *et al.* 1987; Johansson *et al.* 1984); however, some of the EtCN lines observed in this survey appear to be asymmetric and can be fit with two gaussians (*see,* Fig 6.9). There is a narrow component with a mean line width of $\Delta V_{1/2}=5.5$ km s^{-1} and velocity $V_{LSR}=5$ km s^{-1}, and a broad component characterized by $\Delta V_{1/2}=16$ km s^{-1} and $V_{LSR}=3$ km s^{-1}. The line widths would suggest that these components arise from the compact-ridge and the hot-core, respectively. However, the line center velocities are both systematically low by ~ 2 km s^{-1}, which at the observed spectral resolution is equivalent to one channel. More sensitive observations with better spectral resolution will be necessary to confirm the presence of multiple velocity components and better determine the line center velocities.

The partially blended lines have typically $\Delta V_{1/2}=10$ km s^{-1} and $V_{LSR}=6$ km s^{-1}, which most closely matches the above mentioned broad component and are consistent with the findings of ZM93. These line parameters are consistent with hot-core emission. Of the lines which were clearly detected or only slightly blended, the typical line intensities are $T_A^*=0.1-0.4$ K.

Like most of the asymmetric tops studied here, with the notable exception of EtOH, EtCN has a large a-dipole moment and a smaller b-dipole moment. The

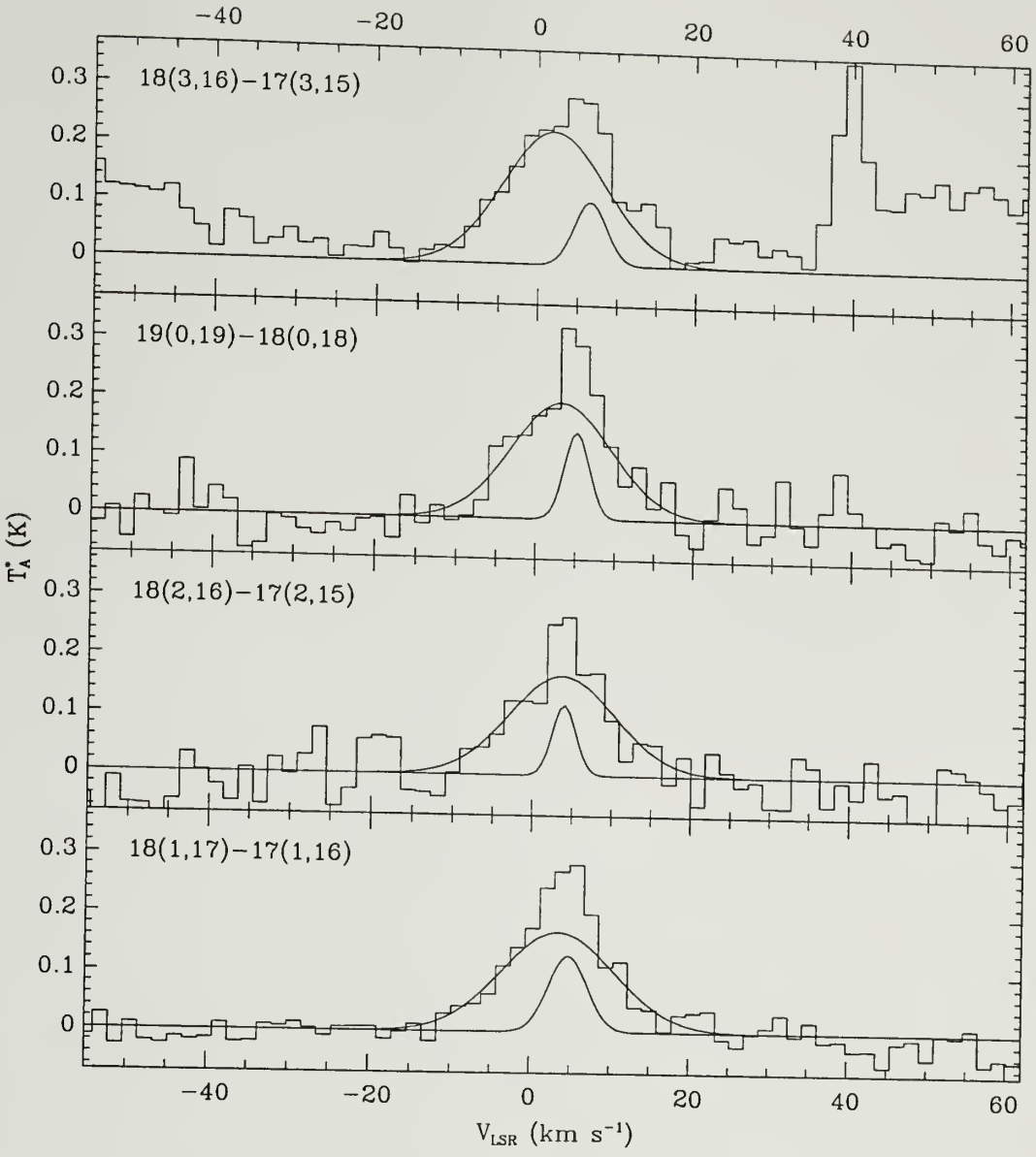

Figure 6.9. Spectra of selected EtCN transitions observed in the 2 mm survey, which indicate the presence of multiple velocity components. The spectra are ordered by increasing energy above the ground state (bottom to top: 68K, 71K, 72K, 75K). The narrow component has typically $V_{LSR}=5$ km s^{-1} and $\Delta V_{1/2}=5$ km s^{-1}, while the broad component line parameters are typically $V_{LSR}=3$ km s^{-1} and $\Delta V_{1/2}=17$ km s^{-1}. Spectral resolution is 1 MHz.

a-dipole transitions are typically a factor of 10 stronger than the b-dipole ones. Of the 16 b-type transitions covered by this survey, 13 were detected and of these two are tentative identifications. Of the 13 features identified as b-type transitions, most have line intensities in the range $T_A^* \sim 0.01 - 0.08$ K, which are consistent relative to the observed a-type line intensities. As mentioned above, there are two tentatively identified b-type transitions with $T_A^* \geq 0.1$ K. Since these lines have intensities similar to the a-type transitions, although they have smaller line strengths, it is unlikely that these features arise from EtCN. Therefore, we have also listed them as U-lines.

Table 6.28. Transitions of CH_3CH_2CN (EtCN)

Transition $J(K_{-1},K_{+1})$	Freq. (MHz)	T_A^* (K)	V_{LSR} (kms^{-1})	$\Delta V_{1/2}$ (kms^{-1})	ΔE (cm^{-1})	Comments
$18(2,17)-17(2,16)$	159888.9[a]	0.19	~ 5	~ 14.6	48.6	250 kHz Res.
$9(2,7)-8(1,8)$	161122.0	~ 0.07	11	3.5	11.2	Blend with I-line ...
$18(8,10)-17(8,9)$ $18(8,11)-17(8,10)$	161261.1	< 0.5	~ 5	< 7	95.1	Coincides with $HCOOCH_3$
$18(9,9)-17(9,8)$ $18(9,10)-17(9,9)$	161265.7	~ 0.36	~ 5	~ 8.0	108.3	Blend with EtCN, H_2CCO
$18(7,12)-17(7,11)$ $18(7,11)-17(7,10)$	161271.3	...	...	...	83.6	Obscured by $HCOOCH_3$
$18(10,8)-17(10,7)$ $18(10,9)-17(10,8)$	161280.7	...	...	...	122.9	Obscured by $(CH_3)_2O$
$18(11,8)-17(11,7)$ $18(11,7)-17(11,6)$ $18(6,13)-17(6,12)$ $18(6,12)-17(6,11)$	161303.5 161303.5 161304.9 161304.9	0.42	~ 4	~ 12.3	139.1 139.1 73.5 73.5	Blend with NS
$18(12,6)-17(12,5)$ $18(12,7)-17(12,6)$	161332.7	...	...	...	156.8	Obscured by NS
$18(13,5)-17(13,4)$ $18(13,6)-17(13,5)$	161367.3	~ 0.06	7	7.9	176.0	500 kHz Res.
$18(5,14)-17(5,13)$ $18(5,13)-17(5,12)$	161379.8 161381.9	0.21	5.9	12.38	65.0	500 kHz Res.
$13(4,9)-13(3,10)$	161402.0	...	...	...	34.2	Obscured by VyCN
$18(14,4)-17(14,3)$ $18(14,5)-17(14,4)$	161406.8	...	...	...	196.7	Obscured by VyCN
$18(15,3)-17(15,2)$ $18(15,4)-17(15,3)$	161450.8	...	...	...	218.9	Obscured by $^{33}SO_2$
$18(3,16)-17(3,15)$	161475.2	0.11 0.23	6.6 2.0	4.79 15.29	52.7	...

Continued, next page.

Table 6.28 continued

Transition $J(K_{-1},K_{+1})$	Freq. (MHz)	T_A^* (K)	V_{LSR} (kms^{-1})	$\Delta V_{1/2}$ (kms^{-1})	ΔE (cm^{-1})	Comments
18(16,3)−17(16,2) 18(16,2)−17(16,1)	161498.8	<0.06	...	...	242.6	...
18(4,15)−17(4,14)	161516.7	~0.07 ~0.15	~5 ~2	~5 ~14	58.1	Blend with U-line.
18(17,1)−17(17,0) 18(17,2)−17(17,1)	161550.8	<0.06	...	...	267.8	...
18(4,14)−17(4,13)	161581.2	0.25	3.7	12.0	58.1	...
11(4,7)−11(3,8)	161843.7	<0.1	...	...	26.7	...
17(4,14)−17(3,15)	161845.6	~0.09	6	8.0	52.7	...
10(4,6)−10(3,7) 19(4,16)−19(3,17)	161978.0 161978.3	~0.07	6	10	23.4 63.8	...
11(4,8)−11(3,9)	162053.3	~0.06	7	10	26.7	Coincides with $HCOOCH_3$
10(4,7)−10(3,8)?	162098.6	~0.1	6	2	23.4	Tentative
20(4,17)−20(3,18) 8(4,4)−8(3,5)	162132.9 162134.9	0.08	16	7	69.8 17.7	Tentative
30(3,28)−30(2,29)	162332.2	<0.10	...	...	140.5	...
18(3,15)−17(3,14)	162475.0	0.21 0.04	4.5 3.0	9.94 26.02	52.8	Odd line shape
18(1,17)−17(1,16)	163016.8	0.13 0.17	4.8 3.5	5.71 16.67	47.4	...
19(1,19)−18(1,18)	163948.7	...	...	...	50.2	Obscured by HNCS
25(4,22)−25(3,23)?	164394.6	0.20	~8	~2	104.1	Blend with HCCCN Tentative
19(0,19)−18(0,18)	164584.7	0.15 0.20	5.2 3.2	3.69 14.85	50.1	...
18(2,16)−17(2,15)	164668.0	0.12 0.17	4.0 3.7	~3.5 ~15.7	49.4	...
19(2,18)−18(2,17)	168630.7	0.24	3.4	12.02	53.9	500 kHz Res.

Table 6.28 continued

Transition $J(K_{-1},K_{+1})$	Freq. (MHz)	T_A^* (K)	V_{LSR} (kms^{-1})	$\Delta V_{1/2}$ (kms^{-1})	ΔE (cm^{-1})	Comments
26(2,24)−25(3,23)	169584.4	∼0.06	6	5	104.1	Coincides with $HCOOCH_3$
20(0,20)−19(1,19)	170020.9	∼0.05	6	12	55.7	Coincides with $^{13}CH_3OH$
29(10,19)−30(9,22) 29(10,20)−30(9,21)	170096.1	∼0.06	4	15	201.5	250 kHz Res.
19(8,11)−18(8,10) 19(8,12)−18(8,11) 19(9,10)−18(9,9) 19(9,11)−18(9,10)	170225.2 170225.2 170227.2 170227.2	0.47	∼6	∼15	100.5 100.5 113.6 113.6	Blend with $HCOOCH_3$
19(7,13)−18(7,12) 19(7,12)−18(7,11) 19(10,9)−18(10,8) 19(10,10)−18(10,9)	170240.2 170240.2 170240.9 170240.9	0.38	∼5	∼16	88.9 88.9 128.3 128.3	Blend with $HCOOCH_3$
19(11,9)−18(11,8) 19(11,8)−18(11,7)	170263.4	...	...	...	144.4	Obscured by OCS
19(6,14)−18(6,13) 19(6,13)−18(6,12)	170282.4 170282.5	...	...	...	78.9	Obscured by OCS and $^{34}SO_2$
19(12,8)−18(12,7) 19(12,7)−18(12,6)	170293.1	0.19	4.6	10.4	162.1	Blend with $^{34}SO_2$
19(13,6)−18(13,5) 19(13,7)−18(13,6)	170328.7	0.12	4.2	10.5	181.3	Coincideswith $HC^{18}O^+$

(a) Frequency from Lovas (1992).

6.5.8.6 CH_3CH_2OH

The presence of ethanol (EtOH) in Sgr B2 has been well established, and Millar *et al.* (1988) observed EtOH towards the GMC, W51M. Tentative detections of EtOH in Orion have been reported by Turner (1991), who suggested that it is present in either the compact or extended ridge. ZM93 reported detecting three b-type transitions, out of the 10 present in their spectral survey

region. They considered only b-type transitions since the a-dipole of EtOH is 30 times smaller than the b-dipole and, hence, has intensities which are smaller by a factor of $\sim$1000. Recently, Ohishi *et al.* (1995) detected EtOH towards Orion(KL), and NGC6334F (Ohishi 1995, *private communications*). They have gone on to map the distribution of EtOH towards Sgr B2, W51, and Orion(KL) using the 7(0,7)-6(1,6) transition. From this work it appears that ethanol is very extended in Sgr B2, peaking towards Sgr B2(N). The map of Orion-KL shows EtOH to peak at the compact ridge. Ohishi *et al.* have estimated the peak column density of EtOH to be 1×10^{15} cm^{-2} with an excitation temperature of $\sim$70 K. This column density corresponds to a fractional abundance relative to H_2 of $\sim3\times10^{-9}$, or five orders of magnitude greater than the abundances calculated for EtOH from a gas-phase chemistry model. Ohishi *et al.* suggest that in light of these results, it is likely that EtOH is formed on grain mantels in the hot core and then evaporated into the gas-phase.

In the spectral region surveyed here, there are nine favorable b-type transitions with $\Delta E < 150$ K above the absolute ground state (see Table 6.29). Of these transitions, only two have been tentatively identified as EtOH, and one of these coincides with a likely transition of $HCOOCH_3$. The 5(2,4)–4(1,3) line's $V_{LSR}=6$ km s^{-1} and $\Delta V_{1/2}=6$ km s^{-1} would be consistent with EtOH arising from the compact ridge.

Table 6.29. Transitions of CH_3CH_2OH (EtOH)

Transition $J(K_{-1},K_{+1})$	Freq. (MHz)	T_A^* (K)	V_{LSR} (kms^{-1})	$\Delta V_{1/2}$ (kms^{-1})	ΔE (cm^{-1})	Comments
$5(2,4)-4(1,3)$	159781.8	~ 0.12	~ 6	~ 6	6.9	Coincides with $HCOOCH_3$. Tentative.
$10(0,10)-9(1,9)$	160699.0	~ 0.06	7.6	7.2	26.1	Tentative.
$9(1,9)-8(0,8)$	161609.1	< 0.06	...	...	20.7	...
$17(4,13)-17(3,14)$	161919.4	< 0.07	...	...	98.2	...
$16(2,15)-16(1,16)$	163171.4	< 0.10	...	...	76.7	...
$17(3,15)-17(2,16)$	163283.6	< 0.10	...	...	91.9	...
$18(3,15)-17(4,14)$	164511.7	< 0.11	...	...	103.5	...
$16(4,12)-16(3,13)$	166441.2	< 0.10	...	...	88.1	...
$18(3,16)-18(2,17)$	169703.3	< 0.06	...	...	102.2	...

6.5.8.7 $(CH_3)_2O$

Dimethyl ether ($(CH_3)_2O$) was readily detected in the frequency range surveyed here. Of the 11 transitions listed in Table 6.30, 8 were detected. Two transition, 18(3,15)–17(4,14) and 21(3,18)–21(4,17), were not detected, though the latter one appears to be present but just below the detection threshold established for this survey. Another transition, 15(3,13)–15(2,14), is obscured by an SO_2 emission feature. The observed transitions all have $\Delta E < 115$ K.

For most of the dimethyl ether emission features, the EE and AA symmetry components are partially blended, while the AE and EA components are superimposed one on another, and together are partially blended with the EE component. We have fit each rotational transition with three gaussians (one gaussian each for the AE+EA, EE, and AA symmetry components) where each gaussian shared a common $\Delta V_{1/2}$ and V_{LSR}, while the inter-gaussian spacing was set equal to the spacing between the symmetry components as determined from laboratory spectroscopy (*see* Equation 6.1). This method resulted in very consistent values for velocity and line widths among the measured rotational transitions, which were typically $V_{LSR} = 8$ km s^{-1} and $\Delta V_{1/2} = 3$ km s^{-1}. For two of the transitions, the symmetry components were separated by approximately ± 1 MHz, which made them unresolvable in this survey. In these cases, the feature was fit with a single gaussian.

Blake *et al.* (1987) assigned dimethyl ether to the compact ridge, while Turner (1991) assigned it to both the compact and extended ridge. However, in this survey and in ZM93, the narrowness of the observed lines lead us to believe that the 2 mm $(CH_3)_2O$ transitions may arise from the extended ridge. Minh *et al.* (1993) mapped dimethyl ether towards Orion(KL) at high angular resolution using the Nobeyama Millimeter Array, and found it to be associated with the compact ridge. However, interferometric observations are insensitive to extended emission.

Hence, given the narrowness of our observed lines, we feel that it would be helpful to map dimethyl ether using a single dish telescope to determine whether $(CH_3)_2O$ has an extended ridge component in addition to its compact ridge component.

Table 6.30. Transitions of $(CH_3)_2O$

Transition $J(K_{-1},K_{+1})$	Freq. (MHz)	T_A^* (K)	V_{LSR} (kms^{-1})	$\Delta V_{1/2}$ (kms^{-1})	ΔE (cm^{-1})	Comments
4(2,3)−3(1,2)EA	160201.6	0.21				
4(2,3)−3(1,2)AE	160201.7					
4(2,3)−3(1,2)EE	160204.1	0.28	7.8	3.11	4.9	...
4(2,3)−3(1,2)AA	160206.6	0.17				
15(2,14)−15(1,15)AE	160518.6	0.07				
15(2,14)−15(1,15)EA						
15(2,14)−15(1,15)EE	160521.7	0.13	∼8	∼3	73.9	Blended with SO_2 and $^{33}SO_2$.
15(2,14)−15(1,15)AA	160524.9	0.09				
14(3,12)−14(2,13)AE	161279.8	0.33				
14(3,12)−14(2,13)EA						
14(3,12)−14(2,13)EE	161282.8	0.40	∼8	∼3	69.9	Blended with $HCOOCH_3$.
14(3,12)−14(2,13)AA	161285.8	0.32				
18(3,15)−17(4,14)AA	162277.4 [a]	<0.07				
18(3,15)−17(4,14)EE	162279.7 [a]	<0.07	...	...	...	...
18(3,15)−17(4,14)AE	162282.1 [a]	<0.07				
18(3,15)−17(4,14)EA						
22(3,19)−22(4,18)AE	162409.5[a]	0.16	8.2	4.14	...	...
22(3,19)−22(4,18)EA	162409.5[a]					
22(3,19)−22(4,18)EE	162410.8[a]					
22(3,19)−22(4,18)AA	162412.0[a]					
8(1,8)−7(0,7)AE	162529.0	0.74	8.0	4.22	17.6	...
8(1,8)−7(0,7)EA	162529.0					
8(1,8)−7(0,7)EE	162529.6					
8(1,8)−7(0,7)AA	162530.3					

Continued, next page.

Table 6.30 continued

Transition $J(K_{-1},K_{+1})$	Freq. (MHz)	T_A^* (K)	V_{LSR} (kms^{-1})	$\Delta V_{1/2}$ (kms^{-1})	ΔE (cm^{-1})	Comments
15(3,13)−15(2,14)EA 15(3,13)−15(2,14)AE	165209.0	...				
15(3,13)−15(2,14)EE	165211.8	...	...	...	79.3	Obscured by SO_2.
15(3,13)−15(2,14)AA	165214.7	...				
21(3,18)−21(4,17)AE 21(3,18)−21(4,17)EA	167678.9 [a]	<0.11				
21(3,18)−21(4,17)EE	167680.4 [a]	<0.11	...	...	...	...
21(3,18)−21(4,17)AA	167682.0 [a]	<0.11				
4(2,2)−3(1,3)AE	167741.5	0.14				
4(2,2)−3(1,3)EA	167741.6					
4(2,2)−3(1,3)EE	167744.1	0.15	8.3	3.78	...	...
4(2,2)−3(1,3)AA	167746.6	0.08				
16(2,15)−16(3,14)AE 16(2,15)−16(3,14)EA	169740.6[a]	0.12				
16(2,15)−16(3,14)EE	169743.4[a]	0.21	7.7	3.14	...	...
16(2,15)−16(3,14)AA	169746.1[a]	0.11				
16(1,16)−16(2,15)AE 16(1,16)−16(2,15)EA	169900.2[a]	0.10				
16(1,16)−16(2,15)EE	169903.6[a]	0.17	7.7	2.79	...	...
16(1,16)−16(2,15)AA	169907.0[a]	0.11				

(a) Frequencies from Anderson, Herbst and De Lucia (1993).

Table 6.31. Recombination Lines

Transition J	Freq. (MHz)	T_A^* (K)	V_{LSR} (kms^{-1})	$\Delta V_{1/2}$ (kms^{-1})	Comments
H34α	160211.6	0.1	-2.4	29	...
H48γ	162956.7	<0.06	...	...	...
H42β	165601.1	...	...	...	Obscured by $^{13}CH_3OH$
He34α	160276.9	<0.06	...	...	...
He48γ	163023.2	...	...	...	Obscured by EtCN
He42β	165668.6	<0.09	...	...	...

6.5.9 Atomic H and He Recombination Lines

There were six reasonably strong radio recombination lines present in the spectral region surveyed (*see* Table 6.31). Three of these lines arise from hydrogen and three from helium. Only the hydrogen H34α line was positively observed. The line profile is broad and partly blended with $(CH_3)_2O$ on the red side. The results of a Gaussian fit to the H34α are listed in Table 6.31 and are consistent with recombination line parameters observed towards Orion(KL) by Johansson *et al.* (1984) and Turner (1991). The H42β line may also be present, though it is mostly obscured by a feature assigned to $^{13}CH_3OH$. Of the four remaining lines, He48γ was obscured by EtCN while the rest were not detected.

6.5.10 Unidentified Spectral Features

Forty-nine unidentified or tentatively identified spectral features were detected in the frequency range, $\sim 160-170$ GHz (*see* 6.32). This density of U-lines is similar to that found by ZM93 in their survey of Orion over the frequency range $\sim 150-160$ GHz. In the ZM93 survey there were forty-six unidentified features. The large number of unidentified lines is partly due to the sensitivity of the survey, but another contributing factor is the use of a single sideband filter. The methods

normally employed to reject the unwanted sideband when using a double side band receiver, such as introducing a small LO shift during the observation or performing a computer convolution, would result in the loss of features which might be blended with stronger lines. A glance at Figure 6.1 quickly reveals that most features in this frequency range are blended with other features. As ZM93 pointed out, for weak and complicated spectra, use of a single sideband receiver is critical.

It is probable that many of these lines may arise from unknown transitions from well known interstellar molecules such as CH_3OH, $HCOOCH_3$, $(CH_3)_2O$, and their isotopic variants. With respect to these molecules, we have supplemented our primary spectral line catalogue (Lovas, 1985) with more recent spectroscopy results. References for these line lists are given in their respective section. In addition, we have used the Lovas list of molecular microwave transitions of astronomical interest (1992) and have searched through the literature for recent detections of new molecular transitions, or recent spectroscopy results on molecules of astronomical interest, which fall within our survey region. We list in Table 6.33 the references which have been consulted in our efforts to identify the U–Lines.

As noted in Table 6.32, fifteen of these features have been tentatively identified as arising from known interstellar molecules. In most of these cases the coincident transition is an unlikely one, usually because it is a high energy level transition. In other cases, the spectral feature was coincident with a transition belonging to a molecule not previously observed towards Orion. Such is the case of U160313, which is coincident with a transition of AlCl. This molecule has been observed towards the evolved star IRC+10216 (Cernicharo and Guélin, 1987), but has not been observed towards Orion. This putative new molecule will, however, require the detection of other AlCl transitions in order to confirm its presence in Orion. In a somewhat similar situation is U162661, which is coincident with a transition of the known molecule NS. However, this NS transition belongs to the so-far

unobserved $^2\Pi_{3/2}$ ladder. Once again, observations of other transitions belonging to the $^2\Pi_{3/2}$ will be required before this identification may be validated.

For each of the unidentified or tentatively identified spectral lines, we calculated their corresponding image-sideband frequency in order to determine if these lines were due to "sideband leakage". In seven cases we found that the image-sideband frequency did correspond to a strong ($T_A^* > 1$ K) emission line in the image-sideband. We have assumed that these features are not U-lines, but are artifacts from the image-sideband and are listed separately in Table 6.34. These features are identified in Figure 6.1 with the label (I).

Having found evidence of sideband leakage in the survey data, we set out to check the image-sideband rejection for each of the spectra. For all frequencies settings in this survey (*see* Table 6.1), except setting 17, their corresponding image-sideband frequencies were either observed in this work or by ZM93. Using this data, we were able to identify all image-sideband lines with $T_A^* > 1$ K and check for sideband leakage in our spectra. For nearly half of the frequency settings, there were no strong emission lines in the image-sideband (settings: 2, 4, 5, 7, 10, 11, 12, 16, 22). Frequency settings 3, 6, 8, 9, 13, 15, 19, 20 and 21 do have strong line(s) in the image-sideband but with no apparent leakage. For these cases we were able to estimate the image band rejection lower limit, based on the strength of the image band feature and the spectral baseline RMS, to be $> 15-21$ dB.

Frequency settings 1, 14, and 18 have features due to image-sideband leakage (*see* Table 6.34), and by comparing the strength of these features and their corresponding image-sideband lines we estimate that the image-sideband rejection was ~ 15 dB. Since some of these features were located in mid-band, where the image-sideband rejection should be ~ 20 dB, we have assumed that there was a problem with the sideband filter during these observations. To make sure that none of the other spectral features in these three spectra were, in fact, due to

strong image-sideband lines, we calculated the corresponding image-sideband frequency for each feature and then checked the image-sideband spectrum for a corresponding line. Except for the features listed in Table 6.34, none of the other spectral lines in spectra 1, 14, or 18 had corresponding image-sideband features and, thus, we conclude that they are valid lines.

Throughout most of this survey, we have required that a would-be feature have an integrated intensity which was at least three times the spectral baseline RMS (*see* Equation 6.2). In the cases of strictly unidentified features (i. e., features without tentative identifications) we required that they be $4\,\sigma$ detections.

Table 6.32. Unidentified Spectral Features

Freq. (MHz)	T_A^* (K)	V_{LSR} [a] (kms^{-1})	$\Delta V_{1/2}$ (kms^{-1})	Comments
159681	0.05	9	5.97	Possible H_2CS, blend $HCOOCH_3$ (see text)
159718	0.08	9	3.56	...
159958	0.05	9	6.37	...
160134	0.05	9	5.30	Possible HC_7N (see text)
160152	0.06	9	5.79	...
160237	0.06	9	4.22	...
160248	0.10	9	2.53	...
160313	0.09	9	2.73	Possible AlCl (see text)
160374	0.04	9	7.47	Possible SiS (see text)
160559	0.05	9	5.03	...
160700	0.06	9	7.16	Possible EtOH (see text)
160799	0.08	9	13.78	...
161472	0.07	9	3.55	Possible H_2CCO, blended EtCN (see text)
161509	0.12	9	28.11	...
161539	0.10	9	11.10	...
161629	0.08	9	8.64	...
161683	0.13	9	4.88	...
161714	0.11	9	7.81	...
161970	0.12	9	2.58	...
162098	0.18	9	1.36	...
162100	0.12	9	2.26	Possible EtCN (see text)
162130	0.08	9	7.20	Possible EtCN (see text)
162570	0.11	9	5.01	...
162580	0.06	9	10.83	Possible SiS (see text)
162589	0.07	9	3.56	...
162598	0.07	9	6.31	...
162661	0.05	9	5.28	Possible NS $^2\Pi_{3/2}$ (see text)
162729	0.06	9	4.02	...
162762	0.05	9	22.26	...
163187	0.10	9	4.80	...
163546	0.09	9	5.09	...
163569	0.06	9	3.42	Possible SO_2 (see text)
163826	0.28	9	4.55	250 kHz Res.
163951	0.25	9	12.88	Possible HNCS (see text)
164035	0.09	9	4.74	...
164395	0.20	9	1.83	Possible EtCN (see text)
164488	0.12	9	5.87	...

Continued, next page.

Table 6.32 continued

Freq. (MHz)	T_A^* (K)	V_{LSR} [a] (kms^{-1})	$\Delta V_{1/2}$ (kms^{-1})	Comments
164549	0.09	9	10.04	...
164949	0.15	9	3.90	...
165075	0.19	9	10.01	...
165085	0.30	9	1.84	...
165719	0.12	9	5.59	...
165909	0.08	9	10.59	...
168826	0.17	9	8.88	Coincides with unlikely SO_2 transition, blend with ^{34}SO (see text)
169720	0.06	9	2.88	Possible OCS (see text)
170157	0.11	9	12.75	250 kHz Res.
170317	0.13	9	5.12	...
170323	0.08	9	5.97	...
170362	0.09	9	4.95	...

(a) Assumed LSR velocity.

6.6 Conclusion

With the completion of this work, in combination with ZM93, we now have a continuous and systematic survey of spectral features in the 2 mm band towards Orion–KL spanning a frequency interval of 20 GHz. Not withstanding the modest sensitivities of these observations, over 415 spectral features were detected (180 features in ZM93; 235 in the present work), and of these ~80 are U–lines. Though many features in this survey are blended together, the use of a single side band receiver has greatly improved our abilities to disentangle such blends. The significant increase in spectral features identified in this work, as compared with ZM93, may be partly due to the use of multiple independent Gaussians in modeling complex spectral features. In ZM93, spectral features were identified by looking for relative maxima in the spectra, a velocity region bracketing this maxima was identified, and moments were then calculated including the velocity

Table 6.33. U–Line Identification Search References

Molecule	Detection	Reference
$C_2H_3^+$	Lab.	Bogey *et al.* (1992)
C_3H, C_3D	Lab. Astro.	Gottlieb *et al.* (1986)
		Yamamoto *et al.* (1990a)
C_3H_4	Lab.	Vrtílek *et al.* (1987)
C_4D	Lab.	Woodward *et al.* (1988)
CH_3CHCH_2	Lab.	Pearson *et al.* (1994)
CCS	Lab. Astro.	Yamamoto *et al.* (1990b)
HCCS	Lab.	Vrtílek *et al.* (1992)
H_2CCC	Lab.	Vrtílek *et al.* (1990)
H_2CCCC	Lab.	Killian *et al.* (1990)
CaNC	Lab.	Steimle, Saito, & Takano (1993)
MgCN	Lab.	Anderson, Steimle, & Ziurys (1994)
MgNC	Lab. Astro.	Kawaguchi *et al.* (1993)
NaCl, KCl, Alf	Astro.	Cernicharo, & Guélin (1987)
SiC	Lab. Astro.	Cernicharo *et al.* (1989)
SiCC	Lab.	Gottlieb, Vrtílek, & Thaddeus (1989)
SiCC, ν_3	Lab.	Bogey *et al.* (1991)

center and full width at half maximum. Only in a few cases was an attempt made to fit a line profile with one or more Gaussians. In this work, all features were modeled with a Gaussians and when significant residuals appeared, hidden spectral lines or velocity components were sometimes exposed. Of course, the reliability of such modeling is inversely proportional to its complexity. However, since most species found in this survey were observed by more than one transition, any putative line revealed by our multiple Gaussian fitting method could usually be checked for consistency by comparing its line parameters with those found for un-blended lines arising from the same species.

This spectral survey has been instrumental in the confirmation of two new interstellar molecular-ions, SO^+ (Irvine 1993; Turner 1992; Woods 1987) and H_2COH^+ (Ohishi *et al.* 1995 *in preparation*).

Table 6.34. Image-Sideband Features

Signal Freq.[a] (MHz)	Image-Sideband Freq.[a] (MHz)	Molecule	Transition	T_A^* (K)
159790	157278	MeOH[b]	2(0)−2(−1)E	2.0
159796	157272	MeOH[b]	1(0)−1(−1)E 3(0)−3(−1)E	2.32
159893	157175	MeOH[b]	5(0)−5(−1)E	2.25
166073	163605	SO_2	14(1,13)−14(0,14)	1.88
168188	165370	MeOH	5(1)−5(0)E	2.08
168326	165232	SO_2	7(1,7)−6(0,6)	2.75
168850	165678	MeOH	6(1)−6(0)E	1.29

(a) Assumed LSR velocity, 9 $km\,s^{-1}$.

(b) image-sideband transitions are from ZM93, the remainder are from this work.

The data set provided by ZM93 and this work provides a great opportunity to apply LTE rotational diagram analysis, as detailed by Johansson *et al.* (1984) and Turner (1991), to a wide variety of species observed in these surveys. The fact that all the data was taken using the same telescope and receiver should greatly simplify the analysis. Moreover, the sheer number of lines observed, especially for the asymmetric tops, should provide for statistically significant results. Unfortunately, time considerations will not allow us to pursue this analysis in the present work; therefore, we shall return to it in a future paper.

Chapter 7

Conclusions

We have carried out radio observations for the interstellar molecules NO, NS, and HCCN in order to investigate the role of nitrogen in the chemistry of the ISM. Abundances of these species and implications for chemical models have been discussed. In addition, we have conducted a spectral line survey towards the star forming region Orion(KL) over the frequency range 160–170 GHz, which revealed a large number of spectral features arising from such nitrogen-bearing molecules as NS, HNCO, HCCCN, CH_3CN, CH_2CHCN, and CH_3CH_2CN. In the following section we summarize our observations and their implications for ion–molecule chemistry models. In section 7.2 we make suggestions for future work.

7.1 Summary

In Chapter 2, we report the results of the first detection of NO in cold dark clouds, specifically in L134N and TMC–1. NO was observed by its two $^2\Pi_{1/2}$ $J=3/2\rightarrow 1/2$ $F=5/2\rightarrow 3/2$ rotational transition hyperfine components at 150.2 and 150.5 GHz. The fractional abundances of NO, relative to H_2, have been found to be $\sim 5\times 10^{-8}$ towards the SO peak in L134N [hereafter L134N(SO)], and $\sim 2\times 10^{-8}$ towards the NH_3 and CH_3CH_2 peak in TMC–1 [hereafter TMC–1(NH_3)]. Most ion–molecule chemistry models predict an NO steady-state fractional abundance of $\sim 10^{-7}$, which is in good agreement with our L134N(SO) abundance. Combining our NO abundance for L134N with observed abundances for N_2H^+ and $H^{13}CO^+$, we deduced a ratio of N_2 to NO > 100. This suggests that the bulk of the gas phase nitrogen is probably in the form of N_2, as gas phase ion–molecule chemistry models predict. The observed NO abundance towards

TMC–1(NH_3) of $\sim 2\times10^{-8}$ is slightly less than the abundance observed for L134N. Our inferred NO abundance for TMC-1(NH_3) is best matched by "early time" ion–molecule chemistry model values which also produce the best match for many other molecular species with abundances observed in TMC–1.

In Chapter 3, we report on the first detection of NS in quiescent dark clouds, again in the sources L134N and TMC–1. In each source, several hyperfine components of the $^2\Pi_{1/2}$ $J=3/2\rightarrow1/2$ (69 GHz) and $J=5/2\rightarrow3/2$ (115 GHz) rotational transitions were observed. The NS emission was found to be extended along the TMC–1 ridge with the highest column density observed towards the TMC–1(NH_3) position, with a secondary maximum coincident with the cyanopolyyne peak position. The NS emission in L134N is also extended, with the strongest emission coinciding with the NH_3 peak [hereafter L134N(NH_3)].

Our most extensive NS dark cloud observations were made towards TMC–1(NH_3). We were able to match the observations only if we assumed an excitation temperature that decreases with increasing energy above the ground state, which gives us a fractional abundance of NS relative to molecular hydrogen of $\sim8\times10^{-10}$ for TMC–1(NH_3), and $\sim6\times10^{-10}$ for L134N(NH_3). Our derived abundances for NS are significantly higher than those predicted by recent gas phase ion-molecule chemistry models, although there are large variations among the model results, $f(NS) \sim 10^{-14} - 10^{-10}$. The inclusion of NS in ion–molecule chemistry models is relatively recent. In at least one model the major production path for NS under dark cloud conditions involves the as yet unobserved species HS and HNS^+. Since the initial hydrogenation of both sulfur and nitrogen in molecular clouds is thought to be indirect, the abundance of NS in the gas-phase may depend on a relatively long chain of reactions. All these factors contribute to the large variation in predicted NS abundances.

In the course of our NS observations towards TMC–1 and L134N, we noticed that our LSR velocities derived from $J=3/2\rightarrow 1/2$ parity–f transitions (see the discussion of spectral notation in the Appendix) were slightly low in comparison to values observed for many molecular lines in these sources, while the corresponding LSR velocities of the $J=3/2\rightarrow 2/2$ parity–e transitions were systematically high. These discrepancies corresponded to about 100 kHz and 200 kHz, respectively, while the quoted precision of the laboratory values was $\pm$50 kHz. We also noticed discrepancies in the spacing of the $J=5/2\rightarrow 3/2$ hyperfine components. Motivated by our findings, new laboratory spectroscopy on NS was carried out which led to significant improvements (precisions of 2 to 10 times over earlier results) in the determination of NS molecular constants such as the Λ–doubling constant, rotational constant, centrifugal distortion constant, and hyperfine coupling constants (Lee, Ozeki and Saito 1995).

In Chapter 4, we have presented the results of the first comprehensive survey of NS towards regions of massive star formation. NS was observed by means of its $^2\Pi_{1/2}$ $J=3/2\rightarrow 1/2$, $J=5/2\rightarrow 3/2$, and $J=7/2\rightarrow 5/2$ transitions at 69 GHz, 115 GHz, and 161 GHz, respectively. Of the 14 GMC's observed, NS was found in 12 of them. The relative strengths of the observed hyperfine components are consistent with optically thin emission, with the possible exception Sgr B2(M). The two sources where NS was not detected were W3(IRS5) and W49(N). We also carried out an unsuccessful search for NS towards the evolved carbon star IRC+10216.

NS abundances were estimated using a statistical equilibrium (SE) model. In this model there are three fit parameters, the gas kinetic temperature, the H_2 density, and the NS fractional abundance relative to H_2. For all our sources, we only had two observed rotational transitions from which accurate line parameters could be measured, and, thus, were unable to fully constrain the model. We

therefore assumed a gas kinetic temperature derived from NH_3 observations. We were then able to duplicate the observed NS line intensities for most sources without assuming a beam filling factor. However, we were unable to exactly match the observed NS line intensities for Orion(KL), Orion(1.5S) and W3(OH). The statistical equilibrium model results indicate that NS emission arises from regions where $n(H_2) \sim 10^5$ cm^3, which is at or below the critical density for the observed transitions; consequently, these transitions have low excitation temperatures. The statistical equilibrium models also agreed that NS emission was optically thin for most sources, with the exception of Sgr B2(M), which is consistent with the findings of our NS hyperfine line intensity analysis.

For those sources with extended and optically thin NS emission, we estimate the fractional abundance of NS relative to H_2 to be in the range $0.5 - 2.0 \times 10^{-11}$, which is consistent with the early-time NS model abundances calculated by Hasegawa, Herbst and Leung (1992) and Hasegawa and Herbst (1993), which are based on the gas-phase reaction networks developed by Herbst and Leung (1989, 1990) but which also include the effects of grain chemistry. Our estimates for the NS fractional abundances in GMC's are one to three orders of magnitude greater than those predicted by the purely gas-phase models of Miller and Herbst (1990) and Miller *et al.* (1991). The disparity in predictions between these two sets of models for NS abundances, as well as for many other species, appears to be linked to the choices each group has made in selecting reaction rate coefficients (*see* Miller, Leung and Herbst 1987) as well as the effects of grains. For Sgr B2(M), where NS appears to be optically thick, the NS fractional abundance of $\sim 14 \times 10^{-11}$ is slightly greater than any of the chemistry model's peak abundance. We hope that our observed abundances for NS will help constrain the model parameters and hence to improve our understanding of both nitrogen and sulfur chemistry in the ISM.

Three sources, Orion(KL), Orion(1.5S) and W3(OH), have $[J=5/2\rightarrow 3/2]/[J=3/2\rightarrow 1/2]$ ratios which are significantly higher (3.6, 2.8 and 3.0 respectively) than the other sources (~ 1.5 on average). The relative line strengths of the $J=3/2\rightarrow 1/2$ and $J=5/2\rightarrow 3/2$ transitions for Orion(KL) and Orion(1.5S) suggest that the NS emission in these clouds arise from higher density regions than for the other sources and, hence, may be thermalized. Mapping the distribution of NS in OMC–1 also suggests that the emission towards (KL) and (1.5S) may not be extended (certainly $\theta_S < 85''$). Both Orion(KL) and Orion(1.5S) are known to have spatially compact emission regions associated with outflows, and our observed NS line parameters toward (KL) are consistent with compact ridge emission. For Orion(KL) and Orion(1.5S) we were able to average together pixels from our NS map in order to generate $J=5/2\rightarrow 3/2$ spectra with spatial resolution similar to that of the $J=3/2\rightarrow 1/2$ observations. In this way, the intensity ratios for both Orion(KL) and Orion(1.5S) became consistent with the other sources (2.0 and 1.2 respectively). Using the averaged data in the SE model resulted in derived molecular hydrogen densities and fractional abundances similar to those found for other clouds.

We have mapped the distribution of NS in the Orion molecular cloud. NS is strongly peaked towards Orion(KL), also shows a peak toward Orion(1.5S), and extends both north and south for $\sim 4'$ along the "extended ridge". We have also found that by fixing $n(H_2)=300\times 10^4$ cm^{-3} and $T_K=45$, and 60 K for (1.5S) and (KL) respectively (Bergin 1995), we could very nearly reproduce the observed line intensities; however, we still can not rule out moderate beam dilution. Comparing the NS distribution in Orion with the results of the FCRAO Orion Chemistry Survey, we find that the pattern of NS distribution is shared by other molecules, such as SO and CH_3OH. It has also been suggested that grain processes may be responsible for the enhanced abundances of SO and CH_3OH towards the compact

ridge (*see* Blake *et al.* 1987; Bergin 1995). CH_3OH has in fact been observed on grain surfaces (Allamandola, Sandford and Tielens 1992). It seems counter intuitive that NS, which is a radical, may be abundant in hot, dense regions such as Orion(KL) and (1.5S). One possible explanation may involve the release of grain-bound NS into the gas-phase as outflows in these regions interact with quiescent material.

In Chapter 5, we report a deep search towards molecular clouds for the newly identified circumstellar molecule HCCN. This molecule has only been detected towards the carbon star IRC+10216. We searched for HCCN by its $N(J)=1(2)\rightarrow 0(1)$ transition towards the dark cloud TMC–1 and toward the GMC's Sgr B2(NW), G34.3+0.2, and W51(H_2O). We did not detect HCCN towards any of these sources; however, we were able to place an upper limit for the fractional abundance of HCCN with respect to H_2 towards TMC–1 of $\leq 2\times10^{-10}$. We also estimated total column density upper limits for the GMC's to be $N_{HCCN} \leq 4 - 10\times10^{13}$ cm s^{-1}.

The predominance of interstellar molecular species with carbon-carbon triple bonds has suggested that carbon chains are formed through the addition of acetylenic units, which would produce molecules such as the cyanopolyynes ($HC_{2n}CN$). Another possibility is that carbon atoms could be added singly, leading to the production of molecules such as HCCN. Thus, the detection of HCCN might indicate a new interstellar carbon chain series ($HC_{2n}N$), which would be useful in studying how carbon chain molecules are formed. Comparing the TMC–1 HCCN fractional abundance upper limit with abundances for HCN and HCCCN, we find HCN:HCCN:HCCCN to be $1 : < 0.02 : 0.3$. The fact that we did not detect HCCN to a very low level would suggest that carbon chain formation by acetylenic units may be the dominant processes. However, destruction pathways must also be considered. Thus, the fact that the HCCN radical has a structure best

approximated by $H-\dot{C}=C=\dot{N}$ may allow it to participate in destruction reactions not available to the more stable, closed shell species HCN and HCCCN.

It has been suggested that the final step in HCCN formation may be a dissociative recombination reaction, $H_3C_2N^+ + e$ resulting in HCCN and H_2. This reaction has also been suggested as a production path for another observed interstellar molecule, H_2C_2N, in which case only one hydrogen atom is liberated. Since the number of hydrogen atoms which dissociate during electron recombination is typically unconstrained by experimental data, measuring the [HCCN]/[H_2C_2N] ratio toward a dark cloud such as TMC–1 provides important constraints on theoretical models pertaining to dissociative recombination reactions. The fact that H_2C_2N has been detected towards TMC–1, while HCCN has not, would suggest that dissociative recombination favors the splitting off of a single H atom. Once again, this result depends on HCCN and H_2C_2N sharing similar destruction rates.

In Chapter 6, we report the results of a 2 mm band spectral line survey of Orion(KL) over the frequency range 159.4–170.4 GHz. Over 235 spectral lines were detected, including $\sim$ 35 unidentified features. Transitions from sixteen known interstellar species were conclusively identified in Orion from this data, with the largest numbers of lines arising from the nitrogen-bearing molecule ethyl cyanide (CH_3CN), followed by methyl formate ($HCOOCH_3$), methanol (CH_3OH), and dimethyl ether [$(CH_3)_2O$]. Lines of several additional molecules have been tentatively identified, including formamide (NH_2CHO), isothiocyanic acid (HNCS), and ethanol (CH_3CH_2OH). We have also reported the possible detection of a new interstellar ion, H_2COH^+. Of the sixteen species clearly present in this survey, five of them are nitrogen-bearing molecules (NS, HCCCN, CH_3CN, CH_2CHCN, and CH_3CH_2CN). Chapter 6 is a continuation of the Ziurys and McGonagle (1993)

survey, which covered the frequencies 150–160 GHz. Taken together, these surveys form the most extensive catalog of interstellar spectral lines in the 2 mm band.

Many of the spectral features observed in the 2 mm band survey have asymmetric line profiles suggesting that they are composed of multiple velocity components. There are several velocity components along the line of sight toward Orion(KL), which are the hot-core, the plateau, the extended ridge, and the compact ridge. By taking advantage of the fact that most species were observed via several transitions, and using multiple Gaussian fits to measure line parameters, we were able to identify which velocity component(s) are present for a particular species. From this analysis we find further evidence for chemical selection in the distribution of molecules amongst the various regions in Orion(KL).

In Chapters 3 and 4, we report the detection of an unidentified spectral feature at $\sim$ 69408 MHz (U69408). This relatively strong feature was first seen towards L134N and is extended in this source (Chapter 3). U69408 has also been detected towards the GMC, W51(MS). We have actively searched for U69408 towards TMC–1, but we have not detected it. In comparison with L134N, TMC–1 is generally the more chemically rich source. Thus, finding a molecule which exists in L134N and not in TMC–1 is intriguing, and its ultimate identification may be helpful in understanding the chemical differences which distinguish these physically similar clouds.

Another U-line was seen blended with the NS $J=3/2\rightarrow 1/2$ $F=3/2\rightarrow 1/2$ hyperfine component in the spectra of DR21(OH), Orion(KL), Orion(1.5S), and W51(MS) (Chapter 4). This feature has since been identified as the ortho $N_{KK}=4_{04}\rightarrow 3_{13}$, $J=3\rightarrow 2$ fine structure transition of methylene, CH_2 (Hollis, Jewell, and Lovas 1994).

7.2 Future Work

The uncertainties in our derived values for NS abundances, in both quiescent dark clouds and regions of active star formation, are partly a result of the modest signal to noise ratios of our spectra. Increasing the signal to noise ratios would naturally reduce these uncertainties. Furthermore, by augmenting our observed $J=3/2 \rightarrow 5/2$ and $J=5/2 \rightarrow 3/2$ transitions with 2 mm band observations of the $J=7/2 \rightarrow 5/2$ transition, we could run statistical equilibrium models on our sources without having to assume gas kinetic temperatures.

To specify the spatial distribution of NO and NS in dark clouds could be useful in studying chemical gradients within such clouds. Identifying a correlation between the abundances of NO and NS, or the lack thereof, would be of interest to investigators working on ion–molecule chemistry models. In addition, FCRAO is currently conducting a chemistry survey of the dark clouds TMC–1 and L134N where 3 mm band transitions of over 20 molecular species are being systematically mapped. At present, NS has not been included in this survey because of its weak line intensities; however, FCRAO plans to significantly increase the sensitivity of their focal plane array within the next few years, which will make it possible to map NS in dark clouds. By comparing the distribution of NS with the distribution of other species we will be able to better understand its role in the chemical evolution of dark clouds. Unfortunately, since the fundamental transition of NO occurs in the 2 mm band, we do not foresee a time in the near future when it will be feasible to extensively map the distribution of NO in dark clouds.

Our current observations towards OMC–1 suggests that NS emission is enhanced towards the outflow regions Orion(KL) and Orion(1.5S) relative to the extended NS emission observed along the ridge. Release of grain-bound NS via grain-grain collisions may account for this observed enhancement, but other desorption mechanisms cannot be ruled out (i. e., simple thermal evaporation).

Observations of NS at higher angular resolution towards these and other outflow sources would help to determine if NS is a tracer of active regions in dense molecular clouds and may prove useful in studying grain processes.

The 2 mm band spectral survey provides several avenues for future observations. Higher spectral resolution observation of the 2 mm band OCS, $(CH_3)_2O$, and CH_3CH_2CN transitions are needed to identify their emission sources in Orion(KL) (i.e., to distinguish between compact ridge and extended ridge emission). Further observations are needed to confirm the tentative detection of H_2COH^+ in Orion, as well as the even more tentative detection of AlCl. Finally, the 2 mm survey has provided us with a rich data base of observed molecular transitions, which could be used to conduct LTE rotational diagram analysis on the wide variety of molecules observed in the survey.

Appendix

THE ROTATIONAL SPECTRA OF NO AND NS

In this appendix the spectra of NO and NS are described. Since both molecules have similar electronic structure, the same quantum mechanical considerations apply to both. The details of the Pi-doublet ($^2\Pi$) spectra are discussed in the context of the NO molecule, but can be equally applied to NS. The description of the NS spectrum is limited to qualities specific to NS. For more information on $^2\Pi$ spectra, see Townes and Schawlow (1975) chapters 7 & 8. In the following discussion, bold face letters denote a vector.

For a molecule with only two atoms, the rotational spectrum of NO is a *tour de force* of quantum mechanical interactions. An unpaired electron results in NO having a $^2\Pi$ ground electronic state. The electron spin is described by the quantum number $S = 1/2$, and the electron orbital angular momentum projection along the molecular axis by $\Lambda = \pm 1$.

Other angular momenta to which these vectors can couple include the orbital angular momentum of the nuclei **O** (rotation of the molecule) and the nuclear spin **I** (if any). These subtleties complicate rotational spectra of molecules and must be taken into account.

In an attempt to systematically approach this problem of coupling schemes, spectroscopists have defined five ideal cases collectively referred to as Hund's cases. In Hund's case (a) both the electron orbital momentum, **L**, and the electron spin, **S**, interact most strongly with the molecular axis, **A** (*see* Figure A.1). Hund's case (a) can be represented (schematically) as,

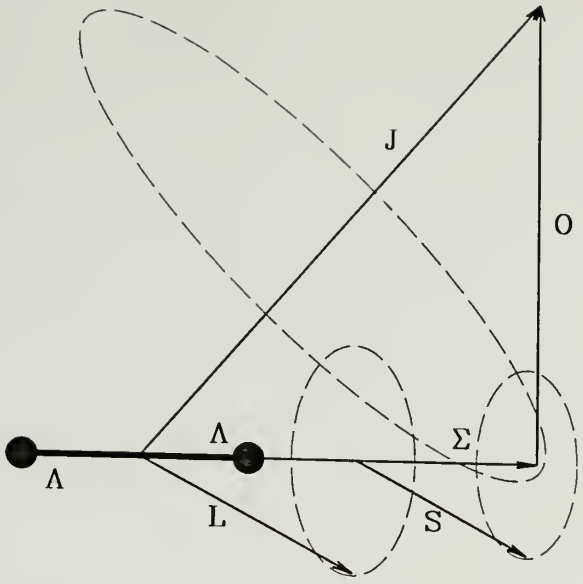

Figure A.1. Vector diagram of Hunds case (a), were the electron orbital momentum vector **L** and spin momentum vector **S** interact most strongly with the molecular axis **A**. **L** and **S** precess rapidly about **A**, which precess more slowly around the total angular momentum vector **J**. Dashed circles indicate precessional motions. Rapid end-over-end rotation of the molecule can, in some cases, lead to a decoupling of **S** from **A**, which causes a transition from Hunds case (a) for low rotational states to (b) for higher states (*After* Townes & Schawlow 1975; see text for more details).

$$\mathbf{LA} \gg \mathbf{LS} \text{ or } \mathbf{LO} \tag{A.1}$$

$$\mathbf{SA} \gg \mathbf{SN} . \tag{A.2}$$

Hund's case (b) differs from (a) in that the electron spin couples more strongly to the orbital–angular momentum, **N**, than it does with the molecular axis **A**. Hund's case (b) is defined by,

$$\mathbf{LA} \gg \mathbf{LS} \text{ or } \mathbf{LO} \tag{A.3}$$

$$\mathbf{SN} \gg \mathbf{SA} . \tag{A.4}$$

Under extreme conditions, rapid end-over-end rotation of the molecule may almost completely uncouple the **S** from the molecular axis **A**. This effect produces a transition from Hunds case (a) for low rotational states to case (b) for higher states.

As the reader may have already guessed, NO is neither a pure Hund's case (a) or (b) but instead is an intermediate Hund's case (a–b). Hund's case (a), however, is a very good approximation for NO, especially for low rotational states. The coupling between the molecular axis and the electron spin produces a projection of the latter on the molecular axis, Σ, which splits the $^2\Pi$ ground state into two subsets or ladders. The ladders are identified by the quantity defined as $\Omega = |\Lambda + \Sigma|$, and are labeled as $^2\Pi_{1/2}$ and $^2\Pi_{3/2}$. Figure A.2 illustrates the rotational energy levels for a regular case (a) $^2\Pi$ molecule.

The spin orbit coupling constant is positive for NO and, hence, the $^2\Pi$ state is regular, which means that the lowest rotational level corresponds to the $^2\Pi_{1/2}$ ladder. A subscript (r) denotes a regular doublet-Pi molecule ($^2\Pi_r$). The lowest $^2\Pi_{3/2}$ rotational level is J = 3/2, which is 180 K above the lowest $^2\Pi_{1/2}$ (J = 1/2) level. Both the NO and NS $^2\Pi_{3/2}$ ladders lie so high in energy above the ground rotational state that these ladders are often ignored in astronomical work, since they are thought unlikely to be populated in quiescent cold dark clouds.

Interaction between the electron angular momentum and the molecule's rotation splits each rotational level J into a doublet whose members are of opposite parity, in a process known as Λ–type doubling (*see* Figure A.3). In each pair of upper and lower levels, one level has even parity and the other has odd. The parities are swapped for each successive J rotational level. This sets up two series of non-degenerate rotational levels. The lower levels are sometimes labeled as belonging to the Π^+ series, while all the upper levels belong to the Π^-. The plus and minus signs are used here to distinguish between the two series and are keyed

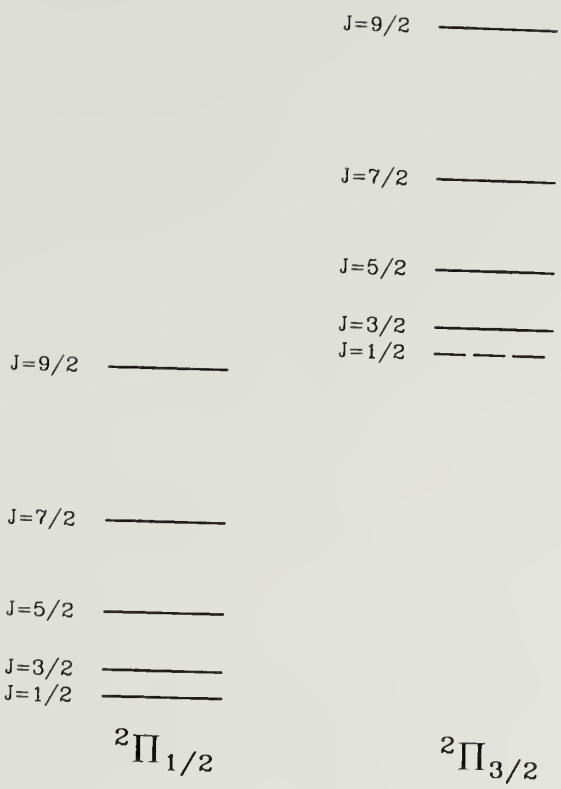

Figure A.2. The lower rotational energy levels of a Hunds case (a) molecule in the $^2\Pi$ state. Λ-doubling of the rotational levels is to small to be seen on this scale (*see* Fig. A.3). The dashed level cannot occur, since J must be greater than or equal to Ω.

to the parity of the series' lowest level (J = 1/2). The parity for each rotational level within each series of the $^2\Pi_{1/2}$ substate is defined by the following expressions:

$$\Pi^+ \quad J = (2n+1)/2 \begin{cases} \text{parity} + \text{for } n = 0, 2, 4, \ldots \\ \text{parity} - \text{for } n = 1, 3, 5, \ldots \end{cases} \tag{A.5}$$

$$\Pi^- \quad J = (2n+1)/2 \begin{cases} \text{parity} - \text{for } n = 0, 2, 4, \ldots \\ \text{parity} + \text{for } n = 1, 3, 5, \ldots \end{cases} \tag{A.6}$$

The lowest Λ-type doublet component of the J = 1/2 level has positive parity and is the first level of the Π^+ series. Likewise, the upper Λ-type doublet component of the J = 1/2 level has odd parity and begins the Π^- series. The selection rules for electric dipole transitions state that transitions may only occur between levels of opposite parity. This requirement leads to two sets of transitions, the Π^+ and Π^- bands, each connecting the levels of the Π^+ or the Π^- series, respectively.

The identifiers for the Λ-type doublets are not standardized. Instead of Π^+ and Π^- used by Gallagher and Johnson (1956) in their study of the NO spectrum, some authors use consecutive letters to differentiate between parities, for example: Lovas and Tiemann (1974b) use parity-a and parity-b, Amano *et al.* (1969) use parity-c and parity-d, and Anacona *et al.* (1986) use parity-e and parity-f. In these labeling schemes the letters a, c, and e correspond to the $^2\Pi_{1/2}$ Λ-type doublet lower levels (Π^+), while b, d, and f label the upper levels (Π^-). The labeling is reversed for the $^2\Pi_{3/2}$ ladder. In this thesis, we have adopted the parity–e, parity–f convention for both NO and NS.

The nitrogen nucleus has a spin angular momentum I = 1, which couples with the molecule's remaining total angular momentum, J, resulting in splitting of the non-degenerate rotational levels into $(2\min(I, J) + 1)$ hyperfine levels (*see* Figure A.3). For NO and NS, the hyperfine splitting occurs through the interaction of both the electric quadrupole moment and the magnetic moment of the nitrogen nucleus with other molecular momenta. This hyperfine structure is consistent with coupling case (a_β) in which the nuclear spin is coupled to the molecular rotation J.

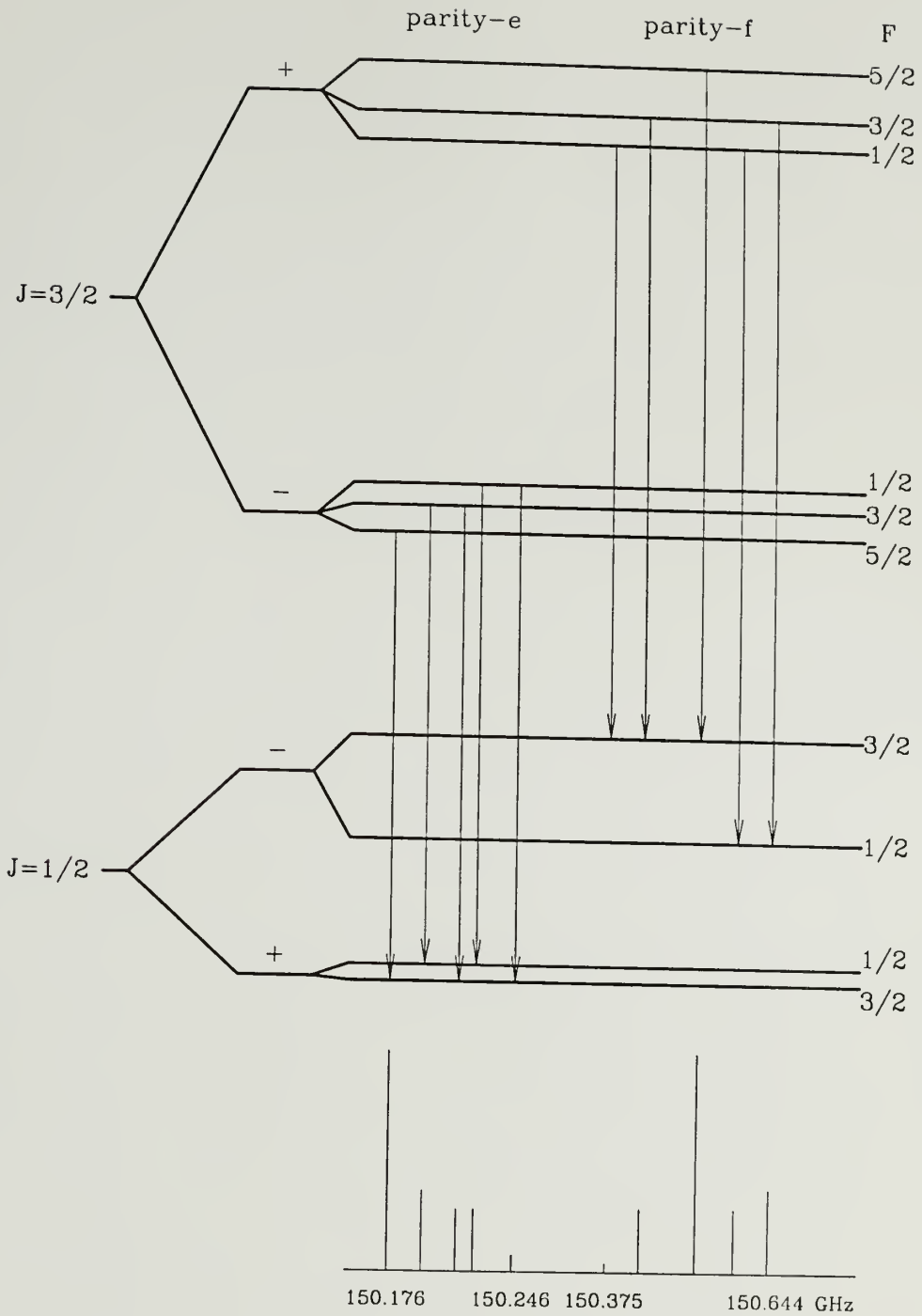

Figure A.3. Energy level diagram and spectrum of the $J=3/2 \rightarrow 1/2$ rotation transition of the $^2\Pi$ state of NO (*After* Townes & Schawlow 1975).

The case (a_β) type hyperfine structure is identical for both members of the Λ-type doublets and applies to the NO $^2\Pi_{3/2}$ state (*see* Townes and Schawlow 1975, pp. 197, 199). The $^2\Pi_{1/2}$ state hyperfine structure has an additional complication of electron spin–nuclear spin interactions which, in the case of NO and NS, result in a different hyperfine structure for the two Λ-type doubling components referred to as hyperfine doubling (Townes and Schawlow 1975, pp. 203–207). Each hyperfine level has a quantum number $F = I + J$, where F ranges from $|I - J|$ to $|I + J|$, and a statistical weight, $g_f = 2F + 1$. The selection rules for transitions between hyperfine components are $\Delta J = \pm 1$ and $\Delta F = 0, \pm 1$. From these selection rules it can be shown that the NO and NS $J = 3/2 \rightarrow 1/2$ transitions have five hyperfine components per parity band, while all other transitions have six.

The line strength for an individual hyperfine component can be written as a fraction of the rotational transition total line strength,

$$S_{J'J''F'F''} = \mathcal{J}_{F'F''} S_{J'J''}, \tag{A.7}$$

where $S_{J'J''}$ is the rotational line strength and $\mathcal{J}_{F'F''}$ is a dimensionless proper fraction which obeys the sum rules:

$$\sum_{F'} \sum_{F''} \mathcal{J}_{F'F''} = 1 \ , \tag{A.8}$$

$$\sum_{F''} \mathcal{J}_{F'F''} = \frac{2F' + 1}{(2I + 1)(2J' + 1)} \ , \tag{A.9}$$

$$\sum_{F'} \mathcal{J}_{F'F''} = \frac{2F'' + 1}{(2I + 1)(2J'' + 1)} \ , \tag{A.10}$$

(Tatum, 1986). The numerical value of $\mathcal{J}_{F'F''}$, thus, depends on the quantum numbers which describe the transition and can be written in functional form as:

$$\mathcal{J}_{F'F''} = H(I; J', F'; J'', F'').$$

Specifically for NO, where I = 1 and $\Delta J = \pm 1$, the function H is defined as:

$$H = \frac{-(2F+1)\left[J^2-(I+F+1)^2\right]\left[J^2-(I-F)^2\right]}{4J(4J^2-1)(2I+1)F(F+1)}\,, \quad \Delta F = 0: \tag{A.11}$$

$$H = \frac{\left[(J\pm F)^2-(I+1)^2\right]\left[(J\pm F)^2-I^2\right]}{4J(4J^2-1)(2I+1)F}\,, \quad \Delta F = \pm I: \tag{A.12}$$

(Tatum, 1986). In equations (A.11) and (A.12) J and F are the larger of the two values describing the transition.

The spectrum of NO was calculated and compared with laboratory measurements by Gallagher and Johnson (1956). The electric-dipole moment for NO is 0.1587 D (Ames & Huebner 1987). The rotational spectrum of NO is further discussed in Gerin *et al.* (1992). A detailed discussion of Hund's classification of molecules, Λ–type doubling, and hyperfine structure may be found in Townes and Schawlow (1975, ch. 7–8).

The molecule NS, like NO, has a $^2\Pi_r$ ground state. Since NO and NS have similar electronic structure, they show the same pattern of hyperfine structure (Amano, 1969). The ratio of the spin-orbit to rotational constants (A/B) is large and positive, which means NS is well characterized by the Hund's case (a) coupling scheme, and the $^2\Pi_{1/2}$ ladder is lower in energy than the $^2\Pi_{3/2}$ ladder. The $^2\Pi_{3/2}$ state begins 322 K above the ground state (Gottlieb *et al.*, 1975). Amano (1969) determined the NS electric-dipole moment to be $\mu_o = 1.81 \pm 0.02$D. The millimeter spectroscopy of NS is presented in Anacona *et al.*, (1986) and has been more recently measured with increased accuracy by Lee, Ozeki, and Saito (1995).

References

Adams, N.G., & Smith, D. 1988a, *Chem. Phys. Letters*, **144**, 11.

Adams, N.G., & Smith, D. 1988b, in *Rate Coefficients in Astrochemistry*, ed. T.J. Millar and D.A. Williams (Dordrecht: Kluwer Academic) p. 173.

Allamandola, L.J., Sandford, S.A., & Tielens, A.G.G.M. 1992, *ApJ*, **399**, 1.

Amano, T., Amano, T., & Warner, H.E. 1991, *J. Molec. Spectrosc.*, **146**, 519.

Amano, T., Saito, S., Hirato, E., & Morino, Y. 1969, *J. Molec. Spectrosc.*, **32**, 97.

Ames, S., & Huebner, W.F. 1977, *Emission Cross Sections for Rotational Transitions of Molecules of Astrophysical Interest*, LA-6366. Los Alomos Scientific Laboratory, University of California.

Anacona, J.L., Bogey, M., Davies, P.B., Demuynck, C., & Destombes, J.L. 1986, *Mol. Phys.*, **59**, 81.

Anderson, M.A., Steimle, T.C., & Ziurys, L.M. 1994, *ApJ*, **429**, L41.

Anderson, T., Herbst, E., & De Lucia, F.C. 1987, *ApJS*, **64**, 703.

Anderson, T., Herbst, E., & De Lucia, F.C. 1993, *J. of Mol. Phys.*, **159**, 410.

Anderson, T., Crownover, R.L., Herbst, E., & De Lucia, F.C. 1988, *ApJS*, **67**, 135.

Anderson, T., De Lucia, F.C., & Herbst, E. 1990, *ApJS*, **72**, 797.

Andersson, M. 1985, in ESO-IRAM-Onsala Workshop on *(Sub)Millimeter Astronomy* (Germany: ESO), p. 353.

Andersson, M., & Garay, G. 1986, *A&A*, **167**, L1.

Askne, J., Höglund, B., Hjalmarson, Å., & Irvine, W.M. 1984, *A&A*, **130**, 318.

Bates, R.D. 1986, *ApJ*, **306**, L45.

Bates, R.D. 1989, *ApJ*, **344**, 531.

Beck, S.C., Bloemhof, E.E., Serabyn, E., Townes, C.H., Tokunaga, A.T., Lacy, J.H., Smith, H.A. 1982, *ApJ*, **253**, L83.

Beckwith, S., Persson, S.E., Neugebauer, G., Becklin, E.E. 1978, *ApJ*, **223**, 464.

Bennett, R.J.M. 1970, *MNRAS*, **147**, 35.

Bergin, E.A. 1995, *Ph.D. Thesis, University of Massachusetts.*

Bergman, P. 1992, *Ph.D. Thesis, Chalmers.*

Blake, G.A., Sutton, E.C., Masson, C.R., & Phillips, T.G. 1986, *ApJS*, **60**, 357.

Blake, G.A., Sutton, E.C., Masson, C.R., & Phillips, T.G. 1987, *ApJ*, **315**, 621.

Bogey, M., Demuynck, C., Destombes, J.L., & Walters, A.D. 1991, *A&A*, **247**, L13.

Bogey, M., Cordonnier, M., Demuynck, C., & Destombes, J.L. 1992, *ApJ*, **399**, L103.

Brotten, N.W., MacLeod, J.M., Avery, L.W., Irvine, W.M., Höglund, B., Friberg, P., & Hjalmarson, Å. 1984, *ApJ*, **276**, L25.

Carlstrom, J.E., & Vogel, S.N. 1989, *ApJ*, **337**, 408.

Castor, J.I. 1970, *MNRAS*, **149**, 111.

Cernicharo, J., & Guélin, M. 1987, *A&A*, **183**, L10.

Cerhicharo, J., Gottlieb, C.A., Guélin, M., Thaddeus, P., & Vrtílek, J.M. 1989, *ApJ*, **341**, L25.

Chomiak, D., Taleb-Bendiab, A. & Amano, T. 1994, *Canadian J. of Phys.*, **72**, 1078.

Churchwell, E., & Hollis, J.M. 1983, *ApJ*, **272**, 591.

Churchwell, E., Felli, M., Wood, D.O.S., and Massi, M. 1987, *ApJ*, **321**, 516.

Crutchers, R.M., & Watson, W.D. 1985, in *Molecular Astrophysics*, ed. G.H.F. Diescksen *et al.* (Dordrecht: Reidel). p. 255.

Cummins, S.E., Linke, R.A., & Thaddeus, P. 1986, *ApJS*, **60**, 819.

deJong, T., Chu, S.L., & Dalgarno, A. 1975, *ApJ*, **199**, 69.

Duley, W.W., Millar, T.J., & Williams, D.A. 1980, *MNRAS*, **192**, 945.

Endo, Y., & Ohshima, Y. 1993, *J. Chem. Phys.*, **98**, 6618.

Erickson, N.R., Goldsmith, P.F., Snell, R.L., Berson, R.L., Huguenin, G.R., Ulich, B.L., & Lada, C.J. 1982, *ApJ*, **261**, L103.

Erickson, N.R., Goldsmith, P.F., Novak, G., Grosslein, R.M., Viscuso, P.J., Erickson, R.B., & Predmore, C.R. 1992, *IEEE Trans. Microwave Theory Tech.*, **40**, 1.

Frerking, M.A., & Linke, R.A. 1979, *ApJ*, **234**, L143.

Friberg, P., Madden, S.C., Hjalmarson, Å., & Irvine, W.M. 1988, *A&A*, **195**, 281.

Gallagher, J.J., & Johnson, C.M. 1956, *Phys. Rev.*, **103**, 1727.

Garay, G., Moran, J.M., & Reid, M.J. 1987, *ApJ*, **314**, 535.

Gaume, R.A., & Claussen, M.J. 1990, *ApJ*, **351**, 538.

Genzel, R., & Stutzki, J. 1989, *ARA&A*, **27**, 41.

Genzel, R., Reid, M.J., Moran, J.M., & Downes, D. 1981, *ApJ*, **244**, 884.

Gerin, M., Viala, Y., & Casoli, F. 1993, *A&A*, **268**, 212.

Gerin, M., Viala, Y., Pauzat, F., & Ellinger, Y. 1992, *A&A*, **266**, 463.

Goldreich, P., & Kwan, J. 1974, *ApJ*, **189**, 441.

Goldsmith, P.F., Krotkov, R., & Snell, R.L., Brown, R.D., & Godfrey, P.D. 1983, *ApJ*, **274**, 184.

Goldsmith, P.F., Krotkov, R., & Snell, R.L. 1985, *ApJ*, **299**, 405.

Goldsmith, P.F., Snell, R.L., & Lis, D. 1987, *ApJ*, **313**, L5.

Goldsmith, P.F., Lis, D.C., Hills, Y., & Lasenby, J. 1990, *ApJ*, **350**, 186.

Goldsmith, P.F., Lis, D.C., Lester, D.F., & Harvey, P.M. 1992, *ApJ*, **389**, 338.

Goldsmith, P.F., Snell, R.L., Deguchi, S., Krotkov, R. & Linke, R.A. 1982, *ApJ*, **260**, 147.

Goldsmith, P.F., Snell, R.L., Hasegawa, T., & Ukita, N. 1987, *ApJ*, **314**, 525.

Gordon, M.A. 1987, *ApJ*, **316**, 258.

Gordon, M.A., Berkermann, U., Mezger, P.G., Zylka, R., Haslam, C.G.T., Kreysa, E., Sievers, A., & Lemke, R. 1993, *A&A*, **280**, 208.

Gottlieb, C.A., Ball, J.A., Gottlieb, E.W., & Penfield, H. 1975, *ApJ*, **200**, L147.

Gottlieb, C.A., Gottlieb, E.W., Thaddeus, P., & Vrtílek, J.M. 1986, *ApJ*, **303**, 446.

Gottlieb, C.A., Vrtílek, J.M., & Thaddeus, P. 1989, *ApJ*, **343**, L29.

Graedel, T.E., Langer, W.D., & Frerking, M.A. 1982, *ApJS*, **48**, 321.

Green, S., & Chapman, S. 1978, *ApJS*, **37**, 169.

Guélin, M., & Cernicharo, J. 1991, *A&A*, **244**, L21.

Guélin, M., Langer, W.D., & Wilson, R.W. 1982, *A&A*, **107**, 107.

Guélin, M., Cernicharo, J, Navarro, S., Woodward, D.R., Gottlieb, C.A., & Thaddeus, P. 1987, *A&A*, **182**, L37.

Hasegawa, T.I., & Herbst, E. 1993, *MNRAS*, **261**, 83. (HH93)

Hasegawa, T.I., Herbst, E., & Leung, C.M. 1992, *ApJS*, **82**, 167. (HHL92)

Heaton, B.D., Matthews, N., Little, L.T., & Dent, W.R.F. 1985, *MNRAS*, **217**, 485.

Henkel, C., Wilson, T.L., & Mauersberger, R. 1987, *A&A*, **182**, 137.

Herbst, E. 1989, in *Physics and Chemistry of Interstellar Molecular Clouds*, ed. G. Winnewisser & J.T. Armstrong (Springer-Verlag), p. 344.

Herbst, E., & Leung, C.M. 1986, *MNRAS*, **222**, 689.

Herbst, E., & Leung, C.M. 1989, *ApJS*, **69**, 271.

Herbst, E., & Leung, C.M. 1990, *A&A*, **233**, 177.

Herbst, E., DeFrees, D.J., & Koch, W. 1989, *MNRAS*, **244**, 668.

Hirahara, Y., Suzuki, H., Yamamoto, S., Kawaguchi, K., Kaifu, N., Ohishi, M., Takano, S., Ishikaua, S., & Masuda, A. 1992, *ApJ*, **394**, 539.

Hjalmarson, Å., & Friberg, P. 1988, in *Formation and Evolution of Low Mass Stars*, ed. A.K. Dupree and M.T.V.T. Lago (Dodrecht: Kluwer), p. 65.

Ho, P.T.P., Martin, R.N., & Barrett, A.H. 1981, *ApJ*, **246**, 761.

Hollis, J.M., Jewell, P.R., & Lovas, F.J. 1995, *ApJ*, **438**, 259.

Hollis, J.M., Snyder, L.E., Blake, D.H., Lovas, F.J., Suenram, R.D., & Ulich, B.L. 1981, *ApJ*, **251**, 541.

Hollis, J.M., Suenram, R.D., Lovas, F.J., & Snyder, L.E. 1983, *A&A*, **126**, 393.

Hollis, J.M., Snyder, L.E., Ziurys, L.M., & McGonagle, D. 1991, in Astron. Soc. Pac. Conf. Ser. Vol. 16, *Interstellar HNO. Confirming the identification.*, ed. A.D.Haschick and P.T. Ho., p. 407.

Irvine, W.M. 1995, *Advances in Space Research*, **15**, (3)35.

Irvine, W.M., Goldsmith, P.F., & Hjalmarson, Å. 1987, in *Interstellar Processes*, ed. D.J. Hollenbach and H.A. Thronson Jr. (Dordrecht: Reidel), p. 561.

Irvine, W.M., Good, J.C., & Schloerb, F.P. 1983, *A&A*, **127**, L10.

Irvine, W.M., Schloerb, F.P., & Hjalmarson, Å. 1985, in *Protostars and Planets II*, ed. D.C. Black and M.S. Matthews (Tuscon: University of Arizona), p. 579.

Irvine, W.M., Avery, L.W., Friberg, P., Metthews, H.E., & Ziurys, L.M. 1987, in *Interstellar Matter*, ed. J.M. Moran and P.T.P Ho (New York: Gordon and Breach), p. 15.

Irvine, W.M., Friberg, P., Hjalmarson, Å., Ishikawa, S., Kaifu, N., Kawaguchi, K., Madden, S.C., Mathews, H.E., Ohishi, M., Saito, S., Suzuki, H., Thaddeus, P., Turner, B.E., Yamamoto, S., & Ziurys, L.M. 1988, *ApJ*, **344**, L107.

Jaffe, D.T., Harris, A.I., & Genzel, R. 1987, *ApJ*, **316**, 231.

Jewell, P.R., Hollis, J.M., Lovas, F.J., & Snyder, L.E. 1989, *ApJS*, **70**, 833.

Johansson, L.E.B. Andersson, C., Elldér, Friberg, P., Hjalmarson, Å., Höglund, B., Irvine, W.M., Olofsson, H., & Rydbeck, G. 1984, *A&A*, **130**, 227.

Kawaguchi, K., *et al.* 1991, *PASJ*, **43**, 607.

Kawaguchi, K., Kagi, E., Hirano, T., Takano, S., & Saito, S. 1993, *ApJ*, **406**, L39.

Kenny, J.D. & Taylor, D.T. 1988, in *The Calibration of the 14 Meter FCRAO Telescope at a Wavelength of 3 Millimeters*, FCRAO Report 323.

Killian, T.C., Vrtilek, J.M., Gottlieb, C.A. Gottlieb, E.W., & Thaddeus, P. 1990, *ApJ*, **365**, L89.

Kleinmann, D.W., & Low, F.J. 1967, *ApJ*, **149**, L1.

Kollberg, E.L., & Zirath, H.H.G. 1983, *IEEE Trans. Microwave Theory and Tech.*, **MTT-31**, 230.

Kuiper, T.B.H., Zuckerman, B., Kakar, R.K., & Rodriguez, E.N., 1975, *ApJ*, **200**, L151.

Langer, W.D., & Graedel, T.E. 1989, *ApJS*, **69**, 241.

Langer, W.D., Graedel, T.E., Frerking, M.A., & Amentrout, P.B. 1984, *ApJ*, **277**, 581.

Lee, S.K., Ozeki, H., & Saito, S. 1995, *ApJS*, **98**, 351.

Linke, R.A., Guélin, M., & Langer, W.D. 1983, *ApJ*, **271**, L85.

Lis, D.C., & Carlstrom, J.E. 1993, in *Protostars and Protogalxies*. APS conference series.

Lis,D.C., Carlstrom, J.E., & Keene, J. 1991, *ApJ*, **380**, 429.

Lis, D.C., & Goldsmith, P.F. 1989, *ApJ*, **337**, 704.

Lis, D.C., & Goldsmith, P.F. 1990, *ApJ*, **356**, 195.

Lis, D.C., Goldsmith, P.F., Carlstrom, J.E., & Scoville, N.Z. 1993, *ApJ*, **402**, 238.

Liszt, H.S., & Turner, B.E. 1978, *ApJ*, **224**, L73.

Little, L.T., MacDonald, G.H., Riley, P.W., & Matheson, D.N. 1979, *MNRAS*, **189**, 539.

Lonsdale, C.J., Becklin, E.E., Lee, T.J., & Stewart, J.M. 1982, *AJ*, **87**, 1819.

Lovas, F.J. 1985, *unpublished spectral line catalog.*

Lovas, F.J. 1992, *J. Phys. Chem. Ref. Data*, **21**, 181.

Lovas, F.J. & Tiemann, E. 1974a, *J. Phys. Chem. Ref. Data*, **3**, 627.

Lovas, F.J. & Tiemann, E. 1974b, *J. Phys. Chem. Ref. Data*, **3**, 739.

Mangum, J.G., Wootten, A., & Mundy, L.G. 1992, *ApJ*, **388**, 467.

Mangum, J.G., Wootten, A., Lorren, R.B., & Wadiak, E.J. 1990, *ApJ*, **348**, 542.

Martin, A.H.M.M. 1973, *MNRAS*, **163**, 141.

Martin-Pintado, J., de Vicente, P., Wilson, T.L., & Johnston, K.J. 1990, *A&A*, **236**, 193.

Masson, C.R., & Mundy, L.E. 1988, *ApJ*, **324**, 538.

Matsakis, D.N., Bologna, J.M., & Schwartz, P.R. 1980, *ApJ*, **241**, 655.

Matthews, H.E., & Sears, T.J. 1983, *ApJ*, **267**, L53.

Mauersberger, R., Wilson, T.L., & Henkel, C. 1988, *A&A*, **210**, 123.

Mauersberger, R., Henkel, C., Wilson, T.L., & Walmsley, C.M. 1986, *A&A*, **162**, 199.

McGonagle, D., & Irvine W.M. 1993, in NARM Proceedings, *Recent Development in Millimeter-wave and Infrared Astronomy*, eds. Se Hyung Cho and Hyun Soo Chung, (Korea: KAO), p. 65.

McGonagle, D., & Irvine W.M. 1995, *in preperation.*

McGonagle, D., Irvine, W., & Minh, Y. 1992, in IAU Symposium, *Astrochemistry of Cosmic Phenomena*, ed. P.D. Singh, p. 227.

McGonagle, D., Irvine, W.M., & Ohishi, M. 1994, *ApJ*, **422**, 621.

McGonagle, D., Irvine, W.M., & Horvath, M. 1995, *in preperation.*

McGonagle, D., Ziurys, L.M. & Irvine, W.M. 1995, *in preperation.*

McGonagle, D., Ziurys, L.M., Irvine, W.M., & Minh, Y.C. 1990, *ApJ*, **359**, 121.

Menten, K.M., & Reid, M.J. 1995, *ApJ*, **445**, L157.

Millar, T.J. 1990, in *Molecular Astrophysics*, ed. T.W. Hartquist (Cambridge: Cambridge University Press), p. 613.

Millar, T.J., & Herbst, E. 1990, *A&A*, **231**, 446.

Millar, T.J., Herbst, E., & Charnley, S.B. 1991, *ApJ*, **369**, 147.

Millar, T.J., Leung, C.M. & Herbst, E. 1987, *A&A*, **183**, 109.

Millar, T.J., Olofsson, H., Hjalmarson, Å, & Brown, P.D. 1988, *A&A*, **205**, L5.

Millar, T.J., Rawlings, J.M.C., Bennett A., Brown P.D., & Charnley S.B. 1991, *A&A Suppl.*, **87**, 585.

Minh, Y.C. 1990, *Ph.D. Thesis, University of Massachusetts.*

Minh, Y.C., Irvine, W.M., & Brewer, M.K. 1991, *A&A*, **244**, 181.

Minh, Y., Irvine, W.M. & Ziurys, L.M. 1989, *ApJ*, **345**, L63.

Minh, Y.C., Ziurys, L.M., Irvine, W.M., & McGonagle, D. 1990, *ApJ*, **360**, 136.

Minh, Y.C., Ziurys, L.M., Irvine, W.M., & McGonagle, D. 1991, *ApJ*, **366**, 192.

Minh, Y.C., Ohishi, M., Roh, D.G., Ihsiguro, M., & Irvine W.M. 1993, *ApJ*, **411**, 773.

Ohishi, M., Hiroko, S., Ishikawa, S., Yamada, C., Kanamori, H., Irvine, W.M., Brown, R.D., Godfrey, P.D., & Kaifu, N. 1991, *ApJ*, **380**, L39.

Ohishi, M., Irvine, W.M., & Kaifu 1992, in IAU Symposium *Astrochemistry of Cosmic Phenomena*, ed. P.D. Singh p. 171.

Ohishi, M., McGonagle, D., Irvine, W.M., Yamamoto, S., & Shuji, S. 1994, *ApJ*, **427**, L51.

Ohishi, M., Ishikawa, S., Yamamoto, S., Saito, S., & Amano, T. 1995, *ApJ*, **446**, L43.

Olano, C.A., Walmsley, C.M., & Wilson, T.L. 1988, *A&A*, **196**, 194.

Olofsson, H., Hjalmarson, Å., & Rydbeck, O.E.H. 1981, *A&A*, **100**, L30.

Olofsson, H., Elldér J., Hjalmarson, Å., & Rydbeck, G. 1982, *A&A*, **113**, L18.

Pearson, J.C., Sastry, K.V.L.N., Herbst, E., & De Lucia, F. 1994 , *J. Mol. Spectro.*, **166**, 120.

Plambeck, R.L., Wright, M.C.H., Welch, W.J., Bieſing, J.H., Baud, B., Ho, P.T.P., & Vogel, S.N. 1982, *ApJ*, **259**, 617.

Plummer, G.M., Herbst, E., De Lucia, F.C., & Blake, G.A. 1986, *ApJS*, **60**, 949.

Powell, F.X., & Lide, D.R. 1964, *J. Chem. Phys.*, **41**, 1413.

Pratap, P., Irvine, W.M., Schloerb, F.P., Snell, R.L., Bergin, E.A., Miralles, M.P. Miralles, Dickens, J., & McGonagle, D. 1994, in *Clouds, Cores, an Low Mass Stars* ASP Conference Series, **65**, p. 25.

Predmore, C.R. 1995, in *Multi-Feed Systems for Radio Telescopes* ASP Conference Series, **75**, p. 259.

Press, W.H., Flannery, B.P. Teukolsky, S.A., & Vetterling, W.T. 1988, *Numerical Recipes in C*, (Cambridge: Cambridge University Press).

Pwa, T.H., & Pottasch, S.R. 1986, *A&A*, **164**, 116.

Rydbeck, O.E.H, Irvine, W.M., Hjalmarson, Å., Rydbeck, G., Elldér, J., & Kollberg, E. 1980, *ApJ*, **235**, L171.

Saito, S., Kawaguchi, K., Yamamoto, S., Ohishi, M., Suzuki, H., & Kaifu, N., 1987, *ApJ*, **317**, L115.

Schiff, H.I., & Bohme, D.K. 1979, *ApJ*, **252**, 740.

Scoville, N.Z., & Solomon, P.M. 1973, *ApJ*, **180**, 31.

Scoville, N.Z., & Solomon, P.M. 1974, *ApJ*, **187**, L67.

Scoville, N.Z., Hall, D.N.B., Kleinmann, S.G., & Ridgeway, S.T. 1982, *ApJ*, **253**, 136.

Smith, D., & Adams, N.G. 1985, in *Molecular Astrophysics*, eds. G.H.F. Diercksen *et al.* (Dodrecht: Reidel), p. 453.

Smith, I.W.M. 1988, in *Rate Coefficients in Astrochemistry*, ed. T.J. Millar and D.A. Williams (Dordrecht: Reidel), p. 103.

Sobolov, V.V. 1960, *Moving Envelopes of Stars* (Cambridge: Havard University Press).

Steimle, T.C, Saito, S., & Takano, S. 1993, *ApJ*, **410**, L49.

Storey, J.W.V., Watson, D.M., Townes, C.H., Haller, E.E., & Hansen, W.L. 1981, *ApJ*, **247**, 136.

Sutton, E.C., Blake, G.A., Masson, C.R., & Phillips, T.G. 1985, *ApJS*, **58**, 341.

Suzuki, H. 1983, *ApJ*, **272**, 579.

Suzuki, H., Morimoto, M., Kaifu, N., Friberg, P., Irvine, W.M., Matthews, H.E., & Saito, S. 1985, in IAU Symposium 112 *The Search for Extraterrestrial Life: Recent Developments*, ed. M.D. Papagiannis, (Dordrecht: Reidel), p. 139.

Swade, D.A. 1987, *Ph.D. Thesis, University of Massachusetts.*

Swade, D.A., & Schloerb, P.F. 1992, *ApJ*, **392**, 543.

Tarafdar, S.P., & Dalgarno, A. 1990, *A&A*, **232**, 239.

Tatum, J.B. 1986, *ApJS*, **60**, 433.

Tölle, F., Ungerechts, H., Walmsley, C.M., Winnewisser, G., & Churchwell, E. 1981, *A&A*, **95**, 143.

Townes, C.H., & Schawlow A.L. 1975, *Microwave Spectroscopy*, (New York: Dover Publications).

Turner, B.E. 1989, *ApJS*, **70**, 539.

Turner, B.E. 1991, *ApJS*, **76**, 617.

Turner, B.E. 1992, *ApJ*, **396**, L107.

Turner, B.E. 1994, *ApJ*, **430**, 727.

Ungerechts, H., Walmsley, C.M., & Winnewisser, G. 1986, *A&A*, **157**, 207.

Ungerechts, H., Bergin, E.A., Carpenter, J., Goldsmith. P.F., Irvine, W.M., Lovell, A., McGonagle, D., Schloerb, F.P., & Snell, R.L., 1992, in IAU Symposium, *Astrochemistry of Cosmic Phenomena*, ed. P.D. Sing, p. 271.

Ungerechts, H., Bergin, E.A., Goldsmith, P.F., Irvine, W.M., Schloerb, F.P., & Snell, R.L. 1994, in *Proceedings of the Zermatt Symposium*, in press.

Vanden Bout, P.A., Mundy, L.G., Davis, J.H., Loren, R.B., & Butner, H. 1985, *ApJ*, **295**, 139.

Vogel, S.N., Genzel, R., & Palmer, P. 1987, *ApJ*, **316**, 243.

Vogel, S.N., Wright, M.C.H., Plambeck, R.L., & Welch, W.J. 1984, *ApJ*, **283**, 655.

Vrtílek, J.M., Gottlieb, C.A., LePage, T.J., & Thaddeus, P. 1987, *ApJ*, **316**, 826.

Vrtílek, J.M., Gottlieb, C.A., Gottlieb, E.W., Killian, T.C., & Thaddeus, P. 1990, *ApJ*, **364**, L53.

Vrtílek, J.M., Gottlieb, C.A., Gottlieb, E.W., Wang, W., & Thaddeus, P. 1992, *ApJ*, **398**, L73.

Watson, W.D., & Walmsley, C.M. 1982, in *Regions of Recent Star Formation*, eds. R.S. Roger and P.E. Dewdney (Dordrecht: Reidel), p. 357.

Wilson, T.L., & Mauersberger, R. 1990, *A&A*, **239**, 305.

Wilson, T.L., Bieging, J., & Downs, D. 1978, *A&A*, **63**, 1.

Wilson, T.L., Gaume, R.A., & Johnston, K.L. 1993, *ApJ*, **402**, 230.

Woods, R.C., 1987, in *Astrochemistry*, ed. M.S. Vardya and S.P. Tarafdar (Dordrecht: D. Reidel), pp. 77.

Woodward, D.R., Pearson, J.C., Gottlieb, C.A., & Thaddeus, P. 1988, *ApJ*, **316**, 826.

Wootten, A., Loren, R.B., & Bally, J. 1984, *ApJ*, **277**, 189.

Wright, M.C.H., Plambeck, R.L., Vogel, S.N., Ho, P.T.P, & Welch, W.J. 1983, *ApJ*, **267**, L41.

Wynn-Williams, C.G., Genzel, R., Becklin, E.E., & Downes, D. 1984, *ApJ*, **281**, 172.

Yamamoto, S., Saito, S., Kawaguchi, K., Kaifu, N., Suzuki, H., & Ohishi, M., 1987, *ApJ*, **317**, L119.

Yamamoto, S., Saito, S., Suzuki, H., Deguchi, S., Kaifu, N., Ishikawa, S., & Ohishi, M. 1990a, *ApJ*, **348**, 363.

Yamamoto, S., Saito, S. Kawaguchi, K., Chikada, Y. Suzuki, H., Kaifu, N., & Ishikawa, S. 1990b, *ApJ*, **361**, 318.

Ziurys, L.M., 1988, *ApJ*, **324**, 544.

Ziurys, L.M., & Friberg, P. 1987, *ApJ*, **314**, L49.

Ziurys, L.M. & McGonagle, D., 1993, *ApJS*, **89**, 155.

Ziurys, L.M., Erickson, N.R., & Grosslein, R.M. 1988, in *Interstellar Matter*, ed. J.M. Moran and P.T.P. Ho (New York: Gorden and Breach), p. 225.

Ziurys, L.M., Wilson, T.L., & Mauersberger, R. 1990, *ApJ*, **356**, L25.

Ziurys, L.M., McGonagle, D., Minh, Y., & Irvine, W.M. 1991, *ApJ*, **373**, 535.

Ziurys, L.M., Apponi, A.J., Hollis, J.M., & Snyder, L.E. 1994, *ApJ*, **436**, L181.